Technische Universität München
TUM School of Engineering and Design

Direct and Inverse Methods to Account for Epistemic and Lack-of-Knowledge Uncertainties in Turbine Development

Norbert Werner Ludwig

Vollständiger Abdruck der von der TUM School of Engineering and Design der Technischen Universität München zur Erlangung eines

Doktors der Ingenieurwissenschaften (Dr.-Ing.)

genehmigten Dissertation.

Vorsitz:

Prof. Dr.-Ing. Kai-Uwe Bletzinger

Prüfer der Dissertation:

1. Prof. Dr.-Ing. habil. Fabian Duddeck
2. Prof. Dr.-Ing. Michael Beer

Die Dissertation wurde am 02.11.2023 bei der Technischen Universität München eingereicht und durch die TUM School of Engineering and Design am 15.02.2024 angenommen.

Declaration of Independence

I hereby declare that this thesis is entirely the result of my own work except where otherwise indicated. I have only used the resources given in the list of references.

Munich, November 2nd, 2023

Norbert Werner Ludwig

Abstract

English

The development process of jet engines is a challenging issue as it includes various engineering disciplines with partially competing goals. In view of rising kerosene prices and the global warming, the main focus still lies on the minimization of the specific fuel consumption. Apart from that, there is an increasing requirement on the engine's robustness because airliners tend to lease instead of buying jet engines. This goes along with a higher financial risk on the engine manufacturer side as they have to take over the costs for unexpected shop visits. In order to ensure a robust design, the development process must be complemented with stochastic methods to account for the uncertainty sources.

Throughout the thesis, an interdisciplinary simulation model of a low-pressure turbine secondary air system is set up. The methodological focus of the work is on the modeling of epistemic uncertainty sources and can be divided into three parts.
The first one is devoted to the uncertainty quantification with a special emphasis on inverse problems. The second focal point deals with the screening of the interdisciplinary model input quantities to cut down the complexity of the system. Based upon the reduced parameter set, the third and last research topic is about conducting a robust design optimization (RDO) of the secondary air system. Due to the limited amount of information about the uncertainty sources, non-probabilistic methods have been developed and adapted from literature for the above-mentioned research goals.

For the inverse uncertainty quantification problem, a novel approach has been introduced where the variation of the model response is described with the help of a minimum-volume enclosing ellipsoid. Compared to state-of-the-art methods from literature, it shows a higher accuracy and efficiency for high-dimensional problems. Throughout the subsequent variable screening, which is based upon repeated Taylor series approximations, a significant reduction of the epistemic input space by more than 60% has been achieved. Nevertheless, it turned out that the remaining input space dimension is too large for a RDO with standard sampling techniques. Thereof, the non-intrusive imprecise stochastic sampling (NISS) strategy has been adapted which allows the modeling of lack-of-knowledge uncertainty sources with probability-boxes. In comparison with a pure probabilistic RDO, the NISS-based approach has shown a superior performance of the secondary air system under changing ambient and flight condition scenarios.

Deutsch

Die Entwicklung von Flugzeugtriebwerken ist ein herausfordernder Prozess, bei dem teilweise konkurrierende Anforderungen verschiedener Fachdisziplinen miteinander vereint werden müssen. Im Hinblick auf steigende Kerosinpreise sowie die globale Erderwärmung liegt der Hauptfokus auf der Optimierung des spezifischen Kraftstoffverbrauchs. Darüber hinaus spielen steigende Anforderungen an die Robustheit eine zunehmend wichtige Rolle für den Entwicklungsprozess, welche vor allem auf die Einführung des „Power-by-the-hour“ Geschäftsmodells zurückgeht. Hierbei werden über einen Leasingvertrag Betriebsstunden an den Kunden verkauft, wodurch Triebwerkshersteller einem höheren finanziellen Risiko im Falle ungeplanter Reparaturen ausgesetzt sind. Zur Erreichung eines robusten Designs bedarf es der Erweiterung des Entwicklungsprozesses um stochastische Methoden.

Im Rahmen dieser Dissertation wird ein interdisziplinäres Simulationsmodell für das Sekundärluftsystem einer Niederdruckturbine aufgebaut. Der methodische Fokus liegt auf der Implementierung von Methoden zur Berücksichtigung von epistemischen Unsicherheiten im Designprozess und kann in drei Schwerpunkte untergliedert werden.
Der erste Bereich befasst sich mit der Quantifizierung epistemischer Unsicherheitsquellen, wobei ein Hauptaugenmerk auf inverse Probleme gelegt wird. Im daran anschließenden Teil geht es um die Entwicklung eines geeigneten Screeningverfahrens zur Reduzierung des epistemischen Parameterraums. Der dritte und letzte Themenbereich beschäftigt sich mit der Robust Design Optimierung (RDO) des Sekundärluftsystems. Aufgrund der teilweise unvollständigen Datenbasis werden für die oben genannten Problemstellungen Methoden diskutiert, die über eine rein probabilistische Betrachtungsweise hinausgehen.

Für die inverse Unsicherheitsquantifizierung wurde eine neue Methodik entwickelt, welche die Parametervariation von epistemischen Unsicherheitsquellen mit Hilfe einer einhüllenden Ellipse beschreibt. Im Vergleich mit etablierten Ansätzen aus der Literatur zeigt dieses Vorgehen eine deutliche Steigerung der Recheneffizienz für hochdimensionale Simulationsmodelle. Durch die darauffolgende Sensitivitätsstudie konnte der epistemische Parameterraum des Sekundärluftsystemmodells um ca. 60% verringert werden. Trotz der deutlichen Reduktion der Komplexität kann für die robuste Optimierung kein standardmäßiges Stichprobenverfahren wie die Monte Carlo Simulation verwendet werden. Aus diesem Grund wurde das „non-intrusive imprecise stochastic sampling“ (NISS) Verfahren angewendet und für Anforderungen an die robuste Optimierung weiterentwickelt. Abschließend wurden die Ergebnisse mit einer rein probabilistischen RDO verglichen. Hierbei zeigte sich, dass die NISS-basierte Optimierung zu einer wesentlich stabileren Performance des Kühlluftsystems unter variierenden Flug- und Umgebungsbedingungen führt.

Acknowledgments

First and foremost, I would like to thank Prof. Fabian Duddeck for offering me the chance to work as research associate at his chair. Especially his positive attitude towards scientific results, which seemed to be sobering at the first glance, have encouraged me to stay on track over this long period of time.

A special thanks goes to Giulia Antinori for the professional supervision of the research topic from the side of MTU Aero Engines. At this point, I would also like to thank Julia Hörmann, Lukas Bruder, Stefan Kimmel, Yannick Muller and Julian von Lautz who have greatly supported me within MTU Aero Engines. Moreover, my appreciation is addressed to Andreas Fischersworring-Bunk who initiated the fruitful cooperation between MTU Aero Engines and the Chair of Computational Solid Mechanics and thereof made this project possible.

My acknowledgments are also directed to my colleagues at the Chair of Computational Solid Mechanics, Koushyar Komeilizadeh, Catharina Czech, Lisa Pretsch, Arne Kaps, Paolo Ascia and Nivesh Dommaraju for the nice scientific discussions over the past years. Thank you also to Marco Daub for the constructive collaboration which has led to successful scientific publications. Another word of thanks goes to my mentor Prof. Michael Beer for the warm welcome at his chair as well as the valuable feedback throughout my midterm presentation.

Finally, I would like to thank my family who has always encouraged me in my plans. I highly appreciate the strong support.

Contents

Chapter 1

INTRODUCTION

The development procedure of modern aircraft engines is a challenging task which can, compared to other engineering products, even stretch out over a period of more than a decade. The reason for the lengthy process comes from the high safety requirements in the aviation industry and the competing objectives from the various disciplines involved in the design process. All of this leads to a volatile situation for the engine manufacturers, as they have to take a high financial risk before generating income on the long term.

A key prerequisite for placing a new jet engine successfully on the market is to reduce the airliner's operating expenses. Since fuel costs account for 35%, and thus for the major share of the overall expenses, a main objective is to minimize the engine's SFC (specific fuel consumption). Apart from that, the maintenance and inspection represent a significant fraction of around 16%. Among the latter, the jet engine maintenance costs is the dominating factor with a portion of about 40%, see Fig. 1.1 [39].

Over the last years, airliners tend more and more towards the conclusion of so-called PBH (power-by-the-hour) contracts instead of buying the engine. In principle, the PBH agreement is a leasing contract between aircraft operator and engine manufacturer. The latter guarantees for a comprehensive maintenance over a certain period of time for which the operator has to pay an hourly rate for each flying hour. For the airliners, this contract type allows a better financial monitoring as the costs pertaining to maintenance and repair can be predicted with certainty. From the suppliers' perspective, the agreement offers on the one hand great benefits if the leasing product runs reliably without any unscheduled downtime. On the other

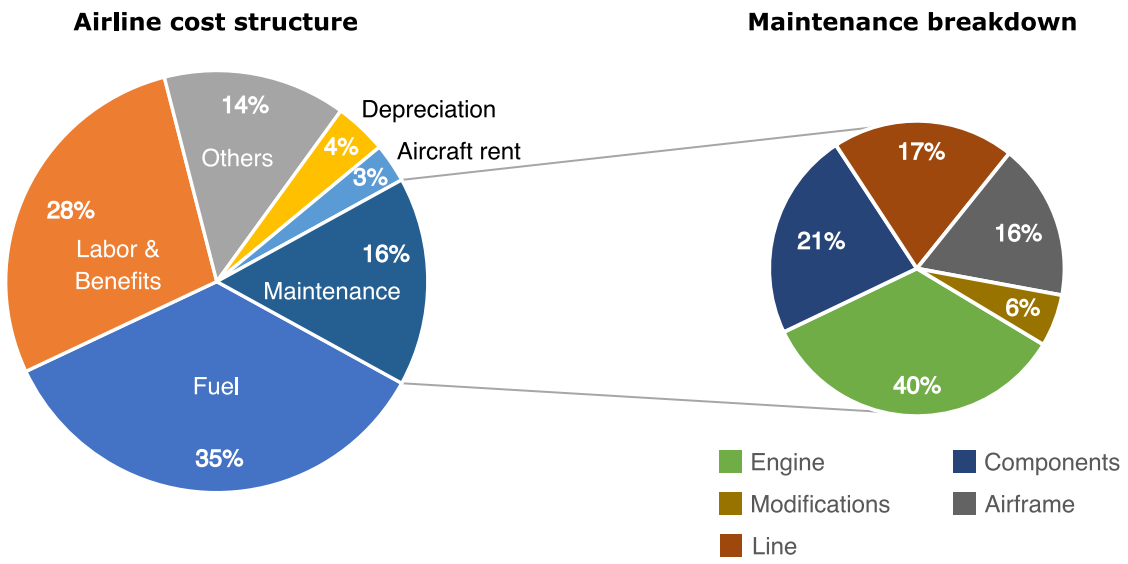

Figure 1.1 Typical airline cost structure (left) and maintenance breakdown (right) [39].

hand, engine owners have to take over the financial risk for unexpected failures causing an aircraft-on-ground scenario in the worst case.

The origin of PBH contracts for jet engines goes back to the year 1962. During that time, Rolls-Royce had severe problems of introducing its *Viper 20* engine to the market as an option for the de Havilland/Hawker Siddeley 125 business jet. The potential customers were skeptic due to the unavailability of spare parts whereas the aircraft mechanics were not willing to service the engine because of its low market share. To solve this "hen and egg" problem, the company decided to launch a new business concept which gives the customer the opportunity to buy flight time instead of the engine itself. [79][1]

Since its invention, the original business model has been enhanced by additional features such as the engine trend monitoring which enables to register the engine's parameters in real time [2]. In 2018, the global PBH market size has reached a value of 20 billion USD and is expected to grow constantly by up to 6% per year within the next decade [85, 140]. The continuous growth rate is mainly a consequence from the increasing number of low-cost airliners which outsource the maintenance to third parties.

As a result of this trend, jet engine manufacturers have to evolve from a classical product designer to a mobility supplier. Apart from the economic consequences, the changing business case also affects the engine's requirements and thereof the key aspects of the development process. Keeping the SFC as low as possible remains the most important design objective but since the financial risk of a possibly high maintenance frequency is carried by the manufacturer, there is an increasing demand for a robust engine design.

An important contribution to achieve this goal is to put more effort into deeper analytical analyses. Especially the implementation of stochastic methods into the development process entails

[1] Citations behind the full stop refer to the preceding paragraph.

a high potential to optimize the design in view of its robustness. Within the scope of this thesis, the focus lies on the jet engine's cooling system. To be more precise, the part of the secondary air system (SAS) being responsible for the cooling of the LPT (low-pressure turbine) disk is investigated in greater detail. In the past, several studies have been conducted to enhance the deterministic design approach by probabilistic concepts. The great benefit comes with the increased insight of the system behavior as well as the knowledge gained from the stochastic analyses.

The application of pure probabilistic methods presumes a sufficient amount of data about the uncertainty sources. However, modelers most of the time face scenarios where the available information is scarce or incomplete. For example, in the early design stage the geometrical variation of a component can hardly be quantified due to the missing measuring data. In such a case, the assignment of a probabilistic distribution is hard to justify and can lead to misleading conclusions.

To tackle this issue, the scope of this thesis concerns the question how to deal with lack-of-knowledge uncertainty sources in the design process of the LPT secondary air system. The overall goal is the development of strong methods to achieve a robust design for the cooling system. The structure of this work is as follows:

Chapter 2 gives a general introduction into the interdisciplinary design process of the SAS (secondary air system) and explains the aims and objectives of the thesis. After that, state-of-the-art methods from literature are discussed throughout Chap. 3 which are related to the aims and objectives of the previous chapter. The literature review is followed by the methodological part in Chap. 4 which introduces new concepts for the quantification of lack-of-knowledge uncertainties. In Chap. 5, the developed methods are applied to the industrial use case of this thesis, i.e., the interdisciplinary model of a jet engine's SAS. Finally, Chap. 6 provides conclusive remarks and an outlook for future research topics.

Chapter 2

MOTIVATION: Challenges in the Jet Engine Development Process

In general, jet engines belong to the group of thermal engines as they convert heat into kinetic energy. In short, the fundamental principle comprises the following steps: (i) intake and compression of air; (ii) addition of heat throughout the combustion of fuel; (iii) expansion of the working fluid while passing through the nozzle. As the fuel-air mixture emitted from the engine has a higher velocity as the ingoing air, a propulsive force is generated in opposite flow direction according to Isaac Newton's third law of motion. Within the scope of this thesis, the application case is a turbofan jet engine which is characterized by a high bypass ratio between $9{:}1$ and $12.5{:}1$ depending on the engine type [3].
In order to better understand the challenges of the jet engine development process, the basic functioning of a turbofan is explained with the help of Fig. 2.1. Apart from the schematic drawing, it includes the nomenclature of the fundamental stations according to the ARP 755A standard [12]. After the engine intake, the inflow hits the fan which leads to a pre-compression of the cold air followed by a separation into bypass and core gas flow. As indicated by the name, the latter enters the core engine which encompasses the components exposed to extremely high temperatures and pressures. In principle, this part of the engine consists of compressor, burner and turbine. Like most of the civil jet engines, the application case of this thesis deals with a two-shaft engine. Hence, the compression of the core gas flow takes place in two steps by passing through the LPC (low-pressure compressor) and thereafter through the HPC (high-pressure compressor). Then, the compressed air flows into the burning chamber

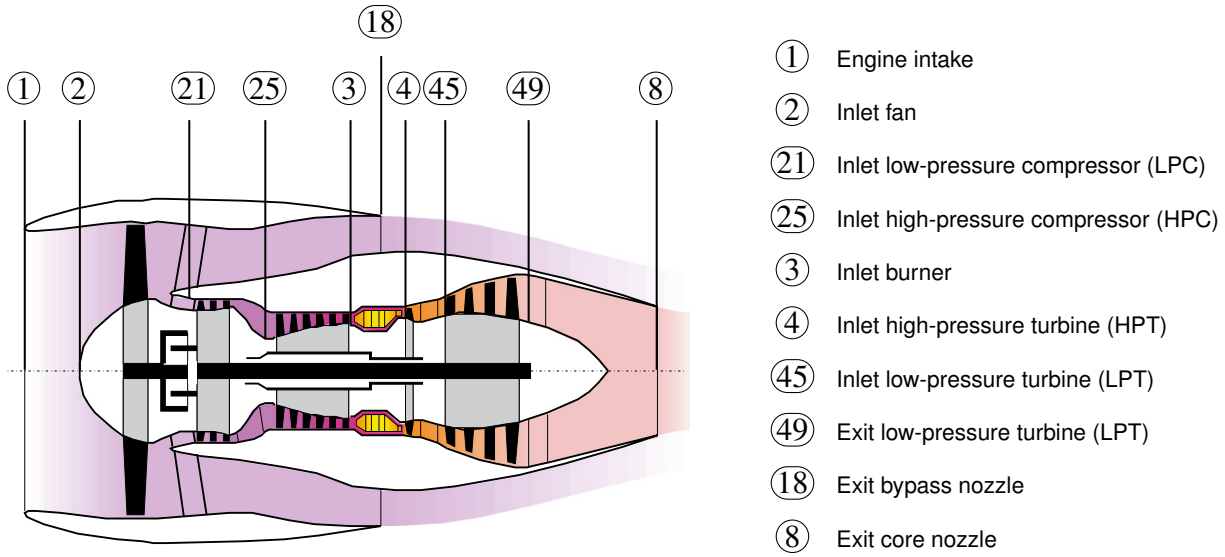

Figure 2.1 Schematic drawing and station numbering of a turbofan engine. Graphical representation taken from [66].

where it is mixed with fuel and burned at constant pressure. The hot fuel-air mixture, which reaches a temperature of more than $1,000^{\circ}\ C$, then enters the HPT (high-pressure turbine) which is connected with the HPC by the high-pressure shaft. The amount of energy extracted from the core gas flow throughout the expansion is in balance with the energy required for the compression process within the HPC and associated losses. After that, the partially expanded gas mixture is guided through the LPT which is linked to the LPC as well as the fan by the low-pressure shaft. Thus, the energy delivered by the LPT is consumed by two compressor modules. Finally, the gas flow gets accelerated while passing through the core nozzle. The thereby generated thrust is only a small portion of the total net thrust provided by the engine. The overwhelming part results from the acceleration of the bypass flow when exiting the engine throughout the bypass nozzle because of the much higher amount of mass flow.

The focus of this thesis lies on the LPT module whose inlet and exit is described by the stations 45 and 49, respectively. More in detail, the secondary air system (SAS) of the module is analyzed which has the purpose to ensure a sufficient cooling of the turbine disk. Since the performance of the SAS is affected by pressure and temperature boundary conditions from the core gas flow, an interdisciplinary model of the cooling system is built which simulates these interactive effects.

The remaining parts of this chapter are arranged as follows: Section 2.1 gives a detailed introduction into the interdisciplinary modeling approach. Further, the uncertainty sources of the various disciplines as well as the categorization of the corresponding model parameters are discussed. After that, Section 2.2 provides a literature review on relevant publications about uncertainty quantification and robust design optimization in the field of turbomachinery and jet propulsion. Finally, the aims and objectives of the thesis are outlined in Section 2.3.

2.1 Interdisciplinary Modeling Approach for a Low-Pressure Turbine Secondary Air System

The design process of jet engine components requires the analysis of multiple engineering disciplines. A stand-alone modeling procedure for the cooling system of the LPT module is therefore not reasonable as it cannot represent dependencies with other components and subsystems. The interdisciplinary SAS model, which serves here as industrial test case for the uncertainty studies, is basically a combination of the following three computational models: performance calculation, aerodynamic simulation and SAS model. Note, that a complete design process requires also thermal and structural analyses which are not considered within the scope of this thesis.
Each of the three above-mentioned disciplines is explained in detail within Section 2.1.1. Then, Section 2.1.2 covers a discussion about the uncertainty sources during an early stage of the design procedure.

2.1.1 Components of the Interdisciplinary Secondary Air System Model

The first discipline of the development process is the **performance calculation** with the help of which the interaction between the engine's components can be predicted for different flight conditions. The basis for this simulation is the lossy Joule-Brayton process which describes the general thermodynamic cycle of gas turbines. The following paragraphs are based upon the publications [30, 38, 141].
Since jet engines are a composition of various components, performance simulation programs have a modular design. This means that every component is represented by a separate module. Figure 2.2 illustrates the modular characteristics and uses the same standard for the station numbering as in Fig. 2.1. The general purpose of the performance calculation is to simulate how the gas flow characteristics change from one component to the next one. The concatenation of all changes yields a representation for the engine's thermodynamic cycle.
As mentioned before, each component is modeled by a separate module whose operating behavior is given by means of a characteristic map. For example, a compressor map describes the relation between pressure ratio, mass flow rate, efficiency and rotational speed. In an early design stage, the data for the derivation of these charts is gathered from simulations and experience from previous engines. Later on, the characteristic maps are validated by gathering experimental data from rig[1] testing.
The core principle behind the performance calculation is to identify a thermodynamic matching between all modules for a given engine operating point. This means that the gas flow parameters (temperature, mass flow, pressure, flow velocity) at the exit of a component must coincide with the gas condition at the inlet of the subsequent module. Furthermore, the components

[1] Test rigs are used to evaluate the capability of jet engine components.

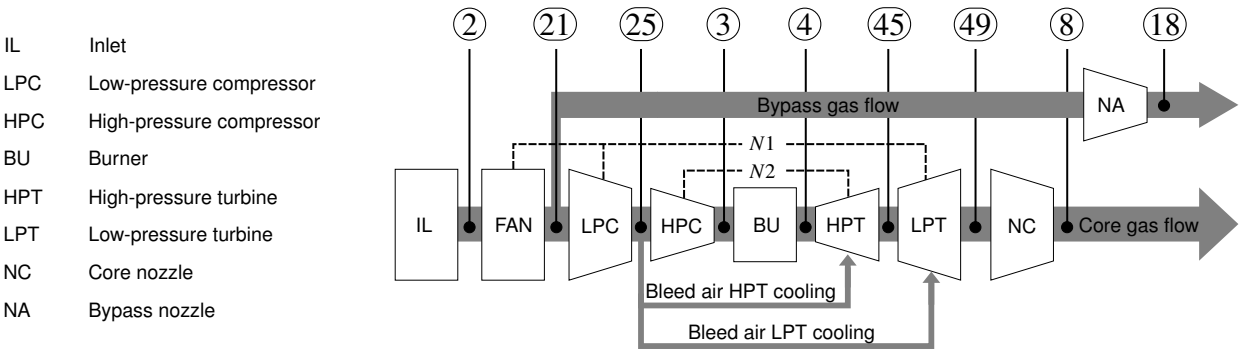

Figure 2.2 Graphical illustration of a two-spool turbofan engine performance model.

being connected by the same shaft are coupled via its rotational speed and energy balance. The starting point for the simulation is to provide the boundary conditions for the operating point under investigation which is done by describing the flight and ambient conditions. The latter are given by the flight altitude, Mach number and ambient temperature whereas the load level is typically regulated by the required amount of propulsive thrust. After that, the goal becomes to determine the modules' matching that fulfills these boundary conditions. As the components' characteristics are not given by analytical expressions, the solution is obtained in an iterative manner. The iteration parameters include gas flow conditions at decisive stations such as the turbine inlet temperature as well as parameters from the characteristic maps like the compressor pressure ratio for example. If possible, the initial guess for the numerical simulation is taken from a similar operating point. As a primary result, the model delivers the gas flow characteristics at the various stations. Even though the characteristic maps are able to capture three-dimensional effects, the representation is given in integrated form.

For the development of jet engine components, the thermodynamic cycle is analyzed for various flight phases. Without any claim to completeness, the most important operation points encounter idle, end take-off, climb and cruise phase. Especially the ADP (aerodynamic design point), which is part of the cruise phase, plays a crucial role in the conceptual design phase. Usually, the ADP is analyzed at first and used to decide about the geometrical parameters and the general setup of the aircraft engine. This includes, inter alia, the number of compressor and turbine stages as well as the bypass ratio. Hence, the purpose of the design point study is to find an engine architecture to meet the customers' requirements. Of course, if it turns out that the engine's performance is not sufficient during the off-design flight phases, a re-iteration of the ADP analysis must be performed.

Due to its high importance for the development procedure, it has been decided to conduct the uncertainty studies within this thesis for the ADP. Nevertheless, we consider a design phase where all geometrical features have been settled, i.e., the characteristic component maps remain unchanged. The MTU-internal performance program is called "MOPS" which stands for modular performance simulation. For further information about the solution procedure, the reader is referred to the manual of "GasTurb" which is a common commercial performance calculation software [66].

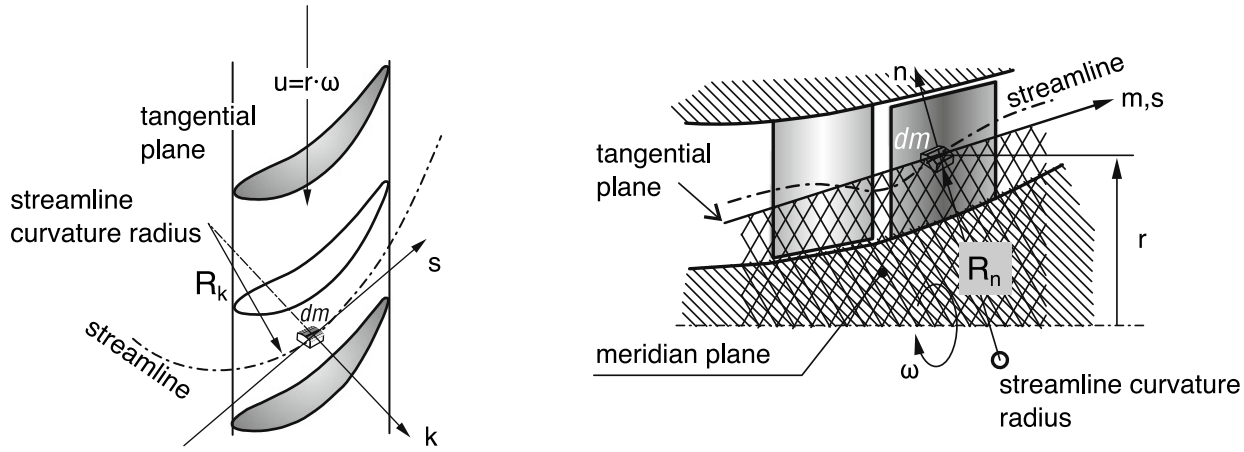

Figure 2.3 Representation of the curved three-dimensional flow through a turbine module [31].

The next step of the design procedure is the **aerodynamic simulation** of the core gas flow within the LPT module. Even though the annulus is rotationally symmetric, the gas flow has a three-dimensional characteristic as shown in Fig. 2.3. With respect to the local coordinate system, given by the s-, k- and n-axis, the equations of motion can be derived from the balance of forces at an infinitesimal small fluid element. Finally, one yields a set of DEQs in the corresponding directions given by [31]:

$$\begin{aligned}
\frac{1}{\rho}\frac{\partial p}{\partial k} &= \frac{v^2}{R_k} - r\omega^2 \sin(\sigma)\cos(\beta) - 2\omega v \sin(\sigma), \\
\frac{1}{\rho}\frac{\partial p}{\partial s} &= -\frac{F_r}{dm} - v\frac{\partial v}{\partial s} + r\omega^2 \sin(\sigma)\sin(\beta), \text{ and} \\
\frac{1}{\rho}\frac{\partial p}{\partial n} &= \frac{v^2}{R_n} + r\omega^2 \cos(\sigma) + 2\omega v \cos(\sigma)\cos(\beta).
\end{aligned} \tag{2.1}$$

All of the parameters are depicted in Fig. 2.3 except the following ones:

- β Angle between flow direction and circumferential direction
- σ Angle between meridian direction and axis of rotation
- v Local relative flow velocity
- ∂p Pressure change along k-, s- and n-direction
- F_r Frictional force in flow direction

In short, the solution of the complex 3D flow problem requires the simultaneous integration of the three partial DEQs given by Eq. (2.1) in compliance with the conservation of energy, continuity equation as well as geometrical boundary and initial conditions. In case the result should

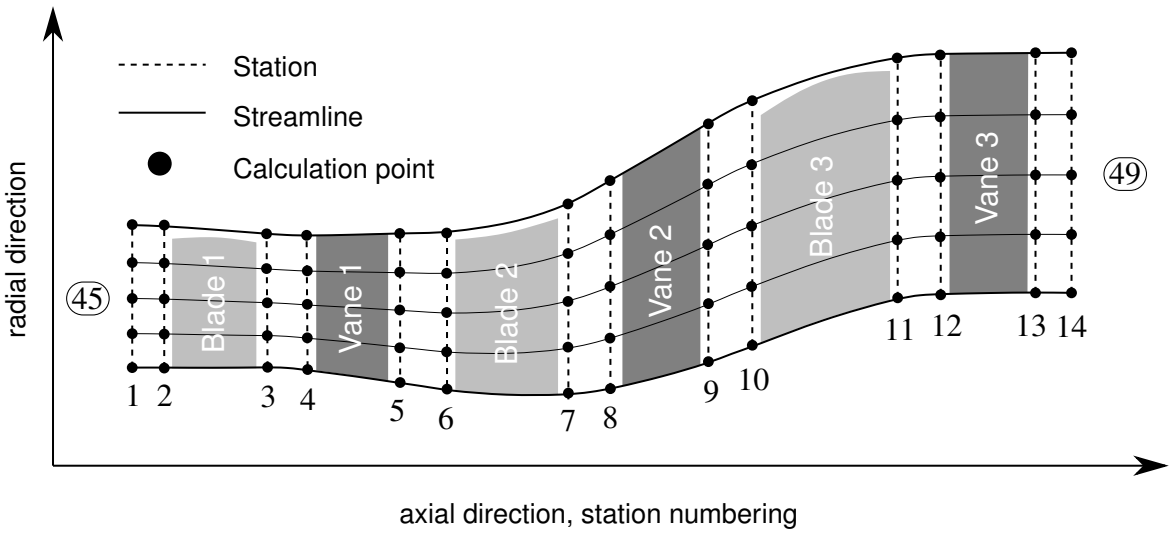

Figure 2.4 Schematic drawing of a LPT annulus projected on the 2D meridian plane, illustration is partially taken from source [96].

also account for the boundary layer along the airfoils, the set of equations must be extended by the Navier-Stokes equations which makes the problem even more complex.

In a general case, there is no closed analytical solution existing. A common approach is to solve the problem in a numerical way which is based upon replacing Eq. (2.1) with difference equations. Thereof, the flow field is discretized by a set of finite cells which build up the basis for the discretized form of the flow problem. Without going into detail, the goal of the numerical simulation is to apply the difference equations on the mesh such that all elements are in equilibrium with each other and the provided boundary conditions. With increasing model and mesh size the simulation time is growing accordingly. Even with the help of the available computer clusters, the aerodynamic simulation of the whole LPT module can take several hours which is too expensive for the conduction of uncertainty studies.

For this reason, it has been decided to derive the solution for the 3D problem by the SCM (streamline curvature method) which is a less precise but all the more efficient method. The great benefit with respect to the computational time results from assuming circumferentially symmetric flow properties. Thus, the 3D flow problem is degraded and solved in the two-dimensional meridian plane with averaged flow properties in the circumferential direction, see Fig. 2.4. The following paragraphs explain the fundamental principle of the SCM without deriving the underlying system of equations. For a more detailed explanation of the approach, the reader is referred to [96, 142].

The first preparation step for the SCM is to subdivide the annulus into several stations in axial direction. Apart from the module's inlet and exit, additional stations are introduced in front of and after each vane and blade row. In addition to that, the radial direction is also partitioned into several stream tubes by a set of streamlines. Since their exact location is not known in advance, they are distributed uniformly in radial direction. Based on that, the streamlines' cur-

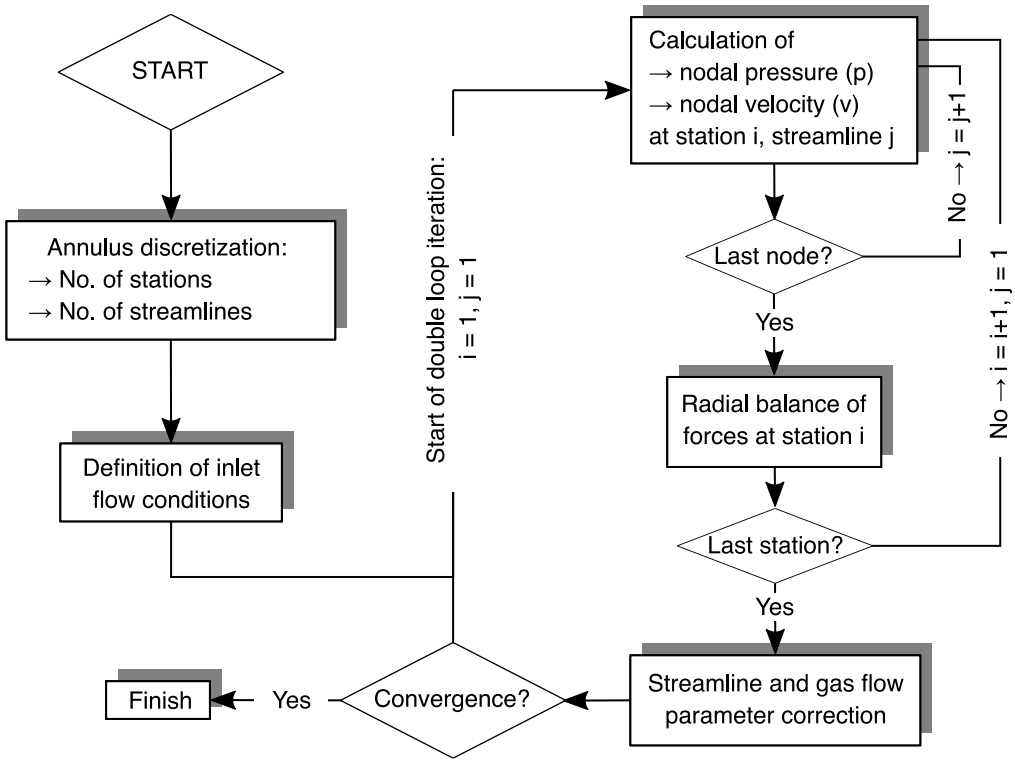

Figure 2.5 Flow chart explaining the aerodynamic simulation with the help of the SCM [96].

vature values can be derived at any station which is required for the radial balance of forces later on. In Fig. 2.4, the annulus for a three-stage turbine is shown schematically with a discretization of 14 stations and four stream tubes. The intersection points between streamlines and stations represent the nodal points at which the gas flow's absolute pressure and velocity will be determined during the calculation process.

The iterative procedure behind the SCM can be explained with the help of the flow chart in Fig. 2.5. At first, the inlet conditions, which correspond to station 45, are derived from the performance calculation. Due to the fact that they are expressed as scalar values, a radial distribution of the gas flow parameters is assumed based on experience. The initial step is followed by an iteration over all remaining stations. Within each iterative step, a second loop is performed that includes the computation of the pressure and velocity change within each stream tube between previous and current station. The governing equations are derived from the conservation of axial and angular momentum, energy balance and continuity equation. To solve the system of equations, either the pressure or velocity must be estimated at every calculation point in advance. Note, that the calculation step depends on whether the stream tube part contains a free flow or bladed section. As a result of the inner loop, the modeler obtains a first approximation for the radial pressure and velocity distribution at every node. Before the algorithm moves to the next station, the radial balance of forces must be checked. If it is not fulfilled, the gas flow parameters are adjusted accordingly.

Once the iteration of the outer loop is finished, it must be verified that the mass flow rate remains constant in every stream tube between LPT inlet and exit. As the streamline positions have been estimated, this step leads typically to a correction of the initial nodal positions and thereof also to different radii of curvature. Furthermore, the new pressure and velocity values are interpolated from the previous ones. Unless the correction step does not lead to a significant change of the gas flow parameters, the nested iteration loop must be repeated. The complete computation takes only a few seconds and is thereof incomparably faster than a three-dimensional flow analysis.
Treating the aerodynamic simulation as stand-alone discipline is not meaningful because the gas flow is directly affected by the station boundary conditions at the inlet and exit of the LPT. In order to set up a thermodynamically consistent simulation process, the performance calculation must be coupled with the aerodynamic model. Thus, the computed gas flow parameters at station 45 and 49 serve as input quantities for the subsequent aerodynamic discipline.

The last part of the interdisciplinary chain encompasses the simulation of the LPT's **cooling system** which is the actual core aspect of the thesis. Even though the secondary air system has no direct influence on the thrust generation, it is of crucial relevance for the mechanical design. Its main purpose is to provide enough cooling air to protect the turbine disk from high temperatures. This is achieved by preventing the ingestion of hot air from the main gas flow path into the disk cavities. Further aspects of the SAS within other engine modules can be found in [118] and [147].
The modeling approach of the SAS is schematically drawn by Fig. 2.6. Once again, the general 3D flow problem is analyzed in a simplified manner. In principle, the cooling flow distribution is described by a one-dimensional network which is a composition of two elements: chambers and flow passages. The first group, also referred to as junction nodes, is illustrated by the green rectangles in Fig. 2.6 and marks locations where a large volume is attributed to the cooling air flow. There, the flow velocity is deemed negligible such that the total pressure and temperature equal their absolute counterparts. On the contrary, the flow passages, represented by the blue lines, describe those parts of the cooling system with a relatively small flown-through area. Within the SAS model, the flow passages are characterized by one-dimensional pipe flows, i.e., the fluid properties are not changing normal to the flow direction. Therefore, flow passages can be seen as connection elements which transform gas flow characteristics from inlet to exit chamber. To repeat, state variables to be determined at the chambers are given by the total pressure and temperature whereas the corresponding characteristic variables for the flow passages are the cross-sectional area and flow velocity.
The overall goal of the SAS model is to simulate the pressure and temperature values at all chambers as well as the mass flow rates within the flow pipes. For the derivation of the three state variable groups, an equation system is set up resulting from the following balance equations:

- Conservation of mass at the chambers
- Conservation of energy at the chambers
- Conservation of momentum within the flow passages

The first two balance equations state that the sum of all mass and heat flow rates are equal to zero at every chamber. The conservation of momentum describes the relationship between the state variables at the inlet and exit chamber as well as the mass flow rate within the connecting flow passage. The resulting equation depends strongly on the underlying type of flow element. A short introduction will be given in context of Sec. 2.1.2 which deals with the uncertainty sources of the model. To solve the resulting system of equations, boundary conditions must be specified which are either defined in terms of temperature and pressure values at certain junction nodes or as predefined mass flow rates.

Due to the nonlinear characteristics of the momentum conservation, the equation system is solved iteratively with the help of the Newton-Raphson method. The solution procedure of the MTU-internal SAS model implementation is strongly related to the publication [99] proposing a nested iteration algorithm. At first, the nodal temperatures are computed by solving the linear energy balance. After that, the pressure values are calculated from the nonlinear momentum equations by a modified Newton-Raphson approach. Finally, the mass flow rates can be computed by putting the derived pressures and temperatures into the conservation of momentum equations.

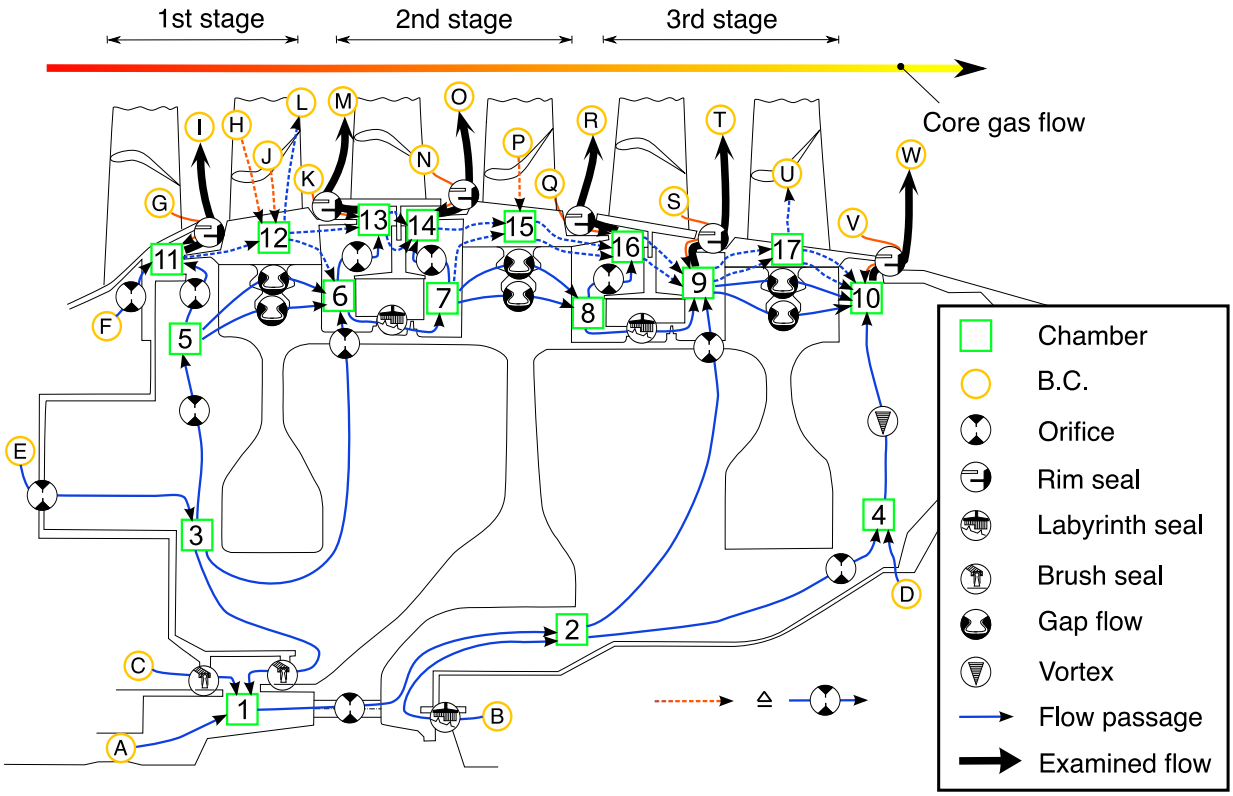

Figure 2.6 Schematic drawing of a LPT secondary air system.

As mentioned before, one main task of the SAS is to prevent the hot gas of the main flow from entering the disk cavities. Of special interest in the design phase are thereof the six flow passages at the transition to the core gas path. The flow paths of interest are localized at the left and right side of all three rotor stages and highlighted by black arrows in Fig. 2.6. Accordingly, the mass flow rates are abbreviated by $Y_{\text{rot\_1\_l}}$, $Y_{\text{rot\_1\_r}}$, $Y_{\text{rot\_2\_l}}$, $Y_{\text{rot\_2\_r}}$, $Y_{\text{rot\_3\_l}}$ and $Y_{\text{rot\_3\_r}}$, where "l" and "r" stands for left and right, respectively. In order to guarantee for a sufficient insulation these cooling gas flows have to point outward into the core gas annulus which is achieved by a positive pressure difference. Otherwise, the entering hot core gas would lead to a huge increase of the disk temperature above the structurally acceptable temperature. As a direct consequence, the component life expectancy is decreased significantly which can even cause a disk fracture.
A key factor for the realistic simulation of the cooling system is the adequate modeling of the boundary conditions denoted by the encircled letters. For this reason, a coupling of the SAS model with both the performance and aerodynamic discipline helps to improve the quality of the simulation results. The pressure and temperature values along the boundary line between SAS and core gas flow (Ⓕ - Ⓦ) are a direct outcome from the aerodynamic simulation. The remaining boundary conditions (Ⓐ - Ⓔ) represent the inflowing cooling air which is diverted from the main gas path at the LPC exit, see Fig. 2.2. Thus, these boundary conditions are directly related to $W^{(25)}$ which stands for the average core gas flow rate and is part of the primary response parameters of the performance calculation.
To summarize, the analysis of the coupled SAS model provides a more realistic modeling approach but requires more computational time due to the preceding aerodynamic and thermodynamic simulations. In the next section, the interdisciplinary process chain is reviewed with regard to the uncertainty sources and their corresponding parameters.

2.1.2 Uncertainty Sources during an Early Stage of the Design Process

As a preparation step of the uncertainty studies, the interdisciplinary process chain has been implemented within the MTU-internal development platform called OPUS (optimization utility system). Basically, the underlying models of the three disciplines are concatenated by transferring the outcome of every single discipline to the subsequent one, see Fig. 2.7. Thus, the simulation of the coupled SAS model consists of the sequential calculation of performance, aerodynamic and cooling system discipline. From the modeler's perspective, analyzing the complete interdisciplinary chain is like running a black box where the parameters of all models must be specified.
In the course of this work, we refer to an early stage of the design process at which the overall architecture of the engine and its components is settled but the amount of information about the model parameters is partially limited. In the following, an introduction over all considered uncertainty sources and their representative descriptors is provided.

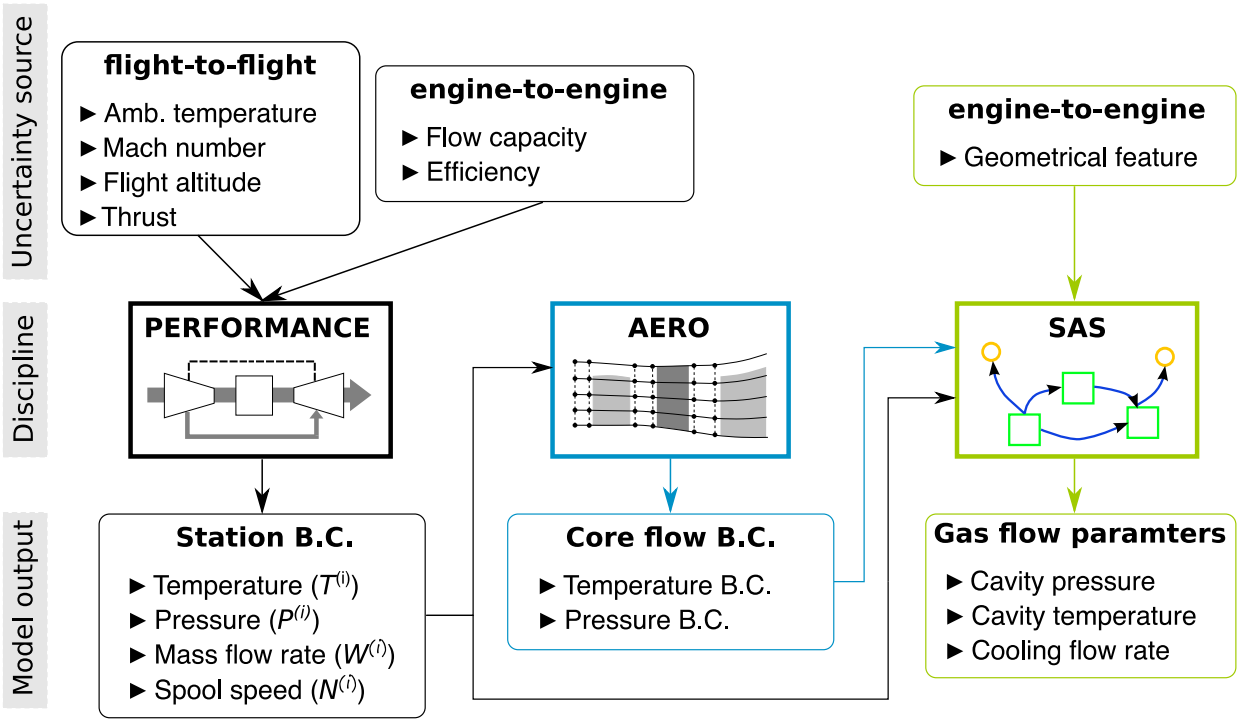

Figure 2.7 Schematic representation of the interdisciplinary process chain.

A useful categorization is to divide the uncertainty sources into two groups: flight-to-flight and engine-to-engine variation. The first refers to the ambient and operating conditions of the aircraft and is described by four parameters, all of which serve as input quantities of the performance discipline. In detail, the group encompasses the flight altitude (X_{Alt}), Mach number (X_{Mach}), ambient temperature (X_{Temp}) and the required thrust (X_{Thr}). Since these quantities cannot be affected by the modeler, they are assigned to the set of noise parameters $\mathbf{X}^{\text{n}}$, see Tab. 2.1. As will be seen within the further scope of the thesis, they play a crucial role for the design assessment because of their huge impact on the cooling system's operation.

In contrast, the engine-to-engine category signifies the production scatter caused by the manufacturing and assembly process. In case of the performance simulation, the engine-to-engine variation is considered by treating the components' efficiency ($X_{\eta^{(i)}}$) and flow capacity ($X_{\Delta W^{(i)}}$) as uncertain. The latter is a dimensionless parameter which characterizes the mass flow through the module. All components depicted in Fig. 2.2 except the inlet and burner module are taken into account which gives a total number of 14 uncertain parameters. Once again, they belong to the noise factors because their nominal values are already fixed at this stage of the design procedure.

In context of the SAS model, the manufacturing process affects the cross-sectional area of various flow passages. For the following investigation, a preselection among all geometrical parameters has been made based on the extensive sensitivity analyses in [28] to reduce the dimensionality of the problem. The remaining flow elements categories comprise labyrinth

seals, brush seals, rim seals, blade-platform gap areas and blade root gap areas. In the sequel, each of the mentioned geometrical features is explained including its associated model parameters.

Labyrinth Seals

One of the most important sealing types of the SAS is the labyrinth seal, also referred to as IAS (inner air seal). As can be seen in Fig. 2.6, the LPT cooling system comprises three labyrinth seals which control the gas flow between chamber 6 and 7 as well as between cavity 8 and 9. The third labyrinth seal controls the incoming cooling air at boundary Ⓑ. Due to its comparatively small share in the total cooling air supply, it is treated in a deterministic manner. The general structure is illustrated by Fig. 2.8(a) and consists of a static and a rotating part. Due to the stepped configuration, the latter is impinged with two pins of different height. Its static counterpart is made of a metallic honeycomb structure with a radial jump to ensure the same distance at the two fins. The flow characteristics are mainly driven by the gap size which results from the radius difference between rotor and stator. For the production induced variation of the gap width, the following four key determinants have been identified:

- Eccentricity of the stator ($X_{\text{IAS1\_stat\_e}}, X_{\text{IAS2\_stat\_e}}$)
- Eccentricity of the rotor ($X_{\text{IAS1\_rot\_e}}, X_{\text{IAS2\_rot\_e}}$)
- Centric stator production scatter ($X_{\text{IAS1\_stat\_c}}, X_{\text{IAS2\_stat\_c}}$)
- Centric rotor production scatter ($X_{\text{IAS1\_rot\_c}}, X_{\text{IAS2\_rot\_c}}$)

Each of them is modeled separately which gives a total number of eight parameters for the two labyrinth seals under investigation. The reason for differing between centric and eccentric effects comes from the fact that the latter leads to an unsymmetric rubbing into the honeycomb structure. In contrast, a pure radial deviation causes a symmetric abrasion if the fin diameter

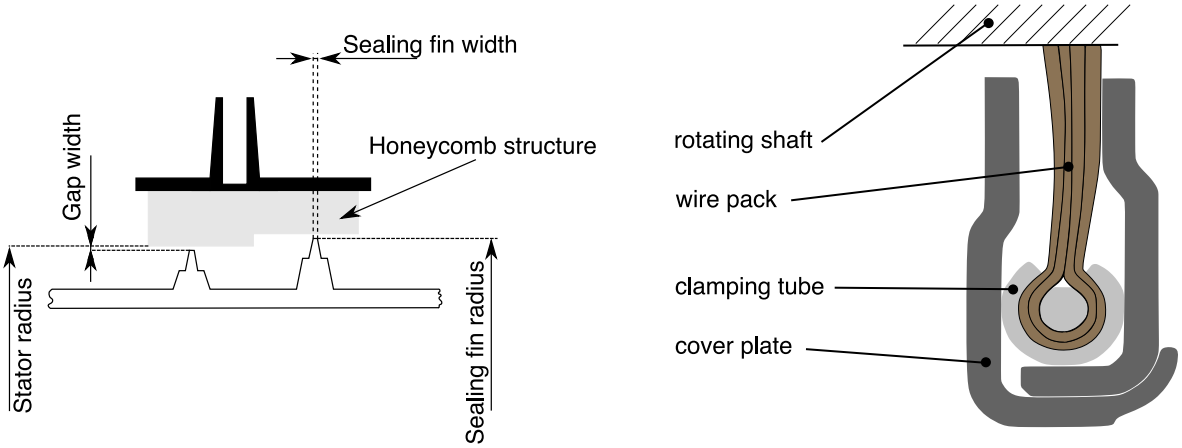

(a) Labyrinth seal representation.

(b) Brush seal representation [32].

Figure 2.8 Schematic illustration of a labyrinth (left) and brush seal (right).

exceeds the rotor diameter due to the centrifugal expansion. The underlying mathematical expressions for the effective gap size is not explained here because it covers experience-based correction factors which are part of the proprietary information.
Within the examined design stage, the nominal IAS gap size is not yet defined. Thereof, the stator diameter at the first ($X_{\text{IAS1\_stat\_c}}$) and second ($X_{\text{IAS2\_stat\_c}}$) labyrinth seal are treated as design parameters. The other six geometrical features are assigned to the noise factor group, see Tab. 2.1.
Apart from the production scatter, the labyrinth seal gap size is also affected by the centrifugal expansion of the rotor as well as the difference in thermal expansion between rotor and stator. The precondition for a significant impact of the centrifugal load is a substantially change of the low-pressure shaft speed. Since we consider only a single design point, given by the ADP, the variation is comparatively low which is why the centrifugal effect is neglected. Instead, the two fin radii are applied with a constant factor to correct the nominal gap size. In case of the thermally induced structure expansion, only a small significance is expected as the temperatures of the two sealing components are similar. This estimation is confirmed by the investigations published in [28]. Again, the nominal gap size at room temperature is corrected by a constant factor.

Brush Seal

This type of sealing plays an important role for the overall distribution of the cooling mass flow within the SAS. As can be seen in Fig. 2.6, the cooling of the first rotor stages is mainly assured by the supply throughout B.C. (E). In contrast, the third rotor stage is fed by the incoming air from B.C. (A) and (B). The main purpose of the brush seals is to control the air exchange between the two supply pipes to ensure a uniform cooling of all parts. Within the scope of this thesis, the focus is put on analyzing the right brush seal of the two as this one is more relevant for achieving a cooling flow balance.
The detailed representation in Fig. 2.8(b) reveals that the brush seal consists of a wire pack and a clamping tube surrounded by a cover plate. Accordingly, the flow through is a superposition of the wire pack and cover plate leakage flow. In context of the SAS model, both components are covered by an effective gap area whose corresponding parameter X_{Brush} is part of the design space.

Rim Seals

The last sealing type is used to model the insulation between cooling system and core gas flow. The underlying flow passage element is described by a separate representation of the incoming hot core flow and the outflowing cooling air. The separation is necessary to account for the circumferentially changing pressure boundary conditions within the annulus. As a conservative approach, the maximum core flow pressure is used for modeling the hot gas flow ingestion whereas a minimum static pressure is assumed for the exiting cooling air.

In accordance with the above-mentioned mass flow rates of interest, the rim seals are labeled in the same manner. To repeat, the indicated number stands for the stage and the letter "l" and "r" corresponds to the left and right position, see Tab. 2.1. All of the six parameters are specified by an effective gap width which holds for both the incoming and outflowing air flow. Since the design is already settled for the aerodynamic calculation, all of the parameters belong to the noise factor group.

Blade Root Gap Area

The connection between the cavities before and after each rotor stage, i.e., from chamber 5 to 6, 7 to 8, and 9 to 10, is made via gap flows between blade root and disk slot. The schematic drawing in Fig. 2.9(a) shows that there are two flow areas ($A2$, $A3$) through which the cooling air can pass. The more relevant one is $A3$ which corresponds to the gap area between disk and blade bottom surface. For the simulation of the interdisciplinary SAS model, the set of design quantities is extended by three parameters representing the gap flow area $A3$ at the first, second and third rotor stage. Due to the comparatively low cross-sectional area, $A2$ is described by a constant value.

Blade Platform Gap Area

The last geometrical feature are the flow areas which result from the gap between the turbine blade platforms, see Fig. 2.9(b). The root cause for the uncertainty on this parameter is twofold. On the one hand, the platform gap is directly affected by geometrical deviations from the turbine blades' nominal geometry caused by the manufacturing process. On the other hand, a misalignment of the disk slot positions leads to an undesired leaning of the blade and thereof to changing gap areas. However, this effect vanishes for the one-dimensional modeling approach as the corresponding descriptors represent the sum over all gap areas which cannot

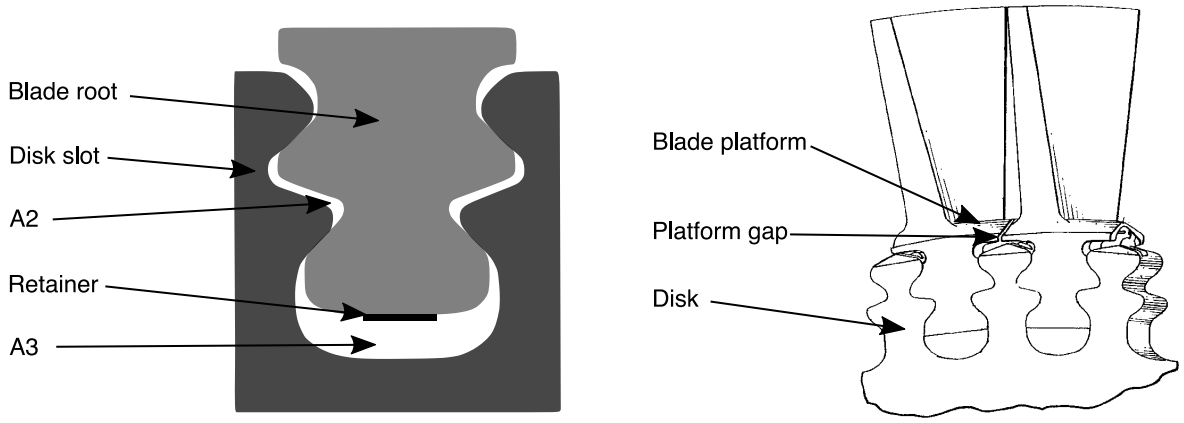

(a) Blade root gap area.

(b) Blade platform gap area, figure taken from [34].

Figure 2.9 Schematic illustration of a blade root (left) and blade platform gap area (right).

capture local misalignments. As the platform gap area is not part of the design process, the parameters $X_{\text{Plat\_1}}$, $X_{\text{Plat\_2}}$ and $X_{\text{Plat\_3}}$ are treated as noise factors.

So far, all models of the interdisciplinary process chain have been discussed including their uncertainty sources and representative parameters except the aerodynamic discipline which is treated in a deterministic fashion. The reason for this decision is the low convergence rate when varying the geometric parameters of the annulus. Here, further research is necessary to improve the stability of the SCM.
Table 2.1 gives a summary over all noise factors and design parameters of the process chain and categorizes them with respect to the uncertainty source and discipline. Despite the preliminary parameter reduction, the model still contains 33 noise factors and six design quantities.
What has not been mentioned so far is the fourth column of Tab. 2.1 which specifies the uncertainty type of every single parameter either as aleatory or epistemic. In short, the decision is primarily formed by the available amount of information about the parameter. The categorization is used throughout this thesis and decides about the uncertainty quantification approach. For the aleatory type probabilistic concepts are used, i.e., the parameters are assigned with distribution functions. However, the main focus of this thesis is on the modeling of epistemic uncertainties, i.e., the quantification of those parameters where the modeler's knowledge is scarce. A comprehensive explanation regarding the difference between these two uncertainty types is given throughout Sec. 3.1. Moreover, the uncertainty quantification approaches for all of the listed parameters are determined within Sections 5.1 and 5.2.

	Disc.	Parameter	Type	Explanation	No.
			Noise parameters $\mathbf{X}^{\mathrm{n}}$		
Flight to Flight	Performance	X_{Thr}	Aleatory	Thrust power generated by the engine	1
		X_{Alt}	Epistemic	Operating flight altitude	2
		X_{Temp}	Epistemic	Ambient temperature deviation from ISA condition	3
		X_{Mach}	Epistemic	Aircraft speed expressed as Mach number	4
Engine to Engine		$X_{\eta^{(i)}}$	Epistemic	Efficiency of the i-th jet engine component	$5,\ldots,11$
		$X_{\Delta W^{(i)}}$	Epistemic	Flow capacity of the i-th jet engine component	$12,\ldots,18$
	Secondary Air System	$X_{\mathrm{Plat\_1}}$	Aleatory	Turbine blade platform gap area of the first rotor stage	19
		$X_{\mathrm{Plat\_2}}$	Aleatory	Turbine blade platform gap area of the second rotor stage	20
		$X_{\mathrm{Plat\_3}}$	Aleatory	Turbine blade platform gap area of the third rotor stage	21
		$X_{\mathrm{Rim\_1\_l}}$	Epistemic	Rim seal gap width at the first turbine rotor stage (left)	22
		$X_{\mathrm{Rim\_1\_r}}$	Epistemic	Rim seal gap width at the first turbine rotor stage (right)	23
		$X_{\mathrm{Rim\_2\_l}}$	Epistemic	Rim seal gap width at the second turbine rotor stage (left)	24
		$X_{\mathrm{Rim\_2\_r}}$	Epistemic	Rim seal gap width at the second turbine rotor stage (right)	25
		$X_{\mathrm{Rim\_3\_l}}$	Epistemic	Rim seal gap width at the third turbine rotor stage (left)	26
		$X_{\mathrm{Rim\_3\_r}}$	Epistemic	Rim seal gap width at the third turbine rotor stage (right)	27
		$X_{\mathrm{IAS1\_lip\_c}}$	Aleatory	Sealing lip diameter deviation at the first labyrinth seal	28
		$X_{\mathrm{IAS1\_lip\_e}}$	Epistemic	Sealing lip eccentricity at the first labyrinth seal	29
		$X_{\mathrm{IAS1\_stat\_e}}$	Epistemic	Stator eccentricity at the first labyrinth seal	30
		$X_{\mathrm{IAS2\_lip\_c}}$	Aleatory	Sealing lip diameter deviation at the second labyrinth seal	31
		$X_{\mathrm{IAS2\_lip\_e}}$	Epistemic	Sealing lip eccentricity at the second labyrinth seal	32
		$X_{\mathrm{IAS2\_stat\_e}}$	Epistemic	Stator eccentricity at the second labyrinth seal	33
			Design parameters $\mathbf{X}^{\mathrm{d}}$		
Engine to Engine	Secondary Air System	X_{Brush}	Aleatory	Brush seal gap width	34
		$X_{\mathrm{IAS1\_stat\_c}}$	Aleatory	Stator diameter of the first labyrinth seal	35
		$X_{\mathrm{IAS2\_stat\_c}}$	Aleatory	Stator diameter of the second labyrinth seal	36
		$X_{\mathrm{A3\_1}}$	Aleatory	Gap area between blade root and disk at the first rotor stage	37
		$X_{\mathrm{A3\_2}}$	Aleatory	Gap area between blade root and disk at the second rotor stage	38
		$X_{\mathrm{A3\_3}}$	Aleatory	Gap area between blade root and disk at the third rotor stage	39

Table 2.1 Overview over all relevant uncertain parameters of the interdisciplinary SAS model.

2.2 Literature Review: Lack-of-Knowledge Uncertainties in Turbomachinery Applications

Before proceeding with the aims and objectives of this thesis, a short literature review is given about publications with a special focus on lack-of-knowledge uncertainty quantification methods in context of turbomachinery application cases.

Due to its high degree of criticality, a wide range of publications can be found which deal with the analysis of the engine's SAS. The authors of [11] and [29] for example have conducted comprehensive sensitivity analyses to quantify the importance of geometrical features and varying performance parameters on the cooling system's operation. The sensitivity metrics used within the two publications are based on the elementary effect method and the Spearman rank correlation coefficient. In [24] a new sensitivity index, referred to as coefficient of nonlinear correlation, has been introduced to capture nonlinear input-output relations which cannot be detected by the classical correlation coefficients. The literature references discussed up to now cover various functions of the secondary air system such as the sealing of the bearing chamber or the required amount of cooling flow supply. Throughout [134], the focus is put on investigating the impact of varying geometrical features as well as operational conditions on the ingestion of core gas into the HPT cooling system. Apart from the different engine module, the study reveals certain similarities with the objectives of the present thesis.

A common characteristic of all above-mentioned publications is the mono-disciplinary modeling approach which lacks the representation of the cooling system's interaction with other disciplines. The paper [10] is basically an extension of [11] discussed before as it couples the SAS model with the subsequent thermomechanical simulation of the LPT. Similar to the monodisciplinary study case, the core aspect is on performing a probabilistic sensitivity study but this time for the LPT rotor life duration assessment. The results of the conference paper have been pursued by a robust design optimization within [9]. The coupling between secondary air system and thermal calculation has also been examined within [120] but without a connection to stochastic analyses. The main goal of the cited work was to set up an interactive SAS-thermal simulation procedure which is not just a concatenation of the disciplines. Thereof, it is able to represent interactions between the models such as the effect of thermal deformations on geometrical SAS features which requires an iterative solution procedure.

The coupling of the SAS with preceding disciplines, especially the performance simulation, is rarely discussed in literature. An exception to this is given by [176] which argues why the conduction of research analyses at component level has only limited informative value. Instead, the authors outline the benefits of including the performance model into the design procedure, regardless of the analyzed engine component. Once again, the publication does not enclose any stochastic aspects.

All of the publications mentioned so far treat uncertainty sources, in case they are covered by the studies, in a probabilistic manner. A noteworthy publication in context of the LPT cooling

system, which deviates from this approach, is given in [91]. There, the emphasis is put on those parameters where the available information is fairly limited. The classical probabilistic modeling is replaced by considering the stochastic moments as uncertain parameters instead of crisp values. Besides from the uncertainty quantification, the publication deals with the extension of the Sobol index concept to assess the importance of the uncertain stochastic moments. A similar approach for the quantification of lack-of-knowledge uncertainties has been chosen in [135] which discusses the impact of a varying compressor blade geometry on the components' performance. Due to the limited set of optical measurements, the authors have decided to assign probability distributions with interval-valued mean and variance to the geometrical parameters.

The modeling of uncertainty sources based on vague information in context of axial gas turbine compressors is also addressed within [149, 155]. The reference [155] analyses the high cycle fatigue capability of compressor blisks under varying material properties and damping ratios. The latter uncertainty source has been modeled by intervals because of the scarce information basis. Within the second reference [149], the failure probability of a four-stage axial compressor is investigated with the help of the survival signature concept. The uncertainty on the components of this network, i.e., the rows of the compressor, are described by the fuzzy probability theory.

All in all, this short literature review has demonstrated a wide range of publications about stochastic methods which aim at reducing the degree of conservatism of existing deterministic design concepts. However, the assortment of publications dealing explicitly with lack-of-knowledge uncertainties is comparatively low, especially in combination with the analysis of the LPT cooling system. In addition to that, most of the research studies are limited to sensitivity analyses and a mono-disciplinary modeling approach, whereas the conduction of a RDO (robust design optimization) is rarely discussed. Next, the aims and objectives of the thesis are outlined.

2.3 Aims and Objectives

As mentioned in the introductory part, the challenges for aircraft engine manufacturers have changed strongly over the last years. Since airlines tend to prefer so-called power-by-the-hour contracts instead of buying the engine, engineers have to take greater account of possible large maintenance costs during the development phase. Hence, a major goal of the design process is to realize a robust design which prevents the engine from premature performance degradation or even failure.

The basic prerequisite for taking the robustness criterion into account is to change the design process from a deterministic approach to stochastic methods. Section 2.1.2 has demonstrated the variety of uncertainty sources of the three development disciplines under investigation. To repeat, two different uncertainty sources have been identified: flight-to-flight and engine-to-

engine variation. From a stochastic point of view, establishing a classification according to the type of uncertainty is more reasonable. A common approach for many engineering applications is to distinguish between aleatory and epistemic uncertainties, see e.g. [42]. The first type is also called irreducible because it is related to the inherent variation of a random process. The state-of-the-art approach for this uncertainty type are probabilistic concepts. On the other hand, epistemic uncertainties are referred to as reducible because they are induced by an incomplete knowledge and can thus be reduced by collecting more information. These two types can occur alone but in many applications a combination of both is present which leads to the framework of mixed probabilistic/non-probabilistic methods [21]. In [9], a concept for the robust design optimization of a LPT under consideration of aleatory uncertainties has been developed. Within the scope of this thesis, the main focus lies on the analysis of epistemic as well as mixed aleatory/epistemic uncertainties.

The following case study will demonstrate the challenges for the design process if parameters from the epistemic category are considered as well. For the sake of simplicity, the SAS is treated as mono-disciplinary mathematical model. Hence, the set of input quantities comprises the geometrical parameters being affected by the manufacturing process. In this small case study, all input quantities are set to their nominal values except the ones representing the gap width between disk and blade root at the three turbine stages ($X_{\text{A3\_1}}, X_{\text{A3\_2}}, X_{\text{A3\_3}}$). The gap width parameter is affected by deviations from the nominal geometry of the corresponding blade root and disk slot, see Fig. 2.9(a). The geometrical variation of the blade can be modeled by a fitted probability distribution because a sufficient number of measured components is available. For quantifying the uncertainty on the disk geometry, only the minimum, maximum and nominal value of each parameter is given. In this study, different modeling approaches have been compared with each other:

- Case 1 - Interval theory:
  The uncertainty modeling is based on the information about the lower ($\underline{x}_i$) and upper bound ($\overline{x}_i$) of the random parameter without making any further assumptions.
- Case 2 - Probability-box concept:
  The disk geometry is characterized by a so-called p-box (probability-box) which represents the uncertainty by a lower ($\underline{F}_X(x)$) and upper bound ($\overline{F}_X(x)$) for the CDF (cumulative distribution function). The two bounding curves are derived from the assumption that the mode and median of the unknown distribution does not deviate by more than 10% from the nominal value.
- Case 3 - Probabilistic approach:
  The geometrical variation of the disk is described by probabilistic concepts. For example, it is modeled by a uniform distribution, characterized by the known minimum and maximum value. Another meaningful approach would be to model the uncertainty by a truncated normal distribution which has its mean (μ_x) at the midpoint of the given interval

and a standard deviation (σ_x) equal to one-sixth of the interval width. Last but not least, the disk variation is described again by a truncated normal distribution which has the same mean and standard deviation as the uniform distribution.

Each of the three modeling approaches is shown exemplarily in Fig. 2.10(a) for the parameter $X_{\text{A3\_1}}$. One can see that the interval approach is the most conservative one because it covers all the other uncertainty representations. Due to additional assumptions a shrinkage of the conservative interval bounds can be achieved which results in a p-box representation. If the distribution type including its parameters is specified, we obtain a unique probability distribution.

As can be seen in Fig. 2.10(b), the chosen modeling approach of the input quantities has a huge impact on the analysis of the cooling system. The graphical illustration shows one selected cooling mass flow rate which is located close to the rim seals at the third rotor stage. Note, that the chosen uncertainty propagation concepts are not discussed here as they are addressed within Sec. 3.3.

The variability of the selected response value has the same characteristics as the input parameters which means that its uncertainty is either given as interval, p-box or CDF. This small example of the SAS shows that the modeling procedure with the least assumptions, i.e., the interval approach, leads to the most conservative cooling mass flow uncertainty representation. On the contrary, the probabilistic treatment reduces the degree of conservatism but is based upon the introduction of additional assumptions which brings us to the first objective of the thesis.

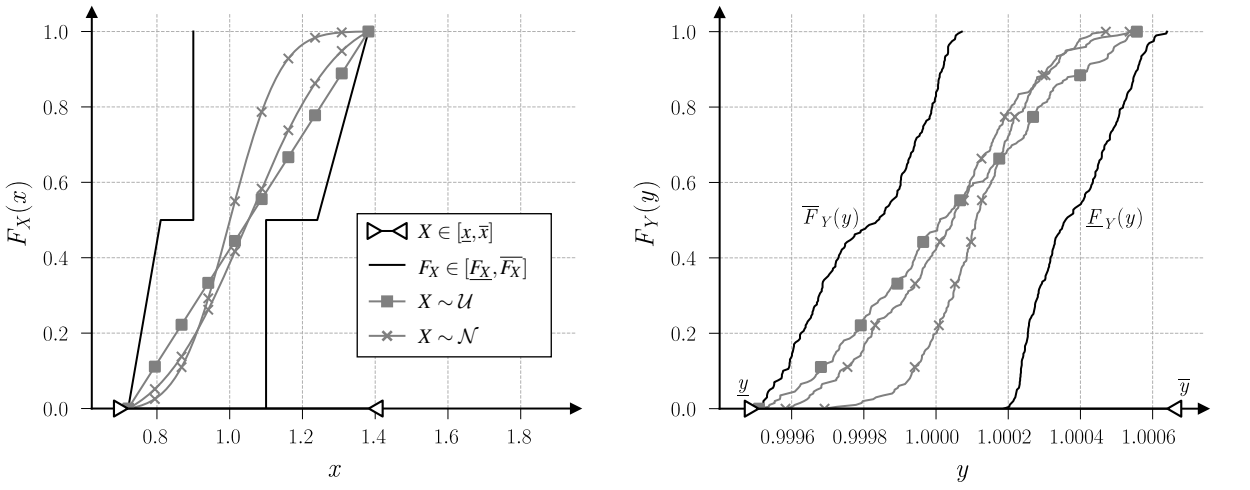

(a) Disk geometry variation at the first turbine stage.

(b) Cooling mass flow close to rim seal at third rotor stage.

Figure 2.10 Geometric variation of the disk geometry at the first turbine stage (left) and cooling mass flow in the vicinity of the third rotor stage rim seal (right). Both parameters have been normalized w.r.t. to their nominal value.

2.3.1 Lack-of-Knowledge Uncertainty Quantification

The first main objective is to find appropriate concepts to represent lack-of-knowledge uncertainties. If the UQ (uncertainty quantification) is based on strong assumptions, there is a certain risk of losing information about the system response. For the case study shown here, one can see this effect when comparing the different CDFs which result from modeling the input as normal or uniform distribution, respectively. If a specific distribution has been chosen, which is significantly different from the true one, the modeler would come up with a wrong interpretation regarding, e.g., the robustness of the system. In contrast, using the interval or p-box concept leads to conservative bounds in the response space. The advantage is that the true (unknown) CDF is most likely covered by the interval or p-box bounds. However, for the modeler it is hard to evaluate the system behavior in case of wide bounds as they include non-meaningful CDFs as well. The lower p-box bound ($\underline{F}_Y(y)$) in Fig. 2.10(b) for example does not even cover the nominal mass flow value and is therefore an unlikely scenario.
To summarize, the modeling approach for lack-of-knowledge uncertainties can have a huge influence on the system evaluation. On the one hand, the challenge is to find modeling approaches which are able to represent the imprecise information without strong, biased assumptions. On the other hand, the test case in Sec. 2.3 has shown that non-probabilistic methods can lead to a high degree of conservatism. Thus, the goal is to find approaches that balance these competitive goals.
The uncertainty representation of imprecise data is even more complicated if the known information does not correspond to the model input parameters. The test case from Sec. 2.3 demonstrates a *forward* UQ problem because the gap widths between blade and disk are directly represented by the parameters $X_{\text{A3\_1}}, X_{\text{A3\_2}}$ and $X_{\text{A3\_3}}$. For the first discipline of the development process, namely the performance calculation, we are faced with an *inverse* problem. In this case, an imprecise set of data is given about the variation of the response quantities but we are interested in quantifying the uncertainty on the input parameters. Thus, the content of this thesis will deal with both, *forward* and *inverse* UQ problems under the condition of scarce data sets.

2.3.2 Reduction of the Epistemic Parameter Space

When considering complicated engineering systems, such as the multidisciplinary jet engine development process, the uncertainty quantification is not the only challenge. Typically, the number of uncertain parameters is rather large in real-world applications leading to long computation times. In order to reduce the system complexity, SA (sensitivity analysis) methods are needed to identify those parameters which are of major importance for the model response under investigation.
Within the framework of probabilistic analyses, a variety of methods is available to determine

how the uncertainty of an input parameter affects the response quantities of a system. As the set of input parameters from the jet engine design process comprises both, epistemic and aleatory uncertainties, an appropriate sensitivity study is needed to account for the epistemic part as well. The main goal of the investigation is to figure out whether the epistemic uncertainty of a parameter should be considered in the modeling approach. If it turns out that the system response is not sensitive with regard to the epistemic uncertainty, a pure probabilistic approach can be used to model the parameter variation. To repeat, the epistemic SA analyzes the reducible uncertainties whereas the aleatory one accounts for the inherent parameter randomness.
To remind, the input space of the case study discussed before covers three parameters, representing the gap width between turbine blade root and disk at each stage. Let us assume that the uncertainty of the disk geometry ($X_{\text{A3\_1,disk}}, X_{\text{A3\_2,disk}}, X_{\text{A3\_3,disk}}$) is modeled by the p-box concept. The goal of applying an epistemic SA is to find out if the system response is sensitive against the missing knowledge about the shape of the CDF inside the p-box. For example, if the system response was insensitive against the epistemic uncertainty part of $X_{\text{A3\_2,disk}}$, the input parameter representation could be reduced to a single CDF.
In literature, the extension of existing aleatory SA concepts for epistemic uncertainties is thoroughly discussed. One of the bottlenecks for many approaches is the computational effort due to the additional epistemic layer in the parameter definition. Especially for high-dimensional problems, like the jet engine design process, an efficient SA strategy is essential.
Within the scope of this thesis, the second main objective is the development of a method to sort out epistemic uncertainties without a significant contribution to selected response quantities. Besides from reducing the model complexity, the gained information helps to get a better understanding about the interdisciplinary system behavior.

2.3.3 Interdisciplinary Robust Design Optimization of the Secondary Air System

The final objective concerns the robust design optimization of the SAS. Generally spoken, robustness means that the performance of a system is insensitive against the variation of controllable and uncontrollable parameters. In contrast to a reliability analysis, robustness studies do not determine the failure of a system in case of rare events. The latter is not covered within the thesis.
At first, the question of how to define a robust system behavior in terms of the SAS must be answered. After that, a metric is required which puts the robustness concept into a mathematical formulation. In many approaches from literature, the metric is based on the mean and standard deviation of the system response. As discussed in the previous chapters, the disciplines of the jet engine design process cover aleatory as well as epistemic uncertainties. Due to the coexistence of both uncertainty types, the stochastic moments are no longer characterized by crisp values. Hence, one problem addressed in this thesis is to establish a metric for

assessing the robustness of the SAS under aleatory and epistemic uncertainties.
Once this issue has been solved, the focus can be put on the actual optimization of the design variables. Even though the epistemic parameter space will be reduced beforehand, the interdisciplinary design process is still a high-dimensional problem. A key aspect for an adequate RDO strategy is thereof to find an efficient approach which enables the modeler to conduct the RDO within a reasonable amount of time. Besides from the computationally efficiency, the RDO procedure has to deliver trustworthy results, i.e., the robustness metric must be predicted with high accuracy. Especially the combination of a high-dimensional model setup and the demanded computational efficiency makes the robustness study a challenging task.
To summarize, the goal of the RDO is to find a design which leads to a stable supply of cooling flow at the transition between secondary air system and core gas path. Expressed in other words, the SAS design should be insensitive against changing ambient conditions and geometrical variabilities from the manufacturing process. A special focus of the RDO is on those uncertainty sources where the available information is scarce and which are thereof not modeled in a probabilistic fashion.
Within the scope of the next chapter, the reader finds a comprehensive literature overview about stochastic methods being relevant for the objectives of this thesis.

Chapter 3

THEORETICAL BACKGROUND

The following chapter is structured according to the aims and objectives of the thesis. Each of the sections provides state-of-the-art methods for the problems outlined in Section 2.3. Moreover, the limitations of existing concepts in context of the jet engine design process are demonstrated which serves as motivation for new approaches introduced in Chapter 4.
First, Section 3.1 deals with the topic of how to categorize different uncertainty sources in the context of this thesis. After that, the focus of Section 3.2 and 3.3 is put on concepts for the forward uncertainty quantification (UQ) followed by Section 3.4 about methods for solving inverse UQ problems. In both cases, the emphasis is placed on the modeling of lack-of-knowledge uncertainties as this is less explored in literature. Section 3.5 refers to approaches for conducting a sensitivity analysis (SA) in context of epistemic uncertainties. Finally, the last section is devoted to the subject area of robustness analysis. One of the main aspects addressed here is to clarify the term robustness under the occurrence of lack-of-knowledge uncertainties. In addition, different mathematical concepts from literature to quantify robustness are discussed.

3.1 Categorization of Uncertainties

Generally spoken, the term uncertainty can be defined as gap between the modeler's present knowledge about a system and the ideal state of complete determinism. In order to find appropriate approaches for the uncertainty quantification, a preceding categorization is reasonable. When looking back in history, such kind of classification can be found for the philosophical

interpretation of probability. In the early 1840s, the French philosopher and mathematician Augustin Cournot has introduced a distinction between "objective possibility" and "subjective probability" [41]. The terminology of this classification has been intensively discussed over the past which has led to a variety of classification concepts [65]. For example, Ian Hacking explains the duality of probability with the terms aleatory and epistemological [72]. The first is related to the inherent randomness of the system whereas the latter is based on incomplete knowledge. For the more general case, namely the categorization of uncertainties, this sort of distinction plays a crucial role in most of the modern concepts. In the following, we leave the philosophical point of view and introduce a model-based uncertainty categorization.
From a mathematical perspective, a computational model is defined as

$$g : \mathbb{R}^{n_x} \rightarrow \mathbb{R}^{n_y},\ \mathbf{x} \mapsto \mathbf{y} = g(\mathbf{x}), \tag{3.1}$$

which maps an n_x-dimensional input vector $\mathbf{x} \in \mathbb{R}^{n_x}$ to a n_y-dimensional vector of response quantities $\mathbf{y} \in \mathbb{R}^{n_y}$. Following the approach in [172], the uncertainty categorization is performed with respect to three different dimensions: location, level and nature.
The first dimension (**location**) describes *where* the uncertainty occurs in the model. When analyzing Eq. (3.1), the following locations, also referred to as uncertainty sources [42], can be identified:

1. Input quantities: In a general non-deterministic case, $\mathbf{x}$ is a realization of the random vector $\mathbf{X}$ which is characterized by a probabilistic model $f_{\mathbf{X}}(\mathbf{x}|\boldsymbol{\Theta}_x)$. Hence, the randomness of the input quantities themselves is a significant uncertainty source.
2. Model form: Regardless of the application case, the computational model $g(\mathbf{x})$ is always a simplification of the real physical system. The assumptions behind the modeling approach lead to a bias between the derived response $\mathbf{y}$ and the physical quantities under investigation. Besides from the computational model, also the choice of the probabilistic model form $f_{\mathbf{X}}(\mathbf{x}|\boldsymbol{\Theta}_x)$ belongs to the group of modeling errors.
3. Model parameters $\boldsymbol{\Theta}_g$ and $\boldsymbol{\Theta}_x$: Defining appropriate physical and probabilistic models includes the calibration of $\boldsymbol{\Theta}_g$ and $\boldsymbol{\Theta}_x$, respectively. The determination of physical model parameters is achieved by comparing the model response with system data obtained, e.g., from measurements. In the ideal case, simulating the model response should coincide with the system data. For the determination of probabilistic model parameters, a probability distribution fitting is conducted. Especially for a small set of system data, the estimation of $\boldsymbol{\Theta}_g$ and $\boldsymbol{\Theta}_x$ is subject to a significant statistical uncertainty.
4. System data acquisition: As mentioned in the previous bullet point, system data is usually obtained from measurements. Since these observations are linked with measurement inaccuracies, an additional uncertainty source must be considered for the model calibration.

5. Output quantities: The uncertainty of the response vector $\mathbf{y}$ is a result of all the uncertainty sources mentioned above. For this reason, $\mathbf{y}$ can be seen as realization of a random vector $\mathbf{Y}$. Besides from that, the derived quantities $\mathbf{y}$ underlie computational errors due to numerical approximations of the analytical model or truncation conditions.

One should keep in mind that the proposed partitioning of uncertainty sources is not a fixed concept but leaves room for interpretation because of the overlap between the classes. The focus of this thesis is mainly put on uncertainty sources which are related to modeling the uncertainties on the input quantities $\mathbf{x}$. Of course, the computational models introduced in Sec. 2.1 are also subject to uncertainties. For example, representing the secondary air system (SAS) by a one-dimensional flow network is a simplified approach. However, for the problems explored here the model accuracy is precise enough. In contrast, for analyzing rare events, such as a catastrophic system failure, one has to investigate the computational model accuracy in greater detail.

In accordance with [172] the second dimension is the uncertainty **level** which describes the gap width between the modeler's knowledge and the unachievable state of determinism. In Fig. 3.1, the transition from determinism to complete ignorance is divided in three stages. The first one is referred to as statistical uncertainty. This level presumes that a sufficient amount of data is available to describe the uncertainty by statistical methods. During the development phases of a jet engine, this uncertainty level is mainly of relevance during a late stage. In this phase enough data, e.g., by the assessment of test specimen, about a component has been gathered. For the case of quantifying the uncertainty on the system input values $\mathbf{x}$, a probability distribution $f_{\mathbf{X}}(\mathbf{x}|\boldsymbol{\Theta}_x)$ is preferable in case of having enough calibration data and if the model form can capture the characteristics of the variation. In general, the level of statistical uncertainty can occur at any location of a computational model. For example, if $g(\mathbf{x}|\boldsymbol{\Theta}_g)$ is represented by a Gaussian process, the uncertainty on the model prediction shows a statistical characteristic.
Going further into the direction of total ignorance, the next level is named scenario uncertainty, which is a rather formal expression. In contrast to the previous level, no clear statistical representation can be derived for the analyzed phenomenon. Coming back to the representation of uncertainties on the input quantities, this would mean that the entries of $\mathbf{x}$ should not be modeled by a unique probability distribution. Due to the additional scenario uncertainty, the model form as well as the set of parameters $\boldsymbol{\Theta}_x$ cannot be considered as fixed values. A similar approach holds for the computational model of the physical system. Again, the scenario uncertainty could be represented by an uncertainty of the model parameters $\boldsymbol{\Theta}_g$ and by different options for the model formulation itself. Regardless of where in the computational system the scenario uncertainty occurs, it always leads to a variety of possible model responses. In the jet engine design process, modelers are faced with scenario uncertainty during an early stage when no detailed information on the uncertainties is provided.

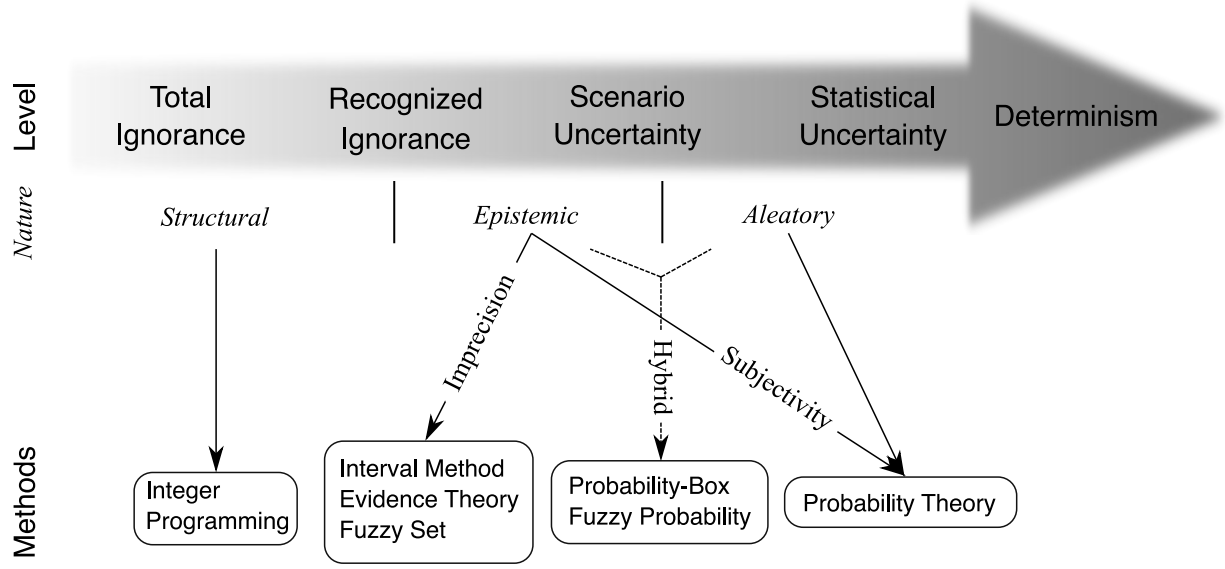

Figure 3.1 Categorization of uncertainties with respect to the level and nature according to [172].

The last level before complete ignorance is the state of recognized ignorance. This level of uncertainty stands out through a very poor knowledge which does not even allow the development of possible scenarios for the phenomena under investigation. The term ignorance stems from the Latin adjective *gnarus* which means knowledgeable. Thus, ignorance can be circumscribed as lacking knowledge [129]. From the author's point of view, the main difference between ignorance and uncertainty is that not all uncertainty sources are known in the state of ignorance. Contrary to total ignorance, the modeler is aware of the missing information in the state of recognized ignorance. Staying in the field of jet engines, this uncertainty level is of importance during the predevelopment phase where the customer's requirements to the engine are not yet fully defined. Consequently, basic engine configuration options, such as the number of turbine stages, are not determined. Since the physical system is not completely specified in this development stage one can neither derive appropriate computational models for it nor evaluate the set of input quantities.

The final level, namely the total ignorance, represents a state of having extremely little knowledge. In contrast to the remaining levels explained before, it covers the group of so-called *unknown unknowns*. This category relates to uncertainties which the modeler is not even aware of their existence. In this state, gathering more information could even increase the uncertainty due to identifying unforeseen uncertainty sources. This uncertainty level plays a role when performing feasibility studies of completely new technologies like a hydrogen powered jet engine.

Within this thesis, an early jet engine design stage is analyzed. Hence, the fundamental structure of the components is settled but not all of the geometrical features are fully defined. The uncertainties can therefore be assigned to the levels of statistical and scenario uncertainty.

Besides from the location and level, a further categorization can be established according to

the **nature**, sometimes also named **type**, of uncertainty. The state-of-the-art approach for this dimension is to distinguish between epistemic and aleatory uncertainty, see e.g. [21, 42, 76, 77, 172]. On the one hand, epistemic uncertainty, originated from the Greek word *episteme* (knowledge), is associated to the modeler's lack of knowledge about the uncertainty sources. There is a variety of reasons causing this type uncertainty: limited or ambiguous information, subjectivity, imprecise data, indeterminacy or vagueness [117, 125]. Since all of them are based on incomplete knowledge, this type is also called reducible because the collection of more data would decrease the uncertainty. On the other hand, aleatory uncertainty, derived from the Latin expression *alea* (incertitude), represents the inherent, natural variability of a phenomenon. Contrary to the epistemic type, aleatory uncertainties cannot be decreased by collecting more information which is why they are classified as irreducible. In some cases, the coexistence of both uncertainty types in a system can be observed which is referred to as hybrid or mixed uncertainty. Apart from this well-established classification, the so-called structural uncertainty can be found in literature [131]. This type corresponds to the problem that a wide range of possible solution approaches is available for an engineering problem. Among these, engineers can determine only a small set of concepts due to lack of time. As a consequence, certain parts of the design space are not evaluated even though they could include a design which fulfills the product requirements better than the chosen one [130].
The author considers that the nature of an uncertainty is not completely independent from its level. This point of view is depicted in Figure 3.1 as well. It shows that the aleatory type correlates strongly with the level of statistical uncertainty. Furthermore, the transition from aleatory to epistemic follows the change from statistical uncertainty to recognized ignorance. Last but not least, structural uncertainty is mainly assigned to the level of recognized ignorance. However, it is common practice to differentiate only between the aleatory and epistemic type. Furthermore, the application case of the thesis deals with a development stage where the basic component structures are finalized. As it is sometimes hard to determine whether an uncertainty source is reducible or not, the classification according to the nature is also a subjective decision by the modeler.
Finally, the necessity as well as the benefit derived from the categorization must be clarified. From a technical point of view, identifying the location of an uncertainty is important for the appropriate preparation of the computational model. Beyond that, grouping the uncertainties according to their sources helps the modeler in deciding where additional research is beneficial for improving, e.g., the robustness, of the product.
As can be seen in Fig. 3.1, the nature of an uncertainty is decisive when it comes to choosing a method for the uncertainty representation. For the aleatory type, it has become established to use the probability theory for the characterization. In case of epistemic uncertainties, a variety of modeling approaches can be found in literature. The authors of [21] propose to distinguish between two different reasons for the lack-of-knowledge uncertainty: subjectivity and imprecision. As indicated by the expression subjectivity, the lack-of-knowledge is caused

by a subjective expert's assessment about the phenomenon of concern. In this case, the uncertainty is treated by assigning a probability distribution to it. If data are available to further specify the uncertainty, the initial probability distribution can be updated with the help of a Bayesian approach. The second reason for epistemic uncertainty, namely imprecision, evolves from scarce, inconsistent or inaccurate information. Applying the probability theory under these conditions is only possible by making biased assumptions. For this reason, non-probabilistic concepts such as interval method, evidence theory or fuzzy sets are required [56, 60, 77, 116]. For the modeling of hybrid uncertainties, the corresponding methods have to combine the characteristics of both types. For example, the p-box as well as the fuzzy randomness approach can be interpreted as extending the probability theory with the interval method or fuzzy set theory, respectively [59, 116]. For dealing with the specific type of structural uncertainty, integer programming is an appropriate method [6, 44, 159].
The level of uncertainty represents the modeler's degree of knowledge. This information is important for interpreting the results of the investigation. Especially if the level of uncertainty is high, one has to keep in mind that even weak assumptions in the modeling approach can have a significant impact on the outcome. Hence, the underlying degree of knowledge affects the trustworthiness of the study findings which must be considered for the subsequent decision making.
The uncertainty categorization introduced in this chapter is aligned to the computational model defined in Eq. (3.1). Another classification strategy can be found in [116] for example which differs between the type and characteristic of an uncertainty. The interested reader is also referred to [143] which discusses the categorization of uncertainties from a more philosophical point of view in context of the risk theory.

3.2 Forward Uncertainty Quantification

The previous section has demonstrated the manifold characteristics of uncertainties in a computational system. To repeat, an early stage of the jet engine development process is considered within the thesis which means that the uncertainty sources cover the level of scenario and statistical uncertainty. Moreover, the research problems outlined in Sec. 2.3 are related to input quantities of the different design disciplines. The quantification of errors introduced by modeling the physical system is not part of the actual research focus.
The following subsections describe state-of-the-art methods to quantify aleatory, hybrid and epistemic uncertainties, respectively. As shown in Fig. 3.1, several methods are available for modeling the hybrid and epistemic uncertainty type. Here, the discussion is narrowed to the p-box and interval concept. The term *forward* means that the available set of data, regardless of its quality and quantity, is directly related to the corresponding quantity of interest in the computational model.

3.2.1 Probability Theory

Mathematical Theory

The standard approach for modeling aleatory uncertainties is based on the probability theory and its underlying axioms which have been introduced by Andrey Kolmogorov [95]. This mathematical concept for representing a random process is defined by the probability space $(\Omega, \mathcal{F}_p, \mathbb{P}_p)$. The following introduction is based on [68].
The first entry Ω is called sample space and covers all possible outcomes ω of the random process. The second element, namely the σ-field $\mathcal{F}_p$, represents the set of events which are of interest for the modeler. Each event $\mathcal{A}_p$ is a subset of the whole probability space. The σ-field has to fulfill the following properties:

1. $\emptyset \in \mathcal{F}_p$,
2. $\mathcal{A}_p \in \mathcal{F}_p \rightarrow \mathcal{A}_p^C \in \mathcal{F}_p,$ and
3. $\mathcal{A}_p^{(i)} \in \mathcal{F}_p$ with $i \in I,$ where I is a countable set $\rightarrow \bigcup_{i \in I} \mathcal{A}_p^{(i)} \in \mathcal{F}_p$.

Note that the tuple $(\Omega, \mathcal{F}_p)$ is also referred to as measurable space. The last entry $\mathbb{P}_p$ of the triple is the probability measure which maps the event space to the unit space. Mathematically, it is defined by $\mathbb{P}_p : \mathcal{F}_p \mapsto [0,1]$ and has to fulfill the axioms:

1. $\mathbb{P}_p(\Omega) = 1,$ and
2. $\mathbb{P}_p(\bigcup_{i=1}^{\infty} \mathcal{A}_p^{(i)}) = \sum_{i=1}^{\infty} \mathbb{P}_p(\mathcal{A}_p^{(i)}),$ with $\mathcal{A}_p^{(i)} \in \mathcal{F}_p,\ \mathcal{A}_p^{(i)} \bigcap \mathcal{A}_p^{(j)} = \emptyset,\ i \neq j.$

Based on the definition of a probability space, a real-valued random variable X is formally defined by the function $X : (\Omega, \mathcal{F}_p) \mapsto (\mathbb{R}, \mathcal{B}_p)$. The mapping transfers $(\Omega, \mathcal{F}_p)$ to a real-valued measurable space. In practice, the characteristics of the random variable X is described by the cumulative distribution function (CDF). The CDF summarizes the properties of the probability space introduced before and is given by

$$F_X(x) = P(X \leq x) = \mathbb{P}_p(X^{-1}((-\infty, x])) = \mathbb{P}_p(\{\omega : X(\omega) \leq x\}), \tag{3.2}$$

where $x \in \mathbb{R}$ and $\omega \in \Omega$. Hence, $F_X(x)$ is a specific probability measure for $\mathcal{B}_p = (-\infty, x]$. Furthermore, it is a right-continuous, increasing function with the following properties:

- The range of $F_X(x)$ is limited to $[0,1]$,
- $\lim_{x \to -\infty} F_X(x) = 0$ and $\lim_{x \to +\infty} F_X(x) = 1$,
- $P(a < x \leq b) = F_X(b) - F_X(a),$ for $a \leq b$, and
- $P(a \leq x < b) = F_X(b) - F_X(a) + P(X = a) - P(X = b),$ for $a \leq b$.

If $F_X(x)$ is absolutely continuous, the derivative $f_X(x) = dF_X(x)/dx$ is called PDF (probability density function). The density function $f_X(x)$ is always greater than zero because $F_X(x)$ is strictly increasing. Throughout the thesis, only absolutely continuous random variables are considered.

So far, the probability theory has been derived for a one-dimensional random variable X. Extending the concept for a multi-dimensional case, a random vector $\mathbf{X}$ is derived by $\mathbf{X} : (\Omega, \mathcal{F}_p) \mapsto (\mathbb{R}^{n_x}, \mathcal{B}_p^{n_x})$ for $n_x > 1$. In accordance with the one-dimensional case, a joint cumulative distribution function is defined which summarizes the underlying probability space

$$F_{\mathbf{X}}(\mathbf{x}) = P\left(\bigcap_{i=1}^{n_x}\{X_i \leq x_i\}\right) \overset{\text{indep.}}{=} \prod_{i=1}^{n_x} F_{X_i}(x_i). \tag{3.3}$$

For the specific case of independent random variables, $F_{\mathbf{X}}(\mathbf{x})$ is given by the product of the marginal CDFs. The joint probability density function is given by

$$f_{\mathbf{X}}(\mathbf{x}) = \frac{\partial^{n_x} F_{\mathbf{X}}(\mathbf{x})}{\partial_{x_1} \dots \partial_{x_{n_x}}} \overset{\text{indep.}}{=} \prod_{i=1}^{n_x} f_{X_i}(x_i). \tag{3.4}$$

Again, $f_{\mathbf{X}}(\mathbf{x})$ is simply computed by the product of the marginal PDFs if all random variables are independent from each other. Moreover, a marginal PDF $f_{X_i}(x_i)$ can be obtained from $f_{\mathbf{X}}(\mathbf{x})$ via the integration

$$f_{X_i}(x_i) = \int_{\mathbb{R}^{n_x-1}} f_{\mathbf{X}}(\mathbf{x}) d\mathbf{x}_{-i}, \tag{3.5}$$

where $\mathbf{x}_{-i} \in \mathbb{R}^{n_x-1}$ denotes the $(n_x-1)-$dimensional vector which includes all variables but x_i.

In order to model dependencies between random variables, copulas can be introduced. Since the application case of the thesis does not require the definition of dependencies between aleatory uncertainty sources, the copula concept is not discussed here. For further information, the reader is referred to [1, 49].

To summarize, the randomness of a phenomenon is expressed by a distribution function in probability theory. There is a variety of different CDFs in literature although the Gaussian one is without doubt the most common one. The shape of the distribution is characterized by an analytical equation and a set of distribution parameters $\mathbf{\Theta}_x$ which results in a more general expression $f_X(x|\theta_x)$ and $F_X(x|\theta_x)$ for the PDF and CDF, respectively. The definitions of the distribution functions analyzed within the thesis are summarized in Appendix A.1. For a more comprehensive overview, the reader is referred to [25].

Instead of analyzing the distribution function in detail, the properties of a random variable can be summarized by stochastic moments. The n-th moment of a random variable is given by

$$E[X^n] = \int_{-\infty}^{\infty} x^n f_X(x) dx. \tag{3.6}$$

The first stochastic moment, also denoted as μ_x, represents the mean value of a random variable and can be interpreted as the arithmetic average of X. Apart from that, the second centralized moment, also called variance,

$$Var[X] = E[(X - \mu_X)^2] = \int_{-\infty}^{\infty} (x - \mu_X)^2 f_X(x) dx \tag{3.7}$$

is used to describe the spreading of X around its mean. The square-root of it represents the standard deviation σ_x. In case of a non-Gaussian probability distribution, also the third (γ_x) and fourth (κ_x) normalized moments may be of interest which are defined by

$$\begin{aligned} \gamma_x &= E\left[\left(\frac{X - \mu_x}{\sigma_x}\right)^3\right] = \frac{\mu_x^3}{\sigma_x^3} \text{ , and} \\ \kappa_x &= E\left[\left(\frac{X - \mu_x}{\sigma_x}\right)^4\right] = \frac{\mu_x^4}{\sigma_x^4}. \end{aligned} \tag{3.8}$$

The former quantifies the skewness which is a measure for the asymmetry of the distribution. A negative value of γ_x denotes a long left tail whereas a positive skewness indicates a long right tail. The fourth normalized moment, referred to as kurtosis, is another metric for the characteristics of the tails. Probability distributions with a high kurtosis have a sharp peak and heavy tails. In contrast, the uniform distribution has no tails and is therefore quantified by a low kurtosis value.

Apart from the stochastic moments, other important descriptors are the mode ($\hat{X}$) and median ($\tilde{X}$) of a distribution. The former is related to the value where $f_X(x)$ takes its maximum value. The median is formally defined as the location where $F_X(x) = 0.5$. Thus, the median can be interpreted as the "middle" value of the distribution. Note, that mean, mode and median describe the same value for a unimodal, symmetric probability distribution. [26]

For a multi-dimensional random vector $\mathbf{X}$, the stochastic descriptors discussed before are represented by n_x-dimensional vectors instead of scalar values. The variance is usually expressed by the covariance matrix $\mathbf{\Sigma}_x$ which is a $[n_x \times n_x]-$ dimensional, positive semi-definite matrix. The entries of $\mathbf{\Sigma}_x$ are defined by

$$\Sigma_{X_i,X_j} = E[(X_i - \mu_{x_i})(X_j - \mu_{x_j})] \quad \text{for } X_i, X_j \in \mathbf{X}. \tag{3.9}$$

Hence, $\mathbf{\Sigma}_x$ is a symmetric matrix where the diagonal entries refer to the variance of the single coordinates of $\mathbf{X}$ such that $\Sigma_{X_i,X_i} = \sigma_{x_i}^2$ holds. The off-diagonal entries represent the pairwise covariance between the random variables which is a measure for the linear dependency between the two corresponding random variables. If all coordinates of $\mathbf{X}$ are independent from each other, the off-diagonal entries are zero. However, a zero-valued covariance could also result from a nonlinear relationship which is not detected by the covariance measure in Eq. (3.9). The major prerequisite for quantifying an uncertainty source with the help of the probability the-

ory is the existence of a sufficient amount of data. In the next paragraph, different methods for conducting a distribution fitting are summarized.

Concepts for Distribution Fitting

Let us consider that we are provided with a set of n_m measurement points denoted by

$$\mathcal{X}_\mathsf{m} = \{\boldsymbol{x}_\mathsf{m}^{(1)}, \ldots, \boldsymbol{x}_\mathsf{m}^{(n_\mathsf{m})}\} \subset \mathbb{R}^{n_x}. \tag{3.10}$$

In principal, a distribution fitting can be conducted by different ways [137]. The following concepts are introduced for the one-dimensional case.
The simplest technique is to determine an empirical CDF which is directly derived from the data set $\mathcal{X}_\mathsf{m}$ by

$$F_X^{\mathsf{emp}}(x) = \frac{1}{n_\mathsf{m}} \sum_{i=1}^{n_\mathsf{m}} \mathbb{1}_{x_\mathsf{m}^{(i)} \leq x}(x), \tag{3.11}$$

where $\mathbb{1}_{x_\mathsf{m}^{(i)} \leq x}(x)$ is an indicator function which takes the value of one if the data point $x_\mathsf{m}^{(i)}$ is smaller or equal than x and the value of zero otherwise. The resulting CDF is characterized by a step-function with jump heights of $1/n_\mathsf{m}$ at every data point. The main disadvantage of this approach is the non-continuous characteristic of the derived CDF.
An alternative approach is the method of moments. At first, the modeler has to choose a certain family of distributions $F_X(x|\Theta_x)$ which could represent the properties of the data well. A graphical representation of $\mathcal{X}_\mathsf{m}$, for example in the form of a histogram plot, can help to make a reasonable decision. After that, the sample mean ($\breve{\mu}_x$) and standard deviation ($\breve{\sigma}_x$) are computed according to

$$\begin{aligned} \breve{\mu}_x &= \frac{1}{n_\mathsf{m}} \sum_{i=1}^{n_\mathsf{m}} x_\mathsf{m}^{(i)}, \text{ and} \\ \breve{\sigma}_x &= \sqrt{\frac{1}{n_\mathsf{m}-1} \sum_{i=1}^{n_\mathsf{m}} (x_\mathsf{m}^{(i)} - \breve{\mu}_x)^2}. \end{aligned} \tag{3.12}$$

The actual distribution fitting is conducted by choosing the parameters Θ_x such that $\breve{\mu}_x$ and $\breve{\sigma}_x$ coincide with the corresponding moments from the chosen distribution.
The maximum likelihood method follows a similar approach. Again, a preliminary distribution type $F_X(x|\Theta_x)$ with unknown parameters Θ_x must be defined. Based on that, the likelihood

$$\mathcal{L}(\Theta_x|\mathcal{X}_\mathsf{m}) = \prod_{i=1}^{n_\mathsf{m}} f_X(x_\mathsf{m}^{(i)}|\Theta_x) \tag{3.13}$$

expresses the probability that $\mathcal{X}_\mathsf{m}$ is an outcome of the chosen probability distribution and parameter set Θ_x. Finally, the optimal parameters Θ_x^* of the predefined distribution are deter-

mined by the following optimization:

$$\Theta_x^* = \underset{\boldsymbol{\Theta}_x}{\text{maximize}}\ \mathcal{L}(\boldsymbol{\Theta}_x|\mathcal{X}_\mathsf{m}). \tag{3.14}$$

To repeat, all of the concepts discussed so far require that the number of points n_m is large enough. If only a scarce set of measurements is available, modelers should account for the uncertainty induced by estimating the model parameters $\boldsymbol{\Theta}_x$ as well as the subjective choice of distribution family. Since the probability theory is not able to capture the additional uncertainties, alternative concepts are needed.

3.2.2 Hybrid Uncertainties

As discussed in the previous section, when characterizing an aleatory uncertainty source with the help of the probability theory, a CDF is used to quantify the event $\{X \leq x\}$ by a single measure. In case of hybrid uncertainties, a mix of aleatory and epistemic uncertainties is existing. One approach to quantify this uncertainty type is the parametric p-box concept which is an extension of the probability theory.

Parametric Probability-Boxes: Theoretical Background

The general p-box approach, introduced by [59], is based on the idea to define a lower ($\underline{F}_X(x)$) and upper bound ($\overline{F}_X(x)$) on the CDF. Hence, the probability of the event $\{X \leq x\}$ is given by an interval

$$F_X(x) \in \left[\underline{F}_X(x), \overline{F}_X(x)\right] \text{ for } x \in \mathbb{R} \tag{3.15}$$

instead of a crisp value. Note, that $\underline{F}_X(x)$ and $\overline{F}_X(x)$ must be a subset of $\mathbb{F}$ defined by Eq. (3.17). The p-box concept can be subdivided into two groups: parametric and distribution-free. The former one is an appropriate UQ method for hybrid uncertainties whereas the distribution-free p-box concept is a more general representation and can be used for epistemic uncertainties, see Sec. 3.2.3. In the following, the focus is put on the parametric type.
The prerequisite for defining a distributional p-box is to have knowledge about the distribution type. In contrast to the probability theory, the corresponding set of parameters $\boldsymbol{\Theta}_x$ is given by intervals. From a mathematical point of view, the p-box is formally defined by the quintuple

$$\left(\underline{F}_X(x), \overline{F}_X(x), \mu_x^I, \sigma_x^I, \mathcal{D}_F\right). \tag{3.16}$$

The first two entries correspond to the basic definition of a distribution-free p-box given in Eq. (3.15). Further, the last element $\mathcal{D}_F \subseteq \mathbb{F}$ defines the admissible set of probability distributions, where $\mathbb{F}$ is a general representation of all CDFs on $\mathbb{R}$ given by

$$\mathbb{F} = \{F \mid F : \mathbb{R} \mapsto [0,1],\ F(x) \leq F(y) \text{ for any } x \leq y\}. \tag{3.17}$$

The remaining two entries $\mu_x^I \subseteq \mathbb{IR}$ and $\sigma_x^I \subseteq \mathbb{IR}$ are interval domains which cover the range of possible values for the mean and standard deviation, respectively. The symbol $\mathbb{IR}$ represents the space of all real-valued intervals. Thus, a feasible CDF lying inside the parametric p-box has to fulfill the criteria

$$\int_{-\infty}^{\infty} x f_X(x) dx \ \in \ \mu_x^I, \tag{3.18}$$

and

$$\sqrt{\int_{-\infty}^{\infty} (x-\mu_X)^2 f_X(x) dx} \ \in \ \sigma_x^I. \tag{3.19}$$

Note, that a parametric p-box could also be represented by other stochastic moments than mean and standard deviation. [21, 54]
An alternative p-box definition to Eq. (3.17) is given by [158]

$$F_X(x) = F_X(x|\boldsymbol{\Theta}_x), \text{ with } \boldsymbol{\Theta}_x \in \boldsymbol{\Theta}_x^I \subseteq \mathbb{IR}^{n_{\theta_x}}, \tag{3.20}$$

where $\boldsymbol{\Theta}_x^I = \bigcup_{i=1}^{n_\Theta} [\underline{\theta}_x^{(i)}, \overline{\theta}_x^{(i)}]$ is an n_Θ-dimensional hypercube representing the feasible parameter space. The notations $\underline{\theta}_x^{(i)}$ and $\overline{\theta}_x^{(i)}$ indicate the lower and upper bound of the parameter $\theta_x^{(i)}$, respectively.
In order to illustrate the parametric p-box concept, we consider a Gaussian distribution $X \sim \mathcal{N}(\mu_x^I, \sigma_x^I)$ with uncertain mean and standard deviation. In this example, the intervals of the stochastic moments are defined by $\mu_x^I = [1.0, 3.0]$ and $\sigma_x^I = [1.0, 2.5]$. The gray curves in Fig. 3.2 give an ensemble of different Gaussian CDFs covered by the p-box definition. The two solid black lines illustrate the lower and upper bounds according to

$$\begin{aligned} \underline{F}_X(x) &= \min_{\boldsymbol{\Theta}_x} F_X(x|\boldsymbol{\Theta}_x), \text{ and} \\ \overline{F}_X(x) &= \max_{\boldsymbol{\Theta}_x} F_X(x|\boldsymbol{\Theta}_x). \end{aligned} \tag{3.21}$$

The lower and upper bound can be a combination of different CDFs. In the example introduced before, the lower bound is a composition of $F_X(x|\mu_X = 1.0, \sigma_X = 1.0)$ and $F_X(x|\mu_X = 1.0, \sigma_X = 2.5)$. From the graphical representation, one can see the clear separation between the two uncertainty types. The aleatory uncertainty is assigned to the distribution type, i.e., the Gaussian distribution in this example, and the epistemic part causes the uncertainty on the distribution parameters. The degree of epistemic uncertainty can be interpreted as the gap width or area between $\underline{F}_X(x)$ and $\overline{F}_X(x)$. If the epistemic uncertainty was reduced completely, the p-box would degenerate to a single CDF.
Similar to the probability theory, the parametric p-box concept can be extended for multi-dimensional cases which raises automatically the question of how to model possible inter-correlations. In principle, two options are available to account for dependencies between the coordinates of the random vector $\mathbf{X}$. The authors of [103] propose to define dependencies at the aleatory level. As in case of the probability theory, the joint CDFs, which represent real-

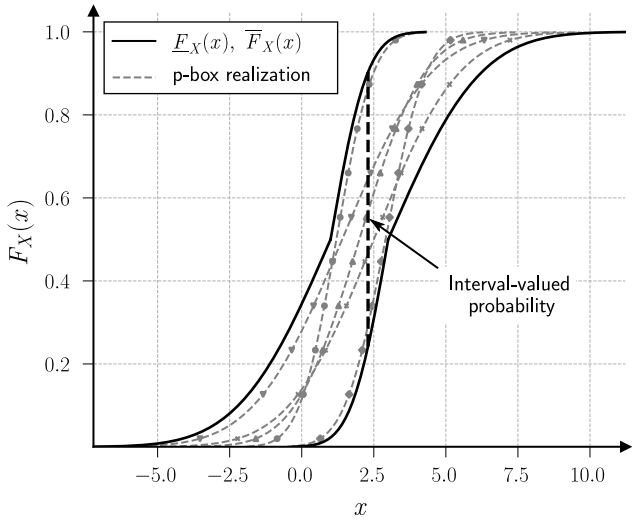

Figure 3.2 P-box derived from the Gaussian distribution family.

izations of the multi-dimensional p-box $F_{\mathbf{X}}(\mathbf{x}|\boldsymbol{\Theta}_x)$, are quantified with the help of copulas. An alternative approach is to consider dependencies at the epistemic level. Hence, the hyperparameter space $\boldsymbol{\Theta}_x^I$, which encloses the possible distributional parameters of all marginals, is no longer a set of independent intervals. In [56], the copula concept is extended to introduce dependencies between intervals.

Within the scope of this thesis, correlations between hybrid uncertainties are modeled by restricting the space of feasible hyperparameter combinations. Thus, $\boldsymbol{\Theta}_x^I$ is not defined as a hyper-rectangle. In the following paragraph, the construction of parametric p-boxes is discussed for one-dimensional cases.

Constructing Parametric Probability-Boxes

Let us consider again the case that a set of n_{m} measurement points is given as represented in Eq. (3.10). Now, we assume that $\mathcal{X}_{\mathrm{m}}$ contains only a small number of samples. Still, one can use the techniques introduced before to fit a specific probability distribution to the data. However, repeating the distribution fitting procedure with a second sample set of equivalent size can lead to significantly different result. Instead of defining the distribution parameters $\boldsymbol{\Theta}_x$ by crisp values, a CI (confidence interval) can be used for the characterization.

The meaning of a CI can be described as follows. Let us assume that we have drawn 25 random samples from an unknown distribution $F_X(x)$ to approximate the true mean by $\check{\mu}_x$, see Eq. (3.12). In order to assess the quality of the estimation, we can compute, for example, the 90% CI of the sample mean. If we repeated this experiment endlessly, the derived CIs would contain μ_x in 90% of all cases. [113]

The mathematical expressions for computing the CI depends on whether the true standard deviation σ_x is known or not. For the most general case, the modeler has neither information about the distribution type of $F_X(x)$ nor about the value of σ_x. According to [177], the γ-level

CI for the mean and variance are given by:

$$\mathrm{CI}_{\mu} = \left[\breve{\mu}_X - q_t\left(\frac{1-\gamma}{2}, n_{\mathrm{m}} - 1\right) \frac{\breve{\sigma}_x}{\sqrt{n_{\mathrm{m}}}},\ \breve{\mu}_X + q_t\left(\frac{1-\gamma}{2}, n_{\mathrm{m}} - 1\right) \frac{\breve{\sigma}_x}{\sqrt{n_{\mathrm{m}}}} \right], \tag{3.22}$$

and

$$\mathrm{CI}_{\sigma^2} = \left[\frac{(n_{\mathrm{m}} - 1)\breve{\sigma}_x^2}{q_{\mathcal{X}^2}((1-\gamma)/2, n_{\mathrm{m}} - 1)},\ \frac{(n_{\mathrm{m}} - 1)\breve{\sigma}_x^2}{q_{\mathcal{X}^2}((1+\gamma)/2, n_{\mathrm{m}} - 1)} \right], \tag{3.23}$$

where $q_t((1-\gamma)/2, n_{\mathrm{m}} - 1))$ and $q_{\mathcal{X}^2}((1-\gamma)/2, n_{\mathrm{m}} - 1))$ denote the $((1-\gamma)/2) - th$ quantile value for a student's t and chi-square distribution with $n_{\mathrm{m}} - 1$ degrees of freedom, respectively. The CIs derived in Eqs. (3.22) and (3.23) can be directly used for the quantification of the distribution parameter intervals μ_x^I and σ_x^I. Usually, the $\gamma-$level of the CI is set to 95%.
In order to demonstrate the benefits of quantifying an uncertainty by a p-box instead of a single CDF, we consider the following case. Let us assume that we are provided with 10 samples drawn from a standard Gaussian distribution $\mathcal{N}(0,1)$, depicted by the solid gray line in Fig. 3.3. In the first approach, the method of moments is used to determine the sample mean and standard deviation according to Eq. (3.12). The corresponding CDF for a Gaussian distribution is given by $\mathcal{N}(-0.397, 1.358)$ and shown by the gray dotted line in Fig. 3.3. In addition, the empirical CDF is represented by the step function. In the second case, a p-box is constructed from the set of data points. Since we assume that the underlying distribution is unknown, the formulas in Eqs. (3.22) and (3.23) are used to derive μ_x^I and σ_x^I based on a confidence level of 95%. As a result, we obtain the intervals $\mu_x^I = [-1.37, 0.57]$ and $\sigma_x^I = [0.93, 2.48]$. Again, a normal distribution is chosen which leads to the parametric p-box shown by the solid black curves. When comparing the different UQ methods in Fig. 3.3 with each other, it becomes obvious that conducting a distribution fitting on the basis of a small data set can lead to a significant offset

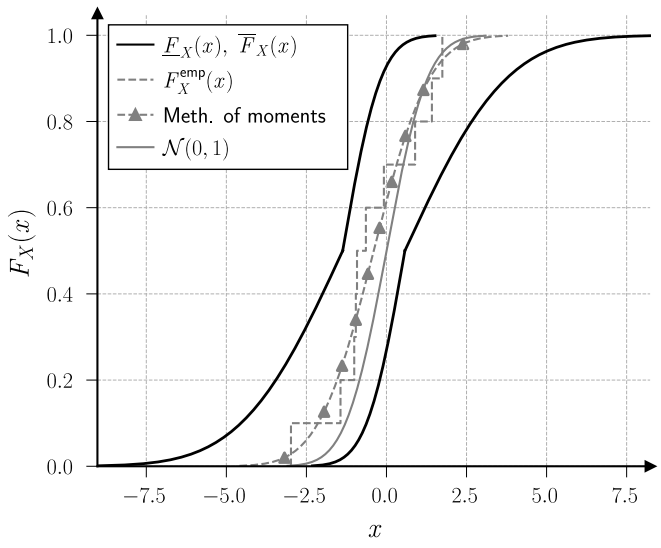

Figure 3.3 Uncertainty Quantification based on distribution fitting and p-box construction.

from the true distribution. Conducting further studies can lead to biased interpretations on the results. In contrast, the parametric p-box tries to counteract the limited knowledge by providing a set of possible CDFs within certain bounds. One can see that the unknown distribution is captured by the bounds.
The example discussed before has highlighted the advantages of the p-box concept but there are also some limitations worth mentioning. First, it is not guaranteed that the p-box really encloses the CDF even though a high confidence level has been chosen. Further, the derivation is still based on an assumption regarding the distribution type. Especially for a low number n_{m} of data points, the choice of the distribution family is a rather biased decision.

3.2.3 Epistemic Uncertainties

The category of epistemic uncertainties is characterized by an even lower state of knowledge about the uncertainty source than for the hybrid type. The concept of parametric p-boxes is therefore not appropriate for the UQ. Instead, the usage of distribution-free, or in short free, p-boxes is more appropriate which is introduced in the following.

Distribution-Free P-Box: Theoretical Background

As can be derived from the expression *distribution-free*, this type of p-box is not related to a specific family of distributions. Roughly spoken, it is only defined by a lower and upper bound as expressed in Eq. (3.15). Any CDF $F_X(x) \in \mathbb{F}$ fulfilling this condition is a valid realization of the p-box. Coming back to the quintuple-based formulation in Eq. (3.16), a distribution-free p-box can be formally derived as

$$\left(\underline{F}_X(x), \overline{F}_X(x), \mu_x^I, \sigma_x^I, \mathbb{F}\right). \tag{3.24}$$

In the most general case, i.e., without any constraints on the stochastic moments, the definition can be reduced to the triple $\left(\underline{F}_X(x), \overline{F}_X(x), \mathbb{F}\right)$.
The free p-box concept is closely related to the so-called Dempster-Shafer theory, also known as evidence theory developed by Arthur Dempster and Glenn Shafer [161]. In accordance with the probability theory, it is based on an event space characterized by $(\Omega, \mathcal{F}_e, \mathbb{P}_e)$. Again, the first entry Ω represents the sample space which contains all possible values of the random process. The second element $\mathcal{F}_e$ represents a set of subsets of the sample space. The subsets $\mathcal{A}_e^{(i)}$ are also referred to as focal elements. In contrast to the probability theory, $\mathcal{F}_e$ is not a $\sigma-$field. Thus, it does not have to fulfill the specific properties listed in Section 3.2.1. Further, $\mathcal{F}_e$ comprises usually a countable collection of focal elements whereas $\mathcal{F}_p$ covers an infinite number of subsets. The last entry $\mathbb{P}_e$ assigns a probability to every focal element

according to

$$\mathbb{P}_e(\mathcal{A}_e^{(i)}) = \begin{cases} > 0 & \text{if } \mathcal{A}_e^{(i)} \in \mathcal{F}_e \\ 0 & \text{if } \mathcal{A}_e^{(i)} \subset \Omega \text{ and } \mathcal{A}_e^{(i)} \notin \mathcal{F}_e \end{cases} \tag{3.25}$$

with

$$\sum_{\mathcal{A}_e^{(i)} \in \mathcal{F}_e} \mathbb{P}_e(\mathcal{A}_e^{(i)}) = 1.0, \quad \text{and} \quad \mathbb{P}_e(\emptyset) = 0. \tag{3.26}$$

In context of the evidence theory, $\mathbb{P}_e$ is called BPA (basic probability assignment). As shown by the formulation in Eq. (3.25), the BPA raises no information about the probability assigned to any subset of the focal element itself. In comparison to the probability theory, $\mathbb{P}_e$ is not the fundamental measure of uncertainty. Instead, two measures of uncertainty can be derived for a subset $\mathcal{S} \subset \Omega$: belief and plausibility. The corresponding equations are given by

$$Bel(\mathcal{S}) = \sum_{\mathcal{A}_p^{(i)} \subset \mathcal{S}} \mathbb{P}_e(\mathcal{A}_p^{(i)}) \tag{3.27}$$

and

$$Pl(\mathcal{S}) = \sum_{\mathcal{A}_p^{(i)} \cap \mathcal{S} \neq \emptyset} \mathbb{P}_e(\mathcal{A}_p^{(i)}). \tag{3.28}$$

The belief $Bel(\mathcal{S})$ in the occurrence of $\mathcal{S}$ can be interpreted as an uncertainty measure which collects all information that must be assigned to the subset $\mathcal{S}$. Thus, the probabilities of all focal elements are summed up which are a subset of $\mathcal{S}$, see Eq. (3.27). On the other hand, the plausibility $Pl(\mathcal{S})$ of the event $\mathcal{S}$ is a measure for the maximum amount of information that could be assigned to $\mathcal{S}$. Consequently, $Pl(\mathcal{S})$ is calculated by summing up the probabilities of all focal elements that intersect the event $\mathcal{S}$, see Eq. (3.28). The difference between the two uncertainty measures comes from the fact, that the BPA provides no information how the assigned probabilities are distributed within the focal elements. A direct relation between belief and plausibility of an event is given by

$$Bel(\mathcal{S}) + Pl(\mathcal{S}^C) = 1, \tag{3.29}$$

where S^C denotes the complement of S. In the following, we consider the case that $\mathcal{F}_e$ is represented by a set of n_f intervals on the real line

$$\mathcal{F}_e = \left\{ \left(\left[\underline{x}^{(1)}, \overline{x}^{(1)} \right], m^{(1)} \right), \left(\left[\underline{x}^{(2)}, \overline{x}^{(2)} \right], m^{(2)} \right), \ldots, \left(\left[\underline{x}^{(n_\mathrm{f})}, \overline{x}^{(n_\mathrm{f})} \right], m^{(n_\mathrm{f})} \right) \right\}, \tag{3.30}$$

where $\underline{x}^{(i)}$ and $\overline{x}^{(i)}$ is the lower and upper bound of the focal element, respectively, and $m^{(i)}$ denotes the BPA.

As discussed in Section 3.2.1, the CDF of a random variable X is used to summarize the

underlying probability space. The same concept is applied for the two uncertainty measures on X for the evidence theory. Accordingly, the uncertainty on the event $\mathcal{S} = (-\infty, x] \subset \mathcal{F}_e$ for a continuous random variable is represented by a CBF (cumulative belief function) and CPF (cumulative plausibility function). Note that the evidence space, unlike the probability space, is directly defined on $\mathbb{R}$. For this reason, no additional mapping is required. The equations for the CBF and CPF are expressed by

$$CBF_X(x) = Bel_X(\mathcal{S} = (-\infty, x]) = \sum_{i=1}^{n_\mathrm{f}} \mathbb{1}_{\overline{x}^{(i)} \leq x}(x)\, m^{(i)}, \tag{3.31}$$

and

$$CPF_X(x) = Pl_X(\mathcal{S} = (-\infty, x]) = \sum_{i=1}^{n_\mathrm{f}} \mathbb{1}_{\underline{x}^{(i)} \leq x}(x)\, m^{(i)}. \tag{3.32}$$

The two expressions from Eqs. (3.31) and (3.32) can be interpreted as the envelopes of the unknown CDF. This means that the CBF and CPF corresponds to the lower $\underline{F}_X(x)$ and upper bound $\overline{F}_X(x)$ of a distribution-free p-box. The meaning and interpretation of focal elements is illustrated in greater detail within the next paragraph which describes the construction of distribution-free p-boxes. Furthermore, the duality between evidence theory and p-box concept is important for the uncertainty propagation techniques discussed in Section 3.3. [76, 78]

Constructing Distribution-Free P-Boxes

For the aleatory as well as the hybrid uncertainty type, we have assumed the existence of a sufficient amount of measurement data $\mathcal{X}_\mathrm{m}$. For epistemic uncertainties, it could be even the case that the modeler's knowledge is based on some stochastic characteristics without having measurement data. In particular, the p-box construction is discussed for two scenarios:

1. The modeler's knowledge is limited to stochastic moments or other descriptors such as the mode, median and the bounds of the CDF.
2. A set of data points $\mathcal{X}_\mathrm{m}$ is provided. Due to the low quantity and/or quality of the measurements, other concepts than the ones introduced for aleatory and hybrid uncertainties are needed for an unbiased UQ.

An extreme case of the first scenario occurs when the modeler only knows the bounds of a random variable. In this situation, an unbiased UQ of the uncertainty on X is given by an interval representation. This formulation can be expressed via the p-box

$$\underline{F}_X(x) = \mathbb{1}_{x \leq \overline{x}}(x), \quad \text{and} \quad \overline{F}_X(x) = \mathbb{1}_{x \leq \underline{x}}(x), \tag{3.33}$$

where $\underline{x}$ and $\overline{x}$ denote the lower and upper bound. However, usually additional information is either available or can be derived from reasonable assumptions to shrink the p-box bounds.

In case of having further information about the range of possible mean values, i.e., $\mu_x \in [\underline{\mu}_x, \overline{\mu}_x]$, tighter p-box bounds can be derived. Based on the findings in [146], the formulas for the updated bounds are given by

$$\underline{F}_X(x) = \begin{cases} 0 & \text{if } x < \overline{\mu}_x \\ (x-\overline{\mu}_x)/(x-\underline{x}) & \text{if } x \geq \overline{\mu}_x \end{cases}, \tag{3.34}$$

and

$$\overline{F}_X(x) = \begin{cases} (\overline{x}-\underline{\mu}_x)/(\overline{x}-x) & \text{if } x < \underline{\mu}_x \\ 1 & \text{if } x \geq \underline{\mu}_x \end{cases}. \tag{3.35}$$

Figure 3.4(a) shows the case of a random variable being limited to the interval $x \in [2.0, 8.0]$. The dotted lines represent the additional constraints on the mean value, given by the range $\mu_x \in [4.5, 5.5]$. Besides from the mean, experts' opinions are sometimes referred to the median $\tilde{X}$, i.e., the location where $F_X(x)$ takes the value 0.5. This type of information can also be transferred to mathematical expressions for the p-box bounds. The lower one is given by a step function with jumps at $\overline{x}$ and the upper median value whereas the upper bound is characterized by jumps at $\underline{x}$ and the lower median value. The dashed line in Fig. 3.4(a) depicts an example, where the median range is limited such that $\tilde{X} \in [4.0, 6.0]$ holds.
As discussed in Section 3.2.1, the median is equal to the $50-$th percentile value. Hence, the same concept can be applied if one has information regarding a different percentile value.
Another typical stochastic descriptor is the mode ($\hat{X}$) of a random distribution which corresponds to the maximum value of the PDF. Under the conditions that $f_X(x)$ is unimodal with $\hat{X} \in [\underline{\hat{x}}, \overline{\hat{x}}]$, the bounds on the true CDF are provided by

$$\underline{F}_X(x) = \begin{cases} 0 & \text{if } x \leq \overline{\hat{x}} \\ (x-\overline{\hat{x}})/(\overline{x}-\overline{\hat{x}}) & \text{if } \overline{\hat{x}} < x \leq \overline{x} \end{cases}, \tag{3.36}$$

and

$$\overline{F}_X(x) = \begin{cases} (x-\underline{x})/(\underline{\hat{x}}-\underline{x}) & \text{if } \underline{x} \leq x < \underline{\hat{x}} \\ 1 & \text{if } x \geq \underline{\hat{x}} \end{cases}. \tag{3.37}$$

The derivations of the Eqs. (3.36) and (3.37) are beyond the scope of the thesis and can be read in [43]. A graphical representation for the mode range $\hat{X} \in [4.0, 6.0]$ is shown in Fig. 3.4(a) by the solid lines. Each of the introduced p-box equations is rigor-preserving and best possible. The former property means that the corresponding uncertainty is covered completely by

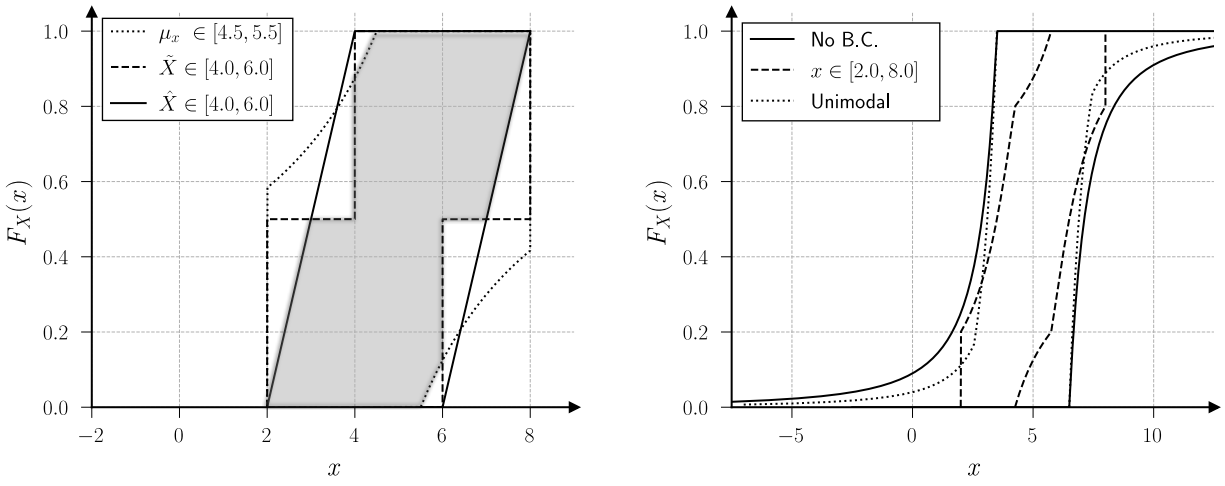

(a) P-boxes for constraints on mean, mode and median.

(b) P-box for fixed mean and standard deviation.

Figure 3.4 P-box definition based on bounds on the mean, mode and median (left) and Chebyshev-based p-box definition for fixed mean and standard deviation (right).

the bounds whereas best possible refers to the fact that the envelopes could not be any tighter without additional information. If the modeler has data for several stochastic descriptors, an aggregation can be performed by intersecting the single p-box formulations. The final bounds are still rigor-preserving as long as all the underlying p-boxes share this property. The gray-shaded area in Fig. 3.4(a), for example, is an aggregation of the p-boxes resulting from the constraints on the mean, mode and median. [60]

All the scenarios discussed so far deal with cases where certain properties of the distribution function are expressed by intervals. However, modelers can face the situation of having precise knowledge about μ_x and σ_x without knowing the underlying distribution type. Instead of assuming a specific CDF, the Chebyshev inequality can be used to construct a p-box. This inequality is given by

$$P(|X - \mu_x| \geq k) < \frac{\sigma_x^2}{k^2}, \tag{3.38}$$

which provides an upper bound for the probability that X deviates from μ_x by more than the threshold k [169]. Due to the missing information about the distribution family, the provided percentile bounds from the Chebyshev inequality are rather conservative. In [123], mathematical expressions have been derived to transfer the inequality to crisp p-box bounds, given by

$$\underline{F}_X(x) = \begin{cases} 0 & \text{if } x < \mu_x + \sigma_x \\ 1 - \frac{\sigma_x^2}{(x-\mu_x)^2} & \text{if } x \geq \mu_x + \sigma_x \end{cases}, \quad \overline{F}_X(x) = \begin{cases} \frac{\sigma_x^2}{(x-\mu_x)^2} & \text{if } x < \mu_x - \sigma_x \\ 1 & \text{if } x \geq \mu_x - \sigma_x \end{cases}. \tag{3.39}$$

Figure 3.4(b) contains the graphical representation of Eq. (3.39) for an example with $\mu_x = 5.0$

and $\sigma_x = 1.5$. Consequently, any CDF fulfilling these two stochastic requirements is captured by the p-box. As in the previous case, additional information about the random quantity is helpful to tighten the bounds. For example, knowing that X is unimodal leads to the envelopes shown by the dotted lines. Another conceivable scenario is to decrease the lack-of-knowledge by restricting the range of possible values to a certain interval. The dashed p-box represents the constraint that X can only take values within $[2.0, 8.0]$. The equations for both of the modified versions are explained in Appendix A.2. Again, each of the bounds is rigor-preserving and best possible.

The second main scenario listed on page 43 is related to cases where the modeler is provided with a data set $\mathcal{X}_\mathsf{m}$. Within the framework of epistemic uncertainties, the information contained in $\mathcal{X}_\mathsf{m}$ is usually scarce, incomplete or ambiguous. Let us assume that each entry $\boldsymbol{x}_\mathsf{m}^{(i)} \in \mathcal{X}_\mathsf{m}$ results from an expert's opinion about the possible values for the random quantity under investigation. Hence, $\mathcal{X}_\mathsf{m}$ is no longer a set of measurements but a collection of intervals coming from independent experts. By adding a certain probability to every interval, $\mathcal{X}_\mathsf{m}$ can be interpreted as a set of focal elements $\mathcal{F}_e$ if the sum of all probabilities equals one, see Eq. (3.26). The BPA is therefore a measure for the trustworthiness in an expert's opinion. Figure 3.5 shows an example where the uncertainty on X is given by four interval-valued estimations, each of them assigned with a different probability. The focal elements can be expressed by $\mathcal{F}_e = \{([2.0, 3.5], 0.2), ([2.5, 4.0], 0.1), ([3.0, 5.0], 0.3), ([3.5, 4.5], 0.4)\}$. According to Eqs. (3.31) and (3.32), the CBF ($\underline{F}_X(x)$) and CPF ($\overline{F}_X(x)$) are derived from the upper and lower bounds of the focal elements, see Fig. 3.5(b). A similar scenario occurs when $\mathcal{X}_\mathsf{m}$ includes a set of data subject to significant measurement inaccuracies. In this case, representing the data as focal elements with a BPA of $1/n_\mathsf{m}$ is more reasonable than treating the measurements as point values. The range of each element corresponds to the measurement uncertainty. Note that the p-box construction is similar to the concept depicted in Fig. 3.5. [60]

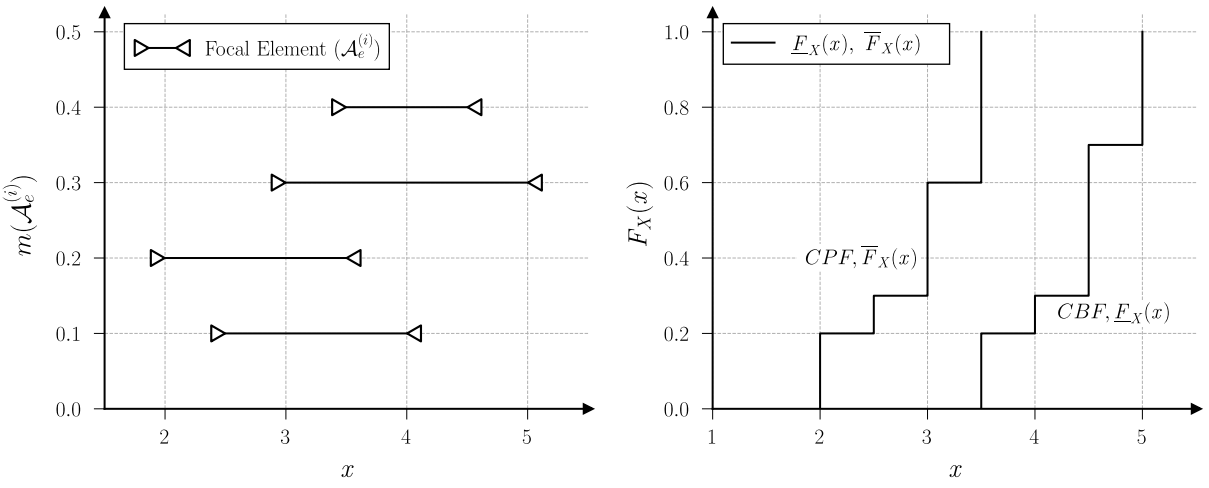

(a) Experts' opinions expressed as focal elements.

(b) P-box derived from the focal elements.

Figure 3.5 P-box definition based on different experts' opinions.

The two study cases discussed in the previous paragraph are related to the poor quality of a data set. Even if $\mathcal{X}_{\mathsf{m}}$ is derived from precise measurements, epistemic uncertainty can still be induced due to a low number of data points. To repeat, the problem aligned with small sample sets is the fact that they are not a comprehensive representation of the whole population. Thus, characterizing the uncertainty by an empirical CDF, see Eq. (3.11), is an extremely biased view. In context of parametric p-boxes, the concept of confidence intervals has been discussed in Sec. 3.2.2 which considers the low data quantity by equipping the estimates of the distributional parameters with intervals. For the construction of a distribution-free p-box, the empirical CDF is provided with the Kolmogorov-Smirnov confidence band such that

$$P(\underline{F}_X(x) \leq F_X(x) \leq \overline{F}_X(x)) \geq (1.0-\gamma) \tag{3.40}$$

holds, where γ describes the confidence level. In contrast to a CI, the confidence band is applied to the whole distribution instead of a single parameter. The mathematical interpretation of Eq. (3.40), however, is similar as the one for a CI. When computing the $\gamma-$level confidence band for the empirical CDF $F_X^{\mathsf{emp}}(x)$, the true CDF is covered by the bounds in at least $(1.0-\gamma)\cdot 100\%$ of the cases. The corresponding lower and upper bound of the p-box are defined by the step functions

$$\underline{F}_X(x) = \begin{cases} F_X^{\mathsf{emp}}(x) - d_\gamma & \text{if } F_X^{\mathsf{emp}}(x) - d_\gamma \geq 0 \\ \\ 0 & \text{if } F_X^{\mathsf{emp}}(x) - d_\gamma < 0 \end{cases}, \tag{3.41}$$

and

$$\overline{F}_X(x) = \begin{cases} F_X^{\mathsf{emp}}(x) + d_\gamma & \text{if } F_X^{\mathsf{emp}}(x) + d_\gamma < 1 \\ \\ 1 & \text{if } F_X^{\mathsf{emp}}(x) + d_\gamma \geq 1 \end{cases}. \tag{3.42}$$

The parameter d_γ refers to the $\gamma-$level confidence band width and depends on the number of sample points contained in $\mathcal{X}_{\mathsf{m}}$. The only prerequisite for deriving the confidence band is that the samples in $\mathcal{X}_{\mathsf{m}}$ are independent and identically distributed. For further information on the mathematical background of the confidence bands, the reader is referred to [80, 94, 114].

All of the methods discussed within the previous paragraphs share the idea of expressing the modeler's information by bounding the space of possible CDFs. In literature, further approaches are discussed, e.g., by defining bounds on the PDF instead of the CDF. The reader is referred to [55, 60, 104].

The great benefit of constructing a distribution-free instead of a parametric p-box is that the modeler gets rid of having to choose a distribution type. For this reason, free p-boxes are definitely less biased especially if the bounds fulfill the criterion of being rigor-preserving.

Moreover, the free p-box concept offers a great flexibility to the modeler because different constraints can be combined via the aggregation of single p-boxes. Apart from the advantages, there is also a decisive drawback. All of the distribution-free p-box discussed within this chapter are rigor-preserving but most of them cover unfeasible CDFs, i.e., distributions which do not fulfill the underlying constraints as well. When analyzing the unconstrained p-box for a specific mean and variance in Fig. 3.4(b), one can see that the envelopes cover CDFs with distributional parameters other than the specified ones. For example, the envelopes themselves represent distribution functions with mean values that are significantly different from the defined one. The modeler should be aware of this effect as it can lead to a certain degree of over-conservatism which makes the interpretation of the uncertainty studies difficult. To counteract this drawback, a novel parametric p-box concept is introduced in Sec. 5.2.1. The basic idea is to find a representation which excludes undesired CDFs from the definition while preserving as much flexibility as possible for modeling the lack of knowledge.
Apart from the quantification, the propagation of uncertainties is an essential part for conducting uncertainty studies. In the next section, a short review on state-of-the-art techniques for uncertainty propagation is given.

3.3 Uncertainty Propagation

The purpose of propagating uncertainties throughout a computational model is to analyze the effect of the input quantity uncertainty on the system response. As a consequence, the response quantities under investigation can be interpreted as random variables $Y_i \in \mathbf{Y}$. Depending on the problem, stochastic moments such as mean (μ_y) and standard deviation (σ_y) can be of interest or even the distribution function $F_Y(y)$ itself. The following subsections summarize appropriate propagation techniques for the uncertainty categories introduced before.

Aleatory Uncertainties

For aleatory uncertainties, the variation on the input quantities $\mathbf{x} \in \mathbb{R}^{n_x}$ is characterized by specific distribution functions. The standard error propagation concept is the MC (Monte Carlo) method which belongs to the group of sampling-based approaches. In case of continuous random variables, it can be summarized by the following steps:

1. At first, a sequence of n_s i.i.d. (independently and identically distributed) random numbers is generated. The random sequence is obtained from deterministic algorithms which is why the generated samples are not perfectly random. Therefore, the random number generator has to fulfill certain properties such as passing statistical tests on the uniformity criterion [97]. In principle, the generation of random numbers $\mathcal{U}_\mathsf{s} = \{\boldsymbol{u}_\mathsf{s}^{(1)}, \ldots, \boldsymbol{u}_\mathsf{s}^{(n_\mathsf{s})}\} \subset \mathbb{R}^{n_x}$ is conducted by drawing samples from the standard uniform distribution $\mathcal{U}_{[0,1]}$. Note that for $n_x > 1$, the procedure has to be extended by sampling from

a multivariate standard uniform distribution.

2. In the second step, the inverse transform method is applied so that the samples follow the desired distribution $F_X(x)$. In general, the inverse CDF is defined as

$$F_X^{-1}(z) = \inf\{x : F_X(x) \geq z\}, \text{ with } 0 \leq z \leq 1. \tag{3.43}$$

Let us consider a random variable $U \sim \mathcal{U}_{[0,1]}$ which represents the random sequence from the first step. By analyzing the CDF of the inverse transform $F_X^{-1}(U)$

$$P(F_X^{-1}(U) \leq x) = P(U \leq F_X(x)) = F_X(x), \tag{3.44}$$

it becomes clear that the realizations of X are obtained by transforming the random sequence according to $X = F_X^{-1}(U)$. The transferred random sequence is denoted as $\mathcal{X}_\mathsf{s} = \{\boldsymbol{x}_\mathsf{s}^{(1)}, \ldots, \boldsymbol{x}_\mathsf{s}^{(n_\mathsf{s})}\} \subset \mathbb{R}^{n_x}$. [180]
Again, the inverse transform method can be easily extended for a multivariate random vector $\mathbf{X}$ as long as the dimensions are independent. In case of correlated random variables, the Nataf or Rosenblatt distribution model can be used [166].

3. Finally, the computational model is evaluated to propagate the samples to the output space. For every simulation run, the input vector $\boldsymbol{x}_\mathsf{s}^{(i)} \in \mathbb{R}^{n_x}$ is mapped to a response vector $\boldsymbol{y}_\mathsf{s}^{(i)} \in \mathbb{R}^{n_y}$, see Eq. (3.1). This step can be very costly if the underlying model is computationally expensive. The resulting sample set is the basis for approximating stochastic descriptors like mean, standard deviation or failure probability.

In the following, we put the focus on deriving the stochastic moments μ_y and σ_y for a one-dimensional response space, i.e., $n_y = 1$.
The set of propagated samples $\mathcal{Y}_\mathsf{s} = \{\boldsymbol{y}_\mathsf{s}^{(1)}, \ldots, \boldsymbol{y}_\mathsf{s}^{(n_\mathsf{s})}\} \subset \mathbb{R}^{n_y}$ is used to estimate the corresponding integrals by the MC integration according to

$$E[g(X)] = \int_{-\infty}^{\infty} g(x) f_X(x) dx \approx \check{\mu}_Y = \frac{1}{n_\mathsf{s}} \sum_{i=1}^{n_\mathsf{s}} y_\mathsf{s}^{(i)}, \tag{3.45}$$

and

$$E[(g(X) - \mu_Y)^2] = \int_{-\infty}^{\infty} (g(x) - \mu_Y)^2 f_X(x) dx \approx \check{\sigma}_Y^2 = \frac{1}{n_\mathsf{s} - 1} \sum_{i=1}^{n_\mathsf{s}} (y_\mathsf{s}^{(i)} - \check{\mu}_Y)^2, \tag{3.46}$$

where $\check{\mu}_y$ and $\check{\sigma}_y$ denote the sample mean and standard deviation, respectively. Since the basis of these estimators is a set of i.i.d. samples, $\check{\mu}_y$ and $\check{\sigma}_y$ converge to their true values as $n_\mathsf{s} \to \infty$ according to the law of large numbers. One of the great benefits of the MC method is its robust convergence behavior which brings us to the CLT (central limit theorem). This proposition

states that the MC integration error for large sample sets follows a normal distribution

$$\varepsilon_{\mathrm{MC}} \approx \frac{\sigma_{\mathrm{MC}}\,\mathcal{N}(0,1)}{\sqrt{n_{\mathrm{s}}}}, \tag{3.47}$$

where σ_{MC} represents the standard deviation of the integrand. In case of the sample mean, σ_{MC} corresponds to σ_Y which means that the MC integration error tends to a normal distribution with $\mu = 0$ and $\sigma = \sigma_Y/\sqrt{n_{\mathrm{s}}}$. Thus, the MC method has a convergence rate of $O(1/\sqrt{n_{\mathrm{s}}})$ which is independent from the number of dimensions. Apart from this advantageous property, the overall convergence behavior shows a relatively poor performance caused by the fact that the random number sampling is subject to clustering. This effect leads to regions in the sample space that exhibit a lower sampling density compared to others. To overcome this drawback, pseudo-random and quasi-random MC methods have been developed. [36]

Pseudo-random MC approaches, also called variance reduction techniques, try to improve the convergence rate by decreasing the value of σ_{MC}. Among this group, one noteworthy approach is the IS (importance sampling). Here, the basic idea is to draw samples from a proposal distribution $h_X(x)$ which is different from the nominal one $f_X(x)$. Consequently, a density weighting factor $f_X(x)/h_X(x)$ must be introduced to approximate the true value of the stochastic descriptor. For example, the estimator for μ_y in Eq. (3.45) yields

$$E_h[g(X)] = \int_{-\infty}^{\infty} \frac{g(x)f_X(x)}{h_X(x)} h_X(x)dx \;\approx\; \breve{\mu}_Y = \frac{1}{n_{\mathrm{s}}} \sum_{i=1}^{n_{\mathrm{s}}} y_{\mathrm{s}}^{(i)} \frac{f_X(x_{\mathrm{s}}^{(i)})}{h_X(x_{\mathrm{s}}^{(i)})}. \tag{3.48}$$

The MC estimator for σ_y in Eq. (3.46) is extended in the same fashion. Finally, the question arises how to choose the proposal distribution to maximize the efficiency gain. When deriving the variance for the new estimator in Eq. (3.48), it follows that $h_X(x)$ should be proportional to $g(x)f_X(x)$ to minimize the variation of the estimator. For further discussions, the reader is referred to [36].

Another widely used variance reduction technique is the LH (Latin hypercube) sampling approach which is a special type of stratified sampling. In contrast to the previous method, the generated sample points are drawn from the nominal distribution but the sampling procedure itself is no longer based on a random sequence. The first step of the LH strategy is to subdivide the sample space of each random variable $X_i \in \mathbf{X}$ into n_{s} intervals of equal probability. After that, a random sample is drawn from every single subset which is assigned with a uniform distribution. This procedure is repeated for every dimension of the random vector $\mathbf{X}$. Finally, the n_{s} sample points are randomly paired without replacement which results in a set of n_{s} n_x-dimensional tuples. [75]

Figure 3.6 compares different sampling strategies in case of $n_{\mathrm{s}} = 16$ for a two-dimensional random vector with $X_1 \sim \mathcal{U}_{[0,1]}$ and $X_2 \sim \mathcal{N}(0,1)$. In every graph, the sample space is subdivided into 16 regions of equal probability. In addition, the dashed lines in Fig. 3.6(b) represent the

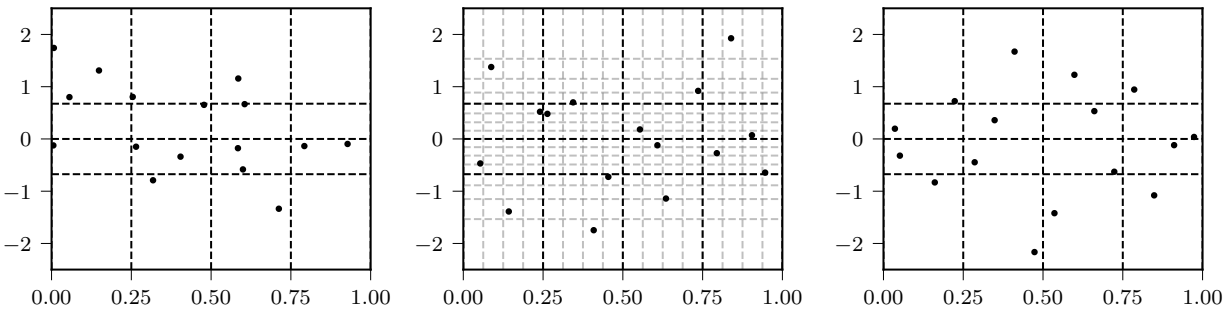

(a) Random sampling. (b) Latin hypercube sampling. (c) Sobol sequence.

Figure 3.6 Comparison between different sampling strategies according to [98].

intervals on which the LH sampling is based on. The scatter plot in Fig. 3.6(a), which corresponds to the MC method, shows clearly the above-mentioned clustering effect. For example, the sampling density in the lower left and upper right corner is low compared to other areas. This impression is confirmed by the fact that five out of 16 regions are not covered by any sample.

In comparison, the sample points obtained from the LH approach result in a better space-filling design. Here, only two regions are empty. In literature, the benefit of the improved sampling scheme on the convergence rate has been widely discussed for different application cases, see e.g. [4, 100]. Unfortunately, the gain in efficiency degrades for high-dimensional problems because the LH sampling scheme is based on the superposition of one-dimensional samples. For this reason, the sample points from the initial LH design must be modified subsequently which leads to an OLH (optimal Latin hypercube) design. For example, the initial sample points can be optimized by maximizing the minimum distance between any two samples. An extensive summary of optimization techniques can be found in [35].

However, the integration error from the standard LH approach is always less than the MC error if the computational model $g(\mathbf{x})$ as well as the integrand are monotonic in all input and response parameters, respectively [112].

Besides from the efficiency degradation in high dimensions, another disadvantage is that additional sampling points cannot be added to an existing LH design. Thus, in order to increase the number of samples a new LH design must be set up from scratch.

Apart from pseudo-random sampling strategies, the MC integration error can be alternatively reduced by quasi-random, also called low-discrepancy, sequences. Contrary to the variance reduction techniques, this approach aims at increasing the convergence rate itself rather than improving the $\sigma_{\mathrm{MC}}-$value. The main difference is that the quasi-random sequence is generated from a deterministic pattern.

There are a variety of techniques available for generating low-discrepancy sequences like the Halton, Hammersley or Sobol sequence [122]. Within this review, we limit the discussion to the latter. In principle, the generation of a Sobol sequence relies on the following two uniformity

conditions introduced by [162]:

- Property A: The sample space is subdivided into 2^{n_x} hyper-octants which result from cutting each dimension into halves. The uniformity condition is fulfilled if there is exactly one sample point in every hyperoctant.
- Property A': Each dimension is cut into four parts of equal length which gives a total number of 4^{n_x} hyperoctants. Again, the criterion is fulfilled if each region is covered by exactly one sample.

Note that the two conditions above are derived for a unit hypercube which refers to the sample space of a multivariate standard uniform distribution. These properties hold for any arbitrary distribution by applying the inverse transform method. Due to the enforced uniformity, the resulting convergence rate for the quasi MC method $O(\log(n_\mathrm{s})^{n_x}/n_\mathrm{s})$ is in many cases superior to the random sampling MC integration.
Figure 3.6(c) depicts the scatter plot generated from a Sobol sequence for the previously introduced test case. Since the number of samples is chosen as $n_\mathrm{s} = 4^{n_x}$, property A and A' are fulfilled. This leads to a design which has even a better space-filling property than the LH approach as each of the 16 regions is covered by one sample.
Nevertheless, low-discrepancy sequences are associated with limitations. For instance, the convergence rate is no longer independent from the number of dimensions. The advantageous effectiveness can be preserved as long as $n_\mathrm{s} > 2^{n_x}$ which leads to a tremendous amount of samples in high dimensions. Furthermore, artificial correlations between pairs of variables can occur when projecting a high-dimensional sequence on orthogonal two-dimensional subspaces [119]. The development of advanced algorithms for improving the uniformity of two-dimensional projections is still an active research field [87].
To summarize, the usage of pseudo- and quasi-random sequences can increase the accuracy of the MC integration significantly especially for low and intermediate dimensions. Care must be taken when it comes to high-dimensional problems. In this case, the OLH sampling is preferred over the standard LH approach to ensure a high degree of uniformity. If optimizing the sample points is too time-consuming, quasi-random sequences can be used alternatively. Since the samples are produced by deterministic algorithms, additional points can be added easily. This allows the modeler to conduct a convergence study by increasing the number of samples gradually.
The discussion in this section is limited to the comparison of different sampling techniques regarding their efficiencies in approximating a definite integral. The performance of these methods can change for other application cases like the fitting of a response surface or the optimization of an objective function. [98]

Hybrid Uncertainties

For the coexistence of aleatory and epistemic uncertainties, the distributional p-box concept has been introduced in Section 3.2.2. To repeat, the PDF of hybrid uncertainties is denoted as $f_X(x|\boldsymbol{\Theta}_x)$, where $\boldsymbol{\Theta}_x \in \boldsymbol{\Theta}_x^I$ is the n_Θ-dimensional vector of uncertain hyperparameters. A widely used approach for propagating this uncertainty type is the nested sampling scheme which separates the epistemic and aleatory part clearly from each other. This concept involves a sampling procedure that consists of an outer and inner loop.

The outer loop refers to the epistemic uncertainty space, characterized by the set of interval-valued hyperparameters $\boldsymbol{\Theta}_x^I = \{\theta_x^{I,(1)}, \ldots, \theta_x^{I,(n_\Theta)}\} \subset \mathbb{IR}^{n_{\theta_x}}$. The first step of the nested sampling procedure is to generate a set of $n_{\mathrm{s},\theta}$ samples that lie within the specified interval bounds $\theta_x^{I,(i)} = [\underline{\theta}_x^{(i)}, \overline{\theta}_x^{(i)}]$. Then, every single realization Θ_x^* is transferred to the inner loop where n_s sample points are drawn from the corresponding distribution function. Propagating the samples from the inner loop throughout the computational model gives an empirical CDF in the response space. Thus, iterating over the epistemic sample set produces an ensemble of distribution functions where every single CDF corresponds to a realization of the outer loop. As in case of purely aleatory uncertainties, stochastic descriptors can be derived from the numerical integration. A graphical illustration of the double-loop sampling is given in Fig. 3.7.

So far, it has not been discussed how to interpret the statistical quantities from the nested iteration scheme. The authors of [48] have proposed two procedures for the treatment of epistemic parameters which strongly influences the evaluation: IVP (interval-valued probability) and SOP (second-order probability).

In the first case, the epistemic uncertainty on the hyperparameters is treated as a set of intervals without further assumptions. As a consequence of the IVP method, the variation of the aleatory statistics must be interpreted in the same fashion. This means that the empir-

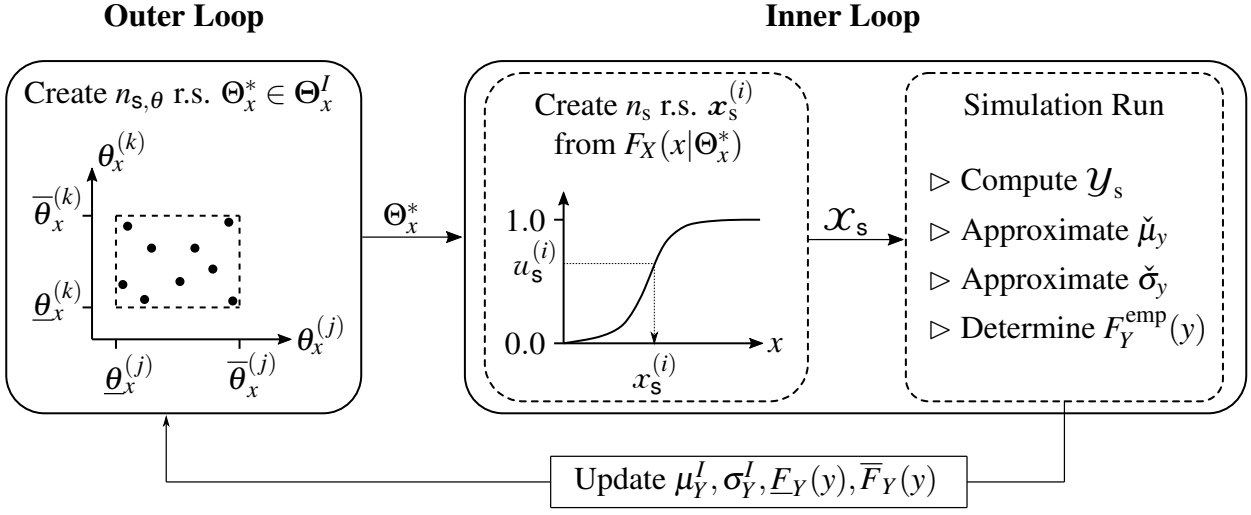

Figure 3.7 Double-loop approach for hybrid uncertainties.

ical CDFs as well as the derived stochastic moments are treated as interval-valued random quantities. Thus, the single CDFs in the response space are not equipped with a probability of occurrence. Instead, the IVP approach determines a range of possible values for the aleatory statistics which preserves the interval character of the hyperparameters.

For the SOP approach, a subjective probability distribution is assigned to every entry of the vector Θ_x^I. In many cases, the lower and upper bounds are used to define a multivariate uniform distribution. Hence, the epistemic uncertainty on the aleatory statistics has a probabilistic character. The propagated CDFs are therefore no longer just a set of possible realizations but they are associated with a probability of occurrence. The same holds for the interpretation of the stochastic descriptors. The SOP approach allows the modeler to compute statistics on the statistical values instead of deriving just the lower and upper bounds.

In both cases, the nested sampling is a computationally expensive approach which leads to the question how to make the uncertainty propagation more efficient. As the inner loop is related to the aleatory uncertainty, all advanced sampling methods discussed in the previous chapter can be used. Apart from improved sampling strategies, the inner loop can be replaced by stochastic expansion techniques which enable the calculation of stochastic moments via analytical expressions [105]. Another surrogate-based approach is to approximate the computational model itself by a response surface which allows the modeler to use sampling strategies due to the significant reduction of the computation time [106].

Choosing an appropriate procedure for replacing the outer loop depends on the treatment of the hyperparameters. Within the scope of the SOP method, the random sampling in the outer loop can be substituted by the same concepts as the inner loop. In contrast, different methods are needed in context of the IVP approach because the goal is to calculate bounds on the statistical values. For this purpose, optimization procedures are usually much more efficient than sampling-based techniques. In general, global optimization procedures are preferred over local approaches [56].

A more general approach for propagating hybrid uncertainties efficiently is the NISS (non-intrusive imprecise stochastic sampling) framework introduced by [174]. This concept is a combination of different strategies to approximate stochastic moments without a nested iteration. The basic idea is to generate only one set of sample points which is drawn from a distribution where all hyperparameters take their nominal values, i.e., $\boldsymbol{\Theta}_x = \Theta_x^*$. In order to propagate distributions where $\boldsymbol{\Theta}_x \neq \Theta_x^*$, the existing sample set has to be reweighted according to the IS scheme. To avoid numerical errors in high-dimensional problems, a decomposition method is applied to the functional response, i.e., the stochastic moments of interest. Similar to a Taylor series expansion, only the low-order interactions of the decomposition are considered. A more detailed introduction to the NISS framework can be found in Section 4.3.1.

In principle, the choice of how to break the double loop is dependent on the type and dimensionality of the problem. A discussion about various approaches can be found in [55, 90].

Epistemic Uncertainties

To remind, for purely epistemic uncertainties the distribution-free p-box representation has been discussed in Section 3.2.3. Similar to hybrid uncertainties, a nested sampling approach is required for the uncertainty propagation. Basically, the sampling procedure is a direct extension of the standard MC method [22].
At first, a set of n_s random numbers $\mathcal{U}_\mathrm{s} = \{\boldsymbol{u}_\mathrm{s}^{(1)}, \ldots, \boldsymbol{u}_\mathrm{s}^{(n_\mathrm{s})}\} \subset \mathbb{R}^{n_x}$ is generated in the unit space. This step corresponds to the outer loop of the sampling procedure. The main difference comes with applying the inverse transform method to $\mathcal{U}_\mathrm{s}$ because it leads to a set of interval vectors denoted as $\mathcal{X}_\mathrm{s}^I = \{\boldsymbol{x}_\mathrm{s}^{I,(1)}, \ldots, \boldsymbol{x}_\mathrm{s}^{I,(n_\mathrm{s})}\} \subset \mathbb{IR}^{n_x}$ instead of a set of scalar vectors. The bounds of every interval-valued entry $\boldsymbol{x}_\mathrm{s}^{I,(i)} = [\underline{\boldsymbol{x}}_\mathrm{s}^{(i)}, \overline{\boldsymbol{x}}_\mathrm{s}^{(i)}] \in \mathcal{X}_\mathrm{s}^I$ are derived by

$$\underline{\boldsymbol{x}}_\mathrm{s}^{(i)} = \overline{F}_\mathbf{X}^{-1}(\boldsymbol{u}_\mathrm{s}^{(i)}), \quad \text{and} \quad \overline{\boldsymbol{x}}_\mathrm{s}^{(i)} = \underline{F}_\mathbf{X}^{-1}(\boldsymbol{u}_\mathrm{s}^{(i)}). \tag{3.49}$$

For the mapping of each interval $\boldsymbol{x}_\mathrm{s}^{I,(i)}$ to the response space, an additional inner loop is required. The determination of the interval bounds $\boldsymbol{y}_\mathrm{s}^{I,(i)} = [\underline{\boldsymbol{y}}_\mathrm{s}^{(i)}, \overline{\boldsymbol{y}}_\mathrm{s}^{(i)}]$ within this loop is achieved by solving the following optimization problems

$$\begin{aligned} &\underline{\boldsymbol{y}}_\mathrm{s}^{(i)} = \min_\mathbf{x} \left(g(\mathbf{x})\right), \quad \text{and} \quad \overline{\boldsymbol{y}}_\mathrm{s}^{(i)} = \max_\mathbf{x} \left(g(\mathbf{x})\right) \\ &\text{s.t. } \mathbf{x} \in \boldsymbol{x}_\mathrm{s}^{I,(i)}. \end{aligned} \tag{3.50}$$

In the standard procedure, the interval propagation is conducted by generating a set of uniformly distributed samples within the bounds of $\boldsymbol{x}_\mathrm{s}^{I,(i)}$. If the computational model is monotonic in all of its input quantities it is sufficient to propagate only the corner points of $\boldsymbol{x}_\mathrm{s}^{I,(i)}$. For the general case of a non-monotonic system behavior, solving the problem in Eq. (3.50) by an optimization algorithm is more efficient than a sampling-based approach.
As a result of the propagation, one obtains a set of intervals $\mathcal{Y}_\mathrm{s}^I = \{\boldsymbol{y}_\mathrm{s}^{I,(1)}, \ldots, \boldsymbol{y}_\mathrm{s}^{I,(n_\mathrm{s})}\} \subset \mathbb{IR}^{n_y}$. Finally, the lower and upper bounds of $\mathcal{Y}_\mathrm{s}^I$ in every dimension are taken as a basis for determining the expressions of the p-box representation. Analyzing the propagated intervals in view of the Dempster Shafer theory, $\mathcal{Y}_\mathrm{s}^I$ can be seen as set of focal elements where each interval is assigned with the same BPA of $1/n_\mathrm{s}$. Therefore, the metrics in Eqs. (3.31) and (3.32) for deriving the CBF and CPF can be used for computing $\underline{F}_Y(y)$ and $\overline{F}_Y(y)$. Figure 3.8 shows a graphical representation of the double-loop approach where both loops are based on a sampling strategy.
In summary, the nested iteration scheme for epistemic uncertainties is based on discretizing the p-box into a set of equally-weighted intervals. Due to the duality between Dempster Shafer theory and p-box concept, the set of propagated intervals is represented as the bounding curves of a p-box. One noteworthy aspect of this propagation technique is the fact that each CDF inside the p-box is considered as valid realization. This can lead to conservative bounds in the response space if the p-box characterizing the input quantities contains undesired distri-

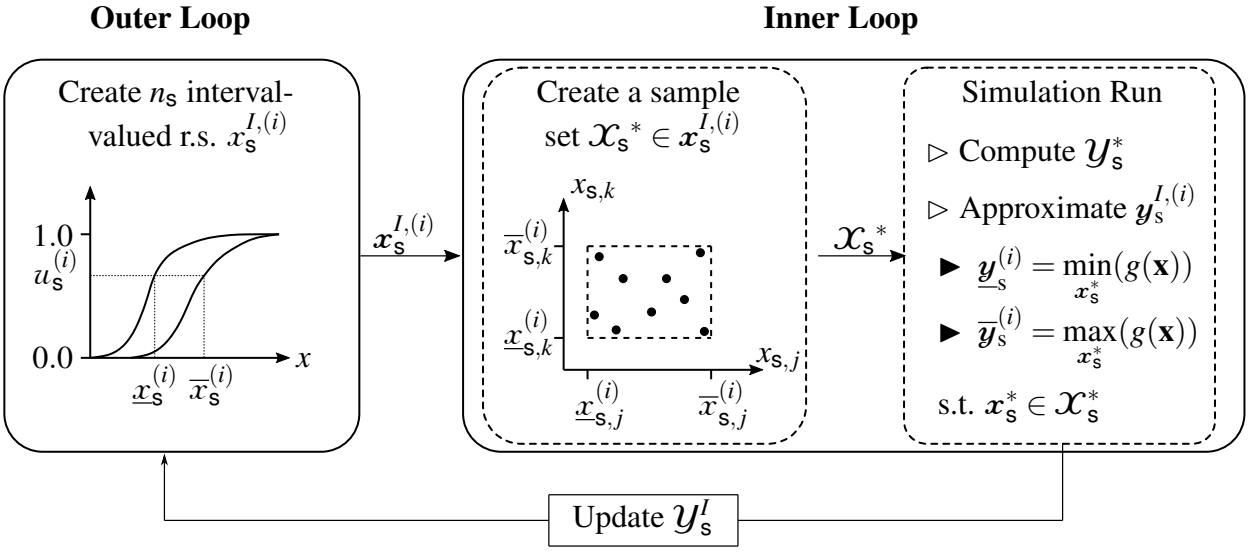

Figure 3.8 Double-loop approach for epistemic uncertainties.

bution functions. For this reason, alternative approaches are examined in Section 5.2.1 which aim at transferring the distribution-free p-box concept into the parametric type via flexible distribution functions.

3.4 Inverse Uncertainty Quantification

In the previous chapters, a comprehensive review on forward uncertainty quantification and propagation techniques has been given. All of the methods suppose that the existing set of data is directly related to the QoI (quantity of interest). In case of an inverse UQ problem, the observations of phenomena refer to the model response whereas the QoI can be a model or input parameter.

Within a probabilistic framework, Bayesian methods have become the standard approach for this type of problem. However, this concept can lead to extremely biased results when dealing with a scarce data set. For this reason, non-probabilistic approaches have been developed recently which do not presume a-priori information on the hidden variables. In the following paragraphs, the Bayesian concept as well as a non-probabilistic framework are introduced.

3.4.1 Bayesian Inference

The Bayesian modeling framework goes back to the publication of Thomas Bayes [18] in the 18th century. A decisive contribution in context of inverse UQ problems are the publications of Katafygiotis and Beck [20, 92].

The general idea of Bayesian inference is to update available knowledge about a random variable with the help of additional observations. The first step of the approach is to assign an

initial PDF to the parameters of interest. After gathering information about the model response, e.g. by conducting measurements, Bayes' theorem is used to update the initial hypothesis. For continuous random variables, Bayes' rule is formulated according to

$$p(\mathbf{x}|\mathcal{Y}_{\mathsf{m}}) = \frac{p(\mathcal{Y}_{\mathsf{m}}|\mathbf{x})\ p(\mathbf{x})}{\int p(\mathcal{Y}_{\mathsf{m}}|\mathbf{x})\ p(\mathbf{x})\ d\mathbf{x}} \propto p(\mathcal{Y}_{\mathsf{m}}|\mathbf{x})\ p(\mathbf{x}), \tag{3.51}$$

where $\mathbf{x}$ covers the unknown random parameters. The terms of the above equation have the following meaning:

- The prior distribution $p(\mathbf{x})$ represents the modeler's initial guess about the unknown parameter variation.
- The term on the left hand side, i.e., $p(\mathbf{x}|\mathcal{Y}_{\mathsf{m}})$, denotes the posterior distribution. It quantifies the updated uncertainty on $\mathbf{x}$ given the measurement set $\mathcal{Y}_{\mathsf{m}} = \{\boldsymbol{y}_{\mathsf{m}}^{(1)}, \ldots, \boldsymbol{y}_{\mathsf{m}}^{(n_{\mathsf{m}})}\} \subset \mathbb{R}^{n_y}$.
- The likelihood $p(\mathcal{Y}_{\mathsf{m}}|\mathbf{x})$ specifies the probability of observing the data $\mathcal{Y}_{\mathsf{m}}$ given a certain realization of the input parameters. Since the likelihood can be seen as a function of $\mathbf{x}$, it is often expressed as $\mathcal{L}(\mathbf{x}|\mathcal{Y}_{\mathsf{m}})$.
- The denominator on the right hand side is referred to as evidence or marginal likelihood as it is obtained by marginalizing out $\mathbf{x}$ from $\mathcal{L}(\mathbf{x}|\mathcal{Y}_{\mathsf{m}})$.

To summarize, the key aspect of the Bayesian framework lies in choosing a prior distribution and defining the likelihood function. The latter comprises a statistical representation of the computational model by taking measurement uncertainties and model inaccuracies into account. In many application cases, independence is assumed between noise and the unknown parameters which leads to a likelihood function with additive noise. The more challenging task in the Bayesian framework is to define a prior distribution that captures the modeler's a-priori knowledge adequately. In principle, $p(\mathbf{x})$ should assign a high density to those realizations $\mathbf{x} \in \mathbb{R}^{n_x}$ which are likely according to the modeler's a-priori expectation. [89]
Based on the definition of these two terms, Eq. (3.51) is used to obtain the posterior distribution. In the specific case of using so-called conjugate distributions for the prior and likelihood, the posterior can be derived analytically [64]. For the general case, solving Problem (3.51) is a non-trivial task because no closed-form solution is available.
The most common numerical solution procedure is the MCMC (Markov Chain Monte Carlo) sampling. Without explaining the method in detail, the aim is to generate a sequence of sample points $(\mathbf{x}^{(1)}, \mathbf{x}^{(2)}, \ldots)$ which follow the unknown posterior distribution. Each element $\mathbf{x}^{(i)}$ of the chain is generated from a proposal distribution which is defined on the basis of the previous sample $\mathbf{x}^{(i-1)}$. Dependent on the likelihood, the candidate sample is either rejected or accepted. In case of rejection, the new point equals the previous one. When generating a sufficient number of sample points, the underlying distribution of the Markov chain converges to the desired posterior. Here, a critical point is to determine when the Markov chain has reached

the stationary point, i.e., the state of following the posterior distribution. [171]
All in all, Bayesian inference is extremely useful for applications where the modeler can propose a reasonable hypothesis which is further specified due to additional observations. For cases without or little a-priori information so-called *non-informative* prior functions, for example Jeffrey's prior, can be used [64]. Nevertheless, a certain degree of subjectivity is always introduced by the choice of the prior distribution. This prior effect fades out as the number of observations is increasing.
However, the absence of prior information can be problematic if $\mathcal{Y}_{\mathrm{m}}$ contains insufficient observations. In such cases, the posterior is strongly influenced by the prior distribution which can lead to biased results. Here, non-probabilistic UQ frameworks can be superior to the Bayesian approach as they require no subjective hypothesis on the random variables. [33, 51]
The subsequent paragraph gives a brief summary about alternative approaches to the Bayesian framework. A special focus is set on the concept introduced by [53] who have proposed an interval-based strategy to solve inverse UQ problems.

3.4.2 Non-Probabilistic Inverse Uncertainty Quantification Concepts

For the following discussion, we consider a scenario where the modeler is equipped with a set of measurement points $\mathcal{Y}_{\mathrm{m}}$ that comprises a very limited number of observations. Furthermore, no prior information about the unknown parameter variation is given. Parts of the subsequent paragraphs have already been published by the author in [108].
As discussed in Section 3.2.3, a common way to model lack-of-knowledge uncertainties is the class of interval methods. Here, the uncertainty on the model parameters is quantified by lower and upper bounds [115]. The propagation of the intervals throughout the model is represented by the minimum and maximum values of the response quantities. Hence, interval methods do not model the dependencies between them.
When using interval methods for the inverse UQ, the variation of the measurement data $\mathcal{Y}_{\mathrm{m}}$ is quantified by a hyperrectangle. The goal of the inverse interval method is to minimize the difference between the interval radii of the measurement set and the radii obtained by the mapping of the input uncertainty throughout the computational model. In order to quantify the discrepancy, a metric is introduced that represents the radii difference by the Euclidean norm [58].
Another approach from the field of non-probabilistic uncertainty quantification is the fuzzy set concept. The uncertainty of the model parameters is quantified by membership functions which indicate the degree of membership to the fuzzy set. In order to propagate fuzzy sets throughout the system model, the membership function is discretized by a finite number of intervals. Thus, the fuzzy set concept can be seen as an extension of the interval method. Without going further into details, the basic principle of the inverse interval method can also be extended to the fuzzy set method as described in [71] for example.

As discussed in [57], also the inverse fuzzy set approach is not able to model dependencies in the output space. In order to overcome this problem, a different approach is proposed in [52, 53]. The following paragraphs provide a review of the method.

The basic idea is to describe uncertainties with the help of a convex hull which is defined as the smallest convex set that contains a finite number of points. For the given set of measurement points $\mathcal{Y}_{\mathsf{m}}$, the convex hull is denoted by $\mathcal{C}_{\mathcal{Y}_{\mathsf{m}}}$ and it holds

$$\mathcal{C}_{\mathcal{Y}_{\mathsf{m}}} = \left\{ \mathbf{y} \in \mathbb{R}^{n_y} \;\middle|\; \mathbf{y} = \sum_{i=1}^{n_{\mathsf{m}}} \beta^{(i)} \, \boldsymbol{y}_{\mathsf{m}}^{(i)}, \; \sum_{i=1}^{n_{\mathsf{m}}} \beta^{(i)} = 1, \; \beta^{(i)} \geq 0 \right\}. \tag{3.52}$$

Then, the goal becomes to identify an uncertainty set in the input variables which leads to a convex hull in the output space that matches $\mathcal{C}_{\mathcal{Y}_{\mathsf{m}}}$ as close as possible. In the current approach, the uncertainty set in the input space is quantified by intervals. Moreover, independence is assumed between the input parameters. Thus, the uncertainty set is described by a hyperrectangle which can be interpreted as a convex hull of its corner points. It is denoted by $\mathcal{C}_x$ and can be expressed as a multi-dimensional interval, i.e.,

$$\mathcal{C}_x = \bigcup_{i=1}^{n_x} [\, \underline{x}_i, \overline{x}_i \,] = [\, \underline{x}_1, \overline{x}_1 \,] \times \ldots \times [\, \underline{x}_{n_x}, \overline{x}_{n_x} \,] = [\, \underline{\mathbf{x}}, \overline{\mathbf{x}} \,] \subset \mathbb{IR}^{n_x}, \tag{3.53}$$

where $\underline{\mathbf{x}}, \overline{\mathbf{x}} \in \mathbb{R}^{n_x}$ contain the lower and upper bounds of the one-dimensional intervals, respectively. Hence, the goal of the inverse uncertainty quantification becomes to determine the entries of $\underline{\mathbf{x}}$ and $\overline{\mathbf{x}}$. The detailed procedure how to identify the optimal hyperrectangle comprises the following steps:

At first, a population of uncertainty sets $\mathcal{C}_x$ with different interval bounds $\underline{\mathbf{x}}, \overline{\mathbf{x}}$ is created. Within each set $\mathcal{C}_x$, a number of n_{s} sample points is generated:

$$\mathcal{X}_{\mathsf{s}} = \left\{ \boldsymbol{x}_{\mathsf{s}}^{(1)}, \ldots, \boldsymbol{x}_{\mathsf{s}}^{(n_{\mathsf{s}})} \right\} \subset \mathcal{C}_x. \tag{3.54}$$

The distribution of the samples is not relevant as long as they represent $\mathcal{C}_x$ well enough. If the computational model is monotonous, it is sufficient to sample only the corner points of the hyperrectangle. The sampling procedure is followed by the propagation of the points to the output space. The uncertainty set in the output space is obtained according to Eq. (3.1) by $\mathcal{Y}_{\mathsf{s}} = g(\mathcal{X}_{\mathsf{s}})$ with

$$\mathcal{Y}_{\mathsf{s}} = \left\{ \boldsymbol{y}_{\mathsf{s}}^{(1)}, \ldots, \boldsymbol{y}_{\mathsf{s}}^{(n_{\mathsf{s}})} \right\} \subset \mathbb{R}^{n_y}, \tag{3.55}$$

and $\boldsymbol{y}_{\mathsf{s}}^{(i)} = g(\boldsymbol{x}_{\mathsf{s}}^{(i)})$ for $i = 1, \ldots, n_{\mathsf{s}}$. Based on the propagated samples, a convex hull $\mathcal{C}_{\mathcal{Y}_{\mathsf{s}}}$ is created which represents the image of $\mathcal{C}_x$ in the output space. By analogy with the measurement set, the convex hull $\mathcal{C}_{\mathcal{Y}_{\mathsf{s}}}$ is determined by Eq. (3.52) but with the difference that $\mathcal{Y}_{\mathsf{s}}$ is used

instead of $\mathcal{Y}_\mathsf{m}$:

$$\mathcal{C}_{\mathcal{Y}_\mathsf{s}} = \left\{ \mathbf{y} \in \mathbb{R}^{n_y} \;\middle|\; \mathbf{y} = \sum_{i=1}^{n_\mathsf{s}} \beta^{(i)}\, \boldsymbol{y}_\mathsf{s}^{(i)},\ \sum_{i=1}^{n_\mathsf{s}} \beta^{(i)} = 1,\ \beta^{(i)} \geq 0 \right\}. \tag{3.56}$$

Ideally, $\mathcal{C}_{\mathcal{Y}_\mathsf{s}}$ is only dependent on the interval boundaries $\underline{\mathbf{x}}$ and $\overline{\mathbf{x}}$ of the hyperrectangle. However, as the computational model is not given by an analytical expression the convex hull is affected by the number of sampling points. Hence, the modeler has to ensure that the amount of samples is large enough to represent the "true" convex hull precisely enough.
The geometric discrepancy between the two convex hulls is specified by the following terms:

$$\Delta V_\mathsf{m} = 1 - \frac{V_\mathsf{s}}{V_\mathsf{m}}, \tag{3.57}$$

$$\Delta V_\mathsf{o} = 1 - \frac{V_\mathsf{o}}{V_\mathsf{m}}, \tag{3.58}$$

$$\Delta c = \|\mathbf{c}_\mathsf{m} - \mathbf{c}_\mathsf{s}\|_2. \tag{3.59}$$

Eq. (3.57) describes the volume difference between $\mathcal{C}_{\mathcal{Y}_\mathsf{m}}$ and $\mathcal{C}_{\mathcal{Y}_\mathsf{s}}$ and in Eq. (3.58) their overlapping volume V_o is set in relation to the volume of $\mathcal{C}_{\mathcal{Y}_\mathsf{m}}$. The Euclidean distance between their centers of gravity $\mathbf{c}_\mathsf{m}$ and $\mathbf{c}_\mathsf{s}$ is expressed in Eq. (3.59). Note that the variables should be normalized to get an objective measure for Δc. In case the two convex hulls are identical, each of the above-mentioned terms takes the value zero.
The actual inverse uncertainty quantification is performed by solving an optimization problem. Therefore, an objective function is minimized which comprises the sum of the terms of Eqs. (3.57)-(3.59):

$$\mathrm{obj}_\mathcal{C}(\underline{\mathbf{x}}, \overline{\mathbf{x}}) = \Delta V_\mathsf{m}^2 + \Delta V_\mathsf{o}^2 + \Delta \mathbf{c}^2. \tag{3.60}$$

The parameters to be optimized are the lower and upper bounds $\underline{\mathbf{x}}$ and $\overline{\mathbf{x}}$ of the multi-dimensional intervals in the input space. They influence the quantities V_s, V_o, and $\mathbf{c}_\mathsf{s}$, and hence ΔV_m, ΔV_o, and Δc. Formally, the optimization problem is expressed by:

$$\begin{aligned} &\underset{\underline{\mathbf{x}}, \overline{\mathbf{x}}}{\text{minimize}} \quad \mathrm{obj}_\mathcal{C}(\underline{\mathbf{x}}, \overline{\mathbf{x}}) \\ &\text{subject to} \quad \underline{\mathbf{x}} \leq \overline{\mathbf{x}}. \end{aligned} \tag{3.61}$$

As the fundamental principle of the inverse UQ is based on an optimization, one has to think about a reasonable type for the optimization algorithm. Usually, the modeler has no a-priori information on the input uncertainty which is why a good performance in exploring the input space is required. Problem (3.61) can be solved by, e.g., a population-based method like the Differential Evolution. In each iteration step, a new population of uncertainty sets $\mathcal{C}_x$ is created.

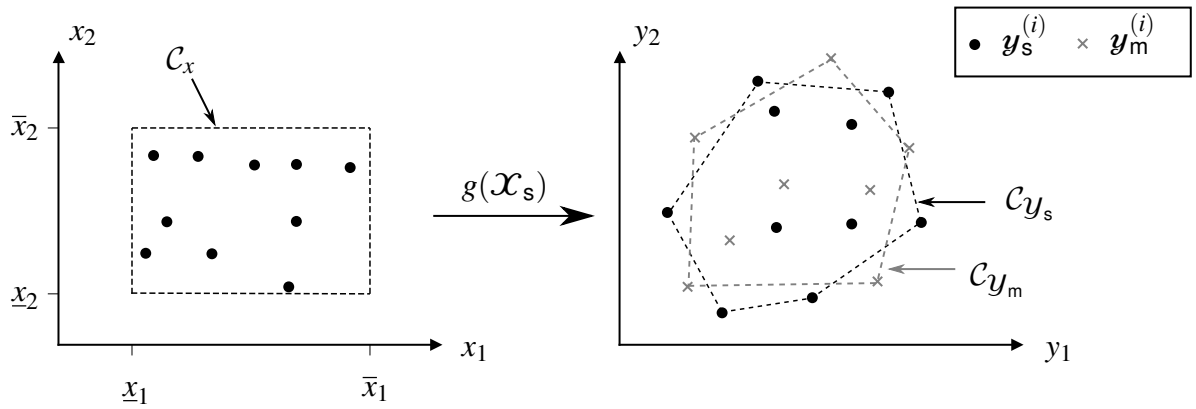

Figure 3.9 Graphical representation of the convex hull approach introduced by [52].

The interval bounds of the individual sets are determined based on the objective function values of the previous population.

To summarize, the algorithm introduced by [53] solves the inverse problem by optimizing the bounds of the multivariate intervals in the input space. Propagating the identified interval uncertainty throughout the model leads to a convex hull that coincides as accurately as possible with the measurement hull. Figure 3.9 shows a graphical representation of the approach.

In contrast to the Bayesian framework, the convex hull approach is able to solve an inverse problem without any prior assumptions regarding the unknown parameter variation. The application of the method might be problematic for high-dimensional problems as the time-complexity for determining a convex hull grows exponentially with respect to its dimensions. For this reason, an alternative non-probabilistic method will be developed in Section 4.1 to derive the parameter's uncertainty from a limited set of measurements [108]. Here, the main idea is to describe the measurement as well as the simulation set by enclosing hyperellipsoids which are less time-consuming to compute. In addition to that, the new method is extended for cases where the provided set of data comprises stochastic descriptors, such as mean and variance, instead of the measurements themselves.

Apart from the quantification and modeling of uncertainty sources, sensitivity analysis also plays a crucial part within a stochastic design procedure. The subsequent chapter gives an overview over state-of-the-art methods for conducting sensitivity studies in presence of hybrid uncertainties. Hence, the focus of the review is put on methods which aim at determining the influence of the parameter's epistemic uncertainty on a certain target value.

3.5 Sensitivity Analysis in Presence of Hybrid Uncertainties

Generally speaking, the purpose of performing a sensitivity study is to analyze the influence of the model input parameters $X_i \in \mathbf{X}$ on target values which are related to response quantities $Y_i \in \mathbf{Y}$ of the computational model. The knowledge gained from the SA can be used further to rank the input quantities with respect to their importance. On the one hand, the modeler can

use the ranking to reduce the model complexity by fixing the set of unessential input parameters to their deterministic values. On the other hand, knowing the most influential parameters is a valuable information for deciding where to allocate additional engineering effort to reduce uncertainties efficiently. [154]
The subsequent section refers to common approaches from literature which are used for problems with random input parameters. After that, Section 3.5.2 opens the discussion about methods to study the sensitivity of input quantities that are categorized as hybrid uncertainties. Here, the focus is put on studying the epistemic part of the uncertainty source.

3.5.1 Sensitivity Analysis Concepts for Aleatory Uncertainties

In literature, two general subtypes of sensitivity analysis are distinguished: local and global approaches. In case of a local SA, the impact of small perturbations around the nominal values of $\mathbf{X}$ on the model outcome is investigated. Typically, interactions between the random quantities are not considered within this framework. Most of the local SA approaches are therefore based on approximating the gradient at the nominal value. For example, the SSC (scaled sensitivity coefficient) of a parameter X_i is obtained by multiplying its nominal value with the partial derivative of the output quantity of interest. Another local sensitivity metric is the SI (sensitivity index). Contrary to the SSC, the partial derivative is scaled by the parameter's standard deviation. The mathematical formulations of the two metrics are given by [111]

$$\mathrm{SSC}_{x_i} = \mu_{x_i} \left.\frac{\partial g(\mathbf{x})}{\partial x_i}\right|_{x_i=\mu_{x_i}} \text{, and} \quad \mathrm{SI}_{x_i} = \sigma_{x_i} \left.\frac{\partial g(\mathbf{x})}{\partial x_i}\right|_{x_i=\mu_{x_i}} . \tag{3.62}$$

Another popular family of local SA methods are OAT (one-at-a-time) concepts which are similar to derivative-based approaches. As indicated by the term OAT, the goal is to examine the model response when changing the value of one parameter while keeping the remaining parameters at their nominal values.
In brief, choosing a local SA approach is appropriate for analyzing the impact of small parameter perturbations in case of quasi-linear input-output relations. Since the number of forward model evaluations is comparatively small, local SA methods are preferred to screen out parameters for high-dimensional problems. Furthermore, no information about the probability distribution type of the parameters is required.
However, the results of a local SA can be misleading for nonlinear models as the expansion point may have a decisive influence on the gradient. Further, the missing information about possible parameter interactions is a strong limitation of the approach. [150]
In order to determine sensitivity measures that consider the entire uncertain parameter space, methods from the field of global SA approaches are needed. In [153], this group is decomposed in regression-based and variance-based methods.

- In the first case, sensitivity metrics are derived from the coefficients of a linear regression between the input and output quantities of interest. For analyzing quasi-linear models, the SRC (standard regression coefficient) and PCC (partial correlation coefficient) are appropriate sensitivity measures. If the model shows a nonlinear but monotonic behavior, a rank transformation of the data can be performed. The corresponding sensitivity metrics, i.e., SRRC (standard rank regression coefficient) and PRCC (partial rank correlation coefficient), are computed in the same fashion as the SRC and PCC but the calculation rules are applied to the transformed data. [74]
- The basic idea of variance-based methods is to decompose the variance σ_y^2 to the single input quantities and their interactions. In contrast to regression-based approaches, even nonlinear models can be analyzed. Among the most popular techniques is the FAST (Fourier amplitude sensitivity testing) method [40] as well as the determination of the Sobol indices [163].

Within the scope of this thesis, only the Sobol method is discussed in greater detail. For further information about alternative global SA concepts, the reader is referred to [152, 154].
For deriving the Sobol index concept, we assume that all random input quantities $\mathbf{X} \in \mathbb{R}^{n_x}$ are defined by independent uniform distributions in the unit space $[0,1]^{n_x}$. Note that this assumption does not represent any limitation on the method as it can be applied to any other distribution type. Moreover, we consider a scalar response quantity of interest, i.e., $n_y = 1$. In the general case of $n_y \neq 1$, the Sobol indices must be evaluated separately for every dimension.
The computation of the Sobol sensitivity indices is based on a HDMR (high-dimensional model representation) of $g(\mathbf{x})$

$$g(\mathbf{x}) = g_0 + \sum_{i=1}^{n_x} g_i(x_i) + \sum_{i=1}^{n_x}\sum_{i<j}^{n_x} g_{i,j}(x_i,x_j) + \ldots + g_{1,\ldots,n_x}(x_1,\ldots,x_{n_x}), \tag{3.63}$$

which decomposes the functional relationship into 2^{n_x} terms of increasing order. Eq. (3.63) is a unique HDMR of $g(\mathbf{x})$, also referred to as ANOVA (analysis of variance) decomposition, if the constant component is computed according to

$$g_0 = \int g(\mathbf{x}) d\mathbf{x} = E[g(\mathbf{x})], \tag{3.64}$$

and the higher-order components are derived from

$$\begin{aligned} g_i &= \int g(\mathbf{x}) d\mathbf{x}_{\sim i} - g_0 = E_{\mathbf{X}_{\sim i}}[g(\mathbf{x})|X_i] - g_0, \text{ and} \\ g_{i,j} &= \int g(\mathbf{x}) d\mathbf{x}_{\sim i,j} - g_i - g_j - g_0 = E_{\mathbf{X}_{\sim i,j}}[g(\mathbf{x})|X_i,X_j] - g_i - g_j - g_0, \end{aligned} \tag{3.65}$$

where $\mathbf{x}_{-i}$ covers all entries of $\mathbf{x}$ except the $i-$th dimension and g_i denotes an abbreviation of $g_i(x_i)$. Using the expressions from Eq. (3.65) ensures that all summands of the ANOVA decomposition are mutually orthogonal. Due to this mathematical property, it holds that

$$\int g_{i_1,\ldots,i_s}\, g_{i_1,\ldots,i_t} d\mathbf{x} = 0, \text{ if } \{i_1,\ldots,i_s\} \neq \{i_1,\ldots,i_t\}. \tag{3.66}$$

Under the assumption that $g(\mathbf{x})$ is square-integrable, Eq. (3.63) can be rewritten according to

$$\underbrace{\int g^2(\mathbf{x}) d\mathbf{x} - g_0^2}_{D} = \sum_{i=1}^{n_x} \underbrace{\int g_i^2 dx_i}_{D_i} + \sum_{i=1}^{n_x}\sum_{i<j}^{n_x} \underbrace{\int\int g_{i,j}^2 dx_i dx_j}_{D_{i,j}} + \ldots + \underbrace{\int \ldots \int g_{1,\ldots,n_x}^2 dx_1 \ldots dx_{n_x}}_{D_{i,\ldots,n_x}}. \tag{3.67}$$

The term on the left-hand side, denoted as D, equals the variance of $g(\mathbf{x})$, whereas the terms on the right-hand side express the variance of the individual component functions. Hence, Eq. (3.67) yields a decomposition of the total variance. [163, 164]

The Sobol indices are obtained by dividing the right-hand side terms of Eq. (3.67) through the total variance. For example, the first-order Sobol indices are given by

$$S_i = \frac{D_i}{D} = \frac{Var_{X_i}\left[E_{\mathbf{X}_{-i}}[g(\mathbf{x})|X_i]\right]}{Var\left[g(\mathbf{x})\right]}. \tag{3.68}$$

This factor expresses the importance of the random variable X_i without considering any interaction. To gain information about possible dependencies between the input parameters, the total Sobol index must be computed which extends the first-order effect with all higher-order effects

$$S_{T,i} = 1 - \frac{Var_{\mathbf{X}_{-i}}\left[E_{X_i}[g(\mathbf{x})|\mathbf{X}_{-i}]\right]}{Var\left[g(\mathbf{x})\right]}. \tag{3.69}$$

If $g(\mathbf{x})$ is an additive model $S_i = S_{T,i}$ holds. In all other cases, the difference between first and total Sobol index can be significant. Thus, the evaluation of the total effects is indispensable to make a reliable statement about the reduction of input parameters. [81]

Unless the computational model is given by analytical expressions, sampling-based methods are required to determine the Sobol indices. As this procedure can be cumbersome in high-dimensions, alternatives to the MC sampling procedure have been developed [19, 151].

3.5.2 Sensitivity Analysis Concepts for Hybrid Uncertainties

In contrast to pure aleatory uncertainty sources, no standard procedures have become established for performing a sensitivity study in presence of hybrid uncertainties. The SA approaches discussed in literature are greatly dependent on the chosen modeling concept. Within this thesis, we follow the p-box method to represent hybrid uncertainty sources which

relies on a strict partition between aleatory and epistemic contribution. Therefore, appropriate sensitivity measures analyze the two parts separately.
Since the modeling of epistemic uncertainties is a young research field, the number of publications in this area is not as extensive as for aleatory uncertainties. Two common techniques are the extension of the Sobol indices and the so-called pinching strategy. For both of them, a short introduction is provided within the following paragraphs.

Extended Sobol Indices

As discussed in Section 3.2.2, a distributional p-box is formally defined by $F_X(x|\boldsymbol{\Theta}_x)$, where the set of hyperparameters can take arbitrary values within certain bounds, i.e., $\boldsymbol{\Theta}_x \in \boldsymbol{\Theta}_x^I$. In accordance to the distinction between IVP and SOP method for the uncertainty propagation, two different approaches are presented to extend the classical Sobol method.

The first approach, sometimes referred to as imprecise Sobol method, treats the uncertainty on the hyperparameters as multivariate interval without any additional assumptions. As a consequence, the Sobol indices from Eqs. (3.68) and (3.69) become an interval-valued quantity which is dependent on the realization of $\boldsymbol{\Theta}_x$. A logical extension of the classical Sobol method is to determine the lower and upper index bound in the following fashion

$$\underline{S}_{i_1,\ldots,i_s} = \min_{\boldsymbol{\Theta}_x \in \boldsymbol{\Theta}_x^I} S_{i_1,\ldots,i_s}(\boldsymbol{\Theta}_x), \quad \text{and} \quad \overline{S}_{i_1,\ldots,i_s} = \max_{\boldsymbol{\Theta}_x \in \boldsymbol{\Theta}_x^I} S_{i_1,\ldots,i_s}(\boldsymbol{\Theta}_x). \tag{3.70}$$

As in case of a pure aleatory SA, the total Sobol index is still playing a decisive role. Its maximum value, i.e., $\overline{S}_{T,i}$, is a suitable measure to decide about the reduction of the aleatory parameter space. If $\overline{S}_{T,i}$ is small, one can fix X_i to its nominal value without reducing the prediction accuracy significantly.
Besides from the maximum total index, a second sensitivity metric is the interval width of the total imprecise Sobol indices given by

$$\Delta S_{T,i} = \overline{S}_{T,i} - \underline{S}_{T,i}, \quad \text{with } i \in \{1,\ldots,n_x\}. \tag{3.71}$$

This quantity is used to examine the overall influence of the epistemic uncertainties. A small interval width $\Delta S_{T,i}$ indicates a negligible lack-of-knowledge effect on the total Sobol index $S_{T,i}$. If this holds for all total Sobol indices, fixing the uncertain hyperparameters is reasonable. [73, 156]
All in all, considering Sobol indices as intervals is an illustrative technique which makes the influence of epistemic uncertainties visible. Furthermore, it preserves the basic idea of the Sobol method to measure uncertainty with the help of variance. The optimization problems in Eq. (3.70) introduce additional computational effort compared to the classical Sobol concept. Hence, efficient propagation methods are needed, e.g., by replacing the crude MC uncertainty

propagation with a polynomial chaos expansion [156].
The second approach is related to the SOP method. Other than from the IVP point of view, subjective probability distributions are assigned to the uncertainty on $\boldsymbol{\Theta}_x$. This concept allows a probabilistic interpretation of the single CDF realizations.
In this context, extending the Sobol method is based on the idea to perform a variance decomposition of the uncertain response mean $E[g(\mathbf{x}|\boldsymbol{\Theta}_x)]$ and variance $V[g(\mathbf{x}|\boldsymbol{\Theta}_x)]$ instead of the functional value $g(\mathbf{x})$ itself. Thus, in order to the assess the main effect of $\theta_x^{(i)} \in \boldsymbol{\Theta}_x$ on the response mean Eq. (3.68) is reformulated according to

$$S_{\mu,\theta_x^{(i)}} = \frac{Var_{\theta_x^{(i)}}\left[E_{\theta_x^{(-i)}}\left[E_{\mathbf{X}}\left[g(\mathbf{x})\middle|\boldsymbol{\Theta}_x\right] \mid \theta_x^{(i)}\right]\right]}{Var_{\boldsymbol{\Theta}_x}\left[E_{\mathbf{X}}\left[g(\mathbf{x})\right]\middle|\boldsymbol{\Theta}_x\right]}, \tag{3.72}$$

where $\boldsymbol{\theta}_x^{(-i)}$ contains all entries of $\boldsymbol{\Theta}_x$ except $\theta_x^{(i)}$. In a similar manner, the epistemic main effect for considering the response variance as QoI is obtained by

$$S_{V,\theta_x^{(i)}} = \frac{Var_{\theta_x^{(i)}}\left[E_{\theta_x^{(-i)}}\left[Var_{\mathbf{X}}\left[g(\mathbf{x})\middle|\boldsymbol{\Theta}_x\right] \mid \theta_x^{(i)}\right]\right]}{Var_{\boldsymbol{\Theta}_x}\left[Var_{\mathbf{X}}\left[g(\mathbf{x})\middle|\boldsymbol{\Theta}_x\right]\right]}. \tag{3.73}$$

Note that the reformulation for higher-order Sobol indices is done in the same way. [91]
In contrast to the imprecise Sobol method, the effect of individual epistemic parameters can be determined. As for the assessment of aleatory uncertainties determining the two total Sobol indices of a parameter, i.e., $S_{T,\mu,\theta_x^{(i)}}$ and $S_{T,V,\theta_x^{(i)}}$, is an appropriate metric to evaluate the importance of $\theta_x^{(i)}$. If both of them have a low value, the corresponding hyperparameter can be fixed to its nominal value.
Due to the probabilistic treatment of $\boldsymbol{\Theta}_x$, the partition of unity is fulfilled for the mean and variance Sobol indices which makes the interpretation of the results easier. Nevertheless, the modeler should keep in mind that the resulting Sobol factors are dependent on the chosen probability distribution. Of course, the epistemic SA is associated with additional computational effort. Compared to the classical Sobol method, an extra loop is required to generate samples from the epistemic parameter space. Applying a crude MC sampling scheme is therefore only possible for low-dimensional models.
Let us consider the case that $g(\mathbf{x})$ is a linear, additive model. Further, the input vector $\mathbf{X}$ is given by a multivariate normal distribution with known variance but uncertain mean values. In this special setup the lack-of-knowledge uncertainty causes a variation of the response mean whereas the variance remains constant.
Applying the imprecise Sobol method to this test case would lead to $\Delta S_{T,i} = 0$ for every $X_i \in \mathbf{X}$ because the total Sobol indices are not affected by the epistemic uncertainty. Thus, the modeler could conclude that all uncertain mean values can be reduced.

In the second approach, one could characterize the mean variation by a multivariate uniform distribution. As the model is additive, the main effects from Eqs. (3.72) and (3.73) are sufficient for the epistemic SA. The set of Sobol indices $S_{V,\theta_x^{(i)}}$ is of no importance as the variation of the response variance is zero due to the linear model property. In contrast, the computation of the main effects $S_{\mu,\theta_x^{(i)}}$ supply more information. Based on that, a meaningful reduction of the epistemic parameter space can be conducted.
From the author's point of view, the latter approach is therefore more suitable for an epistemic SA because it provides more information about the impact of the epistemic uncertainty. Especially if the variation of μ_y is of interest, e.g., for a subsequent design optimization, the imprecise Sobol method could lead to an erroneous parameter reduction.

Pinching Strategy

An alternative approach to the extended Sobol method is the pinching strategy. The basic idea is to quantify the reduction of incertitude on the model response when freezing one or several parameters to a constant value while keeping the uncertainty of the remaining epistemic parameters. In context of a distributional p-box, the PI (pinching index) can be expressed by

$$\mathrm{PI}_{\boldsymbol{\Theta}_{x_i}} = 1 - \frac{\mathrm{unc}_Y(\boldsymbol{\Theta}_{x_i} = \boldsymbol{\Theta}_{x_i}^*)}{\mathrm{unc}_Y(\boldsymbol{\Theta}_x)}, \tag{3.74}$$

where $\mathrm{unc}_Y(\cdot)$ denotes a general uncertainty measure on the response. The numerator of Eq. (3.74) expresses the uncertainty on Y if the hyperparameters of the input quantity X_i are set to a constant value. The denominator considers the total response uncertainty, i.e., if none of the hyperparameters is pinched. [61]
Hence, when analyzing hybrid uncertainties, the pinching strategy degenerates a distributional p-box to a single CDF. Unlike the extended Sobol methods, this concept is also appropriate for pure epistemic uncertainties modeled by distribution-free p-boxes. Typically, the enclosing probability bounds of X_i are degenerated to an averaged CDF given by

$$F_{X_i}(x_i) = \frac{1}{2}\,(\underline{F}_{X_i}(x_i) + \overline{F}_{X_i}(x_i)). \tag{3.75}$$

However, if the *true* value of X_i is known to have no variability, it can be reasonable to replace the p-box with a deterministic value. Further pinching strategies can be found in [62]. Within this thesis, the focus is put on distributional p-boxes.
Especially for nonlinear input-output relations, the value of PI can be strongly affected by the pinching point $\boldsymbol{\Theta}_{x_i}^*$. As the uncertainty on $\boldsymbol{\Theta}_{x_i}$ is given by intervals, there is no clear nominal value such as the mean of a distribution. To get an unbiased result, the average value of PI for different realizations of $\boldsymbol{\Theta}_{x_i}^*$ can be computed. Apart from analytical test cases, this approach is too expensive for many real-world applications. Therefore, the pinching location is usually set to the interval midpoint.

Up to now, the term $\text{unc}_Y(\cdot)$ has been introduced as a general uncertainty without giving a specific metric for it. In the following, a short literature review about various ways to interpret $\text{unc}_Y(\cdot)$ is provided:

- A common measure for the response incertitude is the area A_y enclosed by the response p-box:

$$A_y = \int_0^1 (\underline{F}_Y^{-1}(r) - \overline{F}_Y^{-1}(r))\, dr. \tag{3.76}$$

  Hence, the determination of the PI is based on comparing the p-box area before and after the hyperparameter pinching. In [128], the computational effort of this metric is discussed for a high-dimensional test case. Further, the authors have noticed a significant influence of the pinching point $\Theta_{x_i}^*$ on the SA results which is why they have conducted a repeated computation for varying locations. Within the scope of [124], the area-based metric has been applied for distribution-free p-boxes derived from a known mean and standard deviation with the help of the Chebyshev inequality, see Sec. 3.2.3. In this specific case, the pinching strategy has degenerated the p-box to a deterministic value instead of a single CDF.
- Another incertitude metric is the KS (Kolmogorov-Smirnov) distance which quantifies the maximum vertical distance between the bounding curves of the response p-box

$$d_{KS} = \max_y \{\overline{F}_Y(y) - \underline{F}_Y(y)\}. \tag{3.77}$$

  The authors of [70] have used this metric for an epistemic SA in combination with a OAT sampling method which returns a main and total effect for every epistemic parameter. The latter is equal to Eq. (3.74) whereas the main effect is derived from pinching all epistemic parameters except the one under investigation.
- Apart from geometrical measures, the incertitude of stochastic descriptors is an alternative formulation for $\text{unc}_Y(\cdot)$. This approach is preferable if the modeler is interested in specific statistics of the response. Typically, the epistemic uncertainty on the stochastic descriptor is expressed by its interval width. For example, in [70] the difference between minimum and maximum failure probability has been analyzed which is equal to the p-box height at a predefined limit state. The same procedure can be applied for other statistics such as the response mean or variance [128].

Further sensitivity measures that are not explicitly listed above can be found in [13, 22, 67].
Comparing the extended Sobol method with the pinching concept clarifies that the latter is more oriented towards the assessment of lack-of-knowledge uncertainties. In particular, the large flexibility of the uncertainty measure is helpful for adapting it to the epistemic modeling approach which enables a straightforward interpretation of the resulting sensitivity indices.
The overall goal of this thesis is to achieve a robust design under consideration of aleatory

and epistemic uncertainty sources. Performing sensitivity studies is seen as preparatory step for the subsequent robustness assessment even though these two disciplines are not always strictly separated in literature. For this reason, the focus of Sec. 4.2 is to introduce a computationally inexpensive screening method for ranking the epistemic parameters rather than quantifying the exact contribution of each uncertain parameter.
The next section of the theoretical background part is about robust design optimization (RDO) techniques for the coexistence of aleatory and epistemic uncertainties.

3.6 Robust Design Optimization for Systems under Hybrid Uncertainties

The term robustness is open to diverging interpretations in literature which are strongly dependent on the application field. Within the scope of engineering problems, the concept is often associated to the achievements of the Japanese engineer Genichi Taguchi in the 1980s. The next two sections will shed light into the general definition of robustness as well as the mathematical formulation for a RDO.

3.6.1 Introduction: Robustness in Context of Engineering Applications

In principle, a robust design is characterized by its insensitivity against variations caused by, for instance, the production process or changing environmental conditions [170]. According to Taguchi's perspective, a robust performance is achieved by an optimal setting of the design variables. In contrary, reducing the uncertainty of the design variables should be considered as last option because it usually requires disproportionately higher effort.
The basic principle behind this concept can be illustrated with the help of Fig. 3.10(b). From a deterministic point of view, design A is superior because its nominal value is lower as for design B. In terms of robustness, design B shows a better performance as the variation of the system response is significantly lower. Note that the uncertainty on the design variable, i.e., Δx, is the same for both designs.
As a starting point for the robustness assessment, the parameters of a system are distinguished between three categories, represented in Fig. 3.10(a): design variables, noise factors and response parameters [46]. The difference between the first two groups is that design variables can be controlled by the modeler whereas the parameters of the second group are uncontrollable. Noise factors can be further subdivided into external factors (environmental conditions, operating conditions), manufacturing imperfections and product deterioration [132]. In accordance with the above-mentioned categorization, three different robust design types have been derived [5]:

- Type I considers variations exclusively in the noise factors. Hence, the objective is to find optimal values for the design parameters, which are treated as deterministic quantities, to minimize the performance variation.
- Type II accounts for the fact that design variables are subject to uncertainty. Thus, the performance variation is caused by the design variables themselves. In this framework, the existence of noise factors is ignored.
- Type III puts the focus on the uncertainty of the computational model. Repeating a simulation several times with exactly identical design variables can result in different responses due to the variation of the model parameters. Thus, the goal becomes to find a design which is insensitive against the uncertainty of Θ_g.

In real-world applications, especially a mixture of Type I and II is considered. The Type I robust design coincides with Taguchi's interpretation. His approach for achieving a robust design is based on defining a loss function which quantifies the deviation of the system performance from a certain target value. The higher the offset between target value and actual performance, the larger the loss function. Since the noise factors are causing a variation of the system performance, an optimal robust design is achieved by minimizing the expected value of the quality loss function. In order to solve this optimization problem, Taguchi has introduced a two-step procedure. First, a combination of design parameters is sought to minimize the so-called SNR (signal-to-noise ratio) which presents a metric for the response variation. After that, the group of design parameters which has a negligible effect on the SNR is tuned to minimize the gap between target value and expected performance.
This approach requires the conduction of a DoE (design of experiments) to assess the robustness of different designs. Taguchi has proposed a concept based on the usage of orthogonal arrays. In principle, this approach can be seen as a deterministic DoE which strictly separates

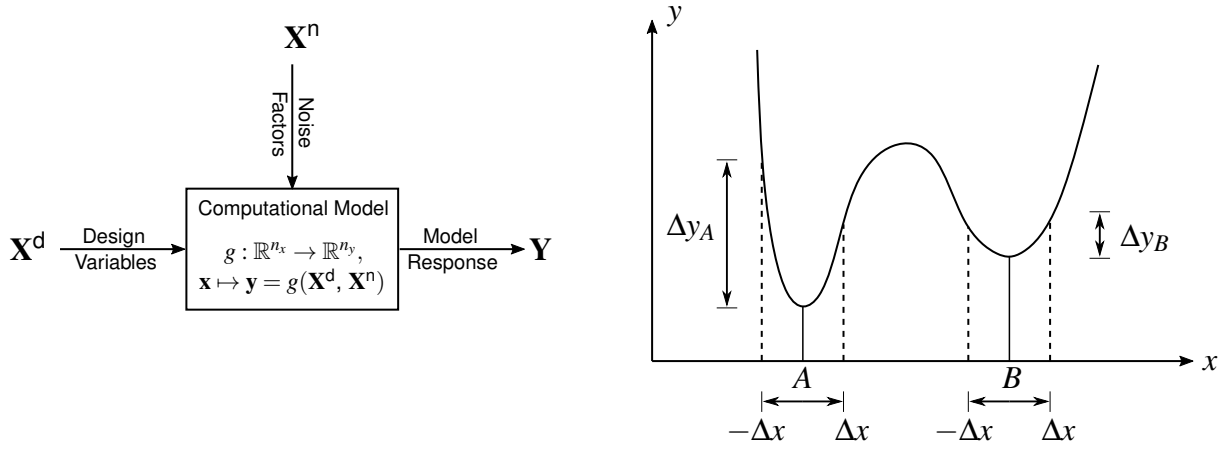

(a) P-diagram.

(b) Graphical illustration of a robust design.

Figure 3.10 Variable classification (left) and graphical illustration (right) of the robust design concept [5, 126].

design variables and noise factors from each other. [88, 126]
Taguchi's work was a decisive contribution towards the consideration of uncertainties in the design process. However, his approach has been criticized especially in regard to the usage of orthogonal arrays for the DoE as well as the separated optimization of the response variation and target value deviation. Further, the original Taguchi method is not able to deal with constraints. For these reasons, classical optimization techniques have been extended to RDO techniques. [121, 126].
With increasing computational power, the robust design concept has gradually entered the field of numerical simulation. The conventional design optimization, which neglects the occurrence of uncertainty, is enhanced by introducing a robustness criterion into the objective function. Compared to a deterministic design optimization, performing a RDO requires a higher number of simulations for mapping the input variations to the response quantities. The usage of efficient uncertainty propagation techniques is decisive.
The variety of RDO approaches can be, regardless of their type, classified into *feasibility robustness* and *sensitivity robustness*. The first group is related to the insensitivity of constraints against variations and is therefore also named *robustness of constraints*. The second class puts the focus directly on minimizing the variation of the performance metric. The difference between these two levels for the RDO formulation is discussed in greater detail within the next chapter. [127]
Within the scope of this thesis, we concentrate on Type I and II and disregard the influence of model uncertainties. The main intention of this thesis is the implementation of lack-of-knowledge uncertainties into the RDO framework. One of the main challenges is to account for the high computational cost. In [7], a Type IV robust design is introduced which refers explicitly to epistemic uncertainties. From the author's perspective, one can also extend the existing types by appropriate modeling approaches for uncertain design variables and noise factors.
The next paragraph provides a review on how to set up a mathematical formulation for a robust design optimization with special emphasis upon lack-of-knowledge uncertainties.

3.6.2 Mathematical Setup for a Robust Design Optimization

As discussed in the previous section, the RDO is an extension of the conventional optimization. A meaningful starting point is to analyze the mathematical formulation for a deterministic design optimization and compare the expression with the one for a RDO.

Robust Design Optimization under Aleatory Uncertainties

The underlying aim of any optimization is to determine the set of design variables such that the deviation between actual and desired performance is minimized. In order to express this goal with an objective function, the modeler has to define a target value y^* which expresses

the desired system performance. In general, one can distinguish between three different types of objective functions: nominal-the-best, larger-the-better and smaller-the-better. The first is characterized by a finite target value whereas the remaining types have their optimum at plus and minus infinity, respectively. In the sequel, all formulations are given for the nominal type.
The optimization framework introduced so far represents the unconstrained case. This setup can be extended by a set of equality and inequality constraints which shrink the feasible space of solutions. In addition, the design space can be limited by defining bounds on $\mathbf{x}^{\mathsf{d}}$. Finally, the deterministic optimization yields

$$\begin{aligned} \min_{\mathbf{x}^{\mathsf{d}}} \quad & \|g(\mathbf{x}^{\mathsf{d}}) - y^*\|_2 \\ \text{s.t.} \quad & c^{(i)}(\mathbf{x}^{\mathsf{d}}) = 0 \qquad \text{for } i = 1,\dots,n_{\text{eq.}} \\ & c^{(i)}(\mathbf{x}^{\mathsf{d}}) \leq 0 \qquad \text{for } i = 1,\dots,n_{\text{ineq.}} \\ & \underline{x}_i^{\mathsf{d}} \leq x_i^{\mathsf{d}} \leq \overline{x}_i^{\mathsf{d}} \qquad \text{for } i = 1,\dots,n_x^{\mathsf{d}}, \end{aligned} \tag{3.78}$$

where $\mathbf{x}^{\mathsf{d}} \in \mathbb{R}^{n_x{}^{\mathsf{d}}}$ is the vector of design variables and $c^{(i)}$ denotes the $i-$th constraint.
To extend the deterministic optimization framework, one has to determine an appropriate measure for robustness. The most common metric is the standard deviation. Alternatively, the distance between two percentiles, e.g., the *5th* and *95th* percentile, could be used as a measure for dispersion. Compared to the standard deviation, the percentile difference contains more information as it accounts for the skewness of a distribution. However, the approximation of two percentile values is rather expensive and not applicable to multimodal distributions. For this reason, the standard deviation is used in the following. [84]
In presence of noise factors $\mathbf{X}^{\mathsf{n}}$ and/or uncertain design variables $\mathbf{X}^{\mathsf{d}}$, Eq. (3.78) is modified in the following fashion. The objective function is now re-formulated to minimize the distance between expected response and target value. Further, the minimization of the performance variation, denoted as σ_y, is part of the objective. Another major difference to Eq. (3.78) is the formulation of the inequality constraints. Due to the uncertainty, the feasible space is reduced by a multiple of the constraint's standard deviation. The extended optimization problem is given by [126]

$$\begin{aligned} \min_{\boldsymbol{\mu}_x^{\mathsf{d}}} \quad & w_1\ (\mu_y - y^*)^2 + w_2\ \sigma_y \\ \text{s.t.} \quad & c^{(i)}(\boldsymbol{\mu}_x^{\mathsf{d}}) = 0 \\ & \mu_c^{(i)} + k\ \sigma_c^{(i)} \leq 0 \\ & \underline{\boldsymbol{\mu}}_x^{\mathsf{d}} \leq \boldsymbol{\mu}_x^{\mathsf{d}} \leq \overline{\boldsymbol{\mu}}_x^{\mathsf{d}}, \end{aligned} \tag{3.79}$$

where w_1 and w_2 represent the weighting factors of the objective function components. Note, that the set of design variables has changed from $\mathbf{x}^{\mathsf{d}}$ to a vector of mean values $\boldsymbol{\mu}_x^{\mathsf{d}}$.

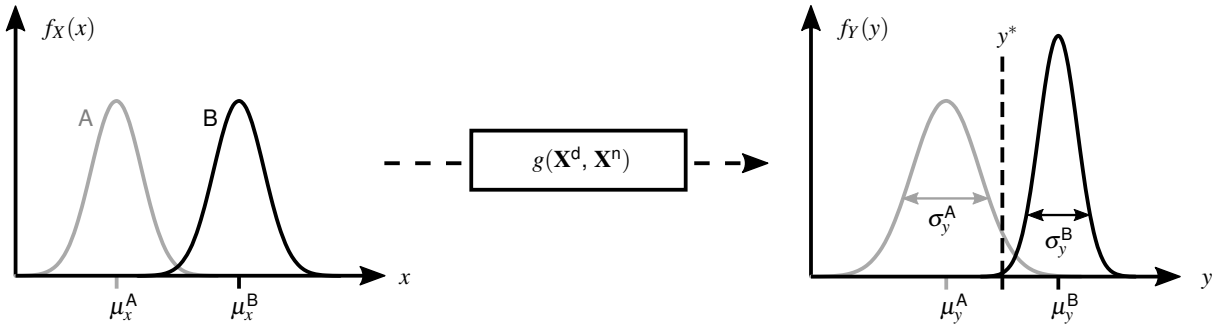

Figure 3.11 Graphical illustration for a RDO under aleatory uncertainties.

Figure 3.11 illustrates the RDO concept for random design variables. Let us assume that the offset from the target value is equal for both designs. Consequently, design B is superior because it leads to a smaller performance variation.

Equation (3.79) shows clearly the aforementioned separation between *feasibility* and *sensitivity robustness*. The first type, given by the inequality constraints, could alternatively be interpreted from a probabilistic point of view. This would change the formulation to [126]

$$P\left(c^{(i)}(\mathbf{X}^d, \mathbf{X}^n) \leq 0\right) \leq P_f^{(i)}, \tag{3.80}$$

which states that the probability of violating the constraint may not exceed $P_f^{(i)}$. Even though this expression is based on reliability analysis it is often referred as measure for the robustness of constraints.

From the author's point of view, the terms reliability and robustness should be strictly separated from each other because of their different interpretations. On the one hand, violating reliability constraints causes a failure of the system. On the other hand, the non-satisfaction of robustness constraints refers to a significant performance degradation which does not necessarily lead to failure. Hence, we keep the original formulation in Eq. (3.79) in the next subsection.

Robust Design Optimization under Hybrid Uncertainties

The RDO framework discussed in the previous section is not able to deal with the coexistence of epistemic and aleatory uncertainties. This means that the objective function as well as the constraint definition of Eq. (3.79) needs to be modified.

In the sequel, we consider the case that $\mathbf{X}^n$ is characterized by a distributional p-box and the design variables $\mathbf{X}^d$ are subject to aleatory uncertainty. The main difference to the RDO framework with pure random noise factors is the additional uncertainty of the stochastic descriptors caused by the epistemic contribution. The mean and standard deviation of the performance measure as well as the constraints are no longer crisp numbers but interval-valued quantities. The authors of [45] have developed the following concept to enhance the classical RDO

framework:

$$\begin{aligned} \min_{\boldsymbol{\mu}_x^{\mathsf{d}}} \quad & w_1 \, \|\tilde{\mu}_y - y^*\|_2 + w_2 \, \tilde{\sigma}_y + w_3 \, \Delta\sigma_y \\ \text{s.t.} \quad & c^{(i)}(\boldsymbol{\mu}_x^{\mathsf{d}}) = 0 && \text{for } i = 1, \ldots, n_{\text{eq.}} \\ & \overline{\mu}_c^{(i)} + k \, \overline{\sigma}_c^{(i)} \leq 0 && \text{for } i = 1, \ldots, n_{\text{ineq.}} \\ & \underline{\boldsymbol{\mu}}_x^{\mathsf{d}} \leq \boldsymbol{\mu}_x^{\mathsf{d}} \leq \overline{\boldsymbol{\mu}}_x^{\mathsf{d}} && \text{for } i = 1, \ldots, {n_x}^{\mathsf{d}}. \end{aligned} \tag{3.81}$$

Compared to the objective function in Eq. (3.79) the stochastic moments have been replaced by the average mean $\tilde{\mu}_y$ and standard deviation $\tilde{\sigma}_y$, i.e., the interval midpoints of $[\underline{\mu}_y, \overline{\mu}_y]$ and $[\underline{\sigma}_y, \overline{\sigma}_y]$, respectively. In addition, the objective function is extended with a third term, denoted as $\Delta\sigma_y$, which evaluates the interval width of the uncertain standard deviation. So, the metric for the *sensitivity robustness* is a combination of two terms characterizing the aleatory and epistemic uncertainty of σ_y.

To account for the epistemic uncertainty in the inequality constraints, the maximum mean $\overline{\mu}_c^{(i)}$ and standard deviation $\overline{\sigma}_c^{(i)}$ is used. Contrary to the objective function, the constraint's formulation itself has not changed. Choosing the maximum value for both stochastic descriptors is a simplified but conservative approach.

The RDO concept in presence of aleatory and epistemic uncertainties is shown in Fig. 3.12. Similar to the previous illustration, both designs show the same average performance because the distance between target and average mean value is the same. However, design B leads to a lower average standard deviation $\tilde{\sigma}_y$ as well as a smaller interval width $\Delta\sigma_y$.

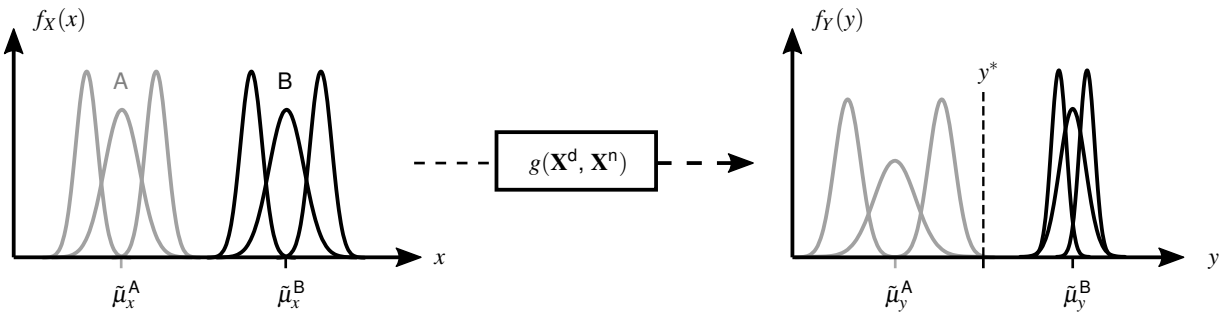

Figure 3.12 Graphical illustration of a RDO under hybrid uncertainties.

All formulations introduced so far share the idea to implement the robustness criterion into the objective function. Furthermore, the epistemic contribution is considered by the extra term $\Delta\sigma_y$. In literature, alternative RDO strategies can be found:

- Instead of extending the deterministic objective function, the robustness metric can be treated as an additional constraint. The authors of [69] for example have formulated an inequality constraint to limit the response standard deviation. A logical extension for hybrid uncertainties is to formulate a restriction for the maximum value of σ_y.
- As an alternative to $\Delta\sigma_y$, the MMR (minimax regret) criterion can be used to account for the epistemic uncertainty [83]. Here, the basic idea is to find a design which mini-

mizes the worst performance in the epistemic space and makes the determination of $\Delta\sigma_y$ thereof superfluous.

The first of the two above-mentioned approaches is given in absence of any other equality/inequality constraints by

$$\begin{aligned} \min_{\boldsymbol{\mu}_x^{\mathrm{d}}} \quad & \|\tilde{\mu}_y - y^*\|_2 \\ \text{s.t.} \quad & \overline{\sigma}_y \leq k\ \tilde{\mu}_y, \end{aligned} \tag{3.82}$$

where the maximum standard deviation $\overline{\sigma}_y$ may not exceed a multiple of the average mean response $\tilde{\mu}_y$. The second modification can be expressed by

$$\min_{\boldsymbol{\mu}_x^{\mathrm{d}}} \left\{ \max_{\boldsymbol{\Theta}_x} \left(w_1\ \|\tilde{\mu}_y - y^*\|_2 + w_2\ \sigma_y \right) \right\}. \tag{3.83}$$

Compared to the RDO concepts in Eq. (3.79) and (3.81), these formulations are more in conformity with a worst-case analysis. To conclude, there is no best practice for setting up a RDO. In the end, the modeler has to find a solution which fits to the requirements of the analysis. Throughout Section 4.3.2, the different RDO formulations will be discussed again in context of an analytical test case scenario.

To summarize, the previous sections have provided an overview over state-of-the-art methods for inverse and forward UQ problems as well as a literature review about the thematic areas of sensitivity analysis and robust design optimization. Furthermore, the limitations of existing methods have been discussed in context of mixed aleatory and epistemic uncertainties. For this reason, new approaches are introduced within the next chapter based on the research questions from Section 2.3.

Chapter 4

METHODS

The subsequent chapter covers the methodological part of this thesis and is structured in a similar fashion as the preceding one. In Section 4.1, a concept for inverse lack-of-knowledge problems is developed. After that, the focus is put on the field of epistemic sensitivity analysis (SA) in Section 4.2. Here, a method is introduced to screen out unimportant parameters in order to reduce the complexity of the computational model. Finally, Section 4.3 deals with the question how to conduct a robust design optimization (RDO) in presence of aleatory and epistemic noise variables. Apart from defining an appropriate formulation for the objective function, developing an efficient RDO framework is key to a successful application in context of high-dimensional problems such as the interdisciplinary secondary air system (SAS) model.

4.1 Inverse Lack-of-Knowledge Uncertainty Quantification

In Section 3.4, a summary about methods for solving inverse problems under stochastic input-output relations has been discussed. To repeat, the Bayesian modeling framework has become established when uncertainty sources are modeled by probabilistic approaches. However, this concept can lead to biased results if the modeler has only little data about the response variation. In this case, non-probabilistic approaches can be beneficial, as they require no a-priori information about the unknown input variation. For example, the method discussed in Section 3.4.2 is based on the idea to describe the variation of a set of measurement points $\mathcal{Y}_{\mathrm{m}}$ by a convex hull $\mathcal{C}_{\mathcal{Y}_{\mathrm{m}}}$. The actual goal of the inverse uncertainty quantification (UQ) is to

identify an n_x-dimensional interval which matches, after propagating it to the response space, the convex hull as much as possible.
A crucial limitation of this concept is the computational burden for the determination of convex hulls in high dimensions. For this reason, an alternative concept is proposed here which uses a so-called MVEE (minimum-volume enclosing ellipsoid) to characterize the uncertainty. First, the fundamental principle is explained in Section 4.1.1. Similar to the convex hull approach shown before, we consider a scenario where the modeler is equipped with a small set of measurement points $\mathcal{Y}_{\mathsf{m}}$. After that, the framework is extended in Section 4.1.3 for cases where the uncertainty is given by descriptive statistics, i.e., the sample mean and standard deviation of the model response, without knowing the underlying data set. The following paragraphs have been partly published by the author in [107, 108].

4.1.1 Hyperellipsoid Approach for Limited Measurement Data

As mentioned before, the new approach to solve an inverse problem introduced in this thesis describes the uncertainty in the output space by a hyperellipsoid instead of a convex hull. A great benefit of using a hyperellipsoid is its simple mathematical formulation. Furthermore, dependencies between the response quantities can be easily represented. Also, from a stochastic point of view, it is reasonable to model uncertainties by ellipsoids. In [50], the uncertainty of a system with two input quantities was represented by different geometric figures like a rectangle, parallelogram, ellipse or triangle. It turned out that modeling the uncertainty by an ellipse leads to the least overestimation of the maximum response in many cases.
The starting point for this approach is the same as in Section 3.4.2. The modeler is faced with a situation where the measurement set given by

$$\mathcal{Y}_{\mathsf{m}} = \left\{ \boldsymbol{y}_{\mathsf{m}}^{(1)}, \ldots, \boldsymbol{y}_{\mathsf{m}}^{(n_{\mathsf{m}})} \right\} \subset \mathbb{R}^{n_y}, \tag{4.1}$$

comprises only a small number of points. Now, the uncertainty in the output space is quantified by a MVEE, i.e., the ellipsoid with the smallest volume that contains all sample points of $\mathcal{Y}_{\mathsf{m}}$. Mathematically, the MVEE of the measurement set $\mathcal{Y}_{\mathsf{m}}$ can be computed by solving the optimization problem

$$\begin{aligned} &\underset{A,b}{\text{minimize}} \quad \log(\det(\boldsymbol{A}^{-1})) \\ &\text{subject to} \quad \|\boldsymbol{A}\boldsymbol{y}_{\mathsf{m}}^{(i)} + \boldsymbol{b}\|_2 \leq 1,\ i = 1, \ldots, n_{\mathsf{m}}, \end{aligned} \tag{4.2}$$

where $\boldsymbol{A} \in \mathbb{R}^{n_y \times n_y}$ must be a symmetric and positive definite matrix and $\boldsymbol{b} \in \mathbb{R}^{n_y}$ [27]. An

optimal solution of Problem (4.2) is denoted by $\boldsymbol{A}_\mathsf{m}$, $\boldsymbol{b}_\mathsf{m}$ and forms the MVEE

$$\mathcal{E}_{\mathcal{Y}_\mathsf{m}} = \{\mathbf{y} \in \mathbb{R}^{n_y} \mid \|\boldsymbol{A}_\mathsf{m}\mathbf{y} + \boldsymbol{b}_\mathsf{m}\|_2 \leq 1\}. \tag{4.3}$$

Here, the inverse matrix of $\boldsymbol{A}_\mathsf{m}$, i.e., $\boldsymbol{A}_\mathsf{m}^{-1}$ contains information regarding the main axis lengths of the MVEE and their orientation whereas the negative vector of $\boldsymbol{A}_\mathsf{m}^{-1}\boldsymbol{b}_\mathsf{m}$, i.e., $-\boldsymbol{A}_\mathsf{m}^{-1}\boldsymbol{b}_\mathsf{m}$ is related to the center of the ellipsoid.
Having quantified the uncertainty in the output space, the question remains how to identify the uncertainty in the input space. In contrast to the convex hull strategy, the input uncertainty set is also described by an ellipsoid, i.e.,

$$\mathcal{E}_x = \{\mathbf{x} \in \mathbb{R}^{n_x} \mid \|\boldsymbol{A}_x\mathbf{x} + \boldsymbol{b}_x\|_2 \leq 1\}, \tag{4.4}$$

with $\boldsymbol{A}_x \in \mathbb{R}^{n_x \times n_x}$ and $\boldsymbol{b}_x \in \mathbb{R}^{n_x}$, where the entries of $\boldsymbol{A}_x$ and $\boldsymbol{b}_x$ need to be determined.
From the author's point of view, it is reasonable to quantify the uncertainty in the input and output space by the same geometrical shape due to the consistent interpretation. This argumentation will be further clarified in Section 4.1.3. Moreover, if the computational model is a perfectly linear map, the inverse of an ellipsoid is also an ellipsoid. The same argument also holds if $g(\mathbf{x})$ is nearly linear on the uncertainty set which might be a feasible assumption if the set is small enough.
For reasons of simplicity, it is assumed that the input parameters are independent from each other. This aspect is discussed for the application case in Section 5.1. Thus, the entries of $\boldsymbol{A}_x$ that need to be determined reduce to its diagonal entries, collected in $\boldsymbol{a}_x \in \mathbb{R}^{n_x}$, and it holds

$$\boldsymbol{A}_x = \begin{bmatrix} a_{x,1} & \cdots & 0 \\ \vdots & \ddots & \vdots \\ 0 & \cdots & a_{x,n_x} \end{bmatrix} \in \mathbb{R}^{n_x \times n_x}. \tag{4.5}$$

Due to this simplification, the uncertainty of the input space can be described completely by the two vectors $\boldsymbol{a}_x, \boldsymbol{b}_x \in \mathbb{R}^{n_x}$.
The basic principle of this approach has a few similarities with the method explained in Section 3.4.2. The goal is to identify the uncertainty of the input space by an ellipsoid which has an image in the output space that coincides with $\mathcal{E}_{\mathcal{Y}_\mathsf{m}}$ as closely as possible. As in case of the previous strategy, the geometry comparison is a key element of the approach. The main difference is how the uncertainty is quantified. Instead of using hyperrectangles and convex hulls in the input and output space, the uncertainties are described by hyperellipsoids.
The basic principle is shown by the illustration in Fig. 4.1. Note, that the ellipsoid $\mathcal{E}_x$ is described by its center point $\boldsymbol{c}_x$ and the vector $\boldsymbol{l}_x$ containing the main axis lengths. For the

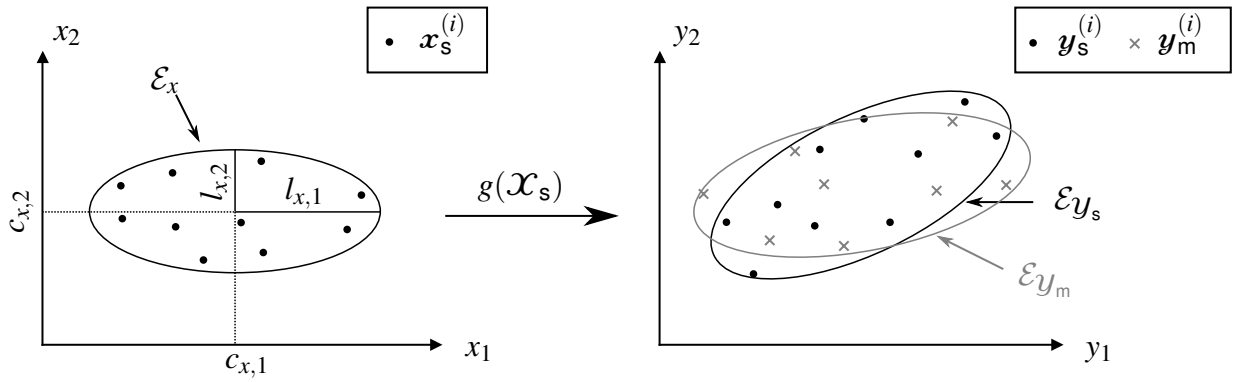

Figure 4.1 2D representation of the hyperellipsoid approach.

non-rotated case, these geometrical quantities can be derived from $\boldsymbol{a}_x$ and $\boldsymbol{b}_x$ via

$$\boldsymbol{l}_x = 1/\boldsymbol{a}_x, \quad \text{and} \quad \boldsymbol{c}_x = -\boldsymbol{A}_x^{-1}\,\boldsymbol{b}_x. \tag{4.6}$$

In the following, the single steps of the approach are explained in detail. As starting point, we consider the case that an ellipsoid $\mathcal{E}_x$ is clearly defined by the vectors $\boldsymbol{a}_x, \boldsymbol{b}_x \in \mathbb{R}^{n_x}$ in the input space. Similar to the convex hull approach, a sampling procedure is necessary to propagate the uncertainty from the input to the output space. Hence, a set of samples is generated within $\mathcal{E}_x$ in accordance to

$$\mathcal{X}_\mathsf{s} = \left\{\boldsymbol{x}_\mathsf{s}^{(1)}, \ldots, \boldsymbol{x}_\mathsf{s}^{(n_\mathsf{s})}\right\} \subset \mathcal{E}_x. \tag{4.7}$$

The modeler has to ensure that $\mathcal{E}_x$ is well represented by the sampling. If the computational model has a monotonic behavior, it is sufficient to create sample points only from the surface of $\mathcal{E}_x$. This modification saves computation time without influencing the mapping to the output space. The generation of samples from an n_x-dimensional hyperellipsoid surface can be done in a two-step procedure. First, a set of samples is generated which lies on the surface of an n_x-dimensional unit ball. Therefore, samples are drawn from an n_x-variate standard normal distribution and subsequently normalized such that each point is represented by a unit vector [109]. After that, a linear transformation is applied to map all points from the unit ball onto the surface of $\mathcal{E}_x$. Note, that the samples are no longer uniformly distributed due to the linear transformation.

After having computed the functional values of the samples, the corresponding uncertainty set in the output space $\mathcal{Y}_\mathsf{s}$ is obtained. The next step of the procedure is to compute the associated MVEE which is defined by

$$\mathcal{E}_{\mathcal{Y}_\mathsf{s}} = \left\{\mathbf{y} \in \mathbb{R}^{n_y} \mid \|\boldsymbol{A}_\mathsf{s}\,\mathbf{y} + \boldsymbol{b}_\mathsf{s}\|_2 \leq 1\right\}. \tag{4.8}$$

Thus, two ellipsoids are available in the output space: $\mathcal{E}_{\mathcal{Y}_\mathsf{m}}$ and $\mathcal{E}_{\mathcal{Y}_\mathsf{s}}$. Similar to the approach from Sec. 3.4.2, a metric has to be introduced to compare the two ellipsoids with each other.

For measuring the discrepancy between $\mathcal{E}_{\mathcal{Y}_\mathsf{m}}$ and $\mathcal{E}_{\mathcal{Y}_\mathsf{s}}$, a linear transformation is used to avoid an influence of the axis scaling. Here, the linear map defined by $\boldsymbol{A}_\mathsf{m}\,\mathbf{y}+\boldsymbol{b}_\mathsf{m}$ for $\mathbf{y}\in\mathbb{R}^{n_y}$ maps $\mathcal{E}_{\mathcal{Y}_\mathsf{m}}$ onto the n_y-dimensional unit ball which is the set of all $\mathbf{y}\in\mathbb{R}^{n_y}$ with $\|\mathbf{y}\|_2\leq 1$. If the same map is applied to $\mathcal{E}_{\mathcal{Y}_\mathsf{s}}$, a set $\acute{\mathcal{E}}_{Y_\mathsf{s}}$ is obtained which shall be close to the unit ball. Using the property that the linear map defined by $\boldsymbol{A}_\mathsf{s}\,\mathbf{y}+\boldsymbol{b}_\mathsf{s}$ for $\mathbf{y}\in\mathbb{R}^{n_y}$ maps $\mathcal{E}_{\mathcal{Y}_\mathsf{s}}$ onto the unit ball with

$$\boldsymbol{A}_\mathsf{s}\,\mathcal{E}_{\mathcal{Y}_\mathsf{s}}+\boldsymbol{b}_\mathsf{s}=\boldsymbol{A}_\mathsf{s}\,\boldsymbol{A}_\mathsf{m}^{-1}\underbrace{(\boldsymbol{A}_\mathsf{m}\,\mathcal{E}_{\mathcal{Y}_\mathsf{s}}+\boldsymbol{b}_\mathsf{m})}_{=\acute{\mathcal{E}}_{Y_\mathsf{s}}}-\boldsymbol{A}_\mathsf{s}\,\boldsymbol{A}_\mathsf{m}^{-1}\,\boldsymbol{b}_\mathsf{m}+\boldsymbol{b}_\mathsf{s}, \tag{4.9}$$

it is desired that $\boldsymbol{A}_\mathsf{s}\,\boldsymbol{A}_\mathsf{m}^{-1}=\boldsymbol{I}_{n_y}$ and $\boldsymbol{A}_\mathsf{s}\,\boldsymbol{A}_\mathsf{m}^{-1}\,\boldsymbol{b}_\mathsf{m}+\boldsymbol{b}_\mathsf{s}=0$ hold, where $\boldsymbol{I}_{n_y}$ is the $n_y\times n_y$ identity matrix. Note that the comparison of $\boldsymbol{A}_\mathsf{s}\,\boldsymbol{A}_\mathsf{m}^{-1}$ against the identity matrix, and not against an arbitrary orthogonal matrix, is sufficient here, as $\boldsymbol{A}_\mathsf{m}$ and $\boldsymbol{A}_\mathsf{s}$ are symmetric positive definite matrices, i.e., they are unique in Eq. (4.3) and (4.8). Hence, the discrepancy between the ellipsoids $\mathcal{E}_{\mathcal{Y}_\mathsf{m}}$ and $\mathcal{E}_{\mathcal{Y}_\mathsf{s}}$ is measured by the following terms:

$$\Delta\boldsymbol{A}=\|\boldsymbol{A}_\mathsf{s}\,\boldsymbol{A}_\mathsf{m}^{-1}-\boldsymbol{I}_{n_y}\|_2, \tag{4.10}$$

$$\Delta\boldsymbol{b}=\|\boldsymbol{b}_\mathsf{s}-\boldsymbol{A}_\mathsf{s}\,\boldsymbol{A}_\mathsf{m}^{-1}\,\boldsymbol{b}_\mathsf{m}\|_2. \tag{4.11}$$

If the two ellipsoids are identical, both terms take the value zero, otherwise their discrepancies are penalized. Hence, the metric to describe the mismatch between the ellipsoids is given by:

$$\mathrm{obj}_\mathcal{E}(\boldsymbol{a}_x,\boldsymbol{b}_x)=\Delta\boldsymbol{A}^2(\boldsymbol{a}_x,\boldsymbol{b}_x)+\Delta\boldsymbol{b}^2(\boldsymbol{a}_x,\boldsymbol{b}_x). \tag{4.12}$$

Based on the mathematical formulation of the objective function, the concept of the inverse UQ is to minimize the geometrical discrepancy by optimizing the vectors $\boldsymbol{a}_x$ and $\boldsymbol{b}_x$. This can be expressed by:

$$\begin{aligned}&\underset{\boldsymbol{a}_x,\boldsymbol{b}_x}{\text{minimize}} \quad \mathrm{obj}_\mathcal{E}(\boldsymbol{a}_x,\boldsymbol{b}_x)\\ &\text{subject to} \quad \boldsymbol{a}_x\geq 0.\end{aligned} \tag{4.13}$$

The basic principle of the discrepancy measure derived in Eq. (4.9) is shown in Figure 4.2 for the 2D case. To both of the ellipsoids, the same linear transformation is applied. In case of the measurement ellipsoid, this leads to a mapping of $\mathcal{E}_{\mathcal{Y}_\mathsf{m}}$ to the unit ball. In contrast, the transformed ellipsoid of $\mathcal{E}_{\mathcal{Y}_\mathsf{s}}$, i.e., $\acute{\mathcal{E}}_{Y_\mathsf{s}}$, deviates from the unit ball unless $\mathcal{E}_{\mathcal{Y}_\mathsf{s}}$ matches $\mathcal{E}_{\mathcal{Y}_\mathsf{m}}$ perfectly.
As a reminder, for the issue of identifying the optimal hyperrectangle C_x, a population-based optimization strategy was recommended. One of the main advantages of using a global optimization strategy is the good performance in exploring the design space. The same approach can be applied to Problem (4.13), with the difference that a population of hyperellipsoids instead of hyperrectangles is generated in every step.
However, the inverse problem can also be solved by a local optimization strategy. In this case,

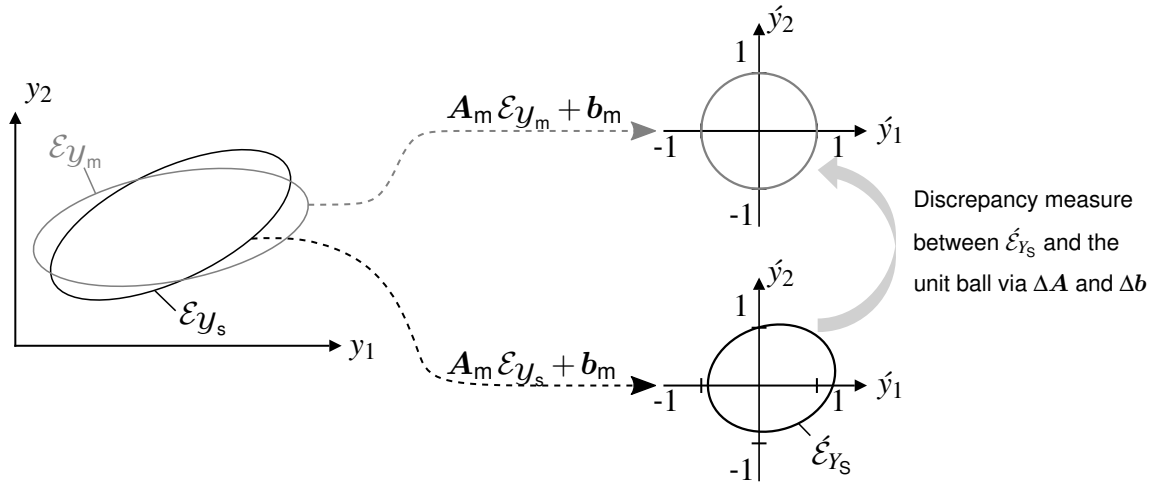

Figure 4.2 Graphical representation of the discrepancy measure.

the solution is developed in two steps. First, the uncertainty in the input space is approximated with the help of a local linearization of the computational model. After that, the obtained solution is used as starting point for the actual optimization procedure. For the first step, we assume that $g(\mathbf{x})$ is approximately linear on the optimal $\mathcal{E}_x$, i.e.,

$$\mathcal{E}_{y_m} \approx g(\mathcal{E}_x). \tag{4.14}$$

If g is perfectly linear, there is an equal sign in Equation (4.14). Under this assumption, the propagation of an ellipsoid throughout the model leads also to an ellipsoid in the output space. Thus, $\mathcal{E}_{y_m}$ is the image of an approximate solution $\tilde{\mathcal{E}}_x = \{\mathbf{x} \in \mathbb{R}^{n_x} \mid \|\tilde{\boldsymbol{A}}_x \mathbf{x} + \tilde{\boldsymbol{b}}_x\|_2 \leq 1\}$ in the input space for the local linearization of g. In order to obtain such a local linear model, a first-order approximation of g at a point $\boldsymbol{x}_0 \in \mathbb{R}^{n_x}$ that maps to the center point of $\mathcal{E}_{y_m}$ is used, i.e., $g(\boldsymbol{x}_0) = -\boldsymbol{A}_m^{-1} \boldsymbol{b}_m$. In order to do so, the Jacobian matrix $\boldsymbol{J}_g$ is computed at $\boldsymbol{x}_0$ and the relation

$$\boldsymbol{A}_x^2 \approx \boldsymbol{J}_g^T \boldsymbol{A}_m^2 \boldsymbol{J}_g \tag{4.15}$$

is used to approximate $\boldsymbol{A}_x$. Again, if g is linear, there is an equal sign in Eq. (4.15). As $\boldsymbol{J}_g^T \boldsymbol{A}_m^2 \boldsymbol{J}_g$ is usually not a diagonal matrix, only their diagonal entries are extracted for $\tilde{\boldsymbol{A}}_x$. Note that this procedure is only possible if these entries are all positive. The point $\boldsymbol{x}_0$ can then be used as the center point of $\tilde{\mathcal{E}}_x$ with $\tilde{\boldsymbol{b}}_x = -\tilde{\boldsymbol{A}}_x \boldsymbol{x}_0$. Hence, the first part of the inverse UQ is completed. The accuracy of the approximate solution $\tilde{\mathcal{E}}_x$ can be checked by computing the value of the objective function according to Eq. (4.12). The precision is strongly dependent on the characteristics of the real model. The stronger the nonlinearity of g the higher the risk that $\tilde{\mathcal{E}}_x$ is further away from the optimum.

If the modeler is already satisfied with the initial approximation of the input uncertainty, the subsequent optimization is not necessary. Otherwise, the identified input uncertainty $\tilde{\mathcal{E}}_x$ is used as starting point for an optimization procedure. Here, a local strategy is practical be-

cause the initial solution should already be close to the optimum. As the optimizer can vary the parameter $\boldsymbol{b}_x$ freely, the center of the optimized ellipsoid does not necessarily have to coincide with the center point of $\mathcal{E}_{\mathcal{Y}_\mathsf{m}}$. Nevertheless, the local strategy might not find the global optimum of Problem (4.13) if the start values $\tilde{\boldsymbol{a}}_x$ and $\tilde{\boldsymbol{b}}_x$ are too far away from it. Instead, the optimizer converges to a local optimum. By assigning weighting factors to the components of Eq. (4.12), the performance of the algorithm can be improved. Alternatively, the modeler can use a population-based optimization strategy.
The general concept of the hyperellipsoid approach as well as the difference between the local and global optimization technique is illustrated by an analytical test case within the next subsection.

4.1.2 Analytical Example

Let us consider a test model g which has two dimensions in the input as well as in the output space in order to have a clear representation of the results. Its analytical description is given by

$$g : \mathbb{R}^2 \to \mathbb{R}^2, \begin{pmatrix} x_1 \\ \\ x_2 \end{pmatrix} \mapsto \begin{pmatrix} y_1 \\ \\ y_2 \end{pmatrix} = \begin{pmatrix} 0.5x_1^2 + 3x_1 + 2x_2 \\ \\ 0.5x_2^2 + x_1 + 4x_2 \end{pmatrix}. \tag{4.16}$$

In order to create a measurement set $\mathcal{Y}_\mathsf{m}$, samples are generated from a known probability distribution. Here, two different cases are considered for which each 40 input samples are generated:

Case 1: The measurement set is sampled from a two-dimensional normal distribution with a mean value at $x_1 = x_2 = 5.0$. The two random variables are not correlated with each other which is why the off-diagonal entries of the covariance matrix take the value zero. Both variables have a standard deviation of one. Moreover, we consider a truncated normal distribution which generates exclusively samples that have a probability of at least 0.05. This modification is intended to prevent the measurement set from outliers.

Case 2: A uniform instead of a normal distribution is used to generate the measurement set. The sample points in the input space are created by a uniform sampling procedure within the region $x_1, x_2 \in [2.5, 7.5]$.

Then, the output samples, which are obtained by propagating the input samples through the model g, are used as measurement set $\mathcal{Y}_\mathsf{m}$ for the subsequent investigations and the realizations in the input space are no longer considered because this information is usually not given for a real application.
The sample points $\mathcal{Y}_\mathsf{m}$ are represented by black points in the output space, see Figures 4.3(b)

and 4.3(d). For both cases, the convex hull $\mathcal{C}_{\mathcal{Y}_\mathrm{m}}$ and the MVEE $\mathcal{E}_{\mathcal{Y}_\mathrm{m}}$ are computed. As $\mathcal{C}_{\mathcal{Y}_\mathrm{m}}$ is the smallest convex set that contains $\mathcal{Y}_\mathrm{m}$, it holds

$$\mathcal{C}_{\mathcal{Y}_\mathrm{m}} \subset \mathcal{E}_{\mathcal{Y}_\mathrm{m}}. \tag{4.17}$$

The corresponding shapes are represented in a light blue ($\mathcal{E}_{\mathcal{Y}_\mathrm{m}} \backslash \mathcal{C}_{\mathcal{Y}_\mathrm{m}}$) and light green ($\mathcal{C}_{\mathcal{Y}_\mathrm{m}}$) color. Using the inverse UQ based on the hyperrectangle identification approach from Section 3.4.2, a dark green rectangle in the input space is yielded, see Figures 4.3(a) and 4.3(c). Note that the convex hull $\mathcal{C}_{\mathcal{Y}_\mathrm{s}}$ can be quantified by propagating the four corner points of $\mathcal{C}_x$ as g is monotonous for positive input values.
For the hyperellipsoid approach from Section 4.1.1, the initial ellipse obtained from Eq. (4.15) is depicted by dotted blue lines and the final result of the optimization by the solid blue lines in Figures 4.3(c) and 4.3(d).
In order to assess the solution, it is also investigated which points in the input space map to $\mathcal{C}_{\mathcal{Y}_\mathrm{m}}$ and $\mathcal{E}_{\mathcal{Y}_\mathrm{m}}$. The set of all these points, i.e., $g^{-1}(\mathcal{C}_{\mathcal{Y}_\mathrm{m}})$ and $g^{-1}(\mathcal{E}_{\mathcal{Y}_\mathrm{m}}) = g^{-1}(\mathcal{E}_{\mathcal{Y}_\mathrm{m}} \backslash \mathcal{C}_{\mathcal{Y}_\mathrm{m}}) \cup g^{-1}(\mathcal{C}_{\mathcal{Y}_\mathrm{m}})$ are colored in light blue and green, similar to the associated images in the output space.
We start with the interpretation of the results from case 1, depicted in Figure 4.3(a). For the hyperrectangle identification approach, the goal of the optimization is to find a rectangle that coincides, after propagating it to the output space, with the convex hull $\mathcal{C}_{\mathcal{Y}_\mathrm{m}}$ in the output space as much as possible. Therefore, $\mathcal{C}_x$ should also be a good representation of the green region in the input space. However, the corner areas of $\mathcal{C}_x$ include points which do not coincide with $\mathcal{C}_{\mathcal{Y}_\mathrm{m}}$ in the output space. This comes from the fact that one term of the objective function (see Eq. (3.60)) compares the areas of $\mathcal{C}_{\mathcal{Y}_\mathrm{m}}$ and $\mathcal{C}_{\mathcal{Y}_\mathrm{s}}$. If $\mathcal{C}_x$ was completely inside the green region, this requirement would be fulfilled badly.
Now, the focus is put on solving the inverse problem with the new approach from Section 4.1.1. It can be observed that the MVEE is a rather good approximation of the measurement set $\mathcal{Y}_\mathrm{m}$ because the ellipse runs mostly close to the convex hull. Thus, the approximation of the uncertainty via the MVEE is only associated with a small overestimation. The ellipsoid $\mathcal{E}_x$ in the input space covers a very small area outside the blue region for small values of x_1 and x_2. However, the image in the output space runs also clearly outside $\mathcal{E}_{\mathcal{Y}_\mathrm{m}}$ if y_1 and y_2 take large values as can be seen in Fig. 4.3(b). The reason for this is the overestimation of the uncertainty set $\mathcal{Y}_\mathrm{s}$ by $\mathcal{E}_{\mathcal{Y}_\mathrm{s}}$. Due to the quadratic terms in Eq. (4.16), the propagated sample points contained in $\mathcal{E}_x$ are not perfectly arranged in an elliptical shape in the output space. Thus, the ellipse $\mathcal{E}_{\mathcal{Y}_\mathrm{s}}$ is not able to describe the uncertainty of $\mathcal{Y}_\mathrm{s}$ without an overestimation. As a consequence, the uncertainty of the input quantities tends to be underestimated by $\mathcal{E}_x$.
In the following, the results of the hyperrectangle and hyperellipsoid approach are opposed to each other for the second case of the analytical example. Again, we start with the analysis of the rectangle identification. Figure 4.3(c) shows that the identified rectangle $\mathcal{C}_x$ is a good

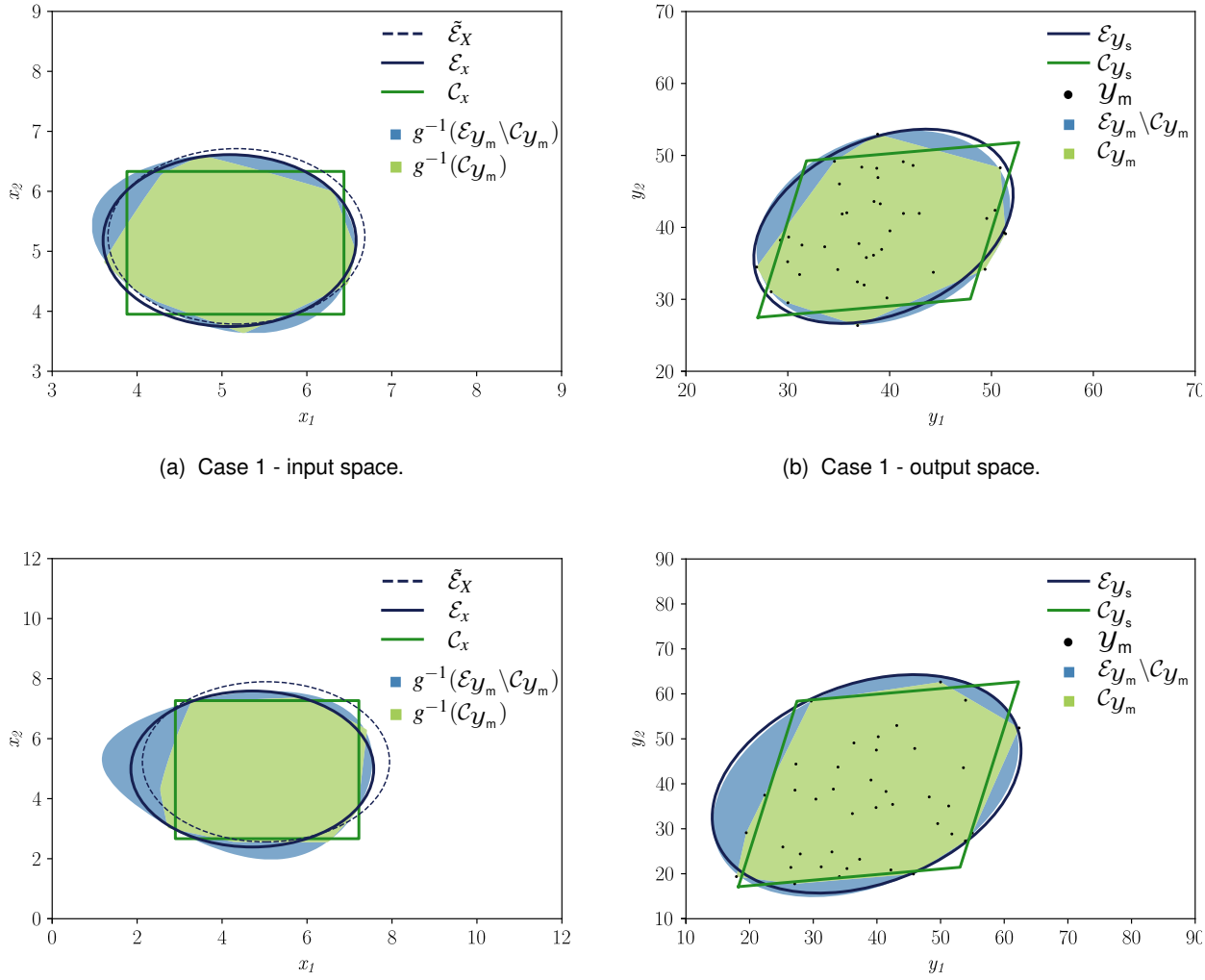

(a) Case 1 - input space.

(b) Case 1 - output space.

(c) Case 2 - input space.

(d) Case 2 - output space.

Figure 4.3 Input and output space representation for the analytical test case.

approximation of the green region. Similar to the previous test case, $\mathcal{C}_x$ includes points in the corner areas with a functional value outside $\mathcal{C}_{y_m}$. Nevertheless, these regions are smaller as in the first test example. One can conclude that the degree of conservatism is not as high as before.

Last but not least, the solution obtained by the ellipse identification is discussed. In Fig. 4.3(d), it can be seen that the measurement set is not so well represented by $\mathcal{E}_{y_m}$ as in the previous test case. Especially for small values of y_1, the ellipse is not really close to the convex hull with the consequence that the uncertainty of y_m is overestimated by the MVEE. Furthermore, Fig. 4.3(d) shows that $\mathcal{E}_{y_s}$ coincides almost exactly with $\mathcal{E}_{y_m}$. The modeler could conclude that the obtained solution is a very precise quantification of the input uncertainty. However, the representation of the input space in Fig. 4.3(c) clarifies that this conclusion should be drawn with caution because a significant part of the ideal image of $\mathcal{E}_{y_m}$ is not captured by $\mathcal{E}_x$. Hence, the identified ellipse is an underestimation of the true input uncertainty. Basically, the same

phenomenon has been observed for the first test case. Again, the reason are the quadratic terms of the underlying function which lead to an image of $\mathcal{E}_x$ in the output space that has not a perfect elliptical shape.
To summarize, both the hyperrectangular and the hyperellipsoid identification show reasonable results. The rectangle identification provides a better solution for the second test case because it is a good approximation of the set of points $g^{-1}(\mathcal{C}_{\mathcal{Y}_\mathsf{m}}) = \{\mathbf{x} \mid g(\mathbf{x}) \in \mathcal{C}_{\mathcal{Y}_\mathsf{m}}\}$. In contrast, the hyperellipsoid approach is more convincing for the first case as $\mathcal{E}_x$ matches the blue region in Fig. 4.3(a) relatively well. However, this conclusion has to be discussed in view of the number of sample points contained in the measurement set $\mathcal{Y}_\mathsf{m}$ and the nonlinearity of the model. In case $\mathcal{Y}_\mathsf{m}$ comprises an extremely small number of samples, the two approaches would lead to similar results in both test cases because the rectangular/elliptical shape is not clearly identifiable in the output space. On the other hand, if $\mathcal{Y}_\mathsf{m}$ contains a lot of points the influence of the different distributions on the measurement sets would become clearer. But then, the question arises if a probability distribution fitting would be more reasonable instead of considering the uncertainty in terms of uncertainty sets.
As mentioned above, also the degree of nonlinearity of g plays an important role. If the underlying function was highly nonlinear, the mapping of uniformly distributed samples in the input space would lead to a measurement set in the output space which is not close to a rectangular shape. To conclude, the question of when to use which of the two approaches is strongly dependent on the characteristics of the model and the amount of data. Giving a general recommendation is therefore not meaningful.

4.1.3 Modified Hyperellipsoid Approach for Stochastic Moments

Now, the following scenario should be analyzed. For a given computational model, a comprehensive number of measurements has been executed to quantify the uncertainty of the output space. However, the modeler is not provided with the raw data itself but with the mean values $\boldsymbol{\mu}_y \in \mathbb{R}^{n_y}$ and variances $\boldsymbol{\sigma}_y^2 \in \mathbb{R}^{n_y}$ of the output quantities. As the measurement points themselves are not given, a probability distribution fitting is not possible without making further assumptions. The modeler has to deal with the question how to describe the uncertainty of the response quantities based on the given mean values and variances.
For this issue, it is referred to the Chebyshev inequality. In general, this inequality provides an upper bound for the probability that a scalar random variable ($n = 1$) deviates from its mean value more than a certain threshold. For the determination of the upper bound only the variance of the random variable must be given without knowing the underlying type of distribution:

$$P(|y - \mu_y| \geq k) < \frac{\sigma_y^2}{k^2}, \tag{4.18}$$

where $k \in \mathbb{R}$ describes the deviation of the random variable from its mean value. In [37], this concept was extended for multivariate random vectors. As in case of a scalar random variable,

the exact distribution is not required:

$$P\left((\mathbf{y}-\boldsymbol{\mu}_y)^{\mathsf{T}}\boldsymbol{\Sigma}_y^{-1}(\mathbf{y}-\boldsymbol{\mu}_y)<k\right)\geq 1-n_y/k, \tag{4.19}$$

where n_y is equal to the dimensionality of the random variable and $\boldsymbol{\Sigma}_y$ is the covariance matrix. The latter is a symmetric, positive semi-definite matrix that describes the dependency between the variables. It is given by

$$\boldsymbol{\Sigma}_y = \begin{pmatrix} \sigma_{y,11}^2 & \cdots & \sigma_{y,1n_y}^2 \\ \vdots & \ddots & \vdots \\ \sigma_{y,n_y1}^2 & \cdots & \sigma_{y,n_yn_y}^2 \end{pmatrix} \in \mathbb{R}^{n_y\times n_y}, \tag{4.20}$$

where $\sigma_{y,ij}^2\geq 0$ and $\sigma_y^2=(\sigma_{y,11}^2,\ldots,\sigma_{y,n_yn_y}^2)$ holds. From Eq. (4.19) one can derive the expression for an ellipsoid in the output space for a given k-factor. Though the measurement data set itself is not provided in this case, the equation is assigned with a subscript "m" to keep the notation introduced in Section 4.1.1

$$\mathcal{E}_{\mathcal{Y}_\mathsf{m}} = \left\{\mathbf{y}\in\mathbb{R}^{n_y} \mid \|\boldsymbol{\Sigma}_{\boldsymbol{Y}}^{-1/2}\mathbf{y}-\boldsymbol{\Sigma}_{\boldsymbol{Y}}^{-1/2}\boldsymbol{\mu}_y\|_2\leq\sqrt{k}\right\}. \tag{4.21}$$

The probability that a sample drawn from the random vector $\mathbf{Y}$ lies inside the ellipsoid is at least $(1-n_y/k)\cdot 100\%$. Thus, the covariance matrix $\boldsymbol{\Sigma}_y$ is related to the matrices $\boldsymbol{A}_\mathsf{m}$ and $\boldsymbol{b}_\mathsf{m}$ by

$$\boldsymbol{A}_\mathsf{m} = \frac{1}{\sqrt{k}}\boldsymbol{\Sigma}_{\boldsymbol{Y}}^{-1/2}, \text{ and} \tag{4.22}$$

$$\boldsymbol{b}_\mathsf{m} = -\frac{1}{\sqrt{k}}\boldsymbol{\Sigma}_{\boldsymbol{Y}}^{-1/2}\boldsymbol{\mu}_y. \tag{4.23}$$

The choice of the k-factor has to be made by the modeler. For a conservative approach, a high value for k should be taken which results in an ellipsoid with large main axes.
However, the derivation of $\boldsymbol{A}_\mathsf{m}$ and $\boldsymbol{b}_\mathsf{m}$ with the help of the Chebyshev inequality requires knowledge about all entries of the covariance matrix $\boldsymbol{\Sigma}_y$. If the correlation between the response quantities is known, the ellipsoid $\mathcal{E}_{\mathcal{Y}_\mathsf{m}}$ can be determined without any additional steps. In this case, the procedure of the inverse UQ is identical to the one introduced in Section 4.1.1. Otherwise, if only the variances are known, one has basically two options how to deal with this problem. The first one is to estimate the dependencies between the response quantities based on experience. The second one is to derive the covariance matrix from the computational model itself under further assumptions.

For the first case, $\boldsymbol{\Sigma}_y$ is assumed to be known and $\mathcal{E}_{\mathcal{Y}_\mathsf{m}}$ can be determined as if the covariance matrix was given from the beginning. As we assume that the input quantities are independent, the covariance matrix yields

$$\boldsymbol{\Sigma}_x = \begin{pmatrix} \sigma_{x,1}^2 & \dots & 0 \\ \vdots & \ddots & \vdots \\ 0 & \dots & \sigma_{x,n_x}^2 \end{pmatrix} \in \mathbb{R}^{n_x \times n_x}, \tag{4.24}$$

where $\sigma_{x,i}^2 \geq 0$, $i = 1, \dots, n_x$ can be collected in $\boldsymbol{\sigma}_x^2 \in \mathbb{R}^{n_x}$ because the off-diagonal entries are all zero.

Similar to the hyperellipsoid identification of a limited set of measurement points, the original model is replaced by a first-order approximation. The linearization of g enables to propagate uncertainties throughout the simplified model by the analytical expression

$$\boldsymbol{\Sigma}_y \approx \boldsymbol{J}_g \, \boldsymbol{\Sigma}_x \, \boldsymbol{J}_g^\mathsf{T}, \tag{4.25}$$

where $\boldsymbol{J}_g \in \mathbb{R}^{n_y \times n_x}$ is the Jacobian matrix. As a reminder, the Jacobian is evaluated at $\mathbf{x} = \boldsymbol{\mu}_x$ which is the image of $\boldsymbol{\mu}_y$ in the input space. Therefore, the corresponding vector $\boldsymbol{\mu}_x$ has to be determined beforehand. The remaining steps of the inverse UQ are identical to those presented in Section 4.1.1.

The task is more challenging, if one has no information about the dependency between the response quantities. Since we are only provided with the variances of the output quantities, the diagonal entries of $\boldsymbol{\Sigma}_y$ are known. So, we want to identify the entries of $\boldsymbol{\sigma}_x^2 \in \mathbb{R}^{n_x}$ such that the diagonal entries of $\boldsymbol{\Sigma}_y$ match with the corresponding entries of $\boldsymbol{J}_g \, \boldsymbol{\Sigma}_x \, \boldsymbol{J}_g^\mathsf{T}$. Thus, a system of linear equations can be set up which has n_x unknowns $\sigma_{x,1}^2, \dots, \sigma_{x,n_x}^2$ and n_y known parameters $\sigma_{y,1}^2, \dots, \sigma_{y,n_y}^2$, i.e.,

$$\underbrace{\begin{pmatrix} \sigma_{y,1}^2 \\ \vdots \\ \sigma_{y,n_y}^2 \end{pmatrix}}_{\boldsymbol{\sigma}_y^2} = \begin{pmatrix} \sum_{i=1}^{n_x} j_{g,1\,i}^2 \; \sigma_{x,i}^2 \\ \vdots \\ \sum_{i=1}^{n_x} j_{g,n_y\,i}^2 \; \sigma_{x,i}^2 \end{pmatrix} = \underbrace{\begin{pmatrix} j_{g,1\,1}^2 & \dots & j_{g,1\,n_x}^2 \\ \vdots & \ddots & \vdots \\ j_{g,n_y\,1}^2 & \dots & j_{g,n_y\,n_x}^2 \end{pmatrix}}_{=:\boldsymbol{J}_g^2} \underbrace{\begin{pmatrix} \sigma_{x,1}^2 \\ \vdots \\ \sigma_{x,n_x}^2 \end{pmatrix}}_{\boldsymbol{\sigma}_x^2}, \tag{4.26}$$

where $j_{g,ji}$ represents the elements of the Jacobian $\boldsymbol{J}_g$. A solution $\boldsymbol{\sigma}_x^2$ to an equation of the form of Eq. (4.26) exists in general if $\operatorname{rang} \boldsymbol{J}_g^2 = \operatorname{rang} (\boldsymbol{J}_g^2 \mid \boldsymbol{\sigma}_y^2)$. However, it is not necessarily

guaranteed then that $\sigma_{x,i}^2 \geq 0,\ i = 1\ldots,n_x,$ holds. If this is the case or if no solution to Eq. (4.26) exists, it is proposed to compute $\boldsymbol{\sigma}_x^2$ by solving the following optimization problem:

$$\begin{aligned} &\underset{\boldsymbol{\sigma}_x^2}{\text{minimize}} \quad \|\boldsymbol{J}_g^2 \boldsymbol{\sigma}_x^2 - \boldsymbol{\sigma}_y^2\|_2 \\ &\text{subject to} \quad \boldsymbol{\sigma}_x \geq 0, \end{aligned} \tag{4.27}$$

where $\boldsymbol{J}_g^2$ is the element-wise square matrix of the Jacobian. By substituting the resulting variances of the input quantities into Eq. (4.25), we obtain the covariance matrix $\boldsymbol{\Sigma}_y$ in the output space.

Once the entries of $\boldsymbol{\Sigma}_y$ are fully determined, the actual inverse UQ can be conducted. The remaining steps described in the following are rather similar to the approach from Section 4.1.1. At first, the modeler decides about the k-factor value to derive an equation for the measurement ellipsoid $\mathcal{E}_{\mathcal{Y}_\mathsf{m}}$ according to Eqs. (4.22) and (4.23). After that, the minimization problem can be set up which is equivalent to the formulation given in Eq. (4.13). Since we maintain the assumption that all input quantities are independent from each other, the goal is again to identify the vectors $\boldsymbol{a}_x \in \mathbb{R}^{n_x}$ and $\boldsymbol{b}_x \in \mathbb{R}^{n_x}$. The geometric dimensions of $\mathcal{E}_x$, i.e., the center point $\boldsymbol{c}_x$ and axis lengths $\boldsymbol{l}_x$, can be derived from Eq. (4.6). However, as the uncertainty on the response parameters is initially provided by stochastic moments, it is reasonable to represent the input variation in the same fashion. The transformation is given by

$$\boldsymbol{\mu}_x = -\boldsymbol{A}_x^{-1}\,\boldsymbol{b}_x, \text{ and} \tag{4.28}$$

$$\boldsymbol{\Sigma}_x = \boldsymbol{A}_x^{-2}/k. \tag{4.29}$$

The k-factor for the input space has to be chosen such that $P(\mathbf{X} \in \mathcal{E}_x) = P(\mathbf{Y} \in \mathcal{E}_{\mathcal{Y}_\mathsf{s}})$ holds. When comparing the expressions from above with Eq. (4.6), one can derive that the midpoint of $\mathcal{E}_x$ is equal to $\boldsymbol{\mu}_x$ and the axis lengths are derived by $\boldsymbol{l}_x = \boldsymbol{\sigma}_x\sqrt{k}$.

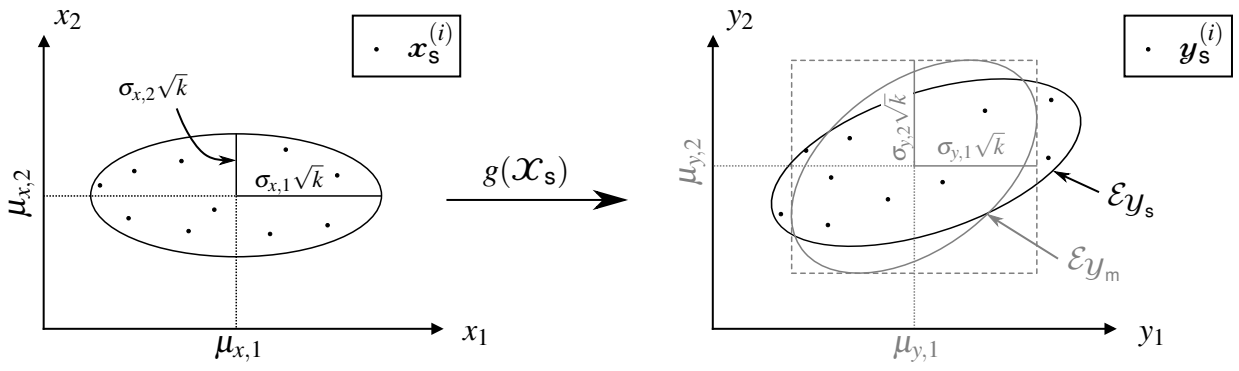

Figure 4.4 2D representation of the modified hyperellipsoid approach.

A graphical representation of the modified hyperellipsoid approach can be seen in Fig. 4.4. The ellipsis ($\mathcal{E}_x$) as well as its image on the output side ($\mathcal{E}_{y_s}$) are colored in black. The ellipsis $\mathcal{E}_{y_m}$ derived from the Chebyshev inequality and the known statistical moments has a gray color. It is completely enclosed by a rectangle which shares the same midpoint. The entries of the variance vector $\boldsymbol{\sigma}_y^2$ are directly related to half the side lengths.
To repeat, the core of the method consists in solving an optimization problem. Again, the modeler has several options how to find a solution. From the author's point of view, it is reasonable to start with a linearization of the computational model. Hence, Eq. (4.26) can be used to obtain an approximation for $\boldsymbol{\sigma}_x^2$. The corresponding ellipsoid $\tilde{\mathcal{E}}_x$ in the input space conforming to $\boldsymbol{\sigma}_x^2$ is given by

$$\tilde{\boldsymbol{A}}_x = \frac{1}{\sqrt{k}} \boldsymbol{\Sigma}_x^{-1/2}, \text{ and} \tag{4.30}$$

$$\tilde{\boldsymbol{b}}_x = -\frac{1}{\sqrt{k}} \boldsymbol{\Sigma}_x^{-1/2} \boldsymbol{\mu}_x. \tag{4.31}$$

It has to be kept in mind that the obtained solution $\tilde{\mathcal{E}}_x$ is derived from a first-order approximation of the computational model. If g is nearly or even perfectly linear for $\mathbf{x} \in \tilde{\mathcal{E}}_x$ the initial solution is close to the optimal one. Otherwise, the corresponding image of $\tilde{\mathcal{E}}_x$ in the output space deviates clearly from $\mathcal{E}_{y_m}$. The quality of the approximated solution can be measured by the metric introduced in Eq. (4.12).
At this point, the modeler has to make the decision if the matching accuracy between the ellipsoids is precise enough. If the initial solution is not close to the measurement ellipsoid, an adjacent optimization can improve the precision of the inverse UQ significantly.
In general, it is recommended to solve the optimization problem with a local strategy and use $\tilde{\mathcal{E}}_x$ as starting point. If there is still a significant mismatch between $\mathcal{E}_{y_m}$ and the final solution $\mathcal{E}_{y_s}$, one should think about a modification of the objective function by introducing weighting factors to its components. As an alternative, a global, population-based optimization method could be used instead. This type of optimization takes usually more time but is less prone to finding only a local optimum.
As the modified approach is applied to a real-world problem in Section 5.1, the analytical example from Section 4.1.2 is only discussed briefly. Basically, only the steps until the determination of $\mathcal{E}_{y_m}$ are different. Instead of deriving the ellipse from a measurement set, $\mathcal{E}_{y_m}$ is defined by a provided mean vector and covariance matrix. If we consider the case that the correlations between the response quantities are unknown, the dependencies must be computed by the first-order approximation of the function.

4.1.4 Post-Processing: Probability-Box Representation

The final step of the inverse hyperellipsoid framework is to find an appropriate representation which enables the simultaneous variation of all uncertain model input quantities. To clarify

this statement, we consider a model characterized by a set of uncertain inputs $\mathbf{X} \in \mathbb{R}^{n_x}$. Let us assume that a subset of $\mathbf{X}$ has been quantified from the hyperellipsoid approach whereas the remaining parameters are described by probability distributions. In order to conduct a sampling-based uncertainty propagation of all input parameters, an adequate representation for $\mathcal{E}_x$ is sought which can be combined with other UQ models.

The first logical step is to express $\mathcal{E}_x$ with the help of Chebyshev's inequality by its stochastic moments. As the inverse UQ process is based on a scarce data set, assigning a specific cumulative distribution function (CDF) to the parameter is hard to justify. Instead, a p-box representation is suitable to account for the epistemic uncertainty. In the following, various p-box concepts are discussed.

A consistent approach is to derive a distribution-free p-box from the Chebyshev inequality according to Eq. (3.39). On the one hand, a great benefit is that no additional assumptions have to be made because the bounding curves rely exclusively on the stochastic moments. On the other hand, the rigor-preserving property can lead to a conservative p-box representation. Hence, the wide envelopes may include CDFs with stochastic properties that differ significantly from the desired ones. This is problematic when it comes to the uncertainty propagation because the resulting lower and upper p-box bounds in the response space tend to overestimate the *true* variation.

This problem is illustrated in Figure 4.5. On the left side, an ellipsis $\mathcal{E}_x$ is shown which characterizes the uncertainty of a two-dimensional input space. The corresponding distribution-free p-boxes, derived from Chebyshev's inequality, are depicted by the solid black lines. On the right, the ellipsis $\mathcal{E}_{y_\mathrm{s}}$ is shown which is defined as the MVEE of the propagated set of sample points $\mathcal{Y}_\mathrm{s}$. Again, the associated p-boxes are aligned to the coordinate axes. The underlying analytical function is equal to the one in Eq. (4.16) from Section 4.1.2.

To compare, the distribution-free p-boxes are directly propagated throughout the model by the *slicing* algorithm. Therefore, they are discretized by a set of $n_\mathrm{s} = 16$ bivariate intervals of equal probability $\mathcal{X}_\mathrm{s}^I = \{\boldsymbol{x}_\mathrm{s}^{I,(1)}, \ldots, \boldsymbol{x}_\mathrm{s}^{I,(n_\mathrm{s})}\} \subset \mathbb{IR}^2$, also referred to as Dempster-Shafer structure. After that, the intervals are propagated separately through the model which yields a set of bivariate intervals $\mathcal{Y}_\mathrm{s}^I$. Finally, the lower and upper bounds in every dimension are used to define the p-box envelopes in the response space. An extensive discussion about this propagation concept can be found in Section 3.3. The intervals as well as the resulting p-boxes are depicted by gray lines in Fig. 4.5. One can see clearly, that the direct p-box propagation leads to even wider, i.e., more conservative envelopes.

Hence, the distribution-free p-box concept is a valid option to represent the uncertainty on the input space but the results from the uncertainty propagation should be treated with caution. Due to the extreme degree of conservatism, the propagated bounds are only useful for analyzing the extreme values.

In order to overcome this issue, distributional p-box representations can offer an alternative. In contrast to free p-boxes, the modeler can exclude undesired CDFs from the definition. How-

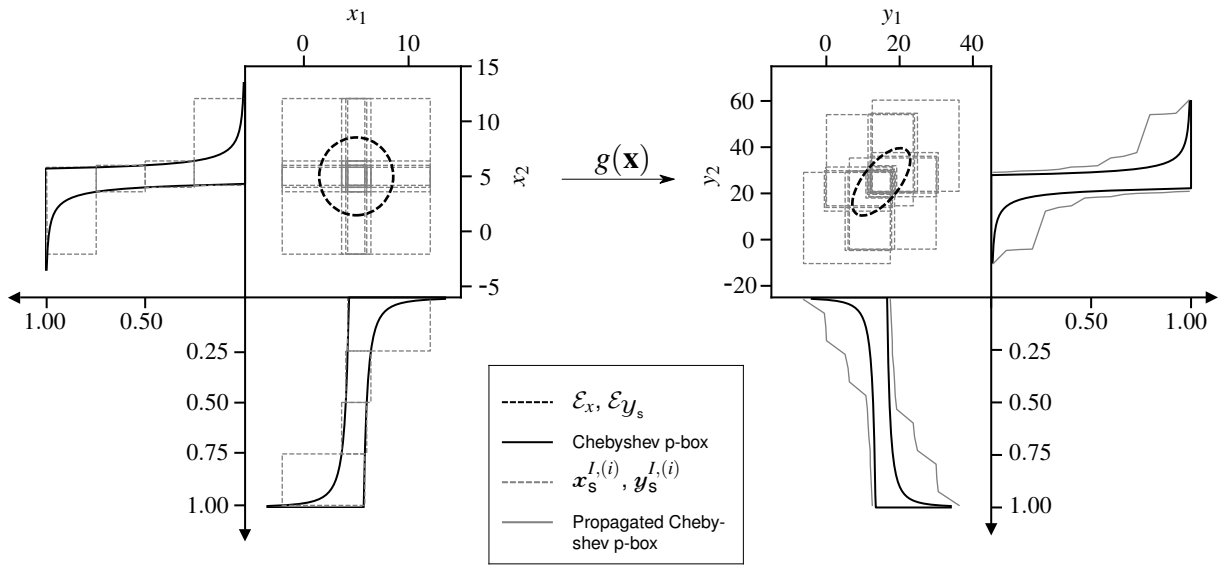

Figure 4.5 2D example: Comparison between distribution-free p-box propagation and ellipsis propagation.

ever, this type offers less flexibility as it requires the specification of a certain distribution type. As a reminder, the goal is to deduce a consistent p-box formulation from a known mean and variance. Here, two concepts are compared with each other that are based on different distribution types: beta and normal distribution.

The first one is a flexible distribution type which can take various shapes. In the standardized form, it is defined on the closed interval $[0,1]$ and described by the shape parameters $\boldsymbol{\Theta}_x = \{\alpha, \beta\} > 0$. Its CDF is given by

$$F_X(x|\alpha,\beta) = \frac{1}{B(\alpha,\beta)} \int_0^x t^{\alpha-1}(1-t)^{\beta-1} dt, \tag{4.32}$$

where $B(\alpha,\beta)$ denotes the beta function. The mean and standard deviation are directly related to the shape parameters and can be determined by the following analytical expressions:

$$\mu_x = \frac{\alpha}{\alpha+\beta}, \qquad \text{and} \qquad \sigma_x = \sqrt{\frac{\alpha\beta}{(\alpha+\beta)^2(\alpha+\beta+1)}}. \tag{4.33}$$

More detailed information about the characteristics of the beta distribution can be found in [8]. To define the beta distribution on a closed interval other than the standardized space, a linear transformation can be applied to Eq. (4.32) which shifts the bounds from $[0,1]$ to $[a,b]$. Accordingly, the transferred mean and standard deviation in the physical space are

$$\mu_x' = a + (b-a)\,\mu_x, \qquad \text{and} \qquad \sigma_x' = (b-a)\,\sigma_x. \tag{4.34}$$

The general idea is to use the beta distribution to generate an ensemble of CDFs which all share the same mean ($\mu_x^\star$) and standard deviation ($\sigma_x^\star$) obtained from the inverse UQ. Thereby,

a set of distribution functions with various shape parameters is defined on the unit space. After that, the lower and upper bound are determined according to

$$a = \mu_x^\star - \frac{\sigma_x^\star}{\sigma_x}\mu_x, \qquad \text{and} \qquad b = \mu_x^\star + \frac{\sigma_x^\star}{\sigma_x}(1-\mu_x), \tag{4.35}$$

such that every single CDF fulfills the desired stochastic properties, i.e., $\mu_x' = \mu_x^\star$ and $\sigma_x' = \sigma_x^\star$. In many cases, it is reasonable to introduce additional constraints which restrict the feasible space for α and β. For example, the modeler could define a lower bound for the standard deviation or restrict the range of other stochastic descriptors in the unit space. With the help of this preliminary setting, one can include experience-based information which has not been considered in the hyperellipsoid identification process.
In the following, we consider a test case where the known stochastic properties are given by $\mu_x^\star = 5.0$ and $\sigma_x^\star = 1.0$. In addition to that, the feasible space for α and β is restricted by the following assumptions:

- The probability density function (PDF) is unimodal $\rightarrow \alpha, \beta > 1.0$;
- The standard deviation in the unit space may not fall below $1/12$;
- The skewness of the distribution lies within $[-0.75, 0.75]$.

The second property ensures that the range of the physical space, i.e., the interval width of $[a,b]$, is not getting too large and thus does not contain meaningless values. In general, the threshold on the standard deviation can be derived from Eq. (4.34) if the modeler wants to restrict directly the physical space. The third and last criterion affects the skewness of the p-boxes such that only CDFs with $\gamma_x \in [-0.75, 0.75]$ are covered. As we apply a linear transformation, the skewness property is not affected by the transition from unit to physical space. In Fig. 4.6(b), the distributional p-box is depicted in gray and compared with the unconstrained Chebyshev p-box. Figure 4.6(c) represents the constraints from the listing above in the α/β-space.

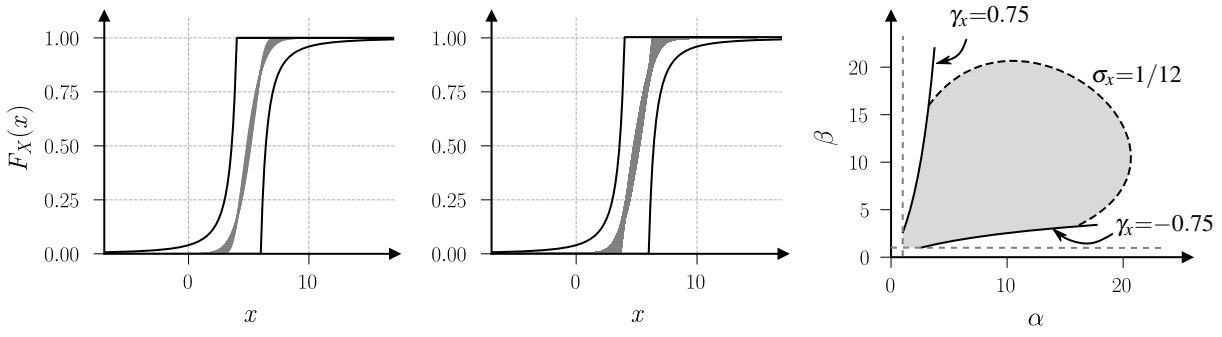

(a) Skew normal p-box. (b) Beta p-box. (c) Feasible $\alpha - \beta$ space.

Figure 4.6 Constructing a distributional p-box from a given mean and variance on the basis of a skew normal (left) and beta distribution (middle).

The enormous flexibility of the beta distribution can also be used to derive p-box representations for other constraints than the one discussed before. For example, one can introduce bounding conditions on other stochastic descriptors like mean, mode or median. A deeper discussion on this can be found in Section 5.2.1.
Since the beta distribution is defined on a closed interval, it is especially appropriate if X is characterized by a crisp minimum and maximum value. A drawback of this property is that it can lead to numerical problems for specific sampling strategies like the non-intrusive imprecise stochastic sampling (NISS) approach discussed in Section 4.3.1. As this concept is based on the importance sampling (IS), computing the ratio of different probability density function values is part of it, see Eq. (3.48). Here, the ratio can take the value zero if the two PDFs are modeled by beta distributions defined on different interval ranges. In [133], different concepts are analyzed to solve this issue, e.g., by adding further restrictions on the shape parameters or introducing artificial density values on the sample points outside the physical range.
As an alternative, a p-box could be derived on the basis of a normal distribution. The reason for choosing this type is related to the principle of maximum (information) entropy. To clarify this, we have to dive into the field of information theory. There, a fundamental principle is to quantify the information content of a random event $P(X = x_i) = p_i$ by

$$I(p_i) := -\log(p_i). \tag{4.36}$$

Basically, Eq. (4.36) states that rare events, i.e., p_i is small, provide more information than common ones. Based on that, the entropy $H(X)$ of a random variable X is formally defined as its expected information content. For a continuous random variable, the following expression holds [86]

$$H(X) := \int_{-\infty}^{+\infty} f_X(x) I(x) dx = -\int_{-\infty}^{+\infty} f_X(x) \log(f_X(x)) dx. \tag{4.37}$$

Coming back to the actual problem, the entropy concept can be used to determine a probability distribution for a given set of data about the random quantity. As implied by the term "principle of maximum entropy", the PDF with the highest entropy is chosen to characterize the random variable. In comparison to all other distributions, the maximum entropy distribution introduces the least amount of additional information and is therefore also the least biased one.
In case of knowing the first and second stochastic moment, the Gaussian distribution fulfills this criterion. Within the framework of distributional p-boxes, the probabilistic modeling approach can be extended easily by the skew normal distribution function which is a generalized form of the Gaussian. This distribution type is obtained by multiplying the Gaussian density function with a skewing function that includes an additional shape parameter. Hence, its PDF is conditional on three hyperparameters [14]

$$f_X(x \,|\, \zeta, \omega, \delta) = \frac{2}{\sqrt{2\pi}\,\omega}\, \mathrm{e}^{-\frac{(x-\zeta)^2}{2\omega^2}} \int_{-\infty}^{\delta\left(\frac{x-\zeta}{\omega}\right)} \frac{1}{\sqrt{2\pi}}\, \mathrm{e}^{-\frac{t^2}{2}} dt, \tag{4.38}$$

where $\zeta \in \mathbb{R}$ and $\omega \in \mathbb{R}^+$ denote the location and scale parameter, respectively. The third parameter $\delta \in \mathbb{R}$ is related to the skewness of the PDF. For the special case of $\delta = 0$, the skew normal distribution coincides with the Gaussian and the two remaining parameters are equivalent to mean and variance.
Figure 4.6(a) shows the skew normal p-box derived from the same boundary conditions on mean, variance and skewness range as the beta-distributional p-box illustrated to the right of it. The enclosed area is in both cases significantly smaller than the one from the Chebyshev p-box. The main reason lies in the rigor-preserving property of the free p-box. Besides from that, the Chebyshev inequality does not consider any limitation on the skewness parameter.
Analyzing the two gray-shaded distributional p-boxes with each other demonstrates the higher flexibility of the beta distribution. This impression is confirmed by measuring the area between the envelopes which is roughly $56\ \%$ higher than for the skew normal type.

In the previous paragraphs, various concepts have been analyzed to model the stochastic moments derived from the inverse UQ in an adequate manner. To summarize, the free p-box concept is beneficial to represent the epistemic uncertainty. Due to the high degree of conservatism, it is not useful for the uncertainty propagation because it leads to extremely wide bounds in the response.
For this reason, two different distributional p-box methods have been introduced. Here, the family of beta distributions provides great flexibility for constructing a p-box from the known mean and variance. A crucial downside is that any CDF is defined on a closed interval which can lead to numerical problems. Alternatively, a p-box can be derived from the skew normal distribution which is a logical approach from the entropy point of view. For a constant mean and variance, the p-box is described by only one uncertain hyperparameter. Compared to the beta distribution, this type is supported on the whole real line but it offers less flexibility with regard to the shape of the CDFs.
In general, one could think about using a different distribution type than the beta and skew normal. For example, if the focus of the uncertainty study is on determining the failure probability the chosen type should allow the modeler to control the tail thickness. The skew normal distribution is not appropriate in this case because its rate of decay is at least as high as the one from a Gaussian [15]. Instead, student's t-distribution would be a better basis because it is equipped with an extra tail weight parameter. Within the scope of this thesis, the overall goal is to optimize the design under robustness criteria. Hence, providing a p-box with a large tail flexibility is of minor importance.

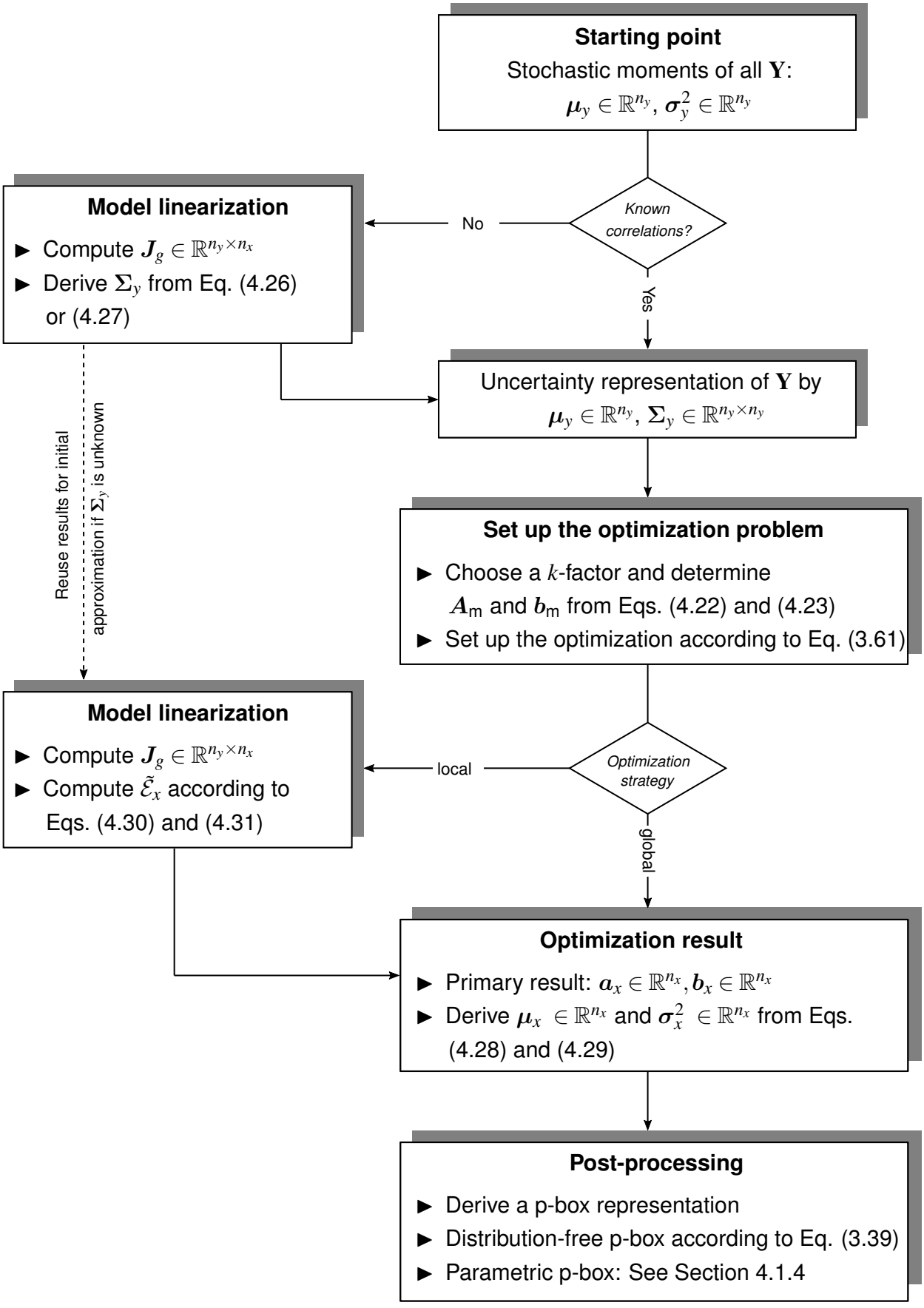

Figure 4.7 Flowchart of the modified hyperellipsoid approach.

4.2 Epistemic Variable Screening

Sensitivity studies play a decisive role for the identification of important parameters and enable to reduce the model complexity. Especially in context of industrial problems, which are usually characterized by a high-dimensional input space, reducing the number of parameters is essential. The review on state-of-the-art sensitivity methods in Section 3.5 has shown that a variety of concepts is available to identify the importance of aleatory uncertainty sources. However, for pure epistemic or hybrid uncertainties comparatively little literature is available.
Within the following paragraphs, a sensitivity concept for hybrid uncertainties is introduced which aims at separating important epistemic parameters from unimportant ones. The principal idea is to quantify the relevance of all uncertain hyperparameters which supposes that mixed aleatory-epistemic uncertainties are modeled by distributional p-boxes. If it turns out that a subset of hyperparameters has a negligible effect, the corresponding epistemic components are reduced to a constant value. This is illustrated by Fig. 4.8 which depicts a three-dimensional input space $\mathbf{X} \in \mathbb{R}^3$ on the left side where every $X \in \mathbf{X}$ is defined by a normal distribution with uncertain mean and variance, i.e., μ_x and σ_x are given as interval-valued parameters. Let us assume that the sensitivity study has revealed a low importance for $\mu_{x,1}$ and $\sigma_{x,1}$ as well as a minor contribution of $\mu_{x,2}$. This allows the modeler to apply a reduction in the epistemic space by setting the mentioned distributional parameters to their nominal values. Thus, X_1 is represented by a single CDF and the p-box representation of X_2 is solely based on the uncertain standard deviation whereas the representation of X_3 remains unchanged. The reduced input space is shown on the right side of Fig. 4.8.
A critical aspect of the sensitivity framework is to introduce an appropriate measure to quantify each parameter's importance. Unlike for aleatory uncertainties, no standardized metric,

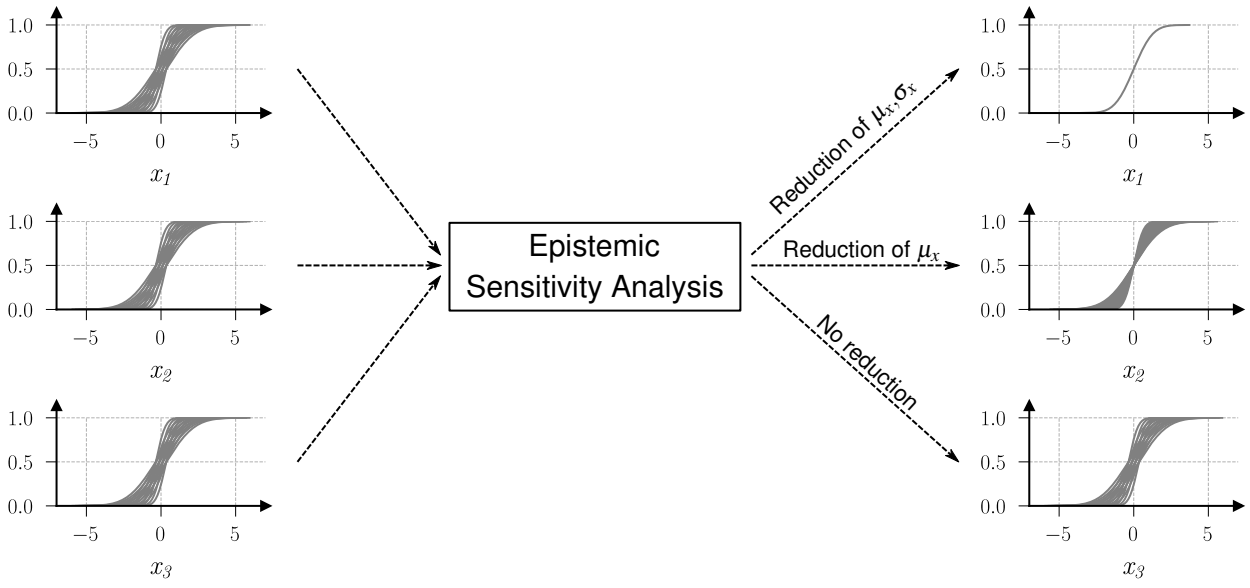

Figure 4.8 Graphical representation of the epistemic variable screening concept.

such as the decomposition of the response variance, has become established. Since we want to achieve a robust design in the end, the SA is based on the analysis of $\Delta\mu_y$ and $\Delta\sigma_y$, i.e., the epistemic uncertainty of the response mean and standard deviation. A hyperparameter $\theta_x^{(i)} \in \boldsymbol{\Theta}_x$ is declared as irreducible if it has a decisive contribution on $\Delta\mu_y$ or $\Delta\sigma_y$.

In the sequel, the epistemic SA concept is explained in a detailed way. At first, the Taylor series method is introduced as an alternative to sampling-based uncertainty propagation techniques. After that, we are dealing with the determination of the epistemic sensitivity indices. The approach we are pursuing here builds upon the one-at-a-time (OAT) sensitivity strategy, see Section 3.5.1. The basic OAT principle will be extended in order to evaluate interactions between the uncertain hyperparameters.

Taylor Series Method

Within the theoretical review provided in Section 3.3, a variety of uncertainty propagation methods has been exemplified which are all based on the calculation of sampling points. As an alternative, a Taylor-series-based uncertainty propagation can be used which is typically more time-efficient but offers therefore less accurate results [144].
Instead of computing functional values of random samples, partial derivatives of the input-output relationship must be derived. For the general multivariate case, i.e., $n_x > 1$, the Taylor series expansion is given by [47]

$$g(\mathbf{x}) = g(\mathbf{x}^\star) + \sum_{i=1}^{n_x} \frac{\partial g}{\partial x_i}\,(x_i - x_i^\star) + \frac{1}{2!}\sum_{i=1}^{n_x}\sum_{j=1}^{n_x} \frac{\partial^2 g}{\partial x_i\,\partial x_j}(x_i - x_i^\star)(x_j - x_j^\star) + \dots\,, \tag{4.39}$$

where $\mathbf{x}^\star$ denotes the expansion point. In many study cases, the function $g(\mathbf{x})$ is approximated by a first-order Taylor series expansion, i.e., the model is linearized at $\mathbf{x} = \mathbf{x}^\star$. Consequently, the uncertainty propagation becomes a cheap operation because only n_x partial derivatives must be evaluated. As outlined before, the gain in computation time happens in expense of the approximation accuracy, especially for a nonlinear behavior of $g(\mathbf{x})$.
For the epistemic variable screening, the potentially low accuracy is not the only reason why we prefer a higher-order series expansion. When applying the method to the industrial application case, the set of hyperparameters $\boldsymbol{\Theta}_x$ comprises uncertain mean values, standard deviations and skewness parameters. In order to take the latter into account, a Taylor series of at least third order is needed to approximate the response mean whereas a second-order series is sufficient for the standard deviation. As we assume independence between all input quantities

$$E\left[(x_i - x_i^\star)(x_j - x_j^\star)\right] = E\left[(x_i - x_i^\star)\right] E\left[(x_j - x_j^\star)\right] = 0 \qquad \text{for } i \neq j \tag{4.40}$$

holds which simplifies the expressions for μ_y and σ_y. The approximation of the first stochastic moment is obtained by applying the expectation operator to Eq. (4.39). Considering the simpli-

fications from the independence assumption, the approximation of the response mean yields for the third order Taylor series

$$\begin{aligned}\mu_y &\overset{3^{\text{rd}}}{\approx} E\left[g(\boldsymbol{\mu}_x)\right] + \frac{1}{2!}\sum_{i=1}^{n_x}\left(\frac{\partial^2 g}{\partial x_i^2}\right) E\left[(x_i - x_i^\star)^2\right] + \frac{1}{3!}\sum_{i=1}^{n_x}\left(\frac{\partial^3 g}{\partial x_i^3}\right) \underbrace{E\left[(x_i - x_i^\star)^3\right]}_{=\gamma_{x,i}\, E\left[(x_i - x_i^\star)^2\right]^{3/2}} \\ &= g(\boldsymbol{\mu}_x) + \sum_{i=1}^{n_x}\left\{\frac{1}{2}\left(\frac{\partial^2 g}{\partial x_i^2}\right)\sigma_{x,i}^2 + \frac{1}{6}\left(\frac{\partial^3 g}{\partial x_i^3}\right)\gamma_{x,i}\,\sigma_{x,i}^3\right\},\end{aligned} \tag{4.41}$$

where the expansion point $\mathbf{x}^\star$ should coincide with the input mean vector $\boldsymbol{\mu}_x$.
To repeat, a second-order Taylor series is sufficient to consider the input skewness for the variance propagation. In a first step, the approximate mean, given by the first two terms of Eq. (4.41), is subtracted from the second-order Taylor's series. Squaring and applying the expectation operator finally gives [110]

$$\begin{aligned}\sigma_y^2 &\overset{2^{\text{nd}}}{\approx} \sum_{i=1}^{n_x}\left\{\left(\frac{\partial g}{\partial x_i}\right)^2\sigma_{x,i}^2 + \gamma_{x,i}\left(\frac{\partial g}{\partial x_i}\right)\left(\frac{\partial^2 g}{\partial x_i^2}\right)\sigma_{x,i}^2\right\} + \sum_{i=1}^{n_x}\left\{\frac{\kappa_{x,i}-1}{4}\left(\frac{\partial^2 g}{\partial x_i^2}\right)^2\sigma_{x,i}^4\right\} \\ &+ \sum_{i=1}^{n_x}\sum_{j>i}^{n_x}\left\{\left(\frac{\partial^2 g}{\partial x_i \partial x_j}\right)^2\sigma_{x,i}^2\,\sigma_{x,j}^2\right\}.\end{aligned} \tag{4.42}$$

The computational effort of Eqs. (4.41) and (4.42) lies in the determination of the first, second and third partial derivative. Unless $g(\mathbf{x})$ is given by analytical expressions, the derivatives must be approximated by a finite difference method. When using the central difference scheme, one has to evaluate $g(\mathbf{x})$ at the expansion point and additionally [17]:

- for the single-variable derivatives at $x_i^\star \pm h$ and $x_i^\star \pm 2h$ in any dimension, and
- for the mixed second order term at $(x_i^\star + h, x_j^\star + h)$ and $(x_i^\star - h, x_j^\star - h)$ in any two-dimensional projection.

The total number of model evaluations for the Taylor-series approximation is given by

$$n_{\text{TS}} = 1 + 4n_x + n_x(n_x - 1). \tag{4.43}$$

Thus, the computational burden increases quadratically with respect to the number of dimensions. For applications with an extremely high-dimensional parameter set, even more efficient techniques are required like clustering methods for example [145].
Nevertheless, for moderate input space dimensions, the Taylor-series based propagation requires typically fewer model evaluations than sampling-based methods. The reason for this is that the latter group suffers more from the curse of dimensionality. As the number of dimensions grows, also the amount of sampling points n_{s} has to be adapted to keep up the

approximation quality. In case of a crude Monte Carlo (MC) sampling, even an exponential increase can be required [168]. It is important to understand that the curse of dimensionality issue is not related to the MC convergence rate itself. The latter is independent from n_x, see Section 3.3.

Epistemic Sensitivity Indices

As mentioned before, the epistemic SA concept is an extension of the OAT procedure. In short, the original strategy varies every single uncertain parameter individually around its nominal value while keeping the remaining ones at their fixed positions. The impact of each parameter is measured by the change of the model response. One decisive property is that no distribution function is required which matches with the interval characteristic of the hyperparameter definition. In order to apply this method for an epistemic parameter screening, the following modifications have been undertaken.
In its original configuration, the OAT belongs to the group of local SA techniques because the parameters of interest are varied by making small changes to the nominal value. Here, we want to consider the whole hyperparameter space $[\underline{\theta}_x^{(i)}, \overline{\theta}_x^{(i)}]$ which is why $\theta_x^{(i)}$ is varied in a comparatively wide range. This changes the character from a local to a global one.
Now, the goal becomes to identify those points within $[\underline{\theta}_x^{(i)}, \overline{\theta}_x^{(i)}]$ which correspond to the extreme values in the output space. Hence, we seek for the minimum and maximum value of μ_y and σ_y. After that, the FOI (first-order index) can be computed for the hyperparameter under investigation, i.e., $\theta_x^{(i)}$, with regard to mean and standard deviation according to

$$\mathrm{FOI}_{\mu}^{(i)} = \frac{\overline{\mu}_y - \underline{\mu}_y}{\mu_y(\theta_x^{\star(i)})} = \frac{\Delta\mu_y}{\mu_y^{\star}}, \qquad \text{and} \qquad \mathrm{FOI}_{\sigma}^{(i)} = \frac{\overline{\sigma}_y - \underline{\sigma}_y}{\sigma_y(\theta_x^{\star(i)})} = \frac{\Delta\sigma_y}{\sigma_y^{\star}}. \tag{4.44}$$

The numerator of the two sensitivity indices expresses the interval width of response mean and standard deviation. The most general way for the determination of $\Delta\mu_y$ and $\Delta\sigma_y$ is to solve four optimization problems given by

$$\underset{\theta_x^{(i)} \in [\underline{\theta}_x^{(i)}, \overline{\theta}_x^{(i)}]}{\text{minimize}} \begin{cases} \mu_y(\theta_x^{(i)}) \\ \sigma_y(\theta_x^{(i)}) \end{cases}, \qquad \text{and} \qquad \underset{\theta_x^{(i)} \in [\underline{\theta}_x^{(i)}, \overline{\theta}_x^{(i)}]}{\text{maximize}} \begin{cases} \mu_y(\theta_x^{(i)}) \\ \sigma_y(\theta_x^{(i)}) \end{cases}. \tag{4.45}$$

If there is a monotonic relationship between $\theta_x^{(i)}$ and the stochastic moments, Eq. (4.45) can be replaced by two model evaluations at $\underline{\theta}_x^{(i)}$ and $\overline{\theta}_x^{(i)}$. For the general non-monotonic case, the optimization procedure can become extremely costly in high dimensions. To counteract this issue, we propose to define a set of equidistant grid points within $[\underline{\theta}_x^{(i)}, \overline{\theta}_x^{(i)}]$ at which an uncertainty propagation must be conducted to determine μ_y and σ_y. The lower and upper bounds are simply approximated by their minimum and maximum value. The number of grid points should be chosen with respect to the available amount of time and required precision.

An alternative to improve the efficiency is to introduce two surrogate models which approximate the relationship between stochastic moments and the hyperparameter $\theta_x^{(i)}$. Thus, a computationally cheap meta-model can be used for the optimization.
Once $\Delta\mu_y$ and $\Delta\sigma_y$ are known, the interval ranges are divided by $\mu_y^\star$ and $\sigma_y^\star$, i.e., the stochastic moments when all hyperparameters take their nominal values. This step is necessary to ensure a normalized sensitivity measure which is independent from the measurement units.

With the help of a FOI, the modeler is able to quantify the importance of every individual uncertain hyperparameter. A small value for FOI_μ and FOI_σ is a first indication for a negligible impact. Nevertheless, this conclusion must be treated with caution because the indices from Eq. (4.44) do not take any interactions into account. For this reason, the OAT approach is extended by a sensitivity measure, denoted as SOI (second-order index), which analyzes the pairwise interactive effects between two hyperparameters. The computation rule for a SOI is equivalent with the one from the first-order effects with the difference that two instead of one hyperparameters are varied simultaneously within their defined interval ranges. The SOI with regard to the response mean is derived according to

$$\begin{aligned} \mathrm{SOI}_\mu^{(i,j)} = \frac{\overline{\mu}_y - \underline{\mu}_y}{\mu_y^\star} \quad \text{with} \quad & \underline{\mu}_y = \min\left\{\mu_y(\theta_x^{(i)}, \theta_x^{(j)})\right\} \\ & \overline{\mu}_y = \max\left\{\mu_y(\theta_x^{(i)}, \theta_x^{(j)})\right\} \\ \text{s.t.} \quad & \left\{\theta_x^{(i)}, \theta_x^{(j)}\right\} \in \left[\underline{\theta}_x^{(i)}, \overline{\theta}_x^{(i)}\right] \times \left[\underline{\theta}_x^{(j)}, \overline{\theta}_x^{(j)}\right]. \end{aligned} \tag{4.46}$$

The metric for SOI_σ is similar to the one from above and therefore not stated here. A key aspect is the determination of the extreme values. Again, the straightforward approach is to set up an optimization procedure which yields the most accurate result if the optimizer identifies the global minima and maxima. In terms of time efficiency, the optimization can be replaced by evaluating the stochastic moments at a finite set of grid points. For a monotonous model relation, only the corner points are of relevance.

The latter is also used for the application case in Sec. 5.2.2 which is why the grid generation is discussed here in greater detail. Figure 4.9 shows two examples of a two-dimensional hyperparameter space. In Fig. 4.9(a), both $\theta_x^{(i)}$ and $\theta_x^{(j)}$ correspond to a mean value. In this case, five equidistantly distributed points (●) have been generated along the main axes which are the basis for the first-order sensitivity indices. In addition, another eight grid points (●) have been added to quantify the interactions, four of which are placed at the corners. The remaining ones are positioned at the quarter points, i.e., at

$$\theta_x^{\star(i)} \pm 1/4\,(\overline{\theta}_x^{(i)} - \underline{\theta}_x^{(i)}) \quad \text{and} \quad \theta_x^{\star(j)} \pm 1/4\,(\overline{\theta}_x^{(j)} - \underline{\theta}_x^{(j)}). \tag{4.47}$$

Hence, the proposed deterministic design of experiments (DoE) is not a full factorial design.

The reason for this is that each grid point is associated with n_{TS} model evaluations, see Eq. (4.43), because it represents an expansion point for the Taylor-series uncertainty propagation. In view of the high-dimensional application case, a full factorial design would not be affordable.

In contrast, Fig. 4.9(b) illustrates the combination between mean and standard deviation. The black dots along the abscissa model the discretization of the uncertain mean value whereas the black crosses (✖) on the ordinate stand for the grid points of the standard deviation. The change in the marking reflects the difference in the computational effort for the uncertainty propagation. If only the standard deviation is varied, no additional evaluations of $g(\mathbf{x})$ are required. Instead, the grid point with the same mean value is chosen to conduct the uncertainty propagation with the help of Eqs. (4.41) and (4.42). Thus, only the value of the standard deviation has to be exchanged in the analytical expressions to determine μ_y and σ_y. The same holds if $\theta_x^{(i)}$ represents a skewness parameter. The negligible amount of computational effort enables to generate a full factorial DoE. Accordingly, the grid points for the SOIs are marked by gray crosses instead of dots, see Fig. 4.9(b).

The screening technique introduced so far can be extended easily for higher order effects which improves the informative value of the study. The final decision whether to reduce an uncertain hyperparameter to a constant is made by comparing all related first- and second-order indices with predefined thresholds. Their precise values are strongly dependent on the application case as well as the modeler's subjective assessment. A discussion can be found within Section 5.2.2.

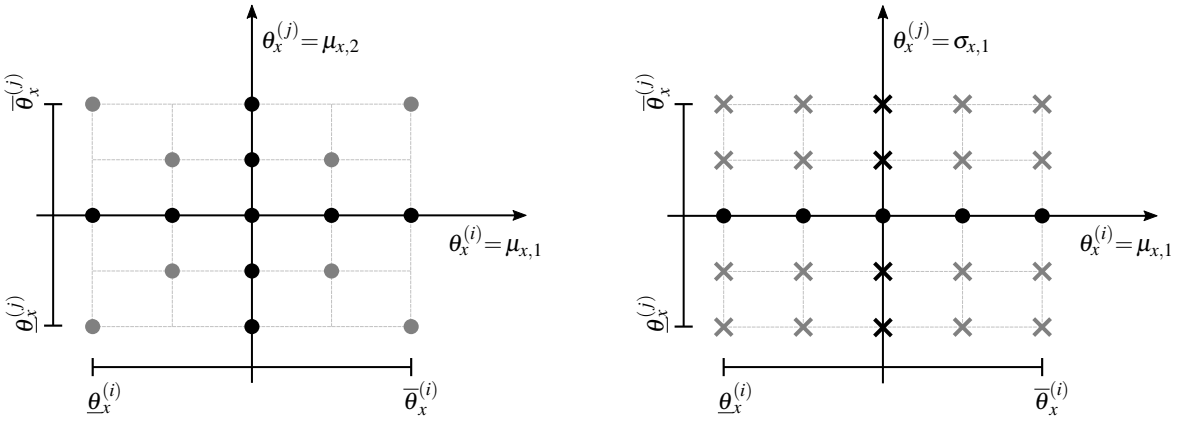

(a) Mean-mean combination.

(b) Mean-standard deviation combination.

Figure 4.9 Arrangement of the grid points in the epistemic space in case of two mean values (left) and a combination between mean and standard deviation (right).

4.3 Robust Design Optimization for Hybrid Uncertainties

The RDO is the last component of the uncertainty study which builds upon the results from the previous studies. Even though the epistemic variable screening can make a significant contribution to reduce the model complexity, efficiency is still playing a key role for the RDO because the considerations of hybrid uncertainties is, compared to a setup with only aleatory parameters, more time-consuming. To counteract this issue, we make use of the so-called NISS framework with the purpose to break the standard double-loop MC sampling for hybrid uncertainties. The sampling scheme is introduced in Section 4.3.1 followed by an analytical test case in Section 4.3.2. The illustrative example is used to discuss different RDO formulations as well as the limitations of NISS. Moreover, some ideas are shown how to improve the sampling procedure gathered in the multi-point non-intrusive imprecise stochastic sampling (MNISS) concept, an extended version of the original NISS.

4.3.1 Non-Intrusive Imprecise Stochastic Sampling

The next paragraphs provide an overview over the NISS strategy developed by the authors of [165, 174, 175]. As indicated by the name, it is a non-intrusive uncertainty propagation technique and thus applicable to any kind of black-box model. In principle, NISS is a composition of two methods, namely EMCS (extended Monte Carlo sampling) and high-dimensional model representation (HDMR), both of which are explained in the following.

Extended Monte Carlo Sampling

The first component, i.e., the EMCS, has been introduced by [173] and is strongly related to the concept of IS, see Section 3.3. As a starting point, we assume that the input space is described by a parameterized p-box formulation given by $f_{\mathbf{X}}(\mathbf{x}|\boldsymbol{\Theta}_x^I)$. As the set of distributional parameters are interval-valued quantities, the probabilistic response depends on the realization $\boldsymbol{\Theta}_x \in \boldsymbol{\Theta}_x^I$. Here, we illustrate the uncertainty propagation by the evaluation of the response mean which is a function of $\boldsymbol{\Theta}_x$:

$$\mu_y(\boldsymbol{\Theta}_x) = \int_{-\infty}^{\infty} g(\mathbf{x}) f_{\mathbf{X}}(\mathbf{x}|\boldsymbol{\Theta}_x) d\mathbf{x}. \tag{4.48}$$

The idea of the EMCS is to create only one set of sample points from a specific PDF denoted by $f_{\mathbf{X}}(\mathbf{x}|\boldsymbol{\Theta}_x^\star)$. In order to determine the mean value for $\boldsymbol{\Theta}_x \neq \boldsymbol{\Theta}_x^\star$, Eq. (4.48) is extended according to

$$\mu_y(\boldsymbol{\Theta}_x) = \int_{-\infty}^{\infty} g(\mathbf{x}) \frac{f_{\mathbf{X}}(\mathbf{x}|\boldsymbol{\Theta}_x)}{f_{\mathbf{X}}(\mathbf{x}|\boldsymbol{\Theta}_x^\star)} f_{\mathbf{X}}(\mathbf{x}|\boldsymbol{\Theta}_x^\star)\, d\mathbf{x}. \tag{4.49}$$

This formulation shows strong similarities with the IS concept where the proposal distribution, i.e., the PDF from which the samples are drawn, is also different from the desired one to in-

crease the convergence rate of the numerical integration. The main difference between IS and EMCS is that the latter provides an approximate relation between uncertain hyperparameters and a stochastic response quantity of interest (QoI) whereas the first is a pure probabilistic method that aims at determining a stochastic quantity in an efficient way. The numerical approximation of Eq. (4.49) for a number of n_s samples drawn from $f_\mathbf{X}(\mathbf{x}|\boldsymbol{\Theta}_x^\star)$ yields

$$\mu_y(\boldsymbol{\Theta}_x) \approx \frac{1}{n_\mathrm{s}} \sum_{i=1}^{n_\mathrm{s}} g(\boldsymbol{x}_\mathrm{s}^{(i)}) \frac{f_\mathbf{X}(\boldsymbol{x}_\mathrm{s}^{(i)}|\boldsymbol{\Theta}_x)}{f_\mathbf{X}(\boldsymbol{x}_\mathrm{s}^{(i)}|\boldsymbol{\Theta}_x^\star)}. \tag{4.50}$$

Within the framework of NISS, the procedure introduced so far is specified as *local* EMCS because it performs better the closer the realizations of $\boldsymbol{\Theta}_x$ are to $\boldsymbol{\Theta}_x^\star$. To achieve a more balanced performance over the design space, an alternative technique has been discussed in [174] where every single sample is drawn from a different distribution. The *global* version of the EMCS requires a random sampling in the hyperparameter space which is usually based on a multivariate uniform distribution. From the author's point of view, the interval characteristics of $\boldsymbol{\Theta}_x^I$ is affected hereby which is why the *local* EMCS is more unbiased in this sense. In the following, we therefore stay with the *local* version of NISS.
Still, the question remains how to determine the value of $\boldsymbol{\Theta}_x^\star$ to enable a proper approximation quality for any $\boldsymbol{\Theta}_x \in \boldsymbol{\Theta}_x^I$. The authors of [173] propose to define $\boldsymbol{\Theta}_x^\star$ for a normal distribution with uncertain mean and standard deviation according to

$$\begin{aligned} \underline{\mu}_x - a\,\overline{\sigma}_x &= \mu_x^\star - a\,\mu_x^\star, \text{ and} \\ \overline{\mu}_x + a\,\overline{\sigma}_x &= \mu_x^\star + a\,\mu_x^\star, \end{aligned} \tag{4.51}$$

where the parameter a is usually set to three. These criteria ensure a sufficient sample coverage of the whole design space. The two criteria can also be used for non-Gaussian types.
One of the great benefits of the EMCS is that the uncertainty propagation relies only on one set of sample points. Furthermore, it offers a great flexibility because it does not establish any requirements on the distribution type. However, the EMCS shows a bad performance in high dimensions which results in a large variance of the estimator [174]. Out of this reason, the EMCS is combined with a HDMR which is reviewed in the subsequent paragraph.

High-Dimensional Model Representation

The underlying idea of the HDMR is to represent a functional relation, such as the input-output mapping $g(\mathbf{x})$, by a decomposition into a finite number of component functions

$$g(\mathbf{x}) = g_0 + \sum_{i=1}^{n_x} g_i(x_i) + \sum_{i=1}^{n_x} \sum_{j>i}^{n_x} g_{ij}(x_i, x_j) + \ldots + g_{1,\ldots,n_x}(x_1, \ldots, x_{n_x}). \tag{4.52}$$

The first term, i.e., g_0, expresses the mean value of $g(\mathbf{x})$ and g_i encompasses the contribution of the i-th variable. All higher-order terms represent correlated effects between the corre-

sponding variables. In most of the application cases, a second-order HDMR gives a sufficient accuracy while simultaneously reducing the computational burden significantly [102].
For the determination of the component functions, various approaches are available in literature which lead to different decomposition schemes. A common feature of every HDMR expansion is that all component functions are mutually orthogonal to each other. Within the scope of Section 3.5.1, the ANOVA-HDMR has already been discussed which is the basis for the determination of the Sobol indices. In context of NISS, the (*local*) EMCS is enriched by the so-called cut-HDMR technique. Similar to a Taylor series, an expansion point $\boldsymbol{x}^\star$ is chosen close to the region of interest. The first component functions up to the second order of the cut-HDMR are given by

$$\begin{aligned} g_0 &= g(\boldsymbol{x}^\star), \\ g_i(x_i) &= g(x_i, \boldsymbol{x}^\star_{\sim i}) - g_0, \text{ and} \\ g_{ij}(x_i, x_j) &= g(x_i, x_j, \boldsymbol{x}^\star_{\sim ij}) - g_i - g_j - g_0, \end{aligned} \tag{4.53}$$

where $\boldsymbol{x}_{\sim ij}$ contains all coordinates except the i-th and j-th one. Comparing the above terms with the Taylor series expansion shows that the first term, i.e., g_0, is equal for both concepts whereas the second HDMR component functions comprise all Taylor series terms which depend exclusively on x_i. Consequently, g_i is not limited to a linear dependency on x_i. The remaining higher-order components can be interpreted in the same fashion.

The last step for the derivation of NISS is to combine the cut-HDMR concept with the EMCS. Hence, the decomposition from Eq. (4.52) is directly transferred to the functional relationship of Eq. (4.49). This leads to the following expansion of $\mu_y(\boldsymbol{\Theta}_x)$ with respect to the n_Θ-variate hyperparameter space

$$\mu_y(\boldsymbol{\Theta}_x) = \mu_{y,0} + \sum_{i=1}^{n_\Theta} \mu_{y,i} + \sum_{i=1}^{n_\Theta} \sum_{j>i}^{n_\Theta} \mu_{y,ij} + \ldots + \mu_{y,\{1,\ldots,n_\Theta\}}. \tag{4.54}$$

Again, the first three component functions are of major interest for us. Applying the cut-HDMR technique from Eq. (4.53) and extending the formulation of $\mu_{y,i}$ and $\mu_{y,ij}$ by $f_{\mathbf{X}}(\mathbf{x}|\boldsymbol{\Theta}^\star_x)$ in the numerator and denominator leads to

$$\begin{aligned} \mu_{y,0}(\boldsymbol{\Theta}^\star_x) &= \int_{-\infty}^{\infty} g(\mathbf{x}) f_{\mathbf{X}}(\mathbf{x}|\boldsymbol{\Theta}^\star_x)\, d\mathbf{x}, \\ \mu_{y,i}(\theta^{(i)}_x) &= \int_{-\infty}^{\infty} g(\mathbf{x}) \frac{f_{\mathbf{X}}(\mathbf{x}|\theta^{(i)}_x, \boldsymbol{\Theta}^{\star(\sim i)}_x)}{f_{\mathbf{X}}(\mathbf{x}|\boldsymbol{\Theta}^\star_x)} f_{\mathbf{X}}(\mathbf{x}|\boldsymbol{\Theta}^\star_x)\, d\mathbf{x} - \mu_{y,0}, \text{ and} \\ \mu_{y,ij}(\boldsymbol{\Theta}^{(ij)}_x) &= \int_{-\infty}^{\infty} g(\mathbf{x}) \frac{f_{\mathbf{X}}(\mathbf{x}|\boldsymbol{\Theta}^{(ij)}_x, \boldsymbol{\Theta}^{\star(\sim ij)}_x)}{f_{\mathbf{X}}(\mathbf{x}|\boldsymbol{\Theta}^\star_x)} f_{\mathbf{X}}(\mathbf{x}|\boldsymbol{\Theta}^\star_x)\, d\mathbf{x} - \mu_{y,i} - \mu_{y,j} - \mu_{y,0}. \end{aligned} \tag{4.55}$$

The term $\boldsymbol{\Theta}_x^{\star(-ij)}$ denotes a set containing all hyperparameters except the one at the i- th and j-th position, i.e., $\boldsymbol{\Theta}_x^{\star(-ij)} = \{\theta_x^{\star(1)}, \ldots, \theta_x^{\star(i-1)}, \theta_x^{\star(i+1)}, \ldots, \theta_x^{\star(j-1)}, \theta_x^{\star(j+1)}, \ldots, \theta_x^{\star(n_\Theta)}\}$. Due to the HDMR, the EMCS becomes suitable for high-dimensional problems because the numerator and denominator of the fractions in Eq. (4.55) differ by not more than two distributional parameters. The component functions take the value zero if at least one of the variables is set to its expansion point value, i.e., $\theta_x^{(i)} = \theta_x^{\star(i)}$. The vanishing property induces the mutual orthogonality between the component functions defined by [101]

$$\mu_{y,\{i_1,\ldots,i_\mathsf{a}\}}\, \mu_{y,\{j_1,\ldots,j_\mathsf{b}\}}\Big|_{\theta_x^{(i_\mathsf{u})}=\theta_x^{\star(i_\mathsf{u})}} = 0 \qquad \text{for } i_\mathsf{u} \in \{i_1,\ldots,i_\mathsf{a}\} \cup \{j_1,\ldots,j_\mathsf{b}\}. \tag{4.56}$$

Finally, the numerical approximation for the three terms in Eq. (4.55) is derived. For a set of n_s independently and identically distributed (i.i.d.) sample points drawn from $f_\mathbf{X}(\mathbf{x}|\boldsymbol{\Theta}_x^\star)$, the cut-HDMR components yield

$$\begin{aligned}
\mu_{y,0} &\approx \frac{1}{n_\mathsf{s}} \sum_{k=1}^{n_\mathsf{s}} g(\boldsymbol{x}_\mathsf{s}^{(k)}), \\
\mu_{y,i}(\theta_x^{(i)}) &\approx \frac{1}{n_\mathsf{s}} \sum_{k=1}^{n_\mathsf{s}} g(\boldsymbol{x}_\mathsf{s}^{(k)})\, r_\mathsf{cut}^{(i)}(\boldsymbol{x}_\mathsf{s}^{(k)}|\boldsymbol{\theta}_x^{(i)}), \text{ and} \\
\mu_{y,ij}(\boldsymbol{\Theta}_x^{(ij)}) &\approx \frac{1}{n_\mathsf{s}} \sum_{k=1}^{n_\mathsf{s}} g(\boldsymbol{x}_\mathsf{s}^{(k)})\, r_\mathsf{cut}^{(ij)}(\boldsymbol{x}_\mathsf{s}^{(k)}|\boldsymbol{\Theta}_x^{(ij)}),
\end{aligned} \tag{4.57}$$

where the expressions of $r_\mathsf{cut}^{(i)}$ and $r_\mathsf{cut}^{(ij)}$ are given by

$$r_\mathsf{cut}^{(i)}(\boldsymbol{x}_\mathsf{s}^{(k)}|\boldsymbol{\theta}_x^{(i)}) = \left(\frac{f_\mathbf{X}(\boldsymbol{x}_\mathsf{s}^{(k)}|\theta_x^{(i)}, \boldsymbol{\Theta}_x^{\star(-i)})}{f_\mathbf{X}(\boldsymbol{x}_\mathsf{s}^{(k)}|\boldsymbol{\Theta}_x^\star)} - 1 \right), \text{ and}$$

$$r_\mathsf{cut}^{(ij)}(\boldsymbol{x}_\mathsf{s}^{(k)}|\boldsymbol{\Theta}_x^{(ij)}) = \left(\frac{f_\mathbf{X}(\boldsymbol{x}_\mathsf{s}^{(k)}|\boldsymbol{\Theta}_x^{(ij)}, \boldsymbol{\Theta}_x^{\star(-ij)})}{f_\mathbf{X}(\boldsymbol{x}_\mathsf{s}^{(k)}|\boldsymbol{\Theta}_x^\star)} - \frac{f_\mathbf{X}(\boldsymbol{x}_\mathsf{s}^{(k)}|\theta_x^{(i)}, \boldsymbol{\Theta}_x^{\star(-i)})}{f_\mathbf{X}(\boldsymbol{x}_\mathsf{s}^{(k)}|\boldsymbol{\Theta}_x^\star)} - \frac{f_\mathbf{X}(\boldsymbol{x}_\mathsf{s}^{(k)}|\theta_x^{(j)}, \boldsymbol{\Theta}_x^{\star(-j)})}{f_\mathbf{X}(\boldsymbol{x}_\mathsf{s}^{(k)}|\boldsymbol{\Theta}_x^\star)} + 1.0 \right). \tag{4.58}$$

From the above equations it can be seen that both, the vanishing as well as the orthogonal property are fulfilled by the approximate component functions. Moreover, it becomes clear that the only computational cost of NISS is to evaluate the functional values of the sample points. The determination of $r_\mathsf{cut}^{(i)}(\boldsymbol{x}_\mathsf{s}^{(k)}|\boldsymbol{\Theta}_x^{(i)})$ and $r_\mathsf{cut}^{(ij)}(\boldsymbol{x}_\mathsf{s}^{(k)}|\boldsymbol{\Theta}_x^{(ij)})$ has basically no contribution because it just involves the evaluation of PDF values and some mathematical operations.

So far, the NISS procedure has been demonstrated for analyzing the response mean function but other stochastic descriptors can be computed in a similar fashion. Within this thesis, the variance σ_y^2 is the second relevant QoI for the robustness assessment. For the sake of

completeness, the numerical approximation of the HDMR expansion is provided for the first three components by

$$\sigma_{y,0}^2 \approx \frac{1}{n_\mathsf{s}} \sum_{i=1}^{n_\mathsf{s}} \left(g(\boldsymbol{x}_\mathsf{s}^{(k)}) - \mu_{y,0} \right)^2,$$

$$\sigma_{y,i}^2(\theta_x^{(i)}) \approx \frac{1}{n_\mathsf{s}} \sum_{k=1}^{n_\mathsf{s}} \left(g(\boldsymbol{x}_\mathsf{s}^{(k)}) - \mu_{y,i} - \mu_{y,0} \right)^2 r_\mathsf{cut}^{(i)}(\boldsymbol{x}_\mathsf{s}^{(k)} | \boldsymbol{\Theta}_x^{(i)}), \text{ and} \tag{4.59}$$

$$\sigma_{y,i}^2(\boldsymbol{\Theta}_x^{(ij)}) \approx \frac{1}{n_\mathsf{s}} \sum_{k=1}^{n_\mathsf{s}} \left(g(\boldsymbol{x}_\mathsf{s}^{(k)}) - \mu_{y,ij} - \mu_{y,i} - \mu_{y,j} - \mu_{y,0} \right)^2 r_\mathsf{cut}^{(ij)}(\boldsymbol{x}_\mathsf{s}^{(k)} | \boldsymbol{\Theta}_x^{(ij)}).$$

The expressions from Eqs. (4.57) and (4.59) are unbiased which means that the expected values of the estimators are equal to the true values. To assess the accuracy for a specific number of sample points, confidence intervals can be derived from the variance of the estimators. The formula for each of the component functions can be found in Appendix B.1.

4.3.2 Analytical Test Case

To illustrate the NISS-framework for RDO problems more in detail, a two-dimensional test case is set up. In the first subsection, the characteristics of the test function are discussed. This is followed by a paragraph about different strategies to formulate a robust design optimization under hybrid uncertainties. Last but not least, the NISS strategy is applied to the analytical example to evaluate its performance. It will be seen that some modifications of the classical NISS are necessary to improve the accuracy.

Test Case Setup

Let us consider an analytical model which maps a two-dimensional input space to a scalar response quantity. The input vector $\mathbf{X} = \{\mathbf{X}^\mathsf{d}, \mathbf{X}^\mathsf{n}\}$ encompasses a single design and noise parameter. The test function can be summarized as

$$\begin{aligned} &g : \mathbb{R}^2 \to \mathbb{R}, \quad \mathbf{x} \mapsto y = -1.5\,x^\mathsf{d} + 5\cos(\pi x^\mathsf{d}) + |x^\mathsf{n}|^{(2.0+\frac{1}{8}(x^\mathsf{d})^2)} \\ &\text{with:} \qquad X^\mathsf{d} \sim \mathcal{N}(\mu_x^\mathsf{d}, 0.1) \\ &\qquad\qquad X^\mathsf{n} \sim \mathcal{N}([-0.75, 0.75], [1/3, 2.5/3]). \end{aligned} \tag{4.60}$$

Problem (4.60) describes a RDO scenario with a mixture between Type I and II because both design and noise parameter are uncertain. The design variable to be optimized is μ_x^d which can take an arbitrary value within $[0.5, 3.25]$. The noise factor is quantified by a Gaussian p-box with uncertain mean and standard deviation.

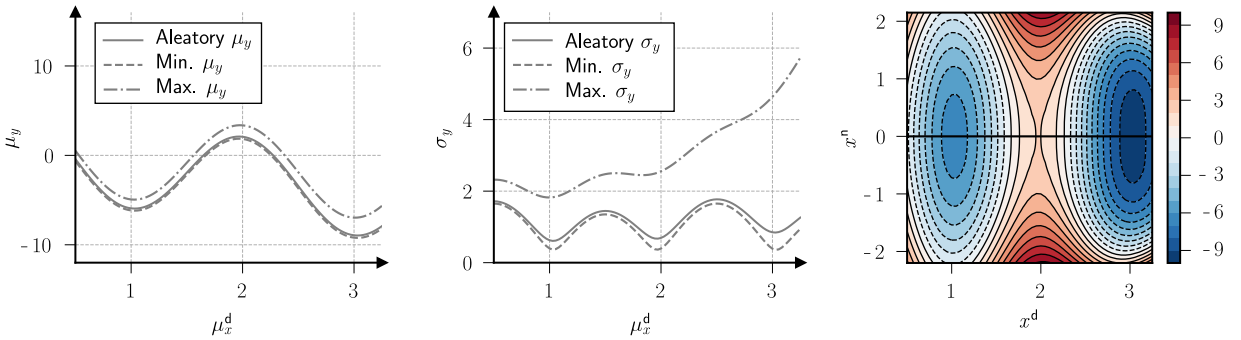

(a) Response mean for different μ_x^{d}. (b) Response stdv. for different μ_x^{d}. (c) Contour plot.

Figure 4.10 Graphical representation of Eq. (4.60).

Figure 4.10(c) shows a contour plot of the functional relationship which is a superposition of the cosine and a linear function in the x^{d}-coordinate. In the direction of the noise factor, $g(\mathbf{x})$ is a power function where the exponent is proportional to the value of x^{d}. This property results in an increasing steepness for $|x^{\mathsf{n}}| > 1.0$ as x^{d} is taking larger values.
In Figs. 4.10(a) and 4.10(b), the response mean and standard deviation is depicted for different realizations of μ_x^{d}, respectively. The solid gray lines represent the pure aleatory case, which means that the noise factor is described by $X^{\mathsf{n}} \sim \mathcal{N}(0.0, 1.75/3)$. In this case, the cosine characteristic is dominating the distribution of μ_y and σ_y whereas the changing exponent leads only to a slight increase of σ_y for large μ_x^{d}.
When taking the epistemic uncertainty components into account, the lower and upper bounds of the stochastic moments are of relevance depicted by the dash-dotted and dashed lines. For the response mean, the epistemic effect is comparatively low recognizable by the small distance between $\underline{\mu}_y$ and $\overline{\mu}_y$. Conversely, a huge deviation of $\overline{\sigma}_y$ from its aleatory value can be observed, especially if μ_x^{d} tends to the upper bound. Thus, the epistemic uncertainty of X^{n} has a significant effect on the response variation and therefore also on the robustness assessment.

RDO Formulations

In this subsection, we want to reopen the discussion from Section 3.6.2 about different RDO formulations. At first, we start with the pure aleatory case for which the robust optimization problem is stated as

$$\begin{aligned} &\underset{\mu_x^{\mathsf{d}}}{\text{minimize}} && w_\mu\, \mu_y + w_\sigma\, \sigma_y \\ &\text{s.t.} && 0.5 < \mu_x^{\mathsf{d}} < 3.25. \end{aligned} \tag{4.61}$$

By analyzing the mean and standard deviation distribution in Figs. 4.10(a) and 4.10(b), it becomes obvious that the solution for Eq. (4.61) is given by $\mu_x^{\mathsf{d}} \approx 3.0$ as long as w_σ is not substantially larger than w_μ. This impression is confirmed by Figs. 4.11(a) and 4.11(b) where

the aleatory objective function is shown for $w_\mu = w_\sigma = 0.5$ by the black solid line.
In contrast, defining a mathematical expression for the RDO in presence of hybrid uncertainties is not possible in a straightforward manner. In the following, we compare two different approaches how to determine the optimal value for μ_x^{d} which have been introduced in Section 3.6.2. The first one is a direct extension of the classical RDO scheme which considers the epistemic effect by adding additional terms to the objective function. For the test case, the extended RDO yields

$$\begin{aligned} \underset{\mu_x^{\mathsf{d}}}{\text{minimize}} \quad & w_\mu\, \tilde{\mu}_y + w_\sigma\, \tilde{\sigma}_y + w_{\Delta\mu}\, \Delta\mu_y + w_{\Delta\sigma}\, \Delta\sigma_y \\ \text{s.t.} \quad & 0.5 < \mu_x^{\mathsf{d}} < 3.25, \end{aligned} \tag{4.62}$$

where $\Delta\mu_y$ and $\Delta\sigma_y$ stand for the epistemic variation of the response mean and standard deviation. To repeat, the specific case of $w_{\Delta\mu} = w_{\Delta\sigma} = 0$ is related to the aleatory scenario. In Fig. 4.11(a) a variety of objective functions is depicted where each graph corresponds to different weighting factors. Note, that all combinations have to fulfill the partition of unity. In summary, two different positions are identified for the optimal choice of μ_x^{d}. The first one, given by $\mu_x^{\mathsf{d}} \approx 3.0$, coincides with the aleatory study. The alternative solution finds the robust optimum at $\mu_x^{\mathsf{d}} \approx 1.0$ characterized by a larger average mean but a significantly lower $\Delta\sigma_y$-value. One can see, that the associated objective functions put a large weight on $\Delta\sigma_y$ or σ_y, respectively. In presence of epistemic uncertainty, the optimum at $\mu_x^{\mathsf{d}} \approx 1.0$ is more reasonable because the worst-case scenario deviates strongly from the aleatory case at $\mu_x^{\mathsf{d}} \approx 3.0$.
Within Section 3.6.2, some other RDO formulations are mentioned. One of them proposes to exclude the epistemic components from the objective function and define additional constraints instead. For the analytical test case, the modified RDO problem is stated by

$$\begin{aligned} \underset{\mu_x^{\mathsf{d}}}{\text{minimize}} \quad & w_\mu\, \tilde{\mu}_y + w_\sigma\, \tilde{\sigma}_y \\ \text{s.t.} \quad & 0.5 < \mu_x^{\mathsf{d}} < 3.25 \\ & \overline{\mu}_y \leq \mu_y^{\mathsf{c}} \\ & \overline{\sigma}_y \leq \sigma_y^{\mathsf{c}}, \end{aligned} \tag{4.63}$$

where μ_y^{c} and σ_y^{c} denote the thresholds of the maximum mean and standard deviation. Similar to the RDO formulation from Eq. (4.62), the method is able to find the same two potential robust designs, depending on the choice of σ_y^{c}. The graphical representation in Fig. 4.11(b) illustrates the objective from Eq. (4.63) and the restriction of the feasible design space for $\mu_y^{\mathsf{c}} = 0.0$ and $\sigma_y^{\mathsf{c}} = 2.75$. Under this condition, all objective functions reach their minimum close to $\mu_x^{\mathsf{d}} = 1.0$, regardless of the underlying weighting factors. Weakening the constraint of the maximum standard deviation can shift the optimum into the region of the aleatory minimum except if w_σ is equipped with an extremely high value.

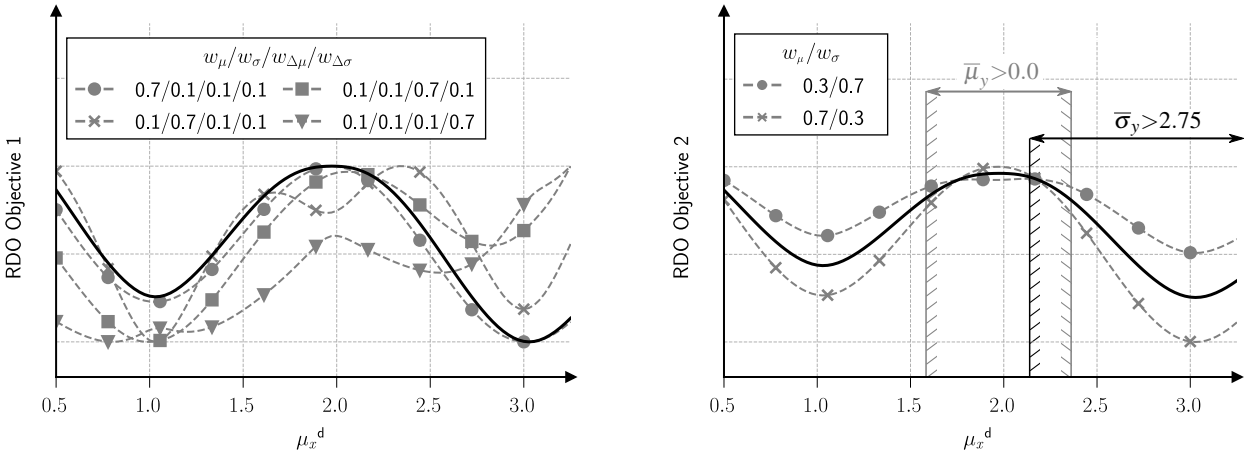

(a) Epistemic RDO according to Eq. (4.62).

(b) Epistemic RDO according to Eq. (4.63).

Figure 4.11 Graphical representation of the objective functions for the epistemic RDO.

The question remains which of the two approaches to prefer with regard to real-world applications. The first option according to Eq. (4.62) gives the modeler more flexibility because the different components of the objective can be weighted individually. Also, the optimizer does not have to deal with any constraints which is usually more efficient. However, it is questionable how precisely $\Delta\sigma_y$ and $\Delta\mu_y$ can be evaluated for high-dimensional problems. In principle, the determination of each term requires two optimization procedures which can be extremely time-consuming.

For the second RDO setup, these two terms must not be computed because of the constraint-based expression. Even though one could argue that approximating the two maxima of the stochastic moments is also associated with non-negligible effort, the RDO expression of Eq. (4.63) is still preferable from the author's point of view for mainly two reasons: First, the determination of $\overline{\mu}_y$ and $\overline{\sigma}_y$ is less time-consuming as it is based on only one instead of two optimizations. Second, the modeler can directly control the maximum response mean and variance which is more intuitive than finding an appropriate combination of the various weighting factors. Therefore, the constraint-based approach will be applied for the interdisciplinary SAS model in Sec. 5.2.3.

For low-dimensional problems, such as the analytical test case, computational time is not playing a role why standard MC techniques can be used. In preparation for the application case, the same problem is analyzed by using the NISS approach.

NISS-based RDO

Conducting a RDO is, compared to a deterministic optimization, coupled with considerably more effort. In particular, for a problem with hybrid uncertainties the evaluation of every single design point requires a double loop MC sampling, see Section 3.3. Except for computationally cheap models, this approach is not usable for any industrial application.

In general, the optimization can be made more efficient by several ways. One option is to replace the original relationship by a mathematical surrogate model which approximates the physical system by inexpensive analytical expressions. After that, standard MC sampling schemes can be used. Within this thesis, we follow the idea to keep the original model and break the double-loop sampling procedure instead. As discussed in Section 4.3.1, the NISS approach is used for this purpose which requires only one set of samples for the uncertainty propagation of different $\boldsymbol{\Theta}_x$-values. Thus, a simplified relation is derived between the uncertain hyperparameters and the stochastic response moments instead of between the model's input and output quantities.

Coming back to the analytical example, we are faced with a two-dimensional input space where both quantities are described by a distributional p-box. Note, that design and noise parameters can be treated in the same fashion by the NISS framework. Thereof, the hyperparameter set is given by $\boldsymbol{\Theta}_x = \{\mu_{x,1}, \sigma_{x,1}, \mu_{x,2}, \sigma_{x,2}\}$, where $\mu_{x,1}$ equals the design parameter μ_x^{d} and $\sigma_{x,1}$ has a constant value. The remaining two parameters belong to the noise factor X^{n}.

The choice of $\boldsymbol{\Theta}_x^\star$ is oriented towards the proposition from Eq. (4.51) which gives a bivariate Gaussian with

$$f_X(x|\boldsymbol{\Theta}_x^\star) = \begin{cases} X_1 \sim \mathcal{N}(1.625, 0.54) \\ X_2 \sim \mathcal{N}(0.375, 1.0) \end{cases} . \tag{4.64}$$

Note that the symmetry of $g(\mathbf{x})$ in the x_2-direction is exploited which leads to the mean value of $\mu_{x,2} = 0.375$. After having drawn samples from $f_X(x|\boldsymbol{\Theta}_x^\star)$, Eqs. (4.57) and (4.59) can be used to determine $\mu_y(\boldsymbol{\Theta}_x)$ and $\sigma_y^2(\boldsymbol{\Theta}_x)$. For the current test case, 6000 samples have been created from Eq. (4.64).

In Fig. 4.12(a), the NISS approximation of the minimum, maximum and average mean value is opposed to the MC solution. Note that the MC approach is based on an extremely large number of samples such that we refer to it as reference solution. All graphs show a high degree of similarity over the whole design space and a decreasing accuracy for the tails of the sampling

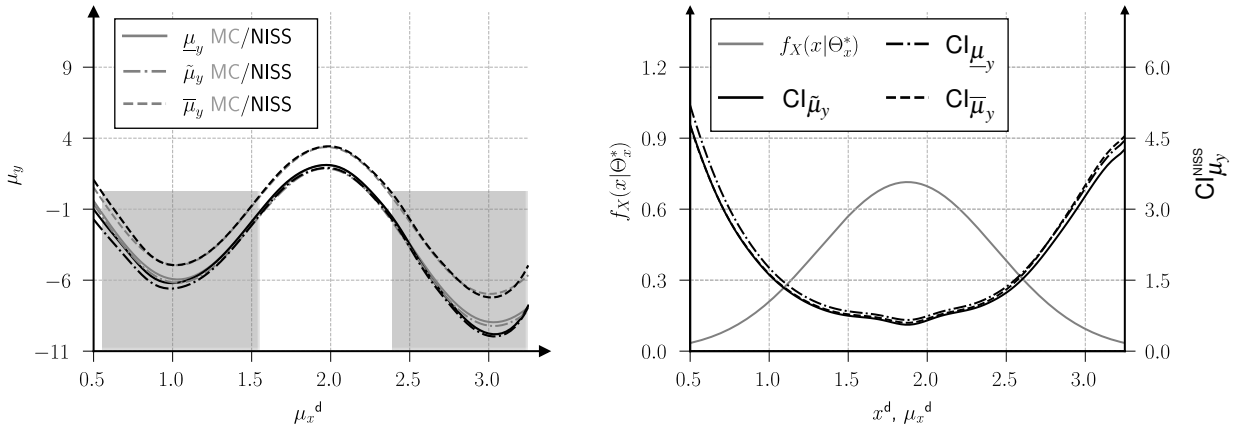

(a) Comparison between NISS and MC approach.

(b) Sampling PDF and approximation error.

Figure 4.12 Evaluation of the NISS-based mean value approximation for the analytical test case.

distribution. This impression is confirmed by Fig. 4.12(b) showing the sampling distribution in x_1-direction as well as the confidence interval of the mean estimator. As expected, the accuracy is indirectly proportional to the sampling density and reaches its maxima at the bounds of the design space. Within the scope of the test case, the confidence interval (CI) of the mean and variance estimator is derived from a $(\pm 2\,\sigma)$-range according to

$$\begin{aligned} \mathrm{CI}_{\mu_y}^{\mathrm{NISS}} &= 4\sqrt{Var[\mu_y]}, \quad \text{and} \\ \mathrm{CI}_{\sigma_y^2}^{\mathrm{NISS}} &= 4\sqrt{Var[\sigma_y^2]}. \end{aligned} \tag{4.65}$$

From a first glance, the number of samples seems to be disproportionately high for a two-dimensional problem. The reason for this lies in the nonlinearity of the model and the small standard deviation of the design parameter. The latter leads to a strong deviation between proposal and desired distribution. The analytical test case has been deliberately constructed in this way to discuss the limitations of the NISS method.

This issue becomes even more acute when we analyze the approximation error of the variance estimator. To give a short impression, the corresponding average CI among all evaluated design points is 44.82 and reaches a maximum of 155.82 close to the upper bound of the design space, i.e., at $\mu_x^{\mathrm{d}} = 3.25$. The poor quality is also indicated by the σ_y^2-values themselves as they even become negative in areas where the true variance is small. The approximation of the second stochastic moment by the classical NISS is therefore not useful.

The simplest approach would be to increase the sample number until the modeler is satisfied with the accuracy. This option is, except for models with a low computation time, out of question as it can require a tremendously high number of samples. That's why we propose an alternative strategy which exploits the knowledge gained about the mean value distribution. The aim is to analyze only those parts of the design space which are of interest for the RDO. Furthermore, an extended version of the standard NISS, abbreviated as MNISS (multi-point non-intrusive imprecise stochastic sampling), is introduced which stands for the multi-point NISS strategy.

The first step is to apply the standard NISS to determine the response mean as discussed in the previous sections. After that, the goal is to identify potential regions within which the robust design optimum could lie. Since the estimation accuracy for σ_y is usually bad, the criterion is solely derived from the μ_y-distribution. Here, the constraint-based RDO formulation (Eq. (4.63)) is beneficial to extract relevant areas from the design space. Based on the mean value constraint, a set of potentially robust design points can be defined according to

$$\mu_x^{\mathrm{p}} = \left\{ \mu_x^{\mathrm{d}} \mid \overline{\mu}_y(\mu_x^{\mathrm{d}}) \leq \mu_y^{\mathrm{c}} \right\}. \tag{4.66}$$

For the analytical test case, any design fulfilling $\overline{\mu}_y \leq 1.0$ is of relevance and covered by μ_x^{p}. In Fig. 4.12(a), the area of interest is shaded in gray. One can see, that the promising region is a composition of two local subregions such that $\mu_x^{\mathsf{p}} = \{\mu_x^{\mathsf{p},(1)}, \mu_x^{\mathsf{p},(2)}\}$ holds.
Once μ_x^{p} has been detected, the next step is to estimate σ_y^2 locally and thereby also the epistemic robustness metric. Consequently, a separate sampling distribution is defined for each $\mu_x^{\mathsf{p},(i)}$ and the standard NISS scheme is applied. The two bivariate Gaussian distributions are once again derived from Eq. (4.51) by

$$f_X(x|\boldsymbol{\Theta}_x^{\star,(1)}) = \begin{cases} X_1^{(1)} \sim \mathcal{N}(1.07, 0.58) \\ X_2^{(1)} \sim \mathcal{N}(0.375, 1.0) \end{cases} \quad , \quad \text{and} \quad f_X(x|\boldsymbol{\Theta}_x^{\star,(2)}) = \begin{cases} X_1^{(2)} \sim \mathcal{N}(2.78, 0.51) \\ X_2^{(2)} \sim \mathcal{N}(0.375, 1.0) \end{cases} . \tag{4.67}$$

As for the mean approximation, 6000 sample points are drawn from both local distributions. Unfortunately, the CI of σ_y^2 shows still a poor performance despite narrowing down the design space. Even a doubling of the sample points leads to an average CI width in both areas of 7.99 which is way more precise than without reducing the design space but still not usable for a resilient proposition about the robustness.
At this point, the MNISS concept comes into play. As indicated by the name, the idea is to define multiple proposal distributions within every region $\mu_x^{\mathsf{p},(i)}$. Hence, the evaluation of a design, i.e., the uncertainty propagation of a certain $\boldsymbol{\Theta}_x$-realization, is derived from a superposition of several NISS frameworks. Before discussing the exact mathematical concept behind MNISS, meaningful hyperparameter values for the different proposal distributions must be determined. In order to have a reasonable decision basis, the CI of every single HDMR component for the variance estimator is analyzed. With the help of this study, one can figure out how the huge approximation error for σ_y^2 is composed. In Table 4.1, the average estimation error of $\tilde{\sigma}_y^2$, $\underline{\sigma}_y^2$ and $\overline{\sigma}_y^2$ is summarized for two designs which are lying in the first area of interest $\mu_x^{\mathsf{p},(1)}$. As we expect the lowest accuracy at the bounds of the design space, the two points represent the lower and upper limit of $\mu_x^{\mathsf{p},(1)}$. One can see, that the overall accuracy of both points is strongly affected by the first and second order components which include the parameter $\sigma_{x,1}$. This is reasonable if we recall that the uncertainty of X^{d} is characterized by an extremely small standard deviation which differs substantially from $\sigma_{x,1}^{\star}$ of the proposal PDF, see Eqs. (4.60) and (4.67). Thus, a noticeable improvement can be achieved if the proposal distribution was modified in the x_1-direction.

		First-order				Second-order					
μ_x^{d}	$\boldsymbol{\Theta}_x^{\star}$	μ_1	σ_1	μ_2	σ_2	μ_1,σ_1	μ_1,μ_2	μ_1,σ_2	σ_1,μ_2	σ_1,σ_2	μ_2,σ_2
0.49	0.53	0.81	2.09	0.56	0.63	2.39	0.77	0.75	1.30	0.95	1.05
1.64	0.53	1.70	2.06	0.55	0.62	2.83	0.96	0.67	1.28	0.95	1.05

Table 4.1 HDMR component errors for the approximation of σ_y^2 from a standard NISS procedure with $n_{\mathsf{s}} = 12,000$.

The core of the MNISS strategy is to decrease the estimation error by introducing a set of proposal distributions which, taken as whole, cover the region of interest. Once the modeler has identified a direction where the MNISS concept can lead to an accuracy enhancement, a proper setup is sought for the decomposition of $f_X(\mathbf{x}|\boldsymbol{\Theta}_x^\star)$. As a rule of thumb, the following propositions are introduced to determine the number and characteristics of the proposal distributions:

- The proposal's standard deviation should not deviate from the desired one by more than a factor of three.
- The distance between the mean values of two neighboring sample distributions should not be larger than four times the standard deviation.

Based on these guidelines, a proper coverage of the design space is ensured. The basis of the MNISS procedure is then given by

$$f_X(\mathbf{x}|\boldsymbol{\Theta}_x^\star) = \bigcup_{i=1}^{n_\mathsf{p}} f_X(\mathbf{x}|\boldsymbol{\Theta}_x^{\star,(i)}), \quad \text{with } i = 1,\dots,n_\mathsf{p}, \tag{4.68}$$

where n_p denotes the number of proposal distributions and $\boldsymbol{\Theta}_x^{\star,(i)}$ the hyperparameter set for the i-th sampling distribution. Within the scope of the thesis, MNISS is introduced for a decomposition in only one direction. Of course, the strategy can be expanded for cases where the modeler wants to modify the sampling distribution in several directions.
In addition to that, a so-called membership function $w_i(\boldsymbol{\Theta}_x)$ must be defined for every entry $f_X(\mathbf{x}|\boldsymbol{\Theta}_x^{\star,(i)})$ which quantifies the importance of the separate proposal distributions. In principle, any kind of functional type can be used as long as the partition of unity is fulfilled, i.e., the sum of all $w_i(\boldsymbol{\Theta}_x)$ equals one for any $\boldsymbol{\Theta}_x$. A straightforward way is to describe $w_i(\boldsymbol{\Theta}_x)$ by a triangular function with a peak value of one at the mean value of the corresponding proposal distribution. The lower and upper limits coincide with the coordinates of the neighboring mean values, i.e., $\boldsymbol{\mu}_x{}^{\star,(i-1)}$ and $\boldsymbol{\mu}_x{}^{\star,(i+1)}$. An exception is provided by the first and last weighting function. To ensure the partition of unity, they take the value of one for $\boldsymbol{\mu}_x \leq \boldsymbol{\mu}_x{}^{\star,(0)}$ and $\boldsymbol{\mu}_x \geq \boldsymbol{\mu}_x{}^{\star,(n_\mathsf{p})}$, respectively, because all remaining membership functions are zero.
Last but not least, the question remains how to modify the calculation rules from Eqs. (4.57) and (4.59) to account for the partition of $f_X(x|\boldsymbol{\Theta}_x^\star)$. In case of μ_y, the HDMR components are given for the MNISS strategy by

$$\mu_{y,0} \approx \sum_{t=1}^{n_\mathsf{p}} w_t(\boldsymbol{\Theta}_x) \left\{ \frac{1}{n_\mathsf{s}} \sum_{k=1}^{n_\mathsf{s}} g(\boldsymbol{x}_\mathsf{s}^{(k)}) \right\} = \sum_{t=1}^{n_\mathsf{p}} w_t(\boldsymbol{\Theta}_x)\, \mu_{y,0}^{(t)},$$

$$\mu_{y,i}(\boldsymbol{\theta}_x^{(i)}) \approx \sum_{t=1}^{n_\mathsf{p}} w_t(\boldsymbol{\Theta}_x) \left\{ \frac{1}{n_\mathsf{s}} \sum_{k=1}^{n_\mathsf{s}} g(\boldsymbol{x}_\mathsf{s}^{(k)})\, r_{\mathsf{cut}}^{(i)}(\boldsymbol{x}_\mathsf{s}^{(k)}|\boldsymbol{\Theta}_x^{(i)}) \right\} = \sum_{t=1}^{n_\mathsf{p}} w_t(\boldsymbol{\Theta}_x)\, \mu_{y,i}^{(t)}, \text{ and}$$

$$\mu_{y,ij}(\boldsymbol{\Theta}_x^{(ij)}) \approx \sum_{t=1}^{n_\mathrm{p}} w_t(\boldsymbol{\Theta}_x) \left\{ \frac{1}{n_\mathrm{s}} \sum_{k=1}^{n_\mathrm{s}} g(\boldsymbol{x}_\mathrm{s}^{(k)})\, r_\mathrm{cut}^{(ij)}(\boldsymbol{x}_\mathrm{s}^{(k)} | \boldsymbol{\Theta}_x^{(ij)}) \right\} = \sum_{t=1}^{n_\mathrm{p}} w_t(\boldsymbol{\Theta}_x)\, \mu_{y,ij}^{(t)}, \tag{4.69}$$

where $\mu_{y,0}^{(t)}$ denotes the contribution of the t-th proposal distribution to the zeroth-order component function $\mu_{y,0}$ and $w_t(\boldsymbol{\Theta}_x)$ the corresponding weight. The same holds for the first- and second-order components. To summarize, the MNISS concept can be interpreted as a superposition of several NISS-evaluations. The contribution of every local approximation is expressed by its weighting factor which, in turn, is derived from so-called membership functions. The MNISS components for the estimation of σ_y^2 are defined in the same fashion and are given in Appendix B.2.

Coming back to the analytical test case, the MNISS concept is applied to both promising regions separately. To repeat, a decomposition in the x_1-domain is meaningful due to the dominating impact of the $\sigma_{x,1}$-parameter, see Tab. 4.1. Following the propositions from before leads to $n_\mathrm{p} = 3$ sampling distributions in each region depicted by the solid lines in Fig. 4.13(c). Moreover, the triangular membership functions are represented as dashed lines in the same plot.

For the test case, 4000 points are drawn from each proposal PDF which gives a total amount of $12{,}000$ samples within every subregion $\mu_x^{\mathrm{p},(i)}$. Figure 4.13(a) compares the evaluation of the response standard deviation from MNISS with the MC reference solution. Even though there is a certain mismatch between the curves, especially close to the upper bound of $\mu_x^{\mathrm{p},(2)}$, the MNISS estimation is able to capture the global characteristics of $\tilde{\sigma}_y$, $\underline{\sigma}_y$ and $\overline{\sigma}_y$. This is confirmed by the analysis of the epistemic robustness metric in Fig. 4.13(b). The upper half, showing the MC solution, is an extract from Fig. 4.11(b) whereas the lower part refers to the MNISS solution. A fundamental finding of the study is that the robust optima identified by MNISS are very close to the reference solution for any weighting factor combination of the robustness metric. Note that the marking style in Fig. 4.13(b) coincides with the one in

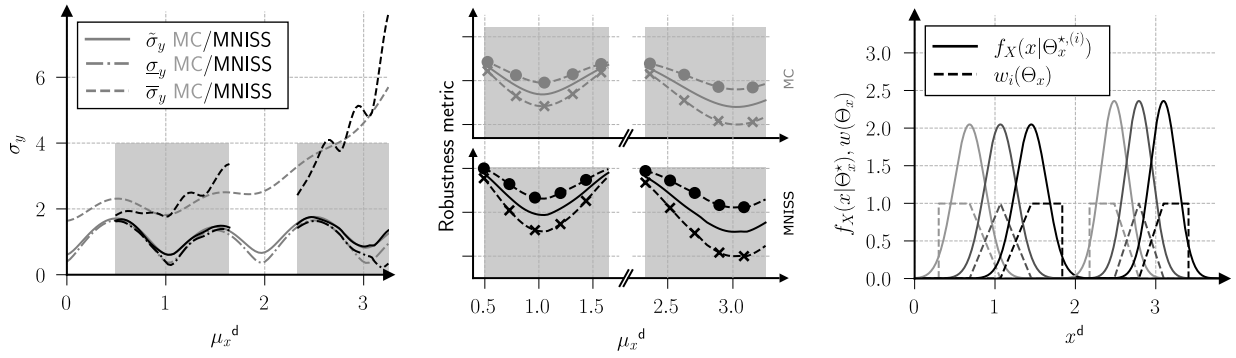

(a) Evaluation of σ_y^2 based on MC and MNISS.

(b) Robustness metric derived from MC and MNISS.

(c) Proposal distributions and weighting factors.

Figure 4.13 Evaluation of the MNISS concept for the analytical test case.

Fig. 4.11(b). To express the result in numbers, the MNISS robust optima deviate by a maximum of 2% from the true solution. Depending on the choice of the $\overline{\sigma}y$-threshold, the robust design is either located within $\mu_x^{\mathsf{p},(1)}$ or $\mu_x^{\mathsf{p},(2)}$.
Finally, the benefit of MNISS is demonstrated once again by a small comparative study. Therefore, we contrast the σ_y-distribution from Fig. 4.13(a) with the initial NISS approach where only a single proposal distribution is defined in each region $\mu_x^{\mathsf{p},(i)}$ according to Eq. (4.67). It is important to notice that the total sample count is exactly the same in both cases. Table 4.2 comprises the average deviation from $\tilde{\sigma}_y$, $\underline{\sigma}_y$ and $\overline{\sigma}_y$ at equally distributed positions within both promising areas. The numbers in the table show clearly the higher global approximation accuracy of the MNISS as the average offset is considerably smaller. Except for some few evaluation points in the middle of the two regions, MNISS provides a more accurate approximation of $\tilde{\sigma}_y$. The reason for this is the higher sampling density of the classical NISS. Thus, the multi-point version of NISS is an advantageous extension to achieve a continuously high performance over the whole design space.

	$\mu_x^{\mathsf{p},(1)}$							$\mu_x^{\mathsf{p},(2)}$						
μ_x^{d}	0.49	0.67	0.87	1.05	1.26	1.44	1.64	2.33	2.47	2.64	2.78	2.94	3.08	3.25
NISS	3.16	1.51	0.16	0.24	1.08	2.80	5.06	5.67	4.49	2.44	0.93	0.46	0.96	1.92
MNISS	0.88	0.54	0.34	0.17	0.58	0.45	1.65	1.97	1.53	0.87	1.07	0.53	0.26	7.75

Table 4.2 Comparison between NISS and MNISS σ_y-deviation with $n_{\mathsf{s}} = 12,000$.

Within the previous paragraphs, a variety of concepts and solution approaches have been discussed for conducting uncertainty studies in presence of epistemic uncertainties. At first, a non-probabilistic concept was introduced to solve inverse problems for scarce data sets. Furthermore, a method to screen out unimportant hyperparameters was discussed to reduce the model complexity and thereof also the computational time. Finally, the focus was put on the development of suitable RDO frameworks for hybrid uncertainties. A special attention has been attached to finding a balance between approximation accuracy and time efficiency which has led to the development of MNISS.
Within the scope of the next chapter, the methods from above are applied to the interdisciplinary jet engine model. It will turn out, that some minor modifications are needed to improve the efficiency of some concept because of the high-dimensional input and output spaces.

Chapter 5

APPLICATION CASE: Early Development Phase of a Low-Pressure Turbine Secondary Air System

The following sections discuss the application of the stochastic methods, which have been developed throughout Chap. 4, in context of an early jet engine development phase. To repeat, the industrial use case is an interdisciplinary secondary air system (SAS) model of a low-pressure turbine (LPT). The primary goal is to ensure a sufficient supply of cooling mass flow in presence of engine-to-engine and flight-to-flight variations. From a methodological point of view, the appropriate treatment of lack-of-knowledge uncertainty sources appears to be a key aspect. The present chapter is structured in accordance to the aims and objectives presented in Sec. 2.3.

Section 5.1 deals with the jet engine performance model which is the first component of the interdisciplinary process chain. Here, the main challenge is to quantify the uncertainty of those parameters being affected by the engine-to-engine variation because it requires to solve an inverse problem. After that, Section 5.2 analyzes the interdisciplinary model of the SAS. As in the section before, the lack-of-knowledge uncertainty quantification of selected input quantities is part of it. Besides from that, the reduction of the epistemic parameter space, based on the technique from Section 4.1.3, is applied. Finally, the goal is to identify the optimal choice of the geometrical design parameters in order to guarantee a stable cooling of the LPT disk. This goal will be achieved by conducting a robust design optimization (RDO).

5.1 Uncertainty Quantification of a Jet Engine Performance Model

As described in Sec. 2.1, the performance model is the starting point of the jet engine design process. A detailed explanation of the thermodynamic simulation is given in Sec. 2.1.1 which also explains the significance for the overall development process. Furthermore, the uncertainty sources of the performance calculation are summarized in Sec. 2.1.2. According to Tab. 2.1, the set of uncertain parameters can be divided into two groups: engine-to-engine and flight-to-flight variation. For the latter, a forward uncertainty quantification (UQ) is possible because the available data set is directly related to the corresponding model parameters. In contrast, the uncertainty on the quantities of the first group must be derived from an inverse strategy. Within the scope of this section, only the inverse problem is analyzed whereas the uncertainty characterization of the remaining quantities is discussed in Sec. 5.2.1.
At first, Section 5.1.1 provides a comprehensive description of the problem. Moreover, the hyperellipsoid approach from Sec. 4.1.3 is applied with different configurations. Then, Sec. 5.1.2 compares the hyperellipsoid with the convex hull strategy for a reduced set of output quantities. Here, the focus is more on the results interpretation of the different strategies. Note that parts of the following paragraphs have been published in [108].

5.1.1 Inverse Problem Definition and Full-Scale Uncertainty Quantification

The final step of a jet engine production process is the so-called pass-off test. Here, the main purpose is to ensure that every manufactured engine delivers the same amount of predefined thrust when setting the throttle lever into take-off position. This is achieved by trimming the rotational speed of the low-pressure spool ($N1$). As a result, the remaining station boundary conditions, e.g., temperature ($T^{(i)}$) and pressure ($P^{(i)}$), are also deviating from their nominal values because of the thermodynamic interrelationships.
In its original configuration, the performance model is used to simulate the jet engine's thermodynamic behavior for a set of design points, i.e., the phases of a flight mission. Every operation point is characterized by different ambient conditions and a specific setting of the thrust level. As a result, one can analyze the change of the station boundary conditions during a flight mission. In order to consider the production scatter, i.e., the trimming effect of the pass-off run, the components' efficiency ($\eta^{(i)}$) and flow capacity ($\Delta W^{(i)}$) must be treated as uncertain parameters. This enables us to determine how the station boundary conditions are affected by the engine-to-engine variation in every flight phase. In addition to that, one can simulate the flight-to-flight variation by varying the ambient conditions at a specific design point. Within this section, we conduct performance calculations for the cruise phase under constant ambient conditions, i.e., the flight-to-flight variation is neglected.
From a mathematical point of view, the performance model can be seen as a black box. The input parameters being relevant for the uncertainty studies are comprised by $\eta^{(i)}$ and $\Delta W^{(i)}$

which stand for the efficiency and flow capacity of the seven jet engine components, see Fig. 2.2. The response space is described by twelve gas flow parameters of interest. For a detailed explanation of the various input and output quantities, the reader is referred to Sec. 2.1.1. A mathematical representation of the performance calculation is given by

$$g : \mathbb{R}^{14} \rightarrow \mathbb{R}^{12}, \begin{pmatrix} \Delta W^{(\mathrm{FAN})} \\ \eta^{(\mathrm{FAN})} \\ \vdots \\ \Delta W^{(\mathrm{NA})} \\ \eta^{(\mathrm{NA})} \end{pmatrix} \mapsto \begin{pmatrix} T^{(25)} \\ P^{(25)} \\ \vdots \\ N1 \\ N2 \end{pmatrix}. \tag{5.1}$$

The actual problem we are facing here is to quantify the uncertainty on the input quantities during an early stage of the development process. In this phase, the main goal is to break down the jet engine's performance requirements to the component level. In detail, the stations' temperature and pressure values as well as the spool speeds are defined for every design point. Consequently, the effect of the production scatter is also expressed by the variation around the nominal station boundary conditions.

In the current application case, we are provided with a set of standard deviations represented as CoV (coefficient of variation) in Tab. 5.1. Note that these values have been manipulated as they are part of the company proprietary information. The epistemic character of the inverse problem comes from the fact that these variations are derived throughout expert estimates. The more reliable measurement data from the pass-off test are not available during this phase of the development process.

To summarize, the aim is to identify the uncertainty of $\eta^{(i)}$ and $\Delta W^{(i)}$ which leads to the given variation of the gas flow parameters. Therefore, we have to backward propagate the response uncertainty through the performance model. The total amount of data encompasses the stochastic moments in Tab. 5.1 and the nominal values for $\eta^{(i)}$ and $\Delta W^{(i)}$ which are not given here for reasons of confidentiality.

Since the station boundary conditions serve as input quantities for the subsequent disciplines, the question arises why not to directly vary these parameters in the interdisciplinary SAS model. In principle, two reasons speak against this approach.

Firstly, the correlations between the gas flow parameters are not part of the provided data set. Hence, running the performance model ensures a thermodynamically consistent variation of the temperature and pressure boundary conditions. Secondly, analyzing the combined effect

QoI	CoV	QoI	CoV	QoI	CoV	QoI	CoV	QoI	CoV	QoI	CoV
$T^{(25)}$	0.62%	$T^{(3)}$	0.58%	$T^{(4)}$	0.63%	$T^{(45)}$	0.79%	$T^{(49)}$	0.85%	$N1$	0.57%
$P^{(25)}$	1.30%	$P^{(3)}$	1.03%	$P^{(4)}$	1.03%	$P^{(45)}$	0.70%	$P^{(49)}$	0.77%	$N2$	0.77%

Table 5.1 Variation of the station boundary condition due to production scatter, expressed by the CoV.

of production scatter and changing ambient conditions is only possible by a simultaneous variation of all performance input parameters.
In the following two subsections, the hyperellipsoid approach from Sec. 4.1.3 is applied to the performance model by using a local and global optimization strategy. Since the inverse UQ strategies require a huge number of samples, the performance model is replaced by a mathematical surrogate model based on the Gaussian process. The training and test set from the high-fidelity model comprises $10,000$ and 100 samples, respectively. As a measure for the approximation quality, the RMSE (root mean square error) is determined which takes a value between 0.5% and 0.9% in the various dimensions. Thus, the quality of the metamodel is precise enough for the uncertainty studies. For further information on the Gaussian process regression, the reader is referred to [139].

Local Optimization

In order to set up the optimization procedure, a linearization of the performance model at the nominal input values is required to approximate the unknown correlations between the gas flow parameters. After that, the measurement ellipsoid $\mathcal{E}_{y_\mathrm{m}}$ can be derived from Chebyshev's inequality.
The linearization is also used to define the starting ellipsoid $\tilde{\mathcal{E}}_x$ for the gradient-based optimization strategy. The analytical solution of the linearized problem did not yield a feasible result as some entries of $\tilde{\sigma}_x^2$ become negative which is why a numerical solution is derived from Eq. (4.27). Unfortunately, this leads to a huge offset from the target standard deviation vector in many response dimensions. Of course, a certain mismatch from the measurement standard deviation was expected because of the nonlinear characteristics of the performance model. However, the absolute difference reaches values up to even 53%. This finding puts into question whether $\tilde{\mathcal{E}}_x$ is a reasonable starting point for the optimization.
To allow a better understanding of the mismatch, the data from Tab. 5.1 is compared with real pass-off measurements from a similar jet engine. As a result, a significant offset is observed for some station boundary conditions. Based on experts' opinion, it can be presumed that the provided set of standard deviations is partially applied with safety factors. As a consequence, the response space is reduced by the parameters $T^{(25)}$, $P^{(25)}$ and $P^{(45)}$ from twelve to nine dimensions. When considering only the reduced set of response quantities, the linear inverse UQ leads to an average offset of less than 10% from the standard deviations in Tab. 5.1.
Based on the reduced configuration, the inverse UQ is conducted with the SciPy[1] implementation of the *L-BFGS-B* algorithm. In short, this optimization technique relies only on the first-order derivative of the objective and is able to deal with specified bounds on the design space. A detailed discussion about this type of local optimizer can be found in [178].
The uncertainty propagation of the hyperellipsoid in every iteration is based on $n_\mathrm{s} = 25,000$

[1] SciPy is an open-source library for Python, see `https://scipy.org/`.

		LPC		FAN		HPC		HPT		LPT		NA		NC		
	k	ΔW	η	ΔW	η	ΔW	η	ΔW	η	ΔW	η	ΔW	η	ΔW	η	CT
$\lvert\Delta\mu\rvert$ [%]	9	0.03	0.21	0.10	0.09	0.24	0.07	0.01	0.03	0.00	0.00	0.27	0.02	0.01	0.23	$37.9\,h$
	13	0.00	0.11	0.10	0.05	0.21	0.02	0.0	0.11	0.19	0.06	0.20	0.01	0.01	0.17	$52.5\,h$
	17	0.00	0.05	0.10	0.07	0.13	0.02	0.00	0.03	0.11	0.03	0.14	0.02	0.03	0.10	$42.6\,h$
	36	0.12	0.16	0.14	0.04	0.03	0.04	0.07	0.23	0.23	0.09	0.28	0.06	0.03	0.20	$23.8\,h$
	90	0.14	0.16	0.13	0.07	0.29	0.06	0.06	0.13	0.24	0.03	0.27	0.05	0.08	0.21	$30.5\,h$
	Lin	0.00	0.00	0.00	0.00	0.00	0.00	0.00	0.00	0.00	0.00	0.00	0.00	0.00	0.00	Obj
CoV [%]	9	0.26	0.56	0.58	0.04	1.04	0.02	0.21	0.52	0.53	0.05	0.21	0.13	0.26	0.15	0.22
	13	0.26	0.56	0.58	0.03	1.02	0.02	0.24	0.50	0.44	0.03	0.18	0.14	0.26	0.13	0.35
	17	0.22	0.56	0.57	0.02	1.01	0.01	0.29	0.46	0.43	0.04	0.16	0.12	0.25	0.11	0.35
	36	0.22	0.55	0.54	0.02	0.96	0.01	0.27	0.46	0.43	0.04	0.17	0.13	0.25	0.12	0.52
	90	0.20	0.49	0.38	0.02	0.93	0.01	0.19	0.39	0.42	0.03	0.15	0.11	0.25	0.11	0.48
	Lin	0.25	0.70	0.71	0.02	1.27	0.02	0.37	0.58	0.52	0.04	0.04	0.15	0.31	0.10	—

Table 5.2 Mean value deviations and CoVs derived from the local hyperellipsoid approach.

samples. As discussed in Section 4.1.1, it is sufficient to create sample points only from the surface of the hyperellipsoid because the performance model has a monotonic behavior.

Within the scope of this study, the inverse UQ is performed several times with different specifications for the corresponding probability bound of $\mathcal{E}_{y_\mathrm{m}}$. To repeat, the parameter k of Chebyshev's inequality determines the minimum probability that a random sample lies inside the derived ellipsoid. Thus, the k-factor decides about the size of $\mathcal{E}_{y_\mathrm{m}}$, see Eq. (4.19). In detail, the parameter is set to four different values which corresponds to a range of minimum probabilities between 0% ($k=9$) and 90% ($k=90$). For every setting, the mean and standard deviation vector is computed according to Eqs. (4.28) and (4.29) from the identified hyperellipsoid $\mathcal{E}_x$.

Since input and output space do not have the same dimensionality, the k-factor in the input space must be modified such that $\mathcal{E}_x$ and $\mathcal{E}_{y_\mathrm{m}}$ represent the same probability bound.

A summary of the study results is given by Tab. 5.2. In the first half, the entries of the mean vector are expressed in terms of their absolute deviation from the nominal values. The second part of the table shows the derived standard deviations, represented as CoV. Every row of the table corresponds to a different realization of k. Note, that the parameter values are related to the response space, e.g., the scenario for $k=17$ describes a hyperellipsoid with $P(\mathbf{y}\in\mathcal{E}_{y_\mathrm{m}})\geq 47\%$. The last row in each section contains the stochastic moments of the linearized solution. Furthermore, the computation time[2] as well as the final objective value is summarized by the very right column.

Coming back to the outcome of the study, it can be seen that the identified mean vector entries deviate only slightly from their nominal values. The identified mean vector is reasonable when considering that the uncertainty is caused by the production scatter. By logic, the mean vector

[2] Intel(R) Core(TM) i9-9900 CPU @ 3.10GHz

of the linearized solution equals the deterministic configuration. The overall review of the CoVs shows a clear consistency between the various UQ settings. Regardless of the k-factor, the derived entries of $\boldsymbol{\sigma}_x$ are all in the same order of magnitude. With only a few exceptions, the standard deviation tends to decrease with increasing value of k. This effect can be attributed to the nonlinearity of the performance model. When choosing a low value for k, which automatically leads to a small enclosed area of $\mathcal{E}_{\mathcal{Y}_\mathrm{m}}$, the nonlinear characteristics has a less strongly influence compared to a large k-factor. The hypothesis is confirmed by the standard deviations obtained from the linearized model approximation. For almost all of the input quantities, $\tilde{\sigma}_x$ is larger than the maximum standard deviation among all hyperellipsoid approaches.

In Fig. 5.1, the response space is illustrated for $k = 17$ by the two-dimensional projections of the hyperellipsoids. Note that the response space has been normalized with respect to the mean values. The linear approach is depicted by the dashed black lines whereas the solid ones stand for the final result of the hyperellipsoid strategy. In all of the subspaces, a high

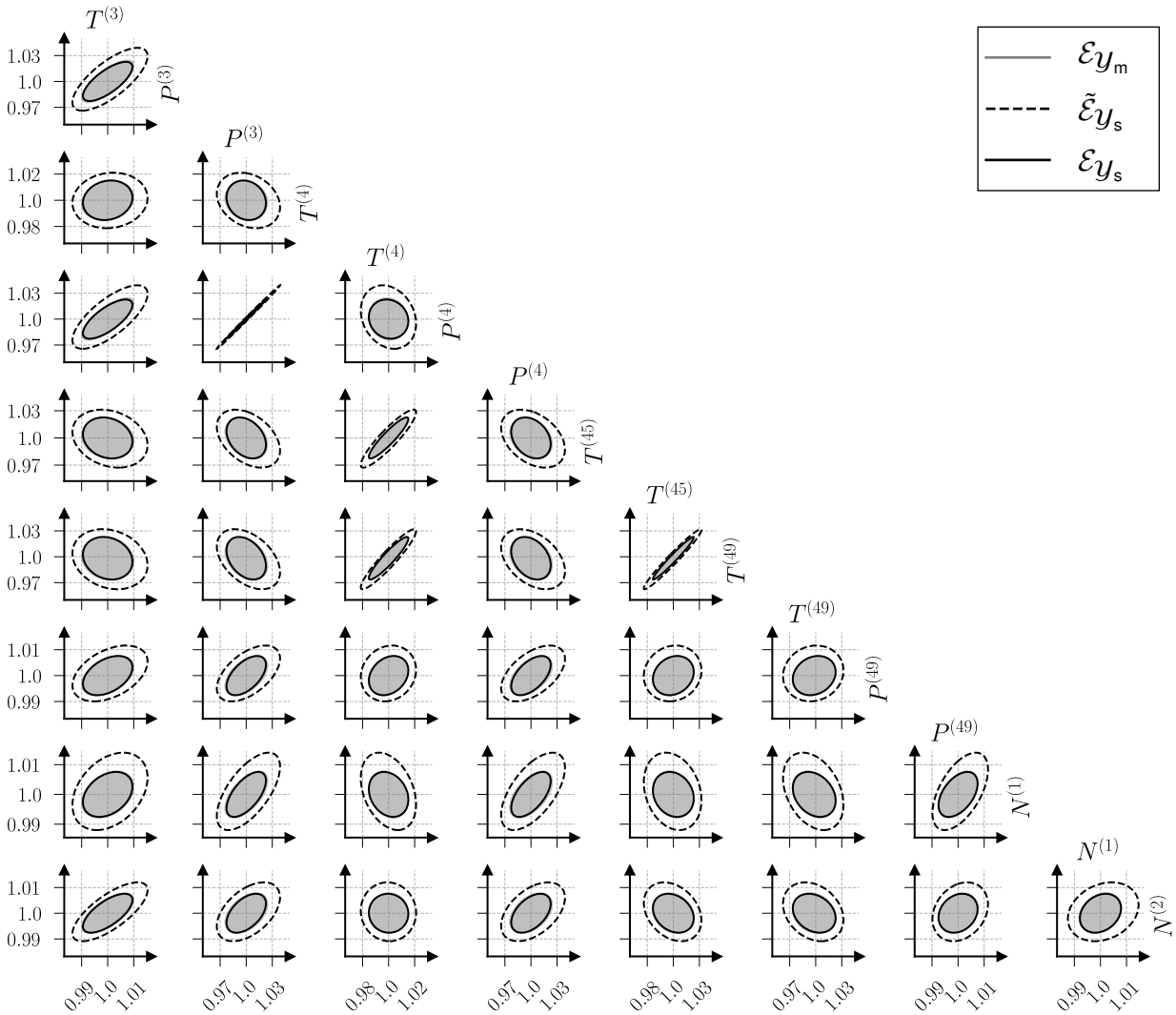

Figure 5.1 2D projections of $\mathcal{E}_{\mathcal{Y}_\mathrm{m}}$, $\mathcal{E}_{\mathcal{Y}_\mathrm{s}}$ and $\tilde{\mathcal{E}}_{\mathcal{Y}_\mathrm{s}}$ from the local hyperellipsoid approach. The response quantities are normalized with respect to the mean values.

conformity between $\mathcal{E}_{\mathcal{Y}_\mathrm{s}}$ and $\mathcal{E}_{\mathcal{Y}_\mathrm{m}}$ can be observed. In contrast, the projections of $\tilde{\mathcal{E}}_{\mathcal{Y}_\mathrm{s}}$ enclose the measurement ellipsis in any dimension which results from the conservative approximation of $\tilde{\boldsymbol{\sigma}}_x$. Apart from assessing the quality of the inverse UQ results, Fig. 5.1 makes the correlations between the gas flow parameters visible. Especially temperatures and pressures at consecutive stations show a high level of dependency. In case $\mathcal{E}_{\mathcal{Y}_\mathrm{m}}$ is based on thermodynamically consistent data, a reduction of the response space can be conducted without loss of information.

Finally, the question remains how to use the derived data from Tab. 5.2 for subsequent studies. The randomness on the stochastic moments themselves could be included into a p-box representation with uncertain mean and variance. In the present study case, it has been decided to use the average mean value for the uncertainty representation due to the small variation of the stochastic descriptor. For the standard deviation, the maximum value is taken out of Tab. 5.2. The reason for choosing a more conservative approach is the early design stage of the development process. Nevertheless, the missing information regarding the shape of the true distribution is considered by the p-box concept from Sec. 4.1.4. To repeat, the distributional p-box is characterized by a set of CDFs with equal mean and standard deviation but different skewness values. Since the p-box representation must be applicable to the non-intrusive imprecise stochastic sampling (NISS) concept, the continuous family of skew normal distributions is used for the characterization.

All in all, the local optimization strategy of the hyperellipsoid has proven to deliver reasonable results for the uncertainty identification of the components' efficiency and flow capacity. A decisive factor for the good performance is certainly the quality of the initial guess. Especially for the determination of $\boldsymbol{\mu}_x$, the linear solution is close to the optimal one which is meaningful for analyzing the production scatter effect. Within the next section, the same study is conducted with a global optimization approach.

Global Optimization

The purpose of this section is to compare the two different optimization strategies with each other in context of a real-world application. One of the main aspects is to assess the computation time as well as the quality of the results.

A great benefit of the global approach is that no initial guess is needed, such as the linearized solution $\tilde{\mathcal{E}}_x$, to set up the optimization problem. Instead, only a lower and upper bound for each of the hyperellipsoids' angular points is required. In case there is no preliminary information, the modeler can select conservative limit points to avoid any interference from subjective assessments.

The term *global* means that a population-based optimization is used in place of the gradient-based strategy from the previous section. Among the large variety of algorithms, the DE (differential evolution) principle has proven to be an efficient method which has even been

adapted by the ESA (European Space Agency) [23]. Within the scope of this thesis, the adaptive version from the SciPy implementation is used.
A clear downside of any global optimization is the increased computational effort. For the inverse UQ, the optimization settings are adjusted such that one population encompasses 28 individuals. This means that a set of 28 hyperellipsoids must be evaluated for a single iteration. Without any changes of the algorithm, a computation time of several weeks must be foreseen which is no viable alternative to the local procedure. For this reason, the following changes are applied to the original setup:

Two-phase optimization strategy:
The first modification is to subdivide the optimization into two phases: exploration and exploitation. In the first stage, the inverse UQ is conducted with a comparatively low sample count and a limited number of iterations to narrow down the initial bounds of the design space. The updated limits are obtained by enlarging the main axis lengths from the identified explorative hyperellipsoid. In the second phase, the inverse UQ is conducted based on a larger number of samples and the updated design bounds.

Data point reduction:
Another improvement concerns the determination of $\mathcal{E}_{\mathcal{Y}_\mathrm{s}}$. In principle, only the surface points of $\mathcal{Y}_\mathrm{s}$ are of relevance for the minimum-volume enclosing ellipsoid (MVEE). In order to filter out non-relevant points, the following transformation is applied to the original point cloud:

$$\acute{\mathcal{Y}}_\mathrm{s} = \boldsymbol{R}^{-1/2}\, \mathcal{Y}_\mathrm{s}^\mathrm{u}, \tag{5.2}$$

where $\mathcal{Y}_\mathrm{s}^\mathrm{u}$ represents the standardized simulation set which is enclosed by the hyperrectangle $[-1,1]^{n_y}$. The term $\boldsymbol{R}$ denotes the empirical correlation matrix derived from $\mathcal{Y}_\mathrm{s}^\mathrm{u}$. After that, the reduced point cloud is derived by

$$\acute{\mathcal{Y}}_\mathrm{s}^\mathrm{red} = \left\{ \acute{\boldsymbol{y}}_\mathrm{s}^{(i)} \mid \|\acute{\boldsymbol{y}}_\mathrm{s}^{(i)}\|_2 > c \right\}, \tag{5.3}$$

where c denotes a threshold value for the Euclidean distance from the coordinate center. Finally, the inverse transformation from Eq. (5.2) must be applied to $\acute{\mathcal{Y}}_\mathrm{s}^\mathrm{red}$ to get back the physical values. As a result, the original set is reduced by those points located around the center and having thereof no influence on the shape of $\mathcal{E}_{\mathcal{Y}_\mathrm{s}}$.
A more comprehensive reduction could be achieved by determining the convex hull of $\mathcal{Y}_\mathrm{s}$. However, the computational burden is extremely high for large dimensions which will be discussed in greater detail within Sec. 5.1.2.

In order to compare the global optimization results with the local ones, the identical weighting factors are used for the components of the objective function. The number of sample points for the explorative and exploitative step has been set to $1,000$ and $25,000$, respectively.

		LPC		FAN		HPC		HPT		LPT		NA		NC		
	k	ΔW	η	ΔW	η	ΔW	η	ΔW	η	ΔW	η	ΔW	η	ΔW	η	CT
$\Delta\mu$ [%]	9	0.06	0.33	0.52	0.79	0.14	0.09	0.01	0.25	0.55	0.20	1.07	0.29	0.09	1.72	$228.9h$
	13	0.03	0.35	0.18	0.08	0.52	0.23	0.01	0.41	0.84	0.29	0.27	0.07	0.04	1.40	$181.0h$
	17	0.17	0.40	0.52	0.44	0.48	0.26	0.00	0.24	0.55	0.21	1.18	0.03	0.04	0.79	$184.5h$
	36	0.17	0.52	0.73	0.53	0.33	0.24	0.01	0.56	1.53	0.58	3.36	0.04	0.16	1.57	$183.7h$
	90	0.32	0.85	0.82	0.36	0.11	0.08	0.02	0.39	1.35	0.47	3.16	0.11	0.19	0.46	$182.0h$
	Lin	0.00	0.00	0.00	0.00	0.00	0.00	0.00	0.00	0.00	0.00	0.00	0.00	0.00	0.00	Obj
CoV [%]	9	0.32	0.49	0.64	0.10	1.18	0.07	0.22	0.38	0.63	0.14	0.24	0.11	0.33	0.16	0.16
	13	0.47	0.59	0.37	0.17	1.63	0.15	0.23	0.38	0.53	0.04	1.14	0.08	0.25	0.32	0.61
	17	0.49	0.54	0.60	0.15	0.96	0.10	0.25	0.44	0.41	0.12	0.49	0.10	0.24	0.13	0.21
	36	0.36	0.48	0.19	0.10	0.87	0.03	0.19	0.39	0.68	0.10	0.51	0.12	0.17	0.19	0.17
	90	0.30	0.49	0.27	0.01	0.80	0.03	0.15	0.38	0.49	0.08	0.15	0.11	0.19	0.42	0.12
	Lin	0.25	0.70	0.71	0.02	1.27	0.02	0.37	0.58	0.52	0.04	0.04	0.15	0.31	0.10	—

Table 5.3 Mean value deviations and CoVs derived from the global hyperellipsoid approach.

In Tab. 5.3, the results of the global inverse UQ are summarized in the same fashion as before, i.e., the first half represents the absolute deviation of the mean vector from the nominal values whereas the second half contains the derived CoVs. The very right column of the table shows clearly that the global strategy is able to identify better solutions in terms of the objective function value except for $k = 13$. However, the required computational time is significantly higher than for the gradient-based optimization. When putting the focus on the first half, one can see that the derived mean values have a stronger deviation from the nominal ones compared to the previous study. For example, the offset for $\Delta W^{(\mathrm{NA})}$ yields more than 3% in case of the two largest k-factors.

The two main reasons for this are the non-uniqueness of the inverse problem and the explorative characteristics of a global optimization. Due to the missing initial solution, the optimizer is given more flexibility to minimize the objective function's components. A deeper analysis reveals that this has been achieved by a lower value for $\Delta \boldsymbol{A}$, i.e., a better matching of the hyperellipsoids arc lengths. At the same time, $\Delta \boldsymbol{b}$ is getting larger which results in a higher discrepancy between the center points of $\mathcal{E}_{\mathcal{Y}_\mathrm{s}}$ and $\mathcal{E}_{\mathcal{Y}_\mathrm{m}}$.

The obtained results for the CoV are lying in a similar range as those from Tab. 5.2. However, the overall consistency between the results is lower because of the reasons discussed before. Once again, the CoV tends to decrease for increasing realizations of the k-factor which goes back to the nonlinear characteristics of the performance model. To repeat, the outcome of the global optimization study is not used in the sequel. Instead, the stochastic moments from the gradient-based approach are the basis for the analysis of the interdisciplinary SAS model as we expect a mean vector close to the parameters' nominal value.

5.1.2 Comparative Study: Hyperellipsoid vs Convex Hull Approach

The following paragraphs put the focus on the comparison between the hyperellipsoid and hyperrectangle approach. Again, the performance model serves as application case for the study but the set of input and output quantities has been decreased beforehand to run the simulations within a reasonable period.
In detail, the original response space from Tab. 5.1 is reduced by the parameters $P^{(25)}$, $P^{(3)}$, $T^{(4)}$, $T^{(49)}$, and $N1$ based on evaluating the correlation coefficients between the gas flow parameters. For the input space, the parameter selection is derived from the correlation coefficients between input and output quantities which leads to a reduction of the parameters $\eta^{(\mathrm{FAN})}$, $\eta^{(\mathrm{LPC})}$, $\eta^{(\mathrm{NC})}$, $\Delta W^{(\mathrm{LPC})}$, $\Delta W^{(\mathrm{LPT})}$ and $\Delta W^{(\mathrm{NA})}$. A deeper discussion about the variable screening is deliberately omitted here because the focus of the comparative study is not on absolute numbers but on the relative difference between the methods' results. From a mathematical point of view, the reduced performance model can be described by $g : \mathbb{R}^8 \rightarrow \mathbb{R}^7$.

Comparison of the Identified Geometrical Shapes

The following paragraphs aim to compare the convex shapes from the hyperellipsoid and hyperrectangle approach. Therefore, the reduced setup of the performance model is analyzed with both inverse UQ techniques.
At first, we start with the analysis of the local hyperellipsoid approach. As for the full-scale model setup, the Jacobian matrix is computed by using a finite difference scheme to approximate the first-order derivatives at the nominal value. After having solved Eqs. (4.25) and (4.26), the off-diagonal entries of $\boldsymbol{\Sigma}_y$ as well as $\tilde{\boldsymbol{A}}_x$ and $\tilde{\boldsymbol{b}}_x$ can be derived. Here, the value of the k-factor was exemplarily set to 15. Thus, the probability that a sample lies inside the corresponding hyperellipsoid is at least 53.3% according to the Chebyshev inequality. If the response quantities were normally distributed, the same hyperellipsoid would contain $\approx 95\%$ of the population.
Based on the approximate solution $\tilde{\mathcal{E}}_x$, the final result of the inverse UQ has been derived by a subsequent local optimization strategy. For the propagation of the uncertainty throughout the performance model, a sampling procedure with $1,000$ samples was chosen. In order to check if the number of realizations is sufficient, $10,000$ samples were generated for the final result $\mathcal{E}_x$. It figured out that only a single sample point was lying outside $\mathcal{E}_{y_\mathrm{s}}$ derived from the reduced sampling scheme.
In Fig. 5.2, the 2D projections of the output space are represented in the lower left part. Every subplot shows the projected ellipsoids $\mathcal{E}_{y_\mathrm{m}}$ and $\mathcal{E}_{y_\mathrm{s}}$ in the normalized subspace. As the objective value of the final result is rather small (< 0.02), the study is not repeated with a global optimization technique.
In a second step, the inverse UQ of the performance model was also conducted with the hyperrectangle approach. Therefore, the convex hull $\mathcal{C}_{y_\mathrm{m}}$ was created by generating $1,000$

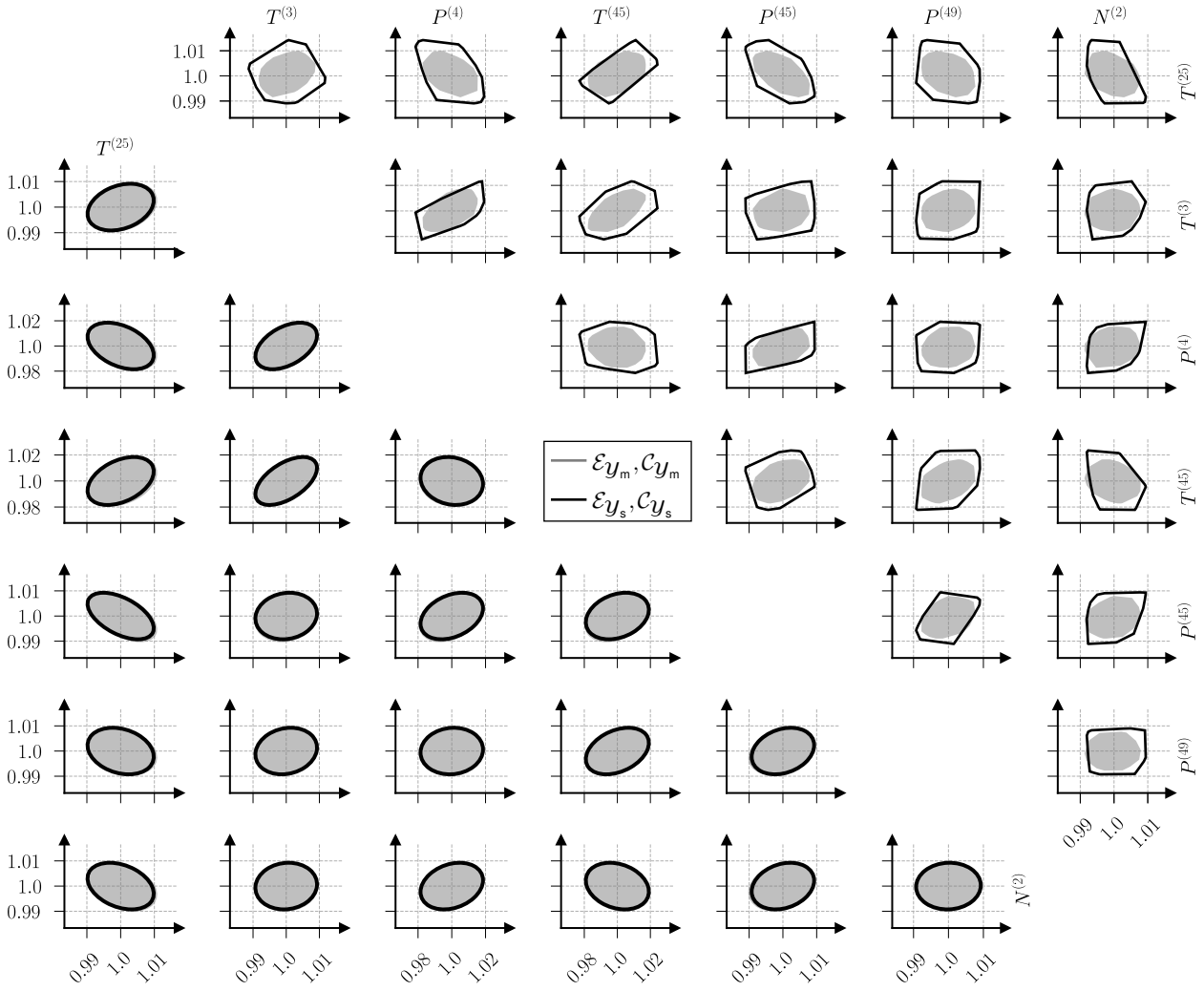

Figure 5.2 2D projections of the reduced performance model output space for the local hyperellipsoid (lower left) and hyperrectangle (upper right) approach. The response quantities are normalized with respect to the mean values.

sample points from the surface of $\mathcal{E}_{y_m}$. As the exact computation of the overlapping volume between $\mathcal{C}_{y_m}$ and $\mathcal{C}_{y_s}$ is rather time-consuming in seven dimensions, it has been replaced by a simplified procedure. The algorithm generates a set of uniformly distributed sample points within $\mathcal{C}_{y_m}$. Then, the overlapping volume is approximated by counting the number of points that lie inside $\mathcal{C}_{y_s}$. The 2D projections of $\mathcal{C}_{y_m}$ as well as the final result $\mathcal{C}_{y_s}$ are depicted in the upper right part of Fig. 5.2.

Comparing the results with the ones from the hyperellipsoid approach, one could get the impression that the discrepancy between $\mathcal{C}_{y_m}$ and $\mathcal{C}_{y_s}$ is larger as between the corresponding hyperellipsoids. However, the value of the objective function indicates a very precise matching between the two convex hulls. The obvious mismatch in Fig. 5.2 is therefore resulting from the projections.

In the following, the input uncertainties identified by the two approaches are compared with each other. For the hyperrectangle approach, the midpoint coordinates and the radii of the

			$\Delta W^{(\text{Fan})}$	$\Delta W^{(\text{HPC})}$	$\Delta W^{(\text{HPT})}$	$\Delta W^{(\text{NC})}$	$\eta^{(\text{HPC})}$	$\eta^{(\text{HPT})}$	$\eta^{(\text{LPT})}$	$\eta^{(\text{NA})}$
HE	$2a_x^{-1}$	[%]	0.07	9.58	3.65	3.19	4.22	2.08	4.27	0.41
	$\Delta\mu_x$	[%]	−0.01	-0.01	−0.04	0.01	−0.02	0.06	−0.02	-0.01
HR	$\bar{x}-\underline{x}$	[%]	0.60	5.21	2.89	1.94	2.54	1.53	1.89	0.11
	$(\bar{x}+\underline{x})/2$	[%]	−0.05	0.73	−0.03	0.01	0.12	−0.12	−0.03	−0.02

Table 5.4 Comparison between the identified hyperellipsoid (HE) and hyperrectangle (HR).

multi-dimensional interval are expressed as percentage deviation from the nominal value. In case of the hyperellipsoid approach, the center point coordinates as well as the main axis lengths of $\mathcal{E}_x$ are represented. Again, the values are normalized with respect to the deterministic solution.

When analyzing the results from Tab. 5.4 in detail, one can observe certain similarities with the analytical example from Section 4.1.2. With the exception of $\Delta W^{(\text{Fan})}$, the uncertainty ranges of $\mathcal{E}_x$ are wider than the interval widths of $\mathcal{C}_x$. This comes from the fact that the hyperrectangle $\mathcal{C}_x$ covers also the extreme combinations of the input quantities. Moreover, the center point of $\mathcal{C}_x$ and $\mathcal{E}_x$ differs only marginally from the nominal value. This confirms the impression from Sec. 5.1.1 that the performance model is approximately linear in the range close to the deterministic solution.

Assessment of the Computational Efficiency

Another important aspect when comparing the two approaches with each other is the computation time. In order to obtain a full picture of the computational efficiency, the hyperellipsoid method is also tested with a global optimization technique. For this investigation, the inverse UQ was repeated several times with a different number of sampling points. Note that the same SciPy implementations have been used as in Sec. 5.1.1.

Figure 5.3(a) compares the computation times of the global and local hyperellipsoid approach with respect to the number of sample points. For every configuration, the global optimization has been repeated three times with a different seed. Thus, it can be checked if the optimization algorithm identifies the same result for different initial populations. Here, it figured out that the repeated optimization runs lead to similar results.

In general, the computation time of the local approach is significantly shorter. Similar to the analysis of the full-scale performance model, the objective values of the final solution are slightly worse than the ones obtained from the global strategy. As discussed in the previous sections, the reason lies in choosing the nominal values as initial solution and the explorative characteristics of the global optimization strategy. Nevertheless, the local strategy provides convincing results especially when taking the savings in computation time into consideration.

Another point of discussion is the influence of the amount of sample points on the final result of

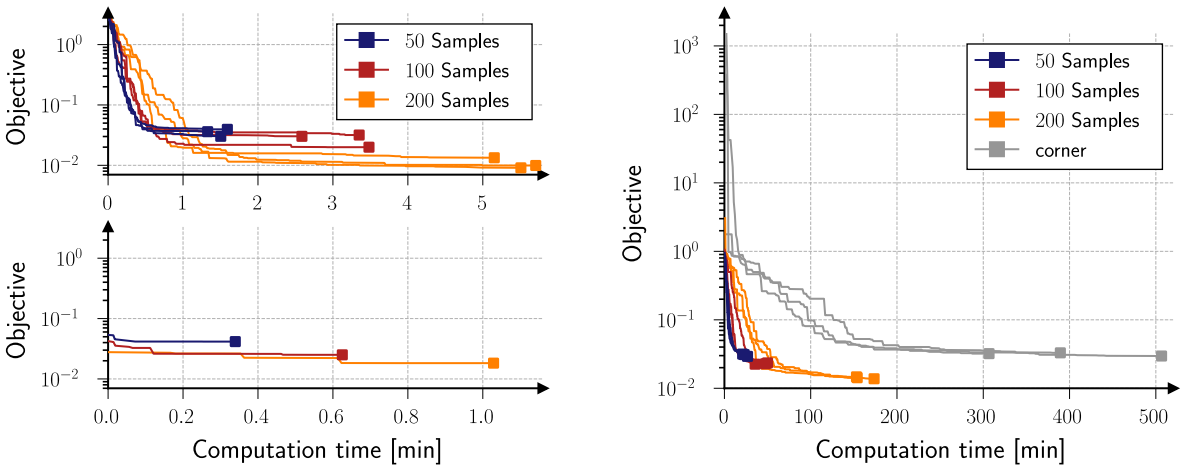

(a) Computation times for global (top) and local (bottom) hyperellipsoid approach.

(b) Computation times for hyperrectangle approach.

Figure 5.3 Comparison of the computation time between hyperellipsoid (left) and hyperrectangle (right) approach.

the optimization. For both the local and the global approach the value of the objective function decreases with an increasing number of samples. Simultaneously, the computation time is getting longer because the determination of the minimum volume ellipsoid is more expensive for a large number of samples. Even for the largest set of sample points, the global method achieves convergence within less than six minutes[3]. The inverse UQ was also conducted with the hyperrectangle approach for a different number of sample points. Again, the optimization was repeated three times with varying seed values to evaluate the robustness of the inverse UQ. In addition, a specific sampling procedure which comprises only the corner points of the hyperrectangle in the input space was applied. The results are summarized in Fig. 5.3(b).

When comparing the results with the hyperellipsoid approach, one can observe certain similarities. Increasing the number of samples has the consequence that the uncertainty quantification requires more time. Furthermore, the objective values of the converged solutions are decreasing.

At first glance, it seems that the results from the corner point sampling do not coincide with the conclusions drawn before. A hyperrectangle in the eight-dimensional input space has 256 corners. Thus, one would expect that the computation time is only slightly higher than in case of 200 sample points. Furthermore, the objective function values should not deviate too much from the sampling procedure with 200 samples. However, the computation takes considerably more time and the objective function values of all optimization runs are even higher than the ones obtained when generating only 50 samples in the input space.

In principle, both observations can be attributed to the approximately linear characteristic of the performance model. In case of the corner point sampling procedure, almost all sample points represent a vertex of the convex hull in the output space. In contrast, when generating

[3] Intel(R) Xeon(R) CPU E3-1271 v3 @ 3.60GHz

sample points uniformly within a hyperrectangle, only a fraction of the samples corresponds to a vertex of $\mathcal{E}_{\mathcal{Y}_s}$. For example, the convex hull which is derived from 200 samples has only 170 vertices. The number of vertices has a direct impact on the computation time of the convex hull as can be seen in Eq. (5.4).

Still the question remains, why the objective function values are comparatively high. Propagating a hyperrectangle throughout the performance model by its corner points leads to a convex hull in the output space which takes the shape similar to a skewed hyperrectangle. Since the convex hull is compared with a hyperellipsoid, a perfect matching between these two geometries is not possible. This hypothesis can be supported by propagating the input uncertainty obtained from the uniform sampling strategy throughout the performance model once again by a corner point sampling strategy and comparing the newly obtained objective function value with the original one. In case of 200 sample points, the optimized solution has an objective value of 0.013. The corresponding objective value obtained from the corner sampling procedure is 0.14.

On the whole it can be stated that the hyperrectangle requires significantly more time than the hyperellipsoid approach. Especially for a large number of samples, the discrepancy becomes extremely clear. For 200 sample points, the inverse UQ takes roughly five minutes in case of the global hyperellipsoid approach but roughly 2.5 hours for the hyperrectangle approach.

The main reason for the discrepancy in the computation time are the different time complexities for determining $\mathcal{C}_{\mathcal{Y}_s}$ and $\mathcal{E}_{\mathcal{Y}_s}$. The complexity for computing the convex hull based on the QuickHull algorithm of a given set of points yields for high dimensions ($d > 10$) in the worst case

$$\mathcal{O}(v^{d/2}/(d/2)!), \tag{5.4}$$

where v is the number of vertices of the hull [16]. Thus, the computation time grows exponentially with respect to the dimensionality of the problem. In contrast, the approximation of the MVEE based upon the Khachiyan algorithm has an upper bound time complexity of

$$\mathcal{O}(pd^2(\varepsilon^{-1} + \ln(p) + \ln\ln(p))), \tag{5.5}$$

where ε is related to the accuracy and p denotes the number of enclosed points [93]. Regarding the computation time, the hyperellipsoid approach is especially beneficial for problems with a high-dimensional output space because the computation of the convex hull can get extremely time-consuming in such cases. Moreover, analyzing the geometric discrepancy between two convex hulls is also a time-consuming operation in high dimensions whereas the comparison between two hyperellipsoids requires less effort.

The previous paragraphs have demonstrated the capability of two different methods to conduct an inverse UQ under scarce data. First, the newly introduced concept from Sec. 4.1.3 has been applied to the full-scale performance model with two different optimization strategies. Within the following studies of the interdisciplinary SAS model, the results from the local opti-

mization algorithm are used because they show a higher consistency for the different setups compared to the global optimization technique.
In addition, a comparison with the interval-based UQ method from Sec. 3.4.2 has been carried out for a reduced setup of the performance model. A main aspect was to show the difference between the input quantities' uncertainty representation, i.e., the geometrical dimensions of the hyperrectangle and hyperellipsoid. Apart from that, a comprehensive study on the computation time has been conducted which shows the superior efficiency of the hyperellipsoid method in high dimensions.

5.2 Analysis of the Interdisciplinary Secondary Air System Model

Upon the stand-alone analysis of the performance calculation, we can proceed with the investigation of the interdisciplinary SAS model. The basis for all of the studies is the input quantities' uncertainty characterization. Section 5.2.1 covers the modeling approach of some selected parameters which are based upon scarce information. After that, an epistemic sensitivity analysis (SA) is performed in Sec. 5.2.2 to reduce the complexity of the interdisciplinary system. Finally, Sec. 5.2.3 addresses the issue of finding a robust optimum for the geometric design parameters.

5.2.1 Forward Uncertainty Quantification of Selected Input Quantities

The extensive summary in Section 2.1.2 has shown that the total set of input parameters can be categorized according to their root cause in two groups: engine-to-engine and flight-to-flight variation. For both classes, the uncertainty quantification is demonstrated for a small set of parameters within the following subsections. Contrary to the inverse UQ studies from Sec. 5.1, the available information is directly related to the parameters which is why it is referred as forward UQ.

Flight-to-Flight Variation

As can be seen from Tab. 2.1 on page 19, the flight-to-flight variation affects the thrust level (X_{Thr}), flight altitude (X_{Alt}), ambient temperature (X_{Temp}) and Mach Number (X_{Mach}). Within the next paragraphs, the underlying data bases and the resulting modeling approaches for these four quantities are discussed.
The parameter X_{Temp} expresses the temperature deviation from the ISA (international standard atmosphere) and is important for the consideration of changing weather and climate conditions. The primary data source comprises two sets of temperature increments describing the offset from the ISA condition for a WWA (world-wide average) as well as a hot operator

scenario. In principle, the two data sources are represented by nine decile values

$$\mathcal{X}_{\text{WWA}} = \left\{ D^{(1)}_{\text{WWA}}, \ldots, D^{(9)}_{\text{WWA}} \right\}, \quad \text{and} \quad \mathcal{X}_{\text{HOT}} = \left\{ D^{(1)}_{\text{HOT}}, \ldots, D^{(9)}_{\text{HOT}} \right\}, \tag{5.6}$$

which represent the cumulative distribution function (CDF) value at the 10th, 20th, $\ldots, 90$th percentile. Both of them are depicted by the black and red step function in Fig. 5.4(a).
Basically, the uncertainty on X_{Temp} is represented as distribution-free p-box. If the temperature deviation of an arbitrarily chosen jet engine is measured over the whole life time, any kind of cumulative distribution between the red and black curve is a possible realization. Jet engines operating exclusively in cold regions could be characterized by a cumulative distribution which is not enclosed by the p-box. Since cold operators are uncritical for the design process, no specific data has been gathered. Thus, the p-box concept is able to account for the lack of knowledge regarding the geographical region in which the jet engine goes into action.
To transfer the free p-box form into a distributional one, we make use of the beta-distribution due to its high flexibility. In short, this family is defined within the unit-interval by two shape parameters α and β. A more comprehensive summary has been given in Sec. 4.1.4. Here, the goal is to extract all combinations for α and β leading to a CDF that lies inside the step-function envelopes in Fig. 5.4(a). Formally, this procedure is formulated by

$$\begin{aligned} \{\alpha, \beta\} = \left\{ \alpha, \beta \;\middle|\; D^{(i)}_{\text{WWA}} \leq F_X^{-1}(q^{(i)} | \alpha, \beta) \leq D^{(i)}_{\text{HOT}} \right\} \qquad & \text{for } i = 1, \ldots, 9 \\ \text{with} \quad \alpha, \beta \quad & > 1.0 \\ \sigma[X_{\text{Temp}}] \quad & \geq 1/12 \, (\overline{X}_{\text{Temp}} - \underline{X}_{\text{Temp}}), \end{aligned} \tag{5.7}$$

where $q^{(i)}$ stands for the above-mentioned percentiles. The first constraint in Eq. (5.7) ensures that exclusively unimodal CDFs are part of the distributional p-box. Further, the possible

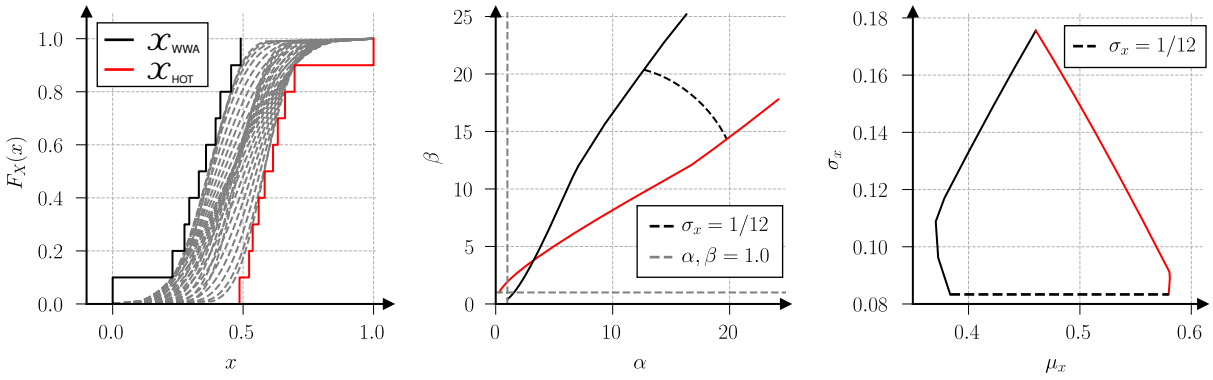

(a) Distribution-free and distributional p-box.

(b) α-β parameter space.

(c) μ_x-σ_x space.

Figure 5.4 Modeling approach for the uncertainty on the ambient temperature (X_{Temp}). The original data set has been normalized to unity.

shape-parameter space is restricted by a lower limit on the standard deviation. In detail, the minimum value for $\sigma[X_{\text{Temp}}]$ is defined by one twelfth of the whole ambient temperature range. Figure 5.4(b) illustrates all restrictions from Eq. (5.7) and the corresponding feasible set of α-β combinations. The black and red solid line depicts the p-box envelopes derived from $\mathcal{X}_{\text{WWA}}$ and $\mathcal{X}_{\text{HOT}}$, whereas the unimodality and standard deviation limitation are shown by dashed lines. Note, that the data from $\mathcal{X}_{\text{WWA}}$ and $\mathcal{X}_{\text{HOT}}$ as well as the σ_x-constraint has been mapped to the unit space beforehand.

A clear drawback of this modeling approach is that the distributional parameters do not contain direct stochastic information. For this reason, the bounds on the α-β space are transferred to the μ_x-σ_x domain shown in Fig. 5.4(c). One can see that the stochastic moments are no longer independent from each other which must be considered in the subsequent studies. The closer μ_x is to the lower or upper bound, the smaller the allowable range for the standard deviation.

Next, we deal with the flight altitude (X_{Alt}) and Mach number (X_{Mach}). Contrary to the ambient temperature, varying FCIs (flight cost indices) are identified as main driver for the uncertainty. In order to understand the relation between this index and the variation of altitude and air speed, we have to dive into the topic of flight profile calculation.

The planning of an optimal flight route is affected by the goal conflict of minimizing time (C_{t}) and fuel costs (C_{f}) at the same time. A low aircraft speed certainly reduces the fuel costs but it automatically leads to higher cabin crew costs, leasing costs or, in the worst case, to compensation payments if passengers cannot get their onward flights. Modern flight management systems thereof take the flight cost index (FCI) into account, which is given by the ratio [160]

$$\text{FCI} = \frac{C_{\text{t}}}{C_{\text{f}}} \quad \left[\frac{\text{kg}}{\text{min}}\right]. \tag{5.8}$$

To summarize, the FCI has a significant impact on the flight trajectory and the aircraft speed during the different flight phases. The latter, also referred to as ECON speed, is of key importance to minimize the overall costs. Doubtlessly, the flight profile is also affected by other

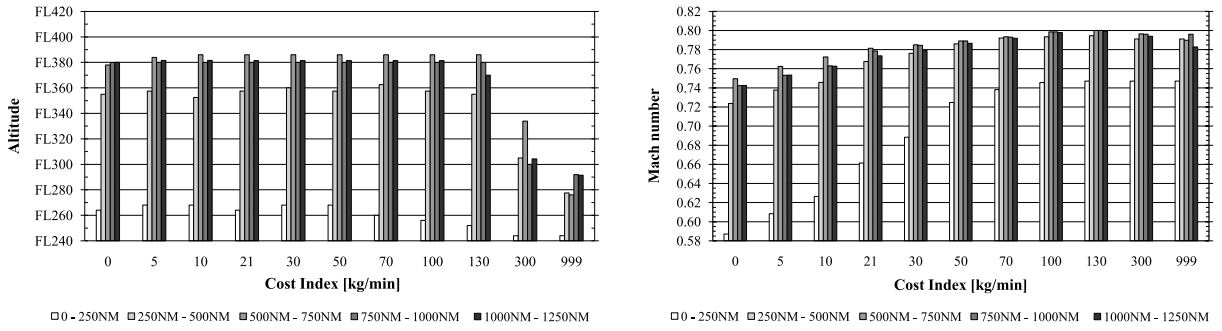

(a) Flight altitude variation.

(b) Cruise speed variation.

Figure 5.5 Flight altitude (left) and cruise speed (right) for different FCIs and flight distances. Both figures are taken from [148].

elements, such as weather or air traffic conditions. For the study case within this thesis, we concentrate exclusively on the FCI due to its predominant role.

In [148], more than $4,000$ flight planes have been simulated for FCIs between 0 and 999 kg/min to analyze its impact on the flight trajectory. The relevant data for our investigation is the average speed and flight altitude during the cruise phase shown by the two diagrams in Fig. 5.5. Both of the plots sort the simulation results with respect to the FCI and flight distance.

The first step of the uncertainty quantification is to extract the minimum and maximum value of X_{Alt} and X_{Mach}. For both parameters, the data points for flight distances of less than 250 NM (nautical mile) are falling out of line. As these missions are extremely scare, they are not considered for the UQ approach. In case of the aircraft speed, the remaining data points are mainly located above 0.77 Mach. This information is considered by introducing an upper bound on the CDF at the 20th percentile. Based on the limitation, a distribution-free p-box is deduced, see Fig. 5.6(a). Together with additional constraints on the standard deviation, a distributional p-box representation is derived with the help of the beta-distribution family. The modeling approach for X_{Mach} is determined in a similar fashion but not explained here in further detail.

A closer examination of Fig. 5.5 reveals a certain correlation between X_{Alt} and X_{Mach} which is why the parameters may not be treated as independent. For high FCI values (> 130 kg/min), a strong decrease of the flight altitude can be observed whereas the cruise speed is placed in the upper range (> 0.78 Mach). Therefore, a coupling between $\mu[X_{\text{Alt}}]$ and $\mu[X_{\text{Mach}}]$ is introduced which prevents the combination of a low mean value for altitude and Mach number. Figure 5.6(b) shows the restricted $\mu[X_{\text{Alt}}]$-$\mu[X_{\text{Mach}}]$ space allowing only mean value combinations inside the polygon.

The last parameter, which has not been mentioned so far, is the adjusted thrust level (X_{Thr}). By logic, the generated thrust is strongly correlated to the Mach number. Again, the dependency is modeled by introducing a coupling between the mean values of X_{Mach} and X_{Thr}.

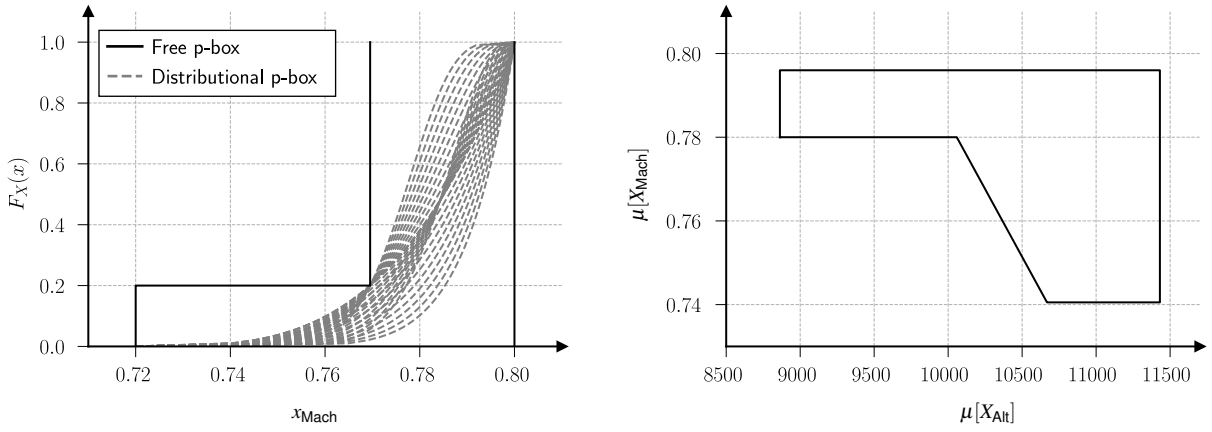

(a) P-box representation of X_{Mach}.

(b) Coupling between $\mu[X_{\text{Alt}}]$ and $\mu[X_{\text{Mach}}]$.

Figure 5.6 Modeling approach for X_{Mach} (left) and mean value coupling (right).

Contrary to the previous case, a one-by-one dependency is introduced which degrades X_{Thr} to a pure aleatory parameter. The functional relationship is derived from an MTU-internal database which comprises the performance parameters for various flight missions.
Of course, the direct dependency is a simplified UQ strategy because it neglects the interaction with other parameters like the X_{Alt} for example. The low level of detail is compensated by assigning a large standard deviation to X_{Thr} which is a reasonable approach during an early stage of the design process.

Engine-to-Engine Variation

The second category encompasses parameters from the performance model as well as geometrical quantities of the SAS. The parameters from the performance model have already been discussed within Sec. 5.1 and will not be covered here. Due to the large number of geometrical parameters of the SAS, a detailed review on the p-box concept is only shown for $X_{\text{IAS1\_lip\_e}}$.
In short, this variable describes the sealing lip eccentricity at the first inner air seal (IAS) which is, in combination with other parameters, one of the main influencing factors on the overall gap width. A detailed description about this sealing type has been given in Sec. 2.1.2. The root cause for the uncertainty on $X_{\text{IAS1\_lip\_e}}$ lies in the manufacturing process. If the component was produced perfectly no eccentricity would occur which corresponds to a value of zero for $X_{\text{IAS1\_lip\_e}}$. However, a certain offset is unavoidable under real conditions and tolerated as long as the eccentricity does not exceed certain threshold values.
As the eccentricity value is not documented, we are facing a typical lack-of-knowledge uncertainty source. Basically, only the nominal and lower/upper bound is available to perform the UQ. The existence of strict bounds makes the usage of distribution families with closed intervals attractive. Again, the beta-distribution type is preferred because of its high flexibility. For the definition of the distributional p-box, also experience-based knowledge from the manufacturing department is used to exclude illogical CDFs. The provided information has led to the assumption that the *true* mean and median value do not deviate by more than 10% from the nominal one. Additionally, a criterion on the unimodality and a lower limit on the standard deviation is introduced.
Figure 5.7 summarizes the known information on $X_{\text{IAS1\_lip\_e}}$ and the resulting modeling approach. On the left, i.e., in Fig. 5.7(a), the free p-box and its distributional representation are illustrated in the unit space. It can be seen that the corresponding constraint regarding the mean does not lead to a further limitation compared to the median value condition. This goes back to the fact that the p-box envelopes, depicted by the dash-dotted line, enclose CDFs with mean values other than the prescribed ones. The remaining two figures depict the constraints in the α-β and μ_x-σ_x space. Due to the dominating role of the median constraints, Fig. 5.7(b) contains exclusively the restrictions on the 50th percentile. Any shape parameter combination

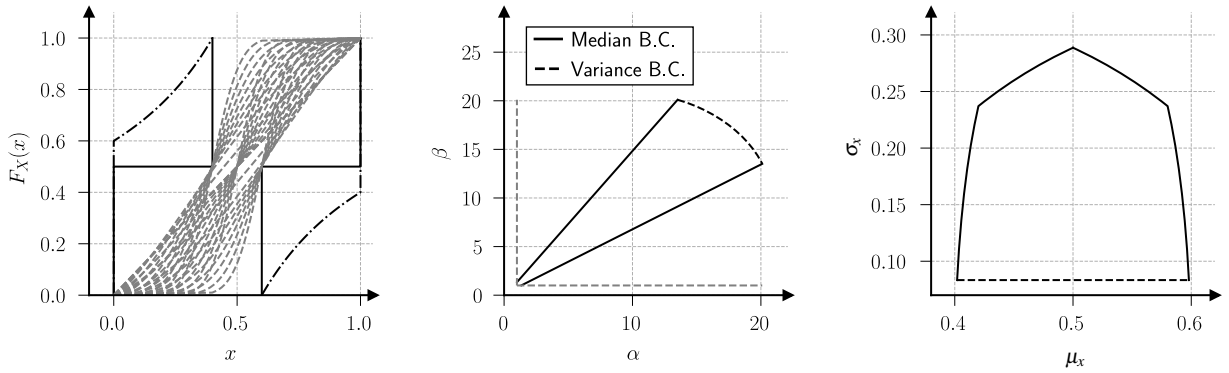

(a) Probability-box representation. (b) Feasible α-β space. (c) μ_x-σ_x space representation.

Figure 5.7 Modeling approach for the sealing lip eccentricity of the first inner air seal ($X_{\text{IAS1\_lip\_e}}$).

complying with this condition leads automatically to a fulfillment of the mean criterion. A noteworthy aspect is that the median constraints repeal the independency between μ_x and σ_x, see Fig. 5.7(c).

To repeat, transferring the available knowledge into a distributional p-box concept is a necessary requirement for applying the NISS strategy in context of the robust design optimization (RDO). Apart from that, the distributional representation helps to reduce the degree of conservatism. In contrast to the modeling of X_{Temp}, the free p-box for $X_{\text{IAS1\_lip\_e}}$ still contains some undesired CDFs such as the envelopes themselves. Thus, the segregation of CDFs caused by the change of the p-box representation cannot be interpreted as a pure loss of information. As mentioned before, the remaining parameters are not analyzed in detail because the UQ concepts for lack-of-knowledge uncertainties differ only slightly from the ones explained so far. For the rim seal parameters ($\#22, \ldots, \#27$) and the variables corresponding to the stator eccentricity of the inner air seals ($\#30, \#33$), the available information is rather similar to the sealing lip eccentricity. On the basis of the manufacturing tolerances, distributional p-boxes are derived which also take assumptions about the expected mean and median range into account.

All the other noise factors listed in Tab. 2.1 are categorized as aleatory because the underlying database enables the assignment of specific distribution functions. For the turbine blade platform gaps ($\#19, \#20, \#21$), we can rely on a set of approximately $1,000$ measurements from a similar jet engine. In Fig. 5.8(a), the histogram including the representative probability distribution is shown for the platform area of the first rotor stage. Here, a Gaussian distribution has been fitted with a p-value of 0.84 which indicates strong evidence in favor of the null hypothesis.

The situation is similar for the parameters related to the sealing lip diameter variation of the first and second inner air seal. In this case, the total data set comprises 682 measurements characterized by the right-skewed histogram in Fig. 5.8(b). It turned out that the three-parameter burr distribution fits the data well with a p-value of 0.45.

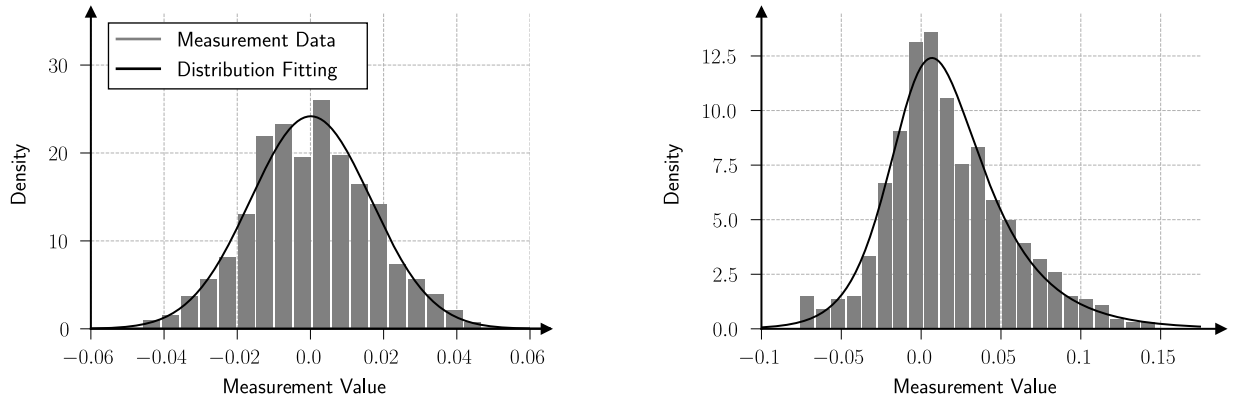

(a) Normalized measurement data for $X_{\text{Plat\_1}}$.

(b) Normalized measurement data for $X_{\text{IAS1\_lip\_c}}$.

Figure 5.8 Measurement data representation and distribution fitting of the turbine blade platform gap width (left) and the sealing lip diameter of the inner air seal (right). Both data sets have been scaled w.r.t. to their nominal values.

Last but not least, some explanatory remarks about the modeling of the design parameters' uncertainty are still to be made which have their origin in the engine-to-engine variation. In general, the uncertainty representation follows the same scheme for every entry of $\mathbf{X}^{\text{d}}$. As for most of the noise factors, strict bounds limit the feasible design space which makes the usage of the beta distribution advantageous. Even though the standard deviation is not exactly quantifiable, an aleatory treatment is preferred by assigning a crisp value to the stochastic moment. Accordingly, a comparatively large standard deviation value is chosen to cover conservative scenarios for the subsequent robustness assessment and optimization. The reason for the probabilistic treatment of the epistemic uncertainty will be described within the scope of Sec. 5.2.3. A thorough explanation of the design parameters' database is skipped at this point because the focus of the dissertation lies on the modeling of epistemic uncertainty sources. Moreover, non-normalized data may not be illustrated for reasons of confidentiality.

Having found an appropriate description for all design and noise factors, the foundation has been laid to continue with the screening of the epistemic parameters. To summarize, the input space of the interdisciplinary SAS model is characterized by 33 noise parameters among which 28 are modeled by distributional p-boxes. Bearing in mind that some performance parameters are quantified by p-box definitions with only one uncertain shape parameter, we are faced with a 40-dimensional uncertain hyperparameter space. Considering all of the shape parameters would require a tremendous computational effort which is why a reduction of the hyperparameter space is inevitable.

5.2.2 Epistemic Variable Screening

For the epistemic SA the method introduced in Sec. 4.2 is applied. Without going into detail, the basic idea is to derive the impact of all uncertain hyperparameters on the variation of the response mean and standard deviations. The core concept of the screening method rests upon the conduction of repeated uncertainty propagations. Instead of using a sampling-based approach, the strategy is based on Taylor series expansions. The great benefit is that only a set of derivatives must be evaluated at the various expansion points in the epistemic space which requires significantly less computational effort in high dimensions.

Before starting with the examination of the screening results, the required modifications are discussed which are necessary for adapting the screening strategy to the industrial use case. In its original configuration, the method assumes a totally independent set of hyperparameters, i.e., the epistemic space can be described by a hyperrectangle. Even though the noise factors themselves are independent, we have to take certain dependencies between the stochastic descriptors of the single parameters into account. Thereof, the mean and standard deviation cannot be varied individually over the full uncertainty range while fixing the other moment to its nominal value.

The modification of the grid point layout for dependent hyperparameters can be explained by Fig. 5.9. The black-dotted points mark the data set for evaluating the first-order index (FOI) associated to the uncertain mean value. It can be seen that changing the first stochastic moment goes along with a change of the standard deviation to avoid unfeasible hyperparameter combinations. In the current example, the effect does not occur for determining the standard deviation's main effect because of the symmetry of the hyperparameter space with respect to μ_x.

The modeler must be aware that the resulting first-order indices (FOI_μ, FOI_σ) may be influenced by the coupling. For this reason, it has been decided not to sort out single hyperparameters of a noise factor. By proceeding in this way, the inadvertent reduction of significant

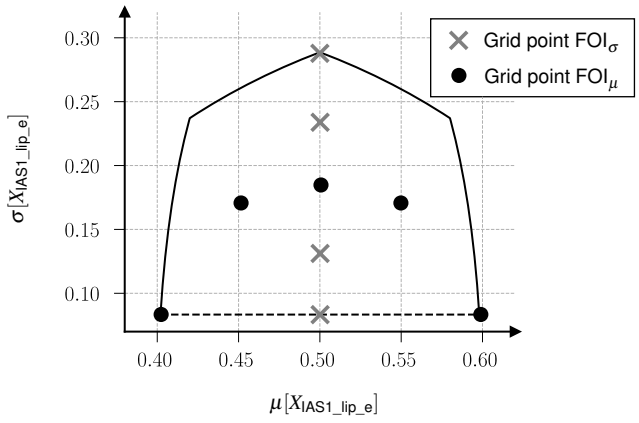

Figure 5.9 Taylor series grid points for the determination of the first-order effects of $X_{\mathrm{IAS1\_lip\_e}}$.

parameters can be ruled out at the price of reaching not the full simplification potential.
Within the next paragraphs, the screening results are summarized. Due to the large number of epistemic variables, a two-step procedure is carried out. First, only the performance model is investigated with the covert goal to scale down the epistemic performance parameter space. After that, we continue with the more time-consuming analysis of the interdisciplinary SAS model.

Monodisciplinary Sensitivity Analysis of the Performance Model

As stated before, we put the focus on running only the performance calculation without considering the subsequent models. The total set of input parameters is then comprised by 18 quantities which are all described by p-boxes. The ones characterizing the ambient conditions are equipped with two hyperparameters whereas the definition of flow capacity and efficiency has only one uncertain hyperparameter, namely the skewness. All in all, the epistemic parameter set encompasses 20 input quantities.
The decision whether to keep or retain the epistemic uncertainty relies on the value of the first- (FOI_{μ}, FOI_{σ}) and second-order (SOI_{μ}, SOI_{σ}) indices, see Eqs. (4.44) and (4.46). The relevant response quantities of the performance calculation are $P^{(45)}$, $T^{(45)}$, $P^{(49)}$ and $T^{(49)}$, which stand for the temperature and pressure at the inlet and outlet of the LPT. In addition, the station boundary conditions $P^{(3)}$ and $W^{(25)}$ are of interest as they play a decisive role for the cooling mass flow supply, see Sec. 2.1.1.
In Fig. 5.10, the indices are displayed as percentage values in tabular form for $P^{(45)}$. The upper triangle represents the screening indices for the response mean and the lower part for the standard deviation. For example, the first-order index $\mathrm{FOI}_{\mu}(\mu[X_{\mathrm{Mach}}])$ indicates that the uncertainty on $\mu[X_{\mathrm{Mach}}]$ causes a variation of 13.18% on $\mu[Y_{P^{(45)}}]$. Note, that the two parts of the table must be viewed separately because they both include the diagonal values.
A p-box is degraded into a pure probabilistic representation if its first- and second-order indices are small for all of the response quantities under investigation. As a threshold value for the parameter reduction, we have chosen 5% and 10% for the mean and standard deviation indices, respectively. From the inspection of Fig. 5.10, none of the parameters comes into question according to the previous criteria. Bearing in mind that the second-order indices also enclose the grid points for deriving the first-order indices, its value should be compared with the corresponding FOIs. As an example, the interactive effect between $\gamma[X_{\eta^{(\mathrm{Fan})}}]$ and $\mu[X_{\mathrm{Mach}}]$ on the response standard deviation is 20.14% but the FOI of the latter is 20.11%. Hence, the pure interactive effect between these hyperparameters is negligible and $\gamma[X_{\eta^{(\mathrm{Fan})}}]$ belongs to the potential group of reducible parameters. The screening results for the remaining station boundary conditions can be found in Appendix C.1. For the final decision, the maximum screening indices among all response quantities are essential. As a result, it has been found out that the variation of the skewness is of subordinate importance and thereof treated as crisp

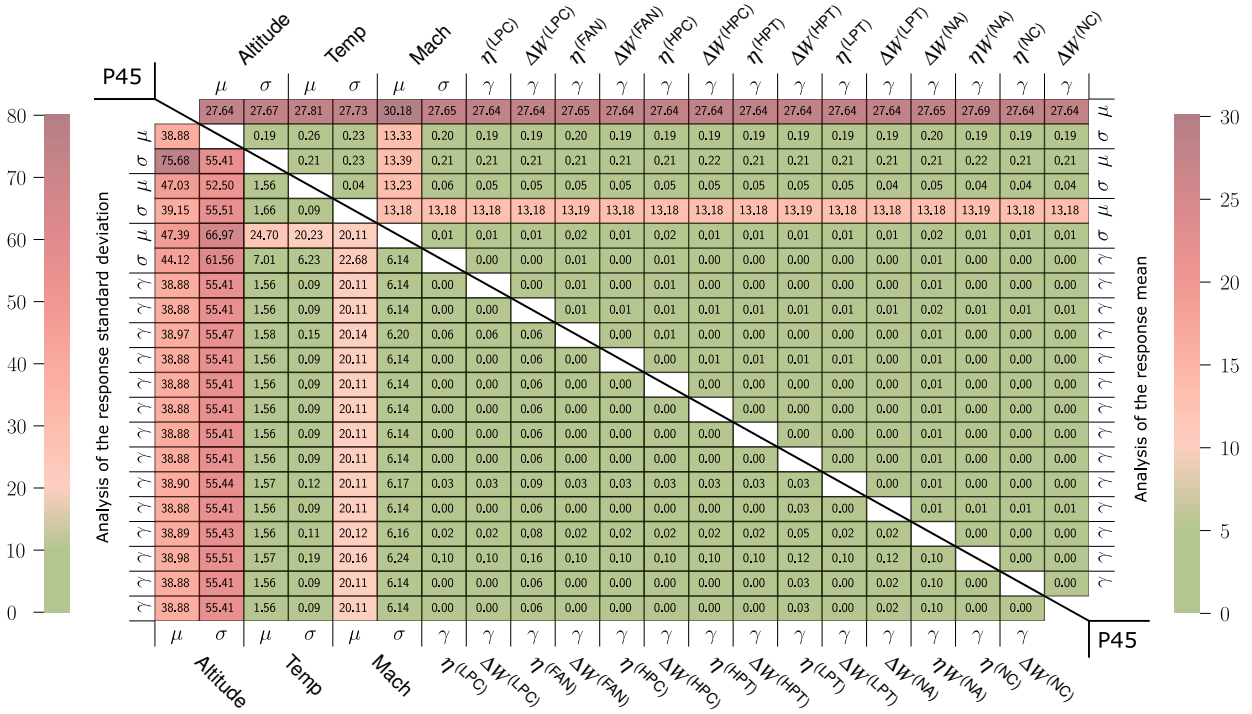

Figure 5.10 Variable screening of the performance model for $P^{(45)}$ showing the first- and second-order indices for the response mean (upper right) and standard deviation (lower left) triangle.

value. Contrary, all p-box definitions of the ambient conditions are retained. With the monodisciplinary investigation, a tremendous reduction has been achieved which saves computational effort for the second step of the screening procedure.

Interdisciplinary Sensitivity Analysis of the Secondary Air System

For the second part, the set of input quantities is extended by the geometrical parameters of the SAS model. Among those, ten quantities are represented as p-box with uncertain mean and standard deviation. Together with the ambient conditions, we have to consider a 26-dimensional uncertain hyperparameter space. A major difference to the previous study is that none of the p-box representations include the skewness.

Since running the multidisciplinary model is more time-consuming, only a first-order Taylor series is used for the uncertainty propagation at the various expansion points. As a reminder, the approximation of μ_y and σ_y in the previous study was derived from a second- and third-order expansion to capture the impact of the varying skewness factor.

The response QoIs are given by six critical cooling mass flow rates located at the transition between SAS and the core gas path. At each of the three LPT rotor stages, the outflowing cooling air before and after the rotor is analyzed. The parameters' abbreviation is $Y_{\text{Rot\_1\_l}}$, $Y_{\text{Rot\_1\_r}}$, $Y_{\text{Rot\_2\_l}}$, $Y_{\text{Rot\_2\_r}}$, $Y_{\text{Rot\_3\_l}}$ and $Y_{\text{Rot\_3\_r}}$ where the number is standing for the stage and the subscripts "l" and "r" for left and right, respectively. For a detailed explanation on the SAS as well as the location of the above-mentioned cooling flows, the reader is referred to Sec. 2.1.

Apart from lowering the order of the Taylor series expansion, the interdisciplinary variable

screening is identical to the stand-alone analysis of the performance parameters. Again, just a single response quantity is shown here whereas the remaining ones can be found in Appendix C.2. In the following, $Y_{\text{Rot\_2\_l}}$ is chosen as exemplary quantity of interest (QoI) and summarized by Fig. 5.11 in the same fashion as before.

One important finding is that the ambient conditions have a significant effect on $Y_{\text{Rot\_2\_l}}$ with regard to its mean value variation which confirms the decision from the previous study to keep those hyperparameters. Taking a look at the response variance, a surprisingly high impact of $\mu[X_{\text{Alt}}]$ and $\mu[X_{\text{Mach}}]$ can be identified compared to the low significance of the parameters' standard deviation. This effect is due to the various coupling conditions which prevents a clear separated evaluation of the hyperparameters' individual importance.

When putting the focus on the set of the geometric SAS quantities, the parameters related to the first inner air seal, i.e., $X_{\text{IAS1\_lip\_e}}$ and $X_{\text{IAS1\_stat\_e}}$, are standing out. Especially the epistemic uncertainty components of the stator eccentricity have a huge impact on the response mean variation expressed by a FOI of more than 100%. In addition, $X_{\text{IAS1\_stat\_e}}$ is one of the few geometrical quantities that has a noticeable impact on the variance of $Y_{\text{Rot\_2\_l}}$. Besides from that, Fig. 5.11 shows also a considerable influence of $\mu[X_{\text{Rim\_2\_l}}]$ on the mean variation. The identification of these specific parameters is a meaningful outcome because the spatial distance between the components and the cooling mass flow location is short.

A closer inspection of the second-order indices reveals that there are only few relevant interactions which occur mainly between those quantities for which high main effects have been detected. Analyzing the interactions between the geometric descriptors shows that the SOIs (second-order indices) are mostly obtained by superposing the main effects.

In case of the ambient condition parameter set, the situation is different. Here, the interactive effect is not directly deducible from the first-order indices. The cause is partially attributable to the fact that the performance parameters influence the cooling system indirectly throughout changing boundary conditions whereas the geometrical quantities have a direct impact on the SAS performance.

Again, the reduction of the hyperparameter space is based on determining the maximum screening indices from the six cooling mass flow rates. The limit values for deciding on whether to degrade a p-box representation remain unchanged compared to the performance model investigation. Finally, all of the uncertain rim seal hyperparameters could have been declared as insignificant except the ones from $X_{\text{Rim\_2\_l}}$. From a first glance, the reduction does not seem to be meaningful because these parameters directly affect the cooling airflows under investigation. However, one has to keep in mind that we analyze the impact on the stochastic moments rather than the model response which does not reflect the importance of the parameters themselves. Furthermore, the significance of a hyperparameter certainly correlates with its interval width.

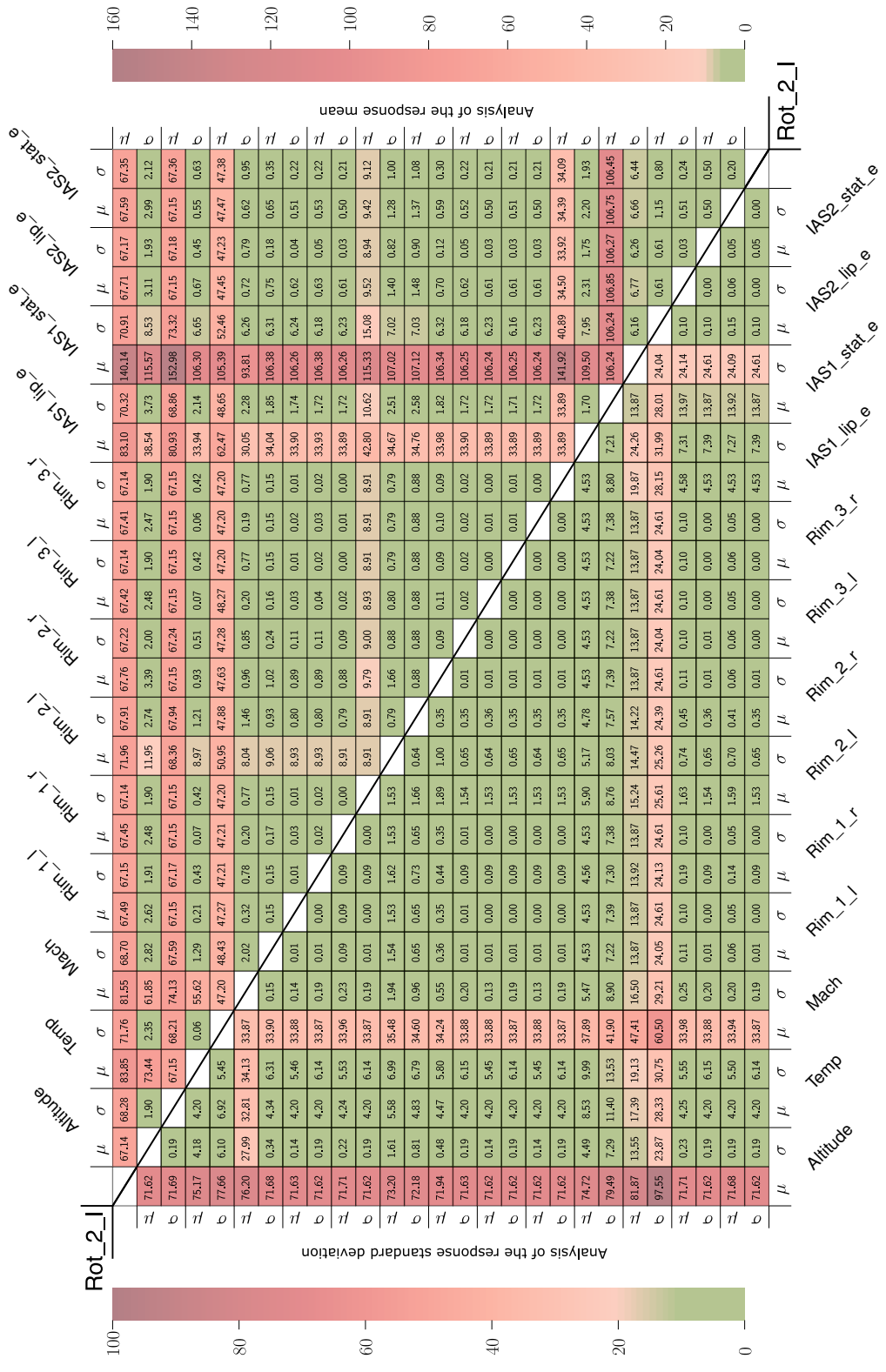

Figure 5.11 Variable screening of the interdisciplinary SAS model for $Y_{\text{Rot\_2\_l}}$ showing the first- and second-order indices for the response mean (upper right) and standard deviation (lower left) triangle.

In Tab. 5.5, a final overview is provided for the noise factors' uncertainty representation after the screening. To summarize, the epistemic SA has helped to clearly simplify the complexity of the parameter setup. The number of uncertain hyperparameters could be decreased from initially 40 to 16 stochastic moments which is equivalent to a reduction of 60%. In view of the subsequent robust design optimization, the parameter screening is an important step because the total parameter space will be further enlarged by the random vector $\mathbf{X}^{\mathrm{d}}$ containing the set of design parameters.
A drawback of the method is that it returns more a qualitative instead of a quantitative measure for the parameters' importance due to the Taylor series based uncertainty propagation. An exact ranking is thereof only possible if the screening indices demonstrate a significant difference.

Model	Source	Aleatory	Hybrid
Performance	engine-to-engine	$\boldsymbol{X}_{\eta^{(i)}}$, $\boldsymbol{X}_{\Delta W^{(i)}}$	—
	flight-to-flight	X_{Thr}	X_{Alt}, X_{Temp}, X_{Mach}
SAS	engine-to-engine	$X_{\mathrm{Plat\_1}}$, $X_{\mathrm{Plat\_2}}$, $X_{\mathrm{Plat\_3}}$, $X_{\mathrm{Rim\_1\_l}}$, $X_{\mathrm{Rim\_1\_r}}$, $X_{\mathrm{Rim\_2\_r}}$, $X_{\mathrm{Rim\_3\_l}}$, $X_{\mathrm{Rim\_3\_r}}$, $X_{\mathrm{IAS1\_lip\_c}}$, $X_{\mathrm{IAS2\_lip\_c}}$	$X_{\mathrm{Rim\_2\_l}}$, $X_{\mathrm{IAS1\_lip\_e}}$, $X_{\mathrm{IAS1\_stat\_e}}$, $X_{\mathrm{IAS2\_lip\_e}}$, $X_{\mathrm{IAS2\_stat\_e}}$
Total number of parameters:		25	8

Table 5.5 Reduced set of noise factors $\mathbf{X}^{\mathrm{n}}$ after the epistemic variable screening.

5.2.3 Robust Design Optimization under Hybrid Uncertainties

The final step deals with optimizing the entries of the design vector $\mathbf{X}^{\mathrm{d}}$ to ensure a sufficient cooling mass flow supply at the transition between SAS and core gas flow. Similar to the uncertainty studies from the previous chapters, the main focus is put on the appropriate treatment of the epistemic uncertainty components.
This section is subdivided into two parts. First, a robustness assessment of the SAS is conducted. The purpose of this paragraph is to illustrate the problem statement for the following optimization as well as the need for the advanced NISS scheme from Sec. 4.3.1. The second paragraph contains the actual RDO. Besides from the results discussion it includes how to further exploit the properties of the NISS approach to maximize the efficiency of the optimization.

Robustness Assessment of the Critical Cooling Mass Flows

Before we dive into the methodological parts of the robustness study, it must be clarified how to define robustness in context of the SAS. For the development of earlier jet engine generations, the evaluation of the SAS was based on deterministic criteria expressed by minimal

QoI	$\underline{\mu}_y$ [%]	max(CoV$_y$)	QoI	$\underline{\mu}_y$ [%]	max(CoV$_y$)	QoI	$\underline{\mu}_y$ [%]	max(CoV$_y$)
$Y_{\text{Rot\_1\_l}}$	3.36×10^{-2}	0.16	$Y_{\text{Rot\_2\_l}}$	3.27×10^{-2}	0.20	$Y_{\text{Rot\_3\_l}}$	3.15×10^{-2}	0.20
$Y_{\text{Rot\_1\_r}}$	3.14×10^{-2}	0.33	$Y_{\text{Rot\_2\_r}}$	3.16×10^{-2}	0.29	$Y_{\text{Rot\_3\_r}}$	3.15×10^{-2}	0.20

Table 5.6 Boundary conditions on the critical cooling mass flows for the robustness assessment.

cooling mass flow rates at certain positions. The goal of the development procedure was to identify a design which fulfills these requirements under nominal conditions.
Within the scope of the robustness analysis, these criteria are re-introduced as boundary conditions on the mass flows' mean value. Apart from that, the second relevant stochastic descriptor for the robustness is the mass flows' variation, expressed in terms of their variance. Since we have no comparable metric from earlier projects, the bounding conditions are based upon personal judgments. In Tab. 5.6, the two criteria are listed for each of the six cooling mass flows introduced before. Note, that the mean values are expressed as percentage of $W^{(25)}$, which represents the core mass flow rate at the LPT inlet. Further, a scaling factor has been added for reasons of confidentiality.
After having defined a set of distinct bounds for the response mean and standard deviation, we are able to proceed with the assessment of the SAS. The complete set of input quantities comprises the noise factors from Tab. 5.5 as well as the six design parameters. For the robustness assessment, the latter are described by a set of distributional p-boxes with uncertain mean but constant standard deviation. Hence, the number of uncertain hyperparameters is increased from 16 to 22. In order to determine the relevance of considering the epistemic uncertainty, we compare three different approaches with each other:

I. Aleatory treatment of the epistemic uncertainty

As indicated by the name, the basic idea is to handle the epistemic uncertainty in a probabilistic manner. Thereof, a multivariate uniform distribution is assigned to the uncertain hyperparameter space. Due to the probabilistic framework, an integration is performed over the epistemic space and the uncertainty representation degrades to a single CDF. As an example, the expression for the response mean yields

$$\mu_y = \int_{\underline{\boldsymbol{\Theta}}_x}^{\overline{\boldsymbol{\Theta}}_x} \int_{-\infty}^{\infty} g(\boldsymbol{x})\, f_X(\boldsymbol{x}|\boldsymbol{\Theta}_x)\, f_{\boldsymbol{\Theta}_x}(\boldsymbol{\Theta}_x)\, d\boldsymbol{x}\, d\boldsymbol{\Theta}_x, \tag{5.9}$$

where $f_{\boldsymbol{\Theta}_x}(\boldsymbol{\Theta}_x)$ stands for the n_Θ-variate uniform distribution. In the same way, the response standard deviation is reduced from an integral to a constant value. For the numerical approximation, a set of n_s sampling points are generated according to the following scheme:

- At first, an $(n_\text{s} \times (n_x + n_\Theta))$-dimensional array is generated where each column contains samples that have been drawn from a standard uniform distribution $\mathcal{U}_{[0,1]}$.

- After that, the inverse transformation method (see Eq. (3.43)) is applied to the last n_Θ columns based upon the multivariate uniform distribution in the epistemic space. The resulting values within the $(n_\mathrm{s} \times n_\Theta)$-dimensional array represent the entries of the hyperparameter sample set $\{\boldsymbol{\theta}_x^{(1)}, \ldots, \boldsymbol{\theta}_x^{(n_\mathrm{s})}\} \subset \mathbb{R}^{n_\Theta}$.
- Finally, the inverse transformation method is carried out for the first n_x columns. This step corresponds to drawing random sample points where each realizations $\boldsymbol{x}_\mathrm{s}^{(i)}$ stems from a different probability density function (PDF) $f_X(x|\theta_x^{(i)})$. The sample sets $\{\boldsymbol{x}_\mathrm{s}^{(1)}, \ldots, \boldsymbol{x}_\mathrm{s}^{(n_\mathrm{s})}\} \subset \mathbb{R}^{n_x}$ are then propagated throughout the computational model.

The previous steps are demonstrated for $X_{\text{IAS1\_lip\_e}}$ in Fig. 5.12 for a set of 30 points. Figure 5.12(b) shows the random samples in the hyperparameter space by the gray dots, which have been generated from the rejection sampling technique to ensure uniformity within the coupled μ_x-σ_x-space. The resulting empirical CDF is shown in Fig. 5.12(a). For comparison, the envelopes of the free p-box are depicted by the two black lines which illustrate the loss of information due to the probabilistic treatment of the epistemic space.
For the aleatory robustness assessment of the interdisciplinary SAS model, no distinction is made between the uncertainty source, i.e., $\boldsymbol{\Theta}_x$ encloses both the uncertain hyperparameters from the engine-to-engine as well as the flight-to-flight variation. The final robustness assessment has been performed with $n_\mathrm{s} = 10,000$ sample points.

II. Evaluation of selected hyperparameter combinations

In the second strategy, we use the standard double-loop Monte Carlo (MC) sampling introduced within the scope of Sec. 3.2. As this method requires an enormous number of samples, the realizations of $\boldsymbol{\Theta}_x$ in the outer loop are chosen manually. It has been decided to analyze exclusively cases where the hyperparameters are taking extreme values. A schematic overview is given by Fig. 5.12(c) which shows the different $\boldsymbol{\Theta}_x$-realizations for an independent μ_x-σ_x-space. As an example, the first point (●) represents the case where all distributional

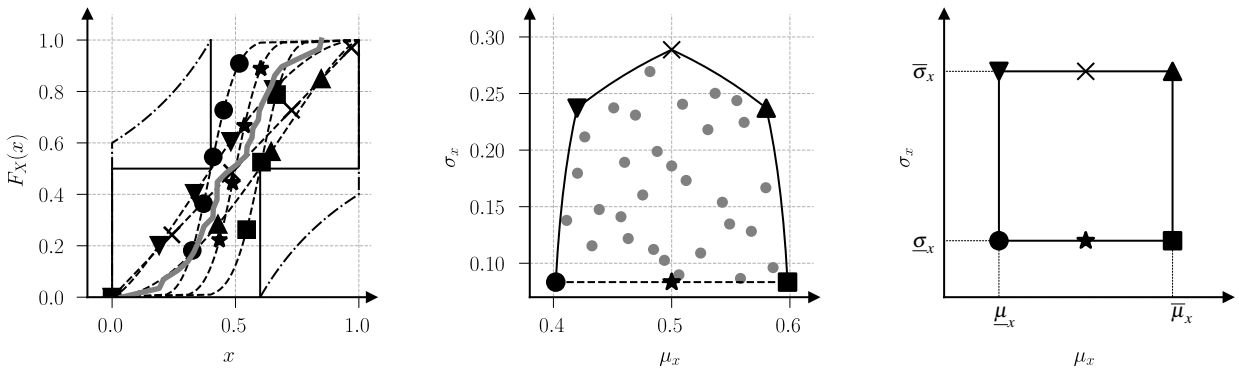

(a) CDF realizations and free p-box. (b) Hyperparameter realizations. (c) Illustration for strategy II.

Figure 5.12 Graphical representation of the robustness assessment strategy I (gray) and II (black) by the example of the first inner air seal eccentricity ($X_{\text{IAS1\_lip\_e}}$).

descriptors take their minimum value. The two points lying not in the corners are selected to regard the maximum value for σ_x if the hyperparameters are subject to a dependency structure. The actual positioning is shown for $X_{\text{IAS1\_lip\_e}}$ in Fig. 5.12(b) by the same labeling as the scheme next to it.

To summarize, the robustness study is made by a double loop MC approach with six manually chosen points in the outer loop and $n_{\text{s}} = 6,000$ samples in the inner loop. The long computational time of around seven days is the decisive factor why the number of CDFs was limited to six. The analysis of a full factorial design, i.e., considering all corner points in the outer loop, would simply take too much effort. For the same reason, there is no separation between engine-to-engine and flight-to-flight variation.

III. NISS-based nested robustness study

The third approach includes the application of the NISS strategy which requires the definition of a proposal distribution denoted as $f_X(x|\boldsymbol{\Theta}_x^\star)$. Next, a set of samples must be drawn from it followed by the repeated simulation of the interdisciplinary SAS model. Once this step is finished, the approximation of $\mu_y(\boldsymbol{\Theta}_x)$ and $\sigma_y(\boldsymbol{\Theta}_x)$ for any $\boldsymbol{\Theta}_x \neq \boldsymbol{\Theta}_x^\star$ is rather cheap as no additional simulation runs are needed. A detailed introduction about the method can be found in Sec. 4.3.1.

The great efficiency of NISS enables us to carry out a more detailed robustness assessment of the cooling system. The idea is to evaluate various randomly chosen CDFs of the geometric parameters by analyzing the system's mean and standard deviation at the critical locations. More in detail, a nested approach is developed which separates engine-to-engine from flight-to-flight variation in a double-loop procedure. The two-step scheme, which may not be confused with the MC sampling from before, is demonstrated in Fig. 5.13.

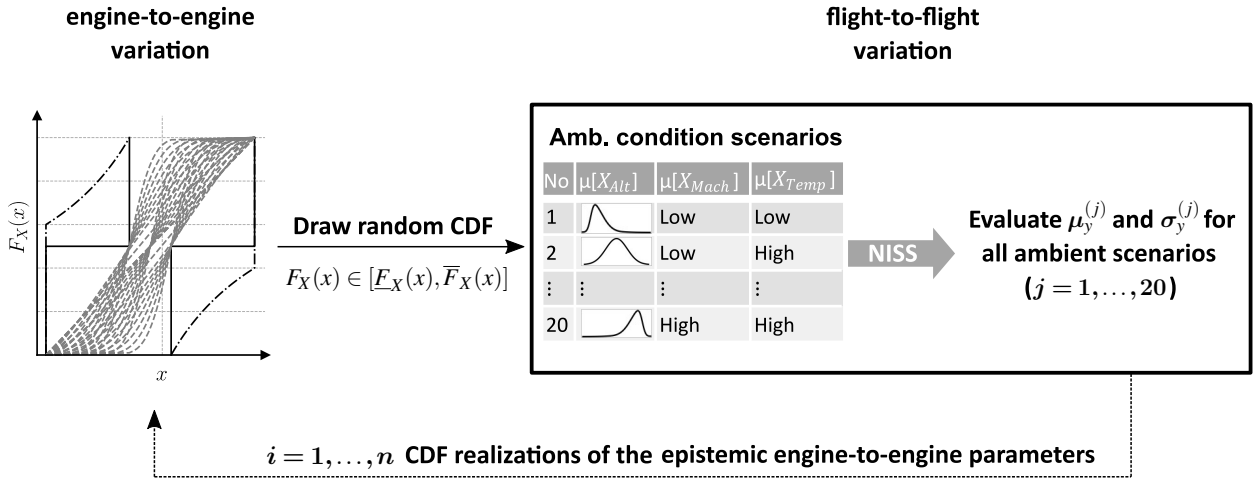

Figure 5.13 Graphical representation of the robustness assessment strategy III.

In detail, the approach comprises the following steps:

- In the outer loop, a random sample is drawn from the hyperparameter space that corresponds to the set of design and noise factors affected by the engine-to-engine variation. Hence, a specific probability distribution is assigned to those parameters of the SAS model being quantified by a p-box. As a reminder, the corresponding parameters from the performance model $(X_{\Delta W^{(i)}}, X_{\eta^{(i)}})$ have all been degraded from a p-box to a single CDF.
- Within the inner loop, the focus is put on the parameters which describe the flight-to-flight variation, i.e., X_{Alt}, X_{Mach} and X_{Temp}. For the uncertain mean value space of those three quantities, a two-level full factorial design is introduced which gives a set of eight corner points. In addition to that, two mean values are added which are located close to the center point. Each of the ten mean value realizations is then combined with the minimum and maximum standard deviation which gives a total number of 20 points, see the table in Fig. 5.13.
- The actual robustness assessment is done by combining each CDF from the outer loop with all scenarios of the inner loop. Finally, we derive the response mean and standard deviation for all combinations with the help of NISS. As a measure for the designs' robustness, the minimum mean and maximum standard deviation is opposed to the limit values from Tab. 5.6.

For the investigation of the interdisciplinary SAS model, the number of iterations in the outer loop has been set to 200. Thus, we have assessed 200 geometrical designs for 20 different scenarios of the ambient conditions. The total number of uncertainty propagations required for this analysis is $4,000$ which is not possible with a standard MC sampling. The approximation with the help of NISS is based upon a set of approximately $100,000$ points which requires a computation time of roughly two weeks.
All of the three above-mentioned robustness strategies have been summarized within Fig. 5.14. The upper right off-diagonal entries refer to the mean value variation whereas the lower subplots depict the standard deviation of the cooling mass flow rates under investigation. Note that only the flow paths at the first and second rotor stage are shown here as they are of higher importance due to the downstream temperature decrease. The results of the robustness assessment are given by the following scheme:

- The first approach is depicted by the green diamond (◆). Due to the probabilistic treatment, only a single value is obtained for the mean and standard deviation in any dimension.
- The resulting stochastic moments of the second strategy are illustrated by the six blue marks from Fig. 5.12. To evaluate the quality of the NISS approximation, the same study

has been repeated based upon the sample set from the third strategy. The respective outcome is shown by the identical symbols colored in black.

- Robustness strategy III corresponds with the gray dots, each of which represents one of the $4,000$ evaluations from the nested robustness strategy.

In all of the subplots, the predefined thresholds on the stochastic moment are plotted by the black dashed lines.

Let us start with the analysis of the upper right half of Fig. 5.14, i.e., the mean value variation. It is first of all apparent that the probabilistic point of view leads to a single mean vector with sufficient safety margin to all mean value boundaries. In contrast, the six scenarios from

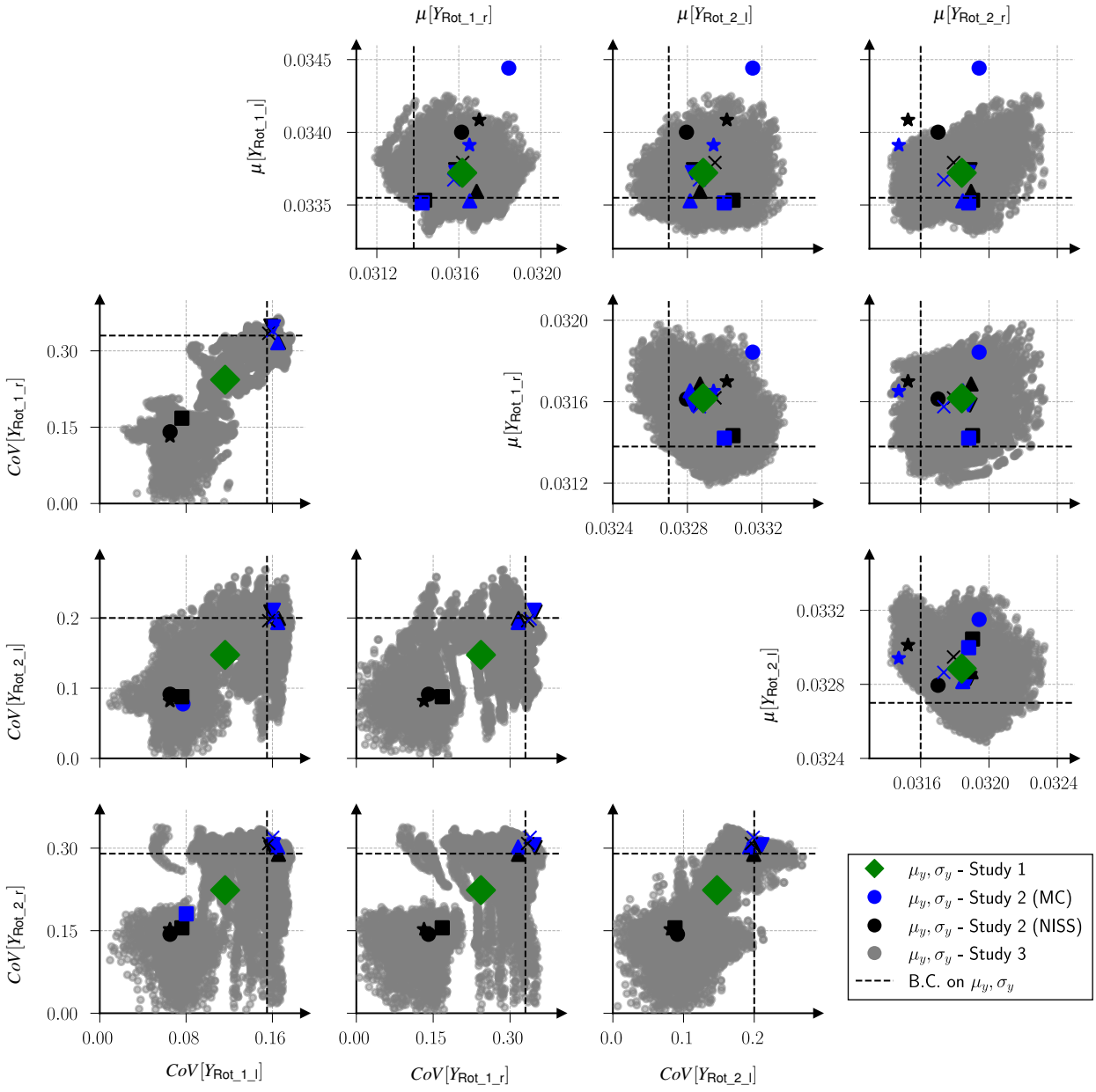

Figure 5.14 Robustness assessment for the cooling mass flows at the first and second rotor stage.

the second approach reveal a certain scatter which includes realizations located close to the threshold or even beyond. For example, the limit on $\mu[Y_{\text{Rot\_1\_l}}]$ is slightly undershot by two CDF realizations. A more distinct deviation can be observed in case of $\mu[Y_{\text{Rot\_2\_r}}]$ for a single CDF (✶). So, the selection of various scenarios demonstrates the importance of treating lack-of-knowledge in a non-probabilistic way.

The comparison between the blue and black markers shows a high level of consistency between the MC and NISS scheme for most of the cases. Overall, the average deviation between the two sampling methods is less than 3.7%. This bears witness to a huge degree of trustworthiness given the fact that the chosen hyperparameter combinations are covering exclusively extreme scenarios. One exception here is the case shown by the black dot which describes the assumption of $\boldsymbol{\Theta}_x = \underline{\boldsymbol{\Theta}}_x$, i.e., all hyperparameters take their minimum values. In order to understand the significant discrepancy, we have to take a look at the proposal distribution. Contrary to the original assumption of setting all hyperparameters to their center values, some entries of $\boldsymbol{\Theta}_x^\star$ have been assigned with deviating values. Due to the fact that high ambient temperatures in combination with high flight altitudes are critical for the engine performance, the values of $\mu^\star[X_{\text{Alt}}]$ and $\mu^\star[X_{\text{Temp}}]$ have been shifted towards their maxima. The above-mentioned desired PDF has therefore the largest difference to the proposal distribution causing the low approximation quality in this case.

Still, the limited selection of $\boldsymbol{\Theta}_x$-realizations does not capture the full variation of $\boldsymbol{\mu}_y$ as can be seen from the comparison with the gray scatter points. The third robustness assessment shows clearly that all of the mean threshold conditions can be undershot for certain ambient scenarios. This observation will be clarified more in detail later on.

When putting the focus on the lower left half of Fig. 5.14 the cooling mass flows' standard deviation, expressed in terms of the CoV, can be analyzed. Starting with the probabilistic approach, the resulting mass flows' variation can be interpreted as an averaged CoV compared to the other two robustness strategies. Once again, none of the threshold limits is exceeded.

In most of the subplots, the second robustness approach leads to a clear separation between input distributions with a low (●, ■, ✶) and high (▲, ▼, ✖) standard deviation. For some of the realizations with a minimum σ_x-value, no corresponding outcome from the NISS-evaluation is depicted. The reason for the missing information is the low approximation quality of NISS which has led to a negative sample variance. Similar to the mean value analysis, the root cause goes back to the enormously higher standard deviation of the proposal distribution. To overcome this problem, the multi-point non-intrusive imprecise stochastic sampling (MNISS) concept from Sec. 4.3.2 can help to increase the approximation quality. Since we are mainly interested in the largest σ_x realizations for the robustness study, no further modification has been applied here.

For the third robustness evaluation, a certain clustering is visible in most of the subplots. This effect stems from the fact that the scenarios are separated into ambient conditions with minimum and maximum variance. Once again, the third robustness approach reveals that the

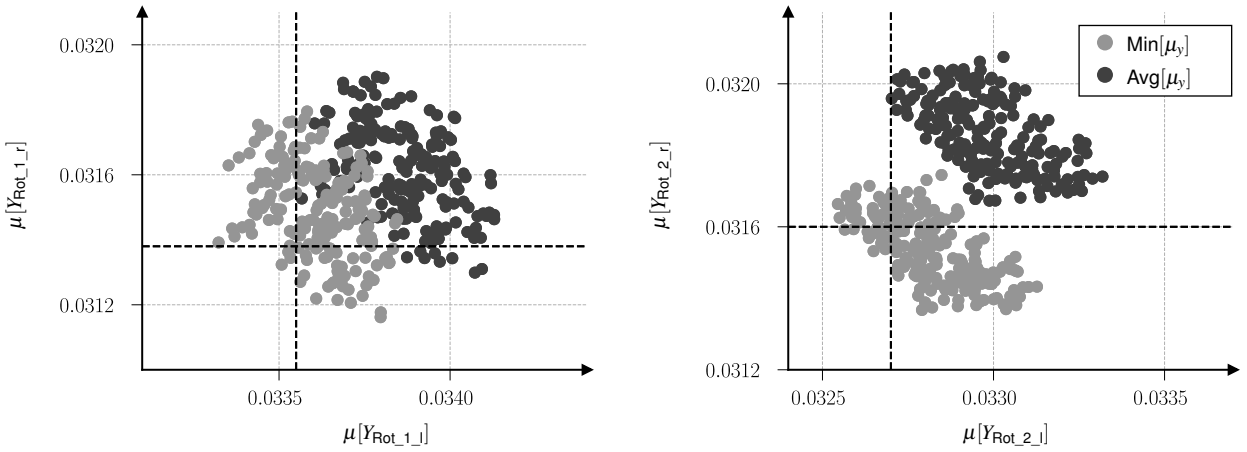

(a) First rotor stage.

(b) Second rotor stage.

Figure 5.15 Average and minimum mean value analysis at the first (left) and second (right) rotor stage.

boundary conditions on the CoV can be violated for certain scenarios.

As stated before, a deeper inspection of the mean value variation from the third robustness strategy is carried out. In Figure 5.15(a) and (b), the minimum as well as the average mean value of the 200 realizations from the outer loop are plotted. Putting the result into numbers, only 4% of the average points are lying within the infeasible range. In contrast, 94.5% of the minimum mean realizations are violating at least one of the bounds from either the first or second rotor stage. A more detailed analysis of the infeasible points has shown that different ambient conditions are responsible for breaking the threshold values. Hence, it is hard to further reduce the hyperparameter space for the RDO.

Optimization of the Geometric Design Parameters

The previous studies have clarified the importance of treating epistemic uncertainties appropriately to judge about the robustness of the cooling system. In the following, the RDO formulation is introduced followed by the discussion about the outcome of the optimization.

Within the scope of Sections 3.6.2 and 4.3.2, various metrics for a robust optimization have been compared. One major finding from the analytical study was that a constraint-based expression offers more flexibility to the modeler for controlling the optimization procedure. The mathematical term for the RDO of the SAS is given by:

$$
\begin{aligned}
&\underset{\boldsymbol{\mu}_x^{\mathsf{d}} \in \mathbb{R}^6}{\text{minimize}} && \left\{ -w_1 \, \tilde{\mu}[Y_{\text{Rot\_2\_l}}] - w_2 \, \tilde{\mu}[Y_{\text{Rot\_2\_r}}] \right\} && \\
&\text{s.t.} && \overline{\sigma}_y^{(i)} < \sigma_y^{\star,(i)} && \text{for } i = 1,\dots,6 \\
& && \underline{\mu}_y^{(i)} > \mu_y^{\star,(i)} && \text{for } i = 1,\dots,6 \\
& && \underline{\mu}_x^{\mathsf{d},(j)} < \mu_x^{\mathsf{d},(j)} < \overline{\mu}_x^{\mathsf{d},(j)} && \text{for } j = 1,\dots,6.
\end{aligned}
\tag{5.10}
$$

The above equation expresses the goal to maximize the cooling mass flows' average mean value. For the purpose of illustration, only the two mass flows at the second rotor stage are part of the objective function. The formulation could be extended easily by further QoIs.
As stated before, the robustness criterion is implemented by limiting the maximum standard deviation instead of extending the objective function. In addition to that, constraints are introduced on the minimum mean values which have been discussed within the robustness analysis in Sec. 5.2.3. To repeat, the corresponding values for $\mu_y^{\star,(i)}$ and $\sigma_y^{\star,(i)}$ are summarized in Tab. 5.6. Contrary to the objective function, all critical mass flow rates at the first, second and third rotor stage are taken into account. The last set of constraints in Eq. (5.10) refers to the bounds of the six design parameters, i.e., the mean vector entries of $\mathbf{X}^{\mathsf{d}}$.
Similar to the robustness assessment strategy III, the RDO is conducted by a nested approach. This time, the outer loop contains the design parameters $\boldsymbol{\mu}_x^{\mathsf{d}} \in \mathbb{R}^6$ whereas the noise factors $\mathbf{X}^{\mathsf{n}} \in \mathbb{R}^{33}$ are assigned to the inner loop. To repeat, eight noise parameters are described by distributional p-boxes with uncertain mean and standard deviation, see Tab. 5.5. As the focus of the RDO metric from Eq. (5.10) is to limit the maximum response standard deviation, the noise factors' uncertain variance is set to their upper bounds. Bearing in mind that all entries of $\mathbf{X}^{\mathsf{d}}$ are assigned with a constant variance, the set of uncertain hyperparameters covers only mean values.
To realize a two-level full factorial design like in case of the robustness assessment, 256 evaluations are required in the inner loop. Due to the large computational effort, it has been decided to perform a random sampling based upon a Sobol sequence of length 100. Thus, the determination of Eq. (5.10) for a single design point requires the evaluation of 100 random CDF realizations. As the computation of the single points can be performed independently, a parallelization of the inner loop is implemented.
In addition, we make use of the NISS characteristics to further reduce the runtime. The basic idea is to exploit the high-dimensional model representation (HDMR) concept by saving a certain portion of the component functions during the optimization. The matrix in Fig. 5.16 is an illustration of the design parameter space $\boldsymbol{\mu}_x^{\mathsf{d}} \in \mathbb{R}^6$ as well as the noise factors' uncertain mean value $\boldsymbol{\mu}_x^{\mathsf{n}} \in \mathbb{R}^8$. Thus, for a single design point 14 first-order and 91 second-order component functions must be evaluated for each of the 100 inner loop random samples to approximate $\boldsymbol{\mu}_y$. The same must be repeated for the approximation of $\boldsymbol{\sigma}_y^2$ which gives a total number of $21,000$ operations.
Due to the fact that some of the component functions remain constant, we do not have to recompute all of them within each iteration. The total set of component functions can be divided into three categories, see Fig. 5.16:

- Category Ⓐ: This part includes first- and second-order components from the design parameter space. The respective computation must be performed only once per design assessment.

- Category Ⓑ: The second group captures all components that correspond exclusively to the noise factors' hyperparameter space. For this reason, a one-time evaluation is sufficient for the whole optimization.
- Category Ⓒ: The last set of component functions represents the interactive effects between $\boldsymbol{\mu}_x^{\mathsf{d}}$ and $\boldsymbol{\mu}_x^{\mathsf{n}}$. Here, no computational effort can be saved.

The reduction is only possible if the sample points in the inner loop are not changed during the optimization, i.e., the same starting point must be chosen for the Sobol sequence. Otherwise, all of the first- and second-order components from category Ⓑ and Ⓒ must be re-determined for every single design iteration. By saving the component functions of category Ⓐ and Ⓑ, the total number of NISS-evaluations can be reduced from $21,000$ to $9,642$ which is a decrease of more than 50%.

Coming back to the RDO of the secondary air system, the differential evolution strategy from the SciPy[4] package is used which has also been applied for the inverse UQ in Sec. 5.1.1. The reason for choosing this global approach is the missing information about promising initial guesses to determine the optimal design. The inequality constraints from Eq. (5.10) are implemented with the help of two quadratic penalty functions which are added to the objective. Compared to a direct constraint formulation, this approach allows the usage of unconstrained optimization algorithms which are more reliable [138].

Finally, the RDO problem has been analyzed for 21 different combinations of w_1 and w_2. A summary of the optimization results is given in Fig. 5.17. On the left hand side, the cooling

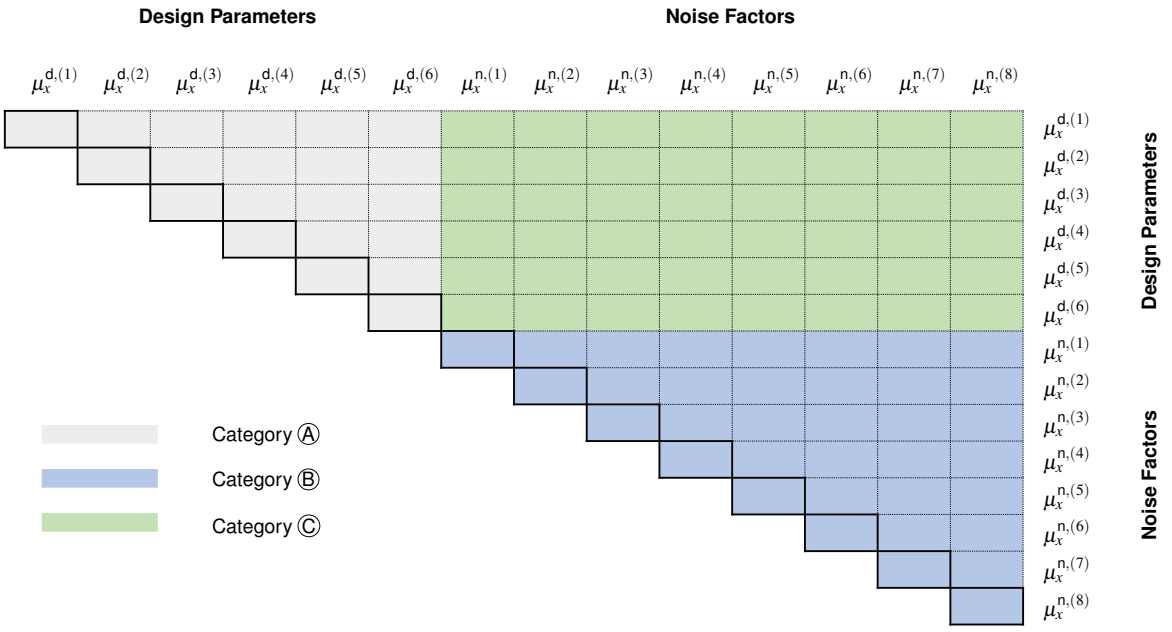

Figure 5.16 Categorization of the HDMR component functions.

[4] SciPy is an open-source library for Python, see `https://scipy.org/`.

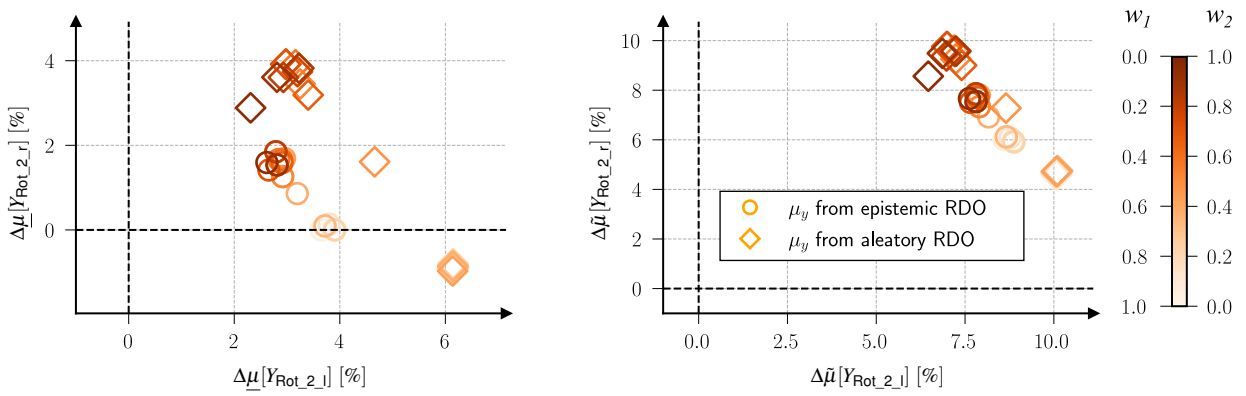

(a) Minimum mean value.

(b) Average mean value.

Figure 5.17 Minimum (left) and average (right) mean value of the cooling mass flows at the second rotor stage for the aleatory and epistemic RDO. Both figures show the percentage deviation from the threshold values.

mass flows' minimum mean value are depicted for the second rotor stage whereas Fig. 5.17(b) denotes the average mean values of the same cooling mass flows. The two coordinates, $\mu[Y_{\text{Rot\_2\_l}}]$ and $\mu[Y_{\text{Rot\_2\_r}}]$, correspond with the components of the objective function. Note, that the axes are scaled w.r.t. the constraints from Tab. 5.6, i.e., they denote the percentage deviation from the required minimum mean values.

Each of the orange circles represents the optimization result of a specific combination between the weighting factors w_1 and w_2. A high color saturation indicates a large value for w_2 and thereof a high importance of $\underline{\mu}[Y_{\text{Rot\_2\_r}}]$ in the objective. As a result, the various weighting factor combinations lead to a Pareto front identification of the multiobjective optimization. However, some of the results are dominated in both coordinates and thereof not contributing to the Pareto set. The reason for this are the additional constraints on the maximum standard deviation, see Eq. (5.10). Since the inequality constraints are implemented by a set of penalty functions, a slight exceedance of the limits is possible without influencing the objective function too much.

A closer inspection of Fig. 5.17(a) reveals that all of the identified designs are in accordance with the postulated constraints on the minimum mean value. Furthermore, they fulfill the boundary conditions on the standard deviations which is shown by Fig. 5.18. The left hand side, i.e., Fig. 5.18(a), illustrates the maximum response CoV ($\overline{CoV}$) for the cooling mass flows at the first rotor stage and Fig. 5.18(b) for the second stage. In accordance with Fig. 5.17, every orange circle represents the outcome for one specific weighting factor combination. One can see, that only very few designs violate the constraints of the maximum standard deviation slightly.

Apart from the epistemic RDO discussed so far, a second study has been conducted which treats the lack-of-knowledge uncertainties in a probabilistic manner. All noise factors, that have been modeled with p-boxes so far, are now assigned with a single CDF characterized by a comparatively high variance. As a consequence, no nested iteration scheme is required

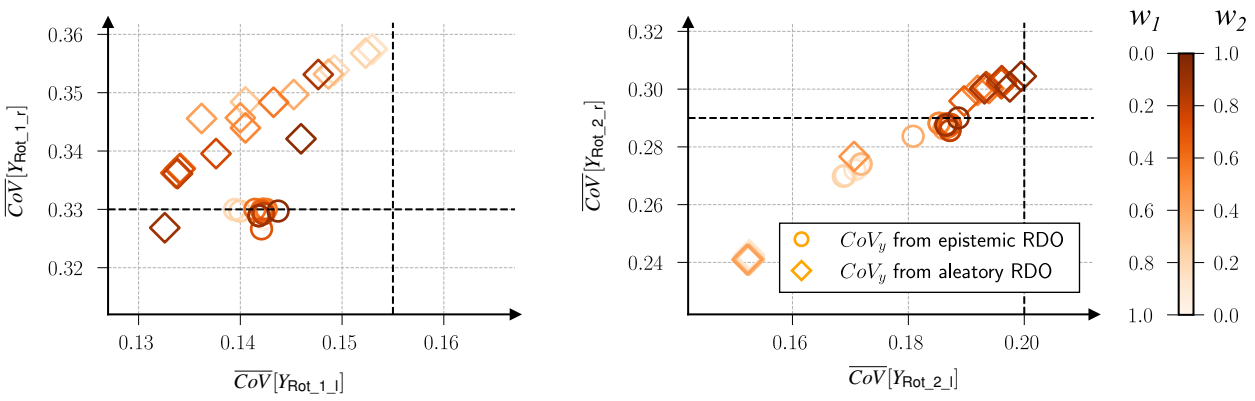

(a) First rotor stage.

(b) Second rotor stage.

Figure 5.18 Maximum coefficient of variation (CoV) for the first (left) and second (right) rotor stage. Both figures show the result from the aleatory and epistemic RDO studies.

anymore for the evaluation of a design which makes the RDO significantly cheaper. Accordingly, the optimization problem from Eq. (5.10) must be modified by replacing the minimum and maximum stochastic moments of the constraint formulations by their aleatory counterparts.

The actual result of the second RDO is shown by the orange diamonds in Fig. 5.17(b). In accordance with the epistemic robust optimization, the identical set of weighting factor combinations has been analyzed. For the comparison with the epistemic results, a subsequent robustness assessment has been conducted by combining the aleatory designs with the same 100 inner loop scenarios from the epistemic RDO.

From the analysis of the two scatters in the right part of Fig. 5.17, one could conclude that the designs from the aleatory optimization are superior as they lead to an overall higher supply of cooling mass flow for all weighting factor combinations. The first impression is revised by the investigation of the minimum mean values in Fig. 5.17(a). For weighting factor combinations with a high value of w_1, the minimum mean values violate the constraint on $\mu[Y_{\text{Rot\_2\_r}}]$ in many cases. In turn, the aleatory RDO seems to provide a better cooling system configuration when increasing the value of w_2, i.e., trying to maximize $\mu[Y_{\text{Rot\_2\_r}}]$. However, a deeper examination of the maximum standard deviations in Fig. 5.18 shows that all aleatory designs are violating at least one of the constraints. Hence, the partially better mean value performance has been achieved at the cost of higher maximum standard deviations.

To summarize, the comparison of the two optimization schemes has demonstrated the importance of taking epistemic uncertainties into account. One of the main findings is that the epistemic RDO is able to detect design points which maximize the average critical cooling mass flows while complying with the constraints under all considered scenarios. In contrast, the aleatory design results show a better SAS performance when assuming an averaged distribution for the lack-of-knowledge parameters but lead to a violation of several constraints when conducting a subsequent epistemic robustness assessment based upon p-box representations for the parameter set with unknown distributions. Thus, the additional effort pays

off to identify a geometrical design which guarantees a stable cooling mass supply under any condition. Especially for nonlinear systems, such as the SAS model, the high efficiency of NISS is beneficial as a large number of uncertainty propagations is required to capture the variation of the stochastic moments.

Since the noise factors' uncertain standard deviation have been deliberately set to their maximum values, the NISS scheme yields a high approximation quality for both of the stochastic moments. To express the accuracy in figures, the average sample standard deviation among all 100 case scenarios has been determined for each of the 21 optimal designs. To remind, the expressions for $Var[\mu_y]$ and $Var[\sigma_y^2]$ are given by Eq. (B.1) and (B.2) in the appendix.

For the response mean, the sample standard deviation reaches from 7% to 10% whereas in case of the variance, the error is lying in a range between 16% and 55%. In order to increase the accuracy of the sample variance, modifications such as the MNISS must be implemented into the robustness assessment. These aspects and future ideas how to improve the RDO are discussed within the conclusion chapter.

Chapter 6

CONCLUSION

The last paragraphs provide a critical reflection and give an outlook for future research topics based upon the study results of this thesis. The structure of the chapter is divided into two parts. At first, the methodological aspects are discussed followed by a section about the technical improvements of the interdisciplinary process chain.

Methodological Conclusion & Outlook

Similar to the previous chapters, the conclusive remarks are oriented towards the aims and objectives of this work. The first main point was the quantification of lack-of-knowledge uncertainty sources with a special focus on inverse problem. The newly introduced hyperellipsoid approach has proven to be an efficient method in context of the performance model. Especially the local version of the algorithm has led to consistent results within a reasonable amount of time. In contrast, the global strategy has shown a superior performance in terms of the objective function but requires significantly more time which offers room for improvement.
Within the current configuration, the minimum-volume enclosing ellipsoid (MVEE) of the propagated samples is determined by the Khachiyan algorithm. The computational efficiency could be increased by replacing it with the algorithm introduced in [167]. The authors of the cited reference have demonstrated the MVEE computation for a 30-dimensional test case with $30,000$ samples in less than 30 seconds on a personal computer. Thus, exchanging the MVEE metric holds great potential to improve the global hyperellipsoid strategy and applying it to problems

of even higher dimensionality.
The second bottleneck is the high number of sample points needed for a sufficient coverage of the hyperellipsoid mapping. For this reason, the jet engine performance model has been replaced by a surrogate model leading to an additional numerical error in the framework. One opportunity to use the more time-consuming high-fidelity model would be the storage and reusage of existing sample points. Alternatively, the hyperellipsoid procedure could be combined with an adaptive surrogate model technique instead of defining one global metamodel at the beginning.
Besides from the inverse also the forward uncertainty quantification (UQ) under scarce information was a significant contribution of the thesis. For many cases, the parameters' uncertainty has been described with distributional p-boxes based upon the beta distribution family. Due to the great flexibility and the existence of distinct bounds on the parameter range, the p-box approach is suitable for representing the incomplete knowledge. A drawback is the resulting dependency structure within the epistemic hyperparameter space which complicates the subsequent uncertainty studies. As a future research task, a distributional p-box definition could be developed with the help of the generalized lambda distribution. The four parametric density function offers even more flexibility as it can take the form of a Weibull, Gaussian, uniform or Student's t distribution [63, 179]. Since it can exhibit an unbounded PDF for certain parameter combinations, the generalized lambda distribution is applicable to the NISS strategy without further modifications. Moreover, one can directly control the tail properties which is beneficial for investigating the reliability of a system.
The second objective of this work concerns the reduction of the epistemic hyperparameter space. To repeat, the goal was to establish a screening methodology for identifying uncertain stochastic moments with a negligible importance on the system response. The developed approach is built upon repeated Taylor series expansions at distinct locations in the epistemic space. As a result, one obtains a sensitivity measure for every single hyperparameter as well as for the first interaction term.
All in all, the screening has helped to clearly reduce the complexity of the interdisciplinary model by degrading more than half of the p-box representations to a single cumulative distribution function (CDF). However, the interpretation of the derived sensitivity coefficients suffers from the above-mentioned loss of independency. Hence, a rather conservative target corridor has been chosen to decide about the reduction of a parameter, thereby undermining the potential of the method. The variable screening serves as a preparation step for the robust design optimization which is why the sensitivity indices are designed for measuring the importance on the response mean and standard deviation. Since the p-box definitions include uncertain third order stochastic moments, a Taylor series expansion of the same order is required to quantify the importance of the input skewness.
In context of the interdisciplinary process chain, the performance model has been analyzed as stand-alone configuration before starting with the variable screening of the coupled secondary

air system (SAS) model. The two-step approach is possible because of the sequential concatenation of the disciplines and has helped to reduce the overall computational burden. For application cases of even higher dimensionality, the Taylor series based uncertainty propagation might be inefficient. However, decreasing the order of the expansion is not reasonable as it is linked to a loss of prediction accuracy for nonlinear models. Instead, the basic screening concept could be combined with alternative mapping techniques such as the point estimation method for example [144, 157]. A good starting point is the work of [82] which introduces an enhancement of the standard point estimation method to efficiently consider the input parameters' skewness for the uncertainty propagation.

The third and last focal point of the thesis entails the robust design optimization of the low-pressure turbine (LPT) cooling system with a special focus on the consideration of epistemic uncertainty sources. The prerequisite for the actual optimization is the definition of an objective function which captures the system's robustness by means of an analytical expression. After an intensive discussion about different metrics throughout Sec. 4.3, it has been decided to follow a constraint-based formulation. From the author's point of view, the modeler has more control over the optimization result compared to a robustness metric with an extended objective function.

The optimization procedure itself is an extremely time-consuming task because it is based upon a nested iteration scheme. Contrary to a pure aleatory robust design optimization (RDO), the evaluation of every single design requires the analysis of various CDF realizations. As the application of standard sampling techniques is limited to low-dimensional problems, it has been made use of the non-intrusive imprecise stochastic sampling (NISS) concept. The great benefit is that only one set of sample points must be generated from a single proposal distribution. However, the gain in efficiency is achieved at the expense of decreasing approximation accuracy, especially if the desired CDF differs significantly from the proposal distribution.

For the optimization of the interdisciplinary SAS model, the NISS approach has demonstrated a high accuracy for the derivation of the first stochastic moment. Further improvement is necessary for the approximation of the response variance which shows a considerably higher inaccuracy. The chosen RDO metric has helped to counteract this deficit because it focuses solely on the maximum standard deviation. A possible way forward to improve the advanced sampling procedure has been outlined by the multi-point non-intrusive imprecise stochastic sampling (MNISS) strategy within Sec. 4.3.2. The general idea is to approximate the output variance in possible robust design regions by locally defined proposal distributions. Here, further research is necessary on how to determine the number and shape of the additional proposal distributions in an automated way. Therefore, a metric could be derived which quantifies the expected gain in approximation accuracy when introducing an additional proposal distribution at a certain location in the epistemic space. A reasonable basis is the publication of [173] about the extended Monte Carlo sampling (EMCS), which is a key component of the NISS concept. The authors address, inter alia, the question how to choose an optimal pro-

posal distribution to minimize the average approximation error of the response mean.
With the help of the modified NISS strategy, also the response variance of high-dimensional problems, such as the interdisciplinary SAS model, could be derived more accurately. This would enable the usage of other RDO metrics which directly optimize the output variance.

Technical Conclusion & Outlook

The coupling of the SAS model with the preceding disciplines makes a more detailed analysis of the cooling system possible. Especially the interface with the performance calculation enables the modeler to investigate the impact of changing ambient and flight conditions in a thermodynamically consistent way. The robustness analyses in Sec. 5.2.3 have demonstrated the need to take performance parameters into account for assessing the operational behavior of the cooling system.
With regard to the aerodynamic simulation, the convergence rate of the streamline curvature method (SCM) must be improved significantly to include the uncertainty sources into the stochastic framework. Within the current configuration, the outcome of the aerodynamic simulation is only affected by changing station boundary conditions at the module's inlet and exit. The production induced variation of geometrical features is not considered as it would lead to an extremely high failure rate of the sampling procedure. Thus, the iterative solution scheme of the SCM must be revised to increase the precision of the simulation results.
An essential aspect for the future development is the extension of the interdisciplinary process chain by the thermal and structural-mechanical discipline. Basically, the derived cooling mass flow rates from the SAS model can be interpreted as a strong indication for or against a sufficient cooling of the LPT disk. A more solid interpretation is only possible with a thermal simulation because the suitability of a design is assessed by certain criteria of the components' material temperature. Here, the results from the SAS model serve as input for a realistic modeling of the thermal boundary conditions.
In order to formulate a statement about the component's life time requirement, one has to make a structural assessment. Without going into detail, this final step requires the conduction of several FE-calculations representing the different points of a flight mission. In context of a stochastic life time validation, the analysis of multiple varying flight missions is necessary which leads to even higher calculative costs. To put this objective into practice, further research is needed to improve the efficiency of both the computational models and stochastic methods.
To summarize, the thesis has shown the necessity to model lack-of-knowledge uncertainties by non-probabilistic frameworks in context of a jet engine design process. Important contributions have been made by the development of an inverse UQ approach and the application of the NISS concept for a robust design optimization. The latter has shown strongly the effect of assuming specific distribution functions when having only limited information about the uncer-

tainty source at hand by comparing the epistemic optimization results with a pure probabilistic RDO formulation. The key issues for most of the objectives are related to the higher computational burden which results from the additional epistemic component in the uncertainty representation. As has been summarized within the previous remarks, new scientific questions have raised throughout the thesis which offers potential for future research proposals.

Appendix A

Statistical Fundamentals

The following sections include amendments to Chap. 3 about the definition of probability distribution functions used throughout the thesis. Furthermore, supplementary details are given about the derivation of p-boxes based upon the Chebyshev inequality.

A.1 Definition of Common Distribution Functions

Within the scope of this work, different distribution functions have been used. Among those, the uniform and Gaussian distribution have not been introduced which will be added here. The definitions given in the next two paragraphs can be found in many literature sources such as [25] for example.

A.1.1 Uniform Distribution

A continuous random variable X_i is said to be uniformly distributed on the interval $[a,b]$ if the probability density function (PDF) has a constant value. Hence, the definition of the density function for $X \sim \mathcal{U}(a,b)$ yields

$$f_X(x) = \begin{cases} \frac{1}{b-a} & \text{if } a < x < b \\ 0 & \text{otherwise.} \end{cases} \tag{A.1}$$

The cumulative distribution function (CDF) of the uniform distribution is given by the integration of Eq. (A.1) according to

$$F_X(x) = \begin{cases} 0 & \text{if } \leq a \\ \frac{x-a}{b-a} & \text{if } a < x < b \\ 1 & \text{if } \geq b. \end{cases} \tag{A.2}$$

A.1.2 Gaussian Distribution

The most widely used distribution function in statistics is the Gaussian, also referred to as normal, distribution. As discussed in Sec. 3.3, its importance stems from the central limit theorem (CLT). This proposition states that the sample mean of independently and identically distributed (i.i.d.) random samples converges, regardless of their underlying distribution, towards a Gaussian one for a sufficiently large population size. The definition of a normal distribution is based upon its mean and standard deviation, i.e., $X \sim \mathcal{N}(\mu, \sigma)$, and its bell-shaped PDF is characterized by

$$f_X(x) = \frac{1}{\sqrt{2\pi\sigma^2}} \exp\left(-\frac{1}{2}\left(\frac{x-\mu}{\sigma}\right)^2\right). \tag{A.3}$$

The expression for the CDF is given by the integral

$$F_X(x) = \frac{1}{\sqrt{2\pi}} \int_{-\infty}^{x} e^{-t^2/2} dt. \tag{A.4}$$

A.2 Probability-Box Definition based on Chebyshev's Inequality

Throughout Sec. 3.2.3, the derivation of a distribution-free p-box has been introduced which is based upon Chebyshev's inequality, see Eq. (3.39). In case of having further information besides the mean and variance, the envelopes can be shrunken, thereof reducing the degree of conservatism.

The authors of [60] have formulated an expression when having knowledge about the minimum ($\underline{x}$) and maximum ($\overline{x}$) value as well as the first two stochastic moments of the random value. The lower and upper bound on the CDF, derived from the one-sided Chebyshev inequality, are expressed by

$$\underline{F}_X(x) = \begin{cases} 0, & \text{if } x \leq \mu + \frac{\sigma^2}{\mu - \overline{x}} \\ 1 - \frac{b(1+a)-c-b^2}{a}, & \text{if } \mu + \frac{\sigma^2}{\mu-\overline{x}} < x < \mu + \frac{\sigma^2}{\mu-\underline{x}} \\ \frac{1}{1+\frac{\sigma^2}{(x-\mu)^2}}, & \text{if } \mu + \frac{\sigma^2}{\mu-\underline{x}} \leq x < \overline{x} \\ 1, & \text{if } x \geq \overline{x} \end{cases}, \tag{A.5}$$

and

$$\overline{F}_X(x) = \begin{cases} 0, & \text{if } x \leq \underline{x} \\ \frac{1}{1+\frac{(x-\mu)^2}{\sigma^2}}, & \text{if } \underline{x} < x \leq \mu + \frac{\sigma^2}{\mu-\overline{x}} \\ 1 - \frac{b^2-ab+c}{1-a}, & \text{if } \mu + \frac{\sigma^2}{\mu-\overline{x}} < x < \mu + \frac{\sigma^2}{\mu-\underline{x}} \\ 1, & \text{if } x \geq \mu + \frac{\sigma^2}{\mu-\underline{x}} \end{cases}, \tag{A.6}$$

with

$$a = \frac{x-\underline{x}}{\overline{x}-\underline{x}}, \qquad b = \frac{\mu-\underline{x}}{\overline{x}-\underline{x}}, \text{ and} \qquad c = \frac{\sigma^2}{(\overline{x}-\underline{x})^2}.$$

Another scenario addressed in Sec. 3.2.3 is the exclusion of multimodal distribution functions from the p-box definition. Here the Vysochanskij–Petunin inequality can help which is a refinement of the general Chebyshev formulation for unimodal distributions with known mean and variance [136]. Based upon the one-sided version of the inequality, a p-box definition can be determined according to

$$\underline{F}_X(x) = \begin{cases} 0 & \text{if } x < \mu + \sigma \\ \frac{4}{3} - \frac{4\sigma^2}{3(x-\mu)^2} & \text{if } \mu + \sigma \leq x \leq \mu + \sqrt{\frac{8}{3}}\sigma \\ 1 - \frac{4\sigma^2}{9(x-\mu)^2} & \text{if } x > \mu + \sqrt{\frac{8}{3}} \end{cases}, \tag{A.7}$$

and

$$\overline{F}_X(x) = \begin{cases} \frac{4\sigma^2}{9(x-\mu)^2} & \text{if } x < \mu - \sqrt{\frac{8}{3}}\sigma \\ -\frac{1}{3} + \frac{4\sigma^2}{3(x-\mu)^2} & \text{if } \mu - \sqrt{\frac{8}{3}}\sigma \leq x \leq \mu - \sigma \\ 1 & \text{if } x > \mu - \sigma \end{cases}. \tag{A.8}$$

The two envelope equations are derived in the same fashion as the Chebyshev p-box construction shown in [123].

Appendix B

Non-Intrusive Imprecise Stochastic Sampling

The non-intrusive imprecise stochastic sampling (NISS) approach plays a crucial for the development of the robust design optimization (RDO) framework. Within this appendix, the equations for the sample variance of the NISS component functions are added. They are required for the determination of the confidence intervals which are used as metric to judge about the quality of the approximated response mean and variance. In addition, the multi-point non-intrusive imprecise stochastic sampling (MNISS) expression for the response variance is stated in the second section.

B.1 Sample Variance Expressions

As stated before, the sample variance for the component functions up to the second order are summarized below. For the first stochastic response moment, the equations are given by [174]

$$Var[\mu_{y,0}] = \frac{1}{n(n-1)} \left[\sum_{k=1}^{n} \left\{ (g(\boldsymbol{x}_{\mathsf{s}}^{(k)}))^2 \right\} - n(\mu_{y,0})^2 \right],$$

$$Var[\mu_{y,i}] = \frac{1}{n(n-1)} \left[\sum_{k=1}^{n} \left\{ (g(\boldsymbol{x}_{\mathsf{s}}^{(k)}))^2 (r_{\mathsf{cut}}^{(i)})^2 \right\} - n(\mu_{y,i})^2 \right], \text{ and}$$

$$Var[\mu_{y,ij}] = \frac{1}{n(n-1)} \left[\sum_{k=1}^{n} \left\{ (g(\boldsymbol{x}_{\mathsf{s}}^{(k)}))^2 (r_{\mathsf{cut}}^{(ij)})^2 \right\} - n(\mu_{y,ij})^2 \right]. \tag{B.1}$$

Accordingly, the following expressions hold for the sample variance of the second stochastic moment:

$$\begin{aligned}
Var[\sigma_{y,0}^2] &= \frac{1}{n(n-1)} \left[\sum_{k=1}^{n} \left\{ (g(\boldsymbol{x}_{\mathsf{s}}^{(k)}) - \mu_y)^4 \right\} - n(\sigma_{y,0}^2)^2 \right], \\
Var[\sigma_{y,i}^2] &= \frac{1}{n(n-1)} \left[\sum_{k=1}^{n} \left\{ (g(\boldsymbol{x}_{\mathsf{s}}^{(k)}) - \mu_y)^4 (r_{\mathsf{cut}}^{(i)})^2 \right\} - n(\sigma_{y,i}^2)^2 \right], \text{ and} \\
Var[\sigma_{y,ij}^2] &= \frac{1}{n(n-1)} \left[\sum_{k=1}^{n} \left\{ (g(\boldsymbol{x}_{\mathsf{s}}^{(k)}) - \mu_y)^4 (r_{\mathsf{cut}}^{(ij)})^2 \right\} - n(\sigma_{y,ij}^2)^2 \right].
\end{aligned} \tag{B.2}$$

B.2 Multi-Point Non-Intrusive Imprecise Stochastic Sampling Variance Equation

Within Sec. 4.3.2, the classical NISS concept has been extended by a multi-point sampling procedure. In Eq. (4.69), the metric for the response mean has been discussed. In the sequel, the MNISS component functions for the response variance are supplemented:

$$\begin{aligned}
\sigma_{y,0}^2 &\approx \sum_{t=1}^{n_{\mathsf{p}}} w_t(\boldsymbol{\Theta}_x) \left\{ \frac{1}{n_{\mathsf{s}}} \sum_{k=1}^{n_{\mathsf{s}}} \left(g(\boldsymbol{x}_{\mathsf{s}}^{(k)}) - \mu_{y,0} \right)^2 \right\} \\
&= \sum_{t=1}^{n_{\mathsf{p}}} w_t(\boldsymbol{\Theta}_x)\, \sigma_{y,0}^{2,(t)}, \\
\sigma_{y,i}^2(\theta_x^{(i)}) &\approx \sum_{t=1}^{n_{\mathsf{p}}} w_t(\boldsymbol{\Theta}_x) \left\{ \frac{1}{n_{\mathsf{s}}} \sum_{k=1}^{n_{\mathsf{s}}} \left(g(\boldsymbol{x}_{\mathsf{s}}^{(k)}) - \mu_{y,i} - \mu_{y,0} \right)^2 r_{\mathsf{cut}}^{(i)}(\boldsymbol{x}_{\mathsf{s}}^{(k)} | \boldsymbol{\Theta}_x^{(i)}) \right\} \\
&= \sum_{t=1}^{n_{\mathsf{p}}} w_t(\boldsymbol{\Theta}_x)\, \sigma_{y,i}^{2,(t)}, \text{ and} \\
\sigma_{y,ij}^2(\boldsymbol{\Theta}_x^{(ij)}) &\approx \sum_{t=1}^{n_{\mathsf{p}}} w_t(\boldsymbol{\Theta}_x) \left\{ \frac{1}{n_{\mathsf{s}}} \sum_{k=1}^{n_{\mathsf{s}}} \left(g(\boldsymbol{x}_{\mathsf{s}}^{(k)}) - \mu_{y,ij} - \mu_{y,i} - \mu_{y,j} - \mu_{y,0} \right)^2 r_{\mathsf{cut}}^{(ij)}(\boldsymbol{x}_{\mathsf{s}}^{(k)} | \boldsymbol{\Theta}_x^{(ij)}) \right\} \\
&= \sum_{t=1}^{n_{\mathsf{p}}} w_t(\boldsymbol{\Theta}_x)\, \sigma_{y,ij}^{2,(t)}.
\end{aligned} \tag{B.3}$$

Appendix C

Epistemic Screening Results

The last section of the appendix deals with the summary of the epistemic variable screening for those parameters which are not covered in the main part. To repeat, the sensitivity analysis has been conducted for the performance model and the interdisciplinary secondary air system (SAS) model. For the first, only the sensitivity w.r.t. to the response mean and variance of $P^{(45)}$ has been shown. In case of the secondary air system, Sec. 5.2.2 discusses the sensitivity indices exemplarily for the cooling mass flow rate $Y_{\text{Rot\_2\_I}}$. In the following two sections, the results for all the remaining response parameters are shown.
The tabular structure is the same for every figure. The first- and second-order sensitivity indices for the response mean are in the upper right part whereas the lower left triangle contains sensitivity indices for the response standard deviation.

C.1 Performance Model

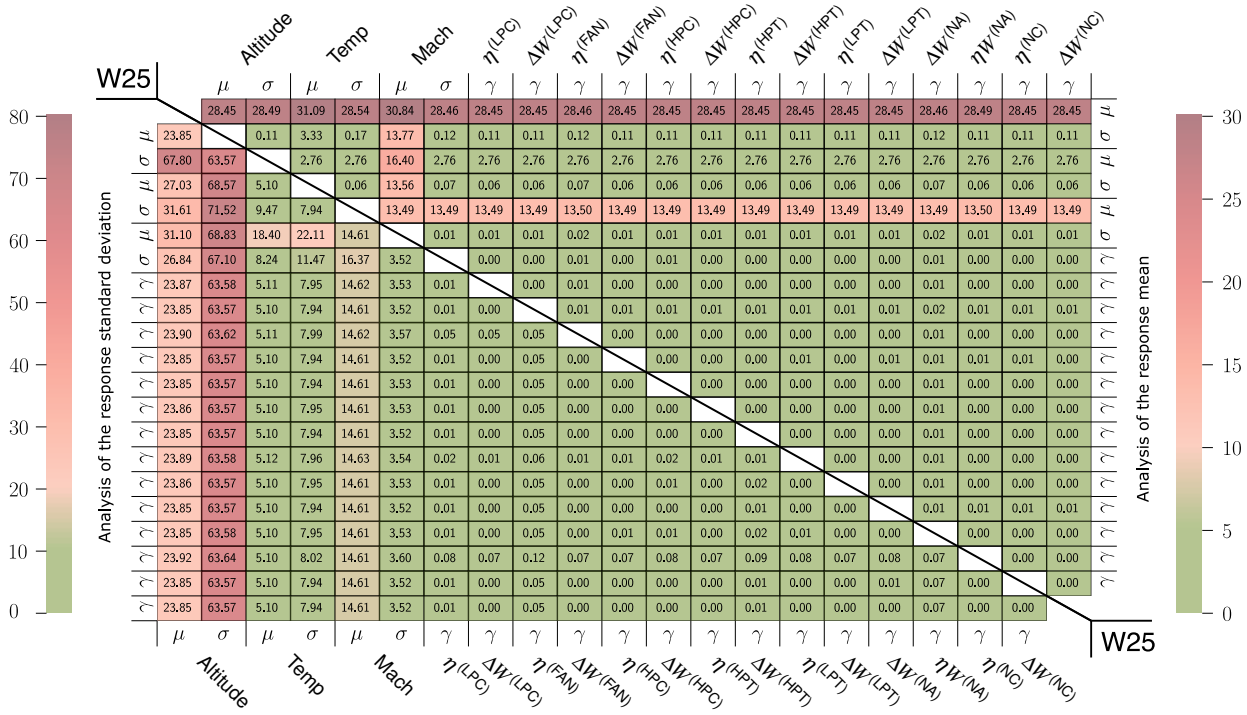

Figure C.1 Variable screening of the performance model for $W^{(25)}$.

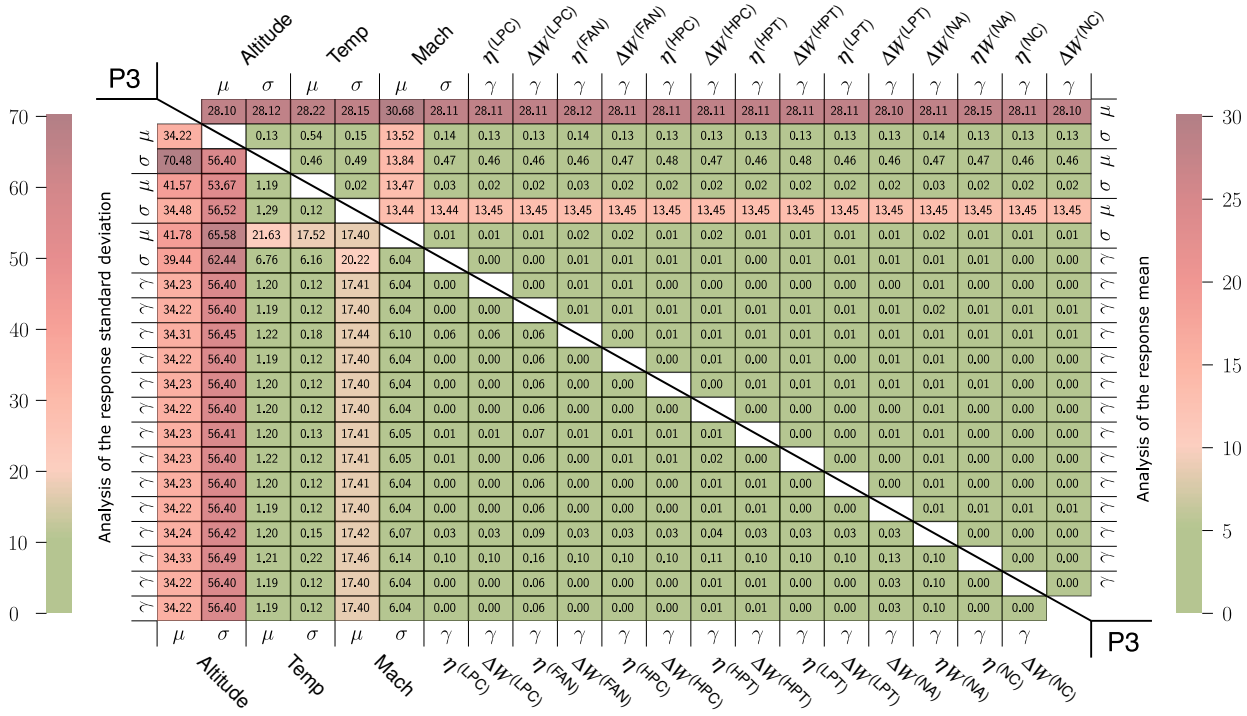

Figure C.2 Variable screening of the performance model for $P^{(3)}$.

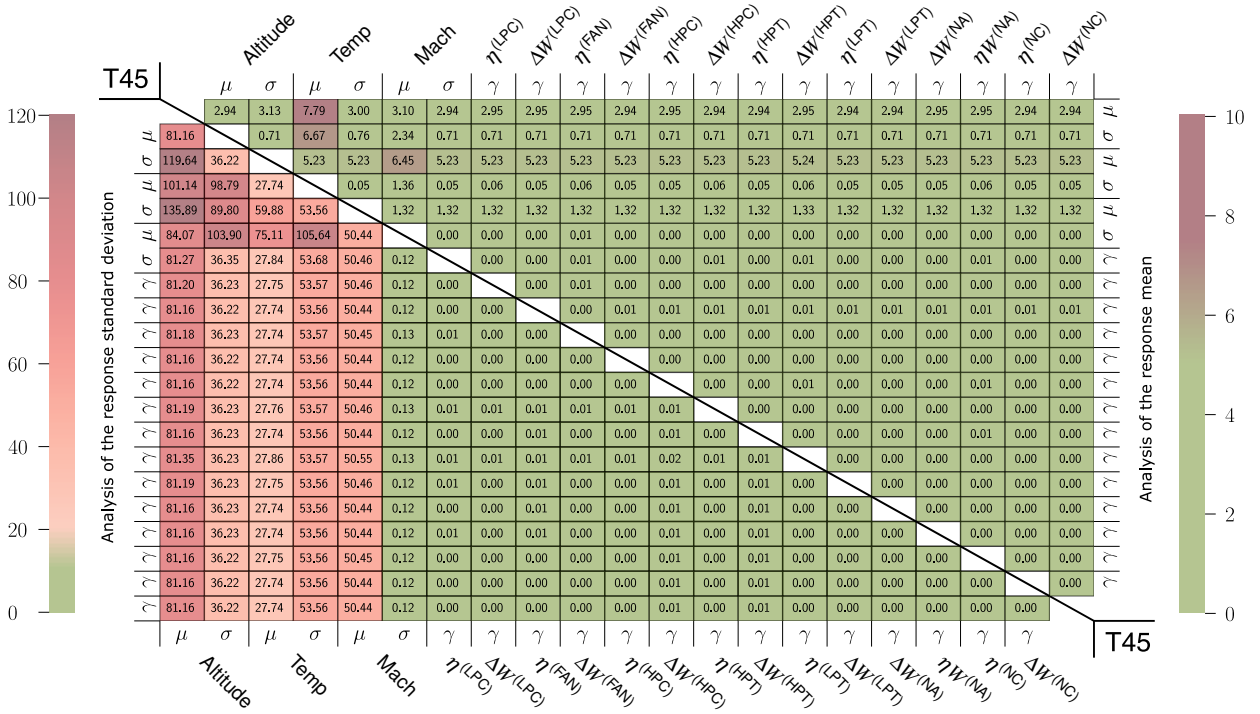

Figure C.3 Variable screening of the performance model for $T^{(45)}$.

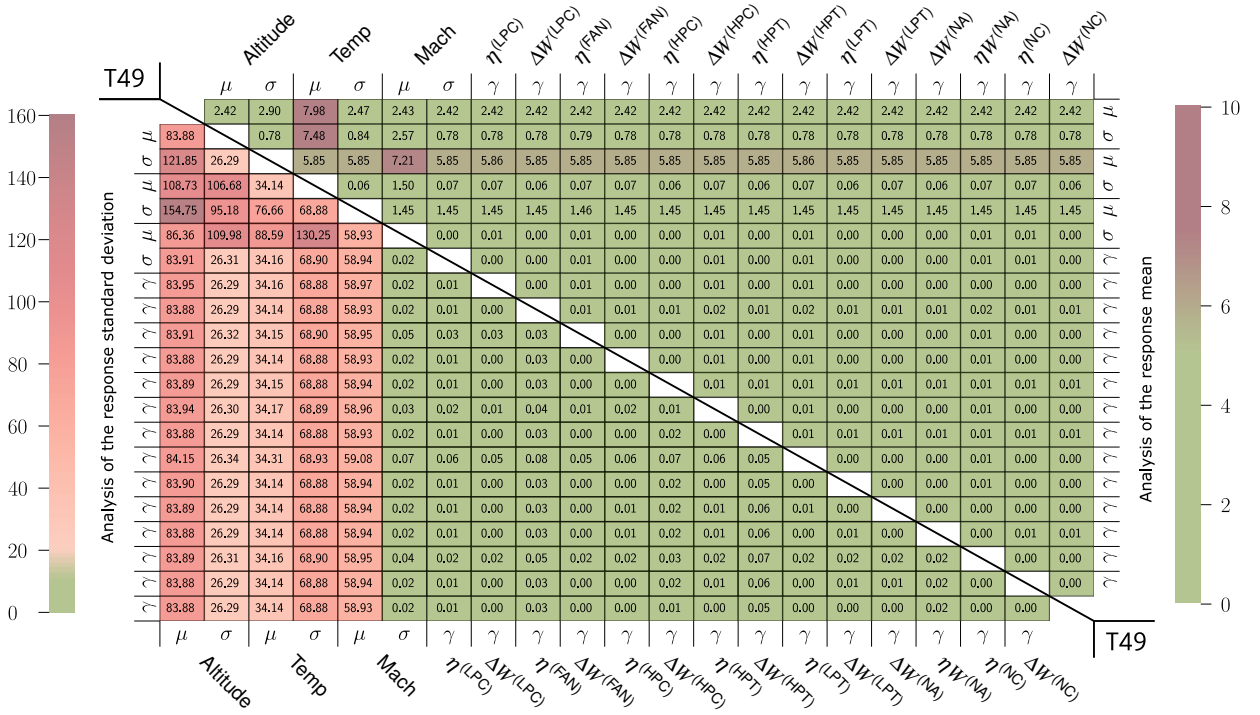

Figure C.4 Variable screening of the performance model for $T^{(49)}$.

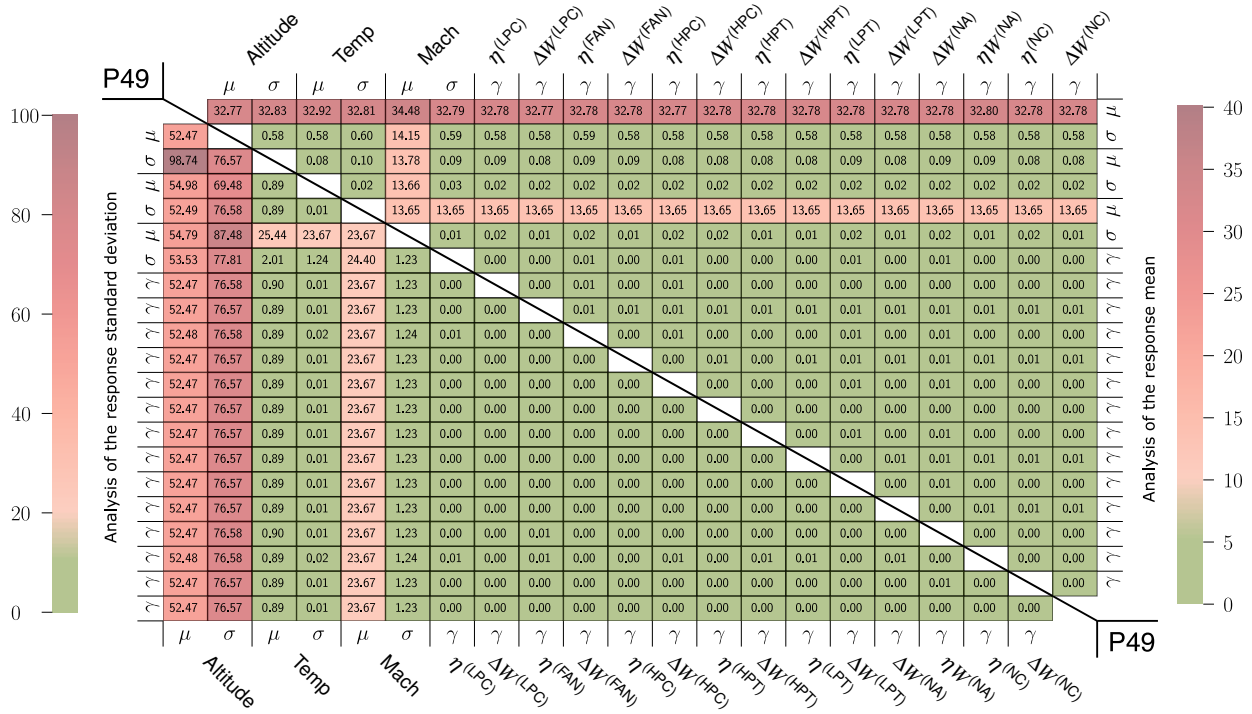

Figure C.5 Variable screening of the performance model for $P^{(49)}$.

C.2 Interdisciplinary Secondary Air System Model

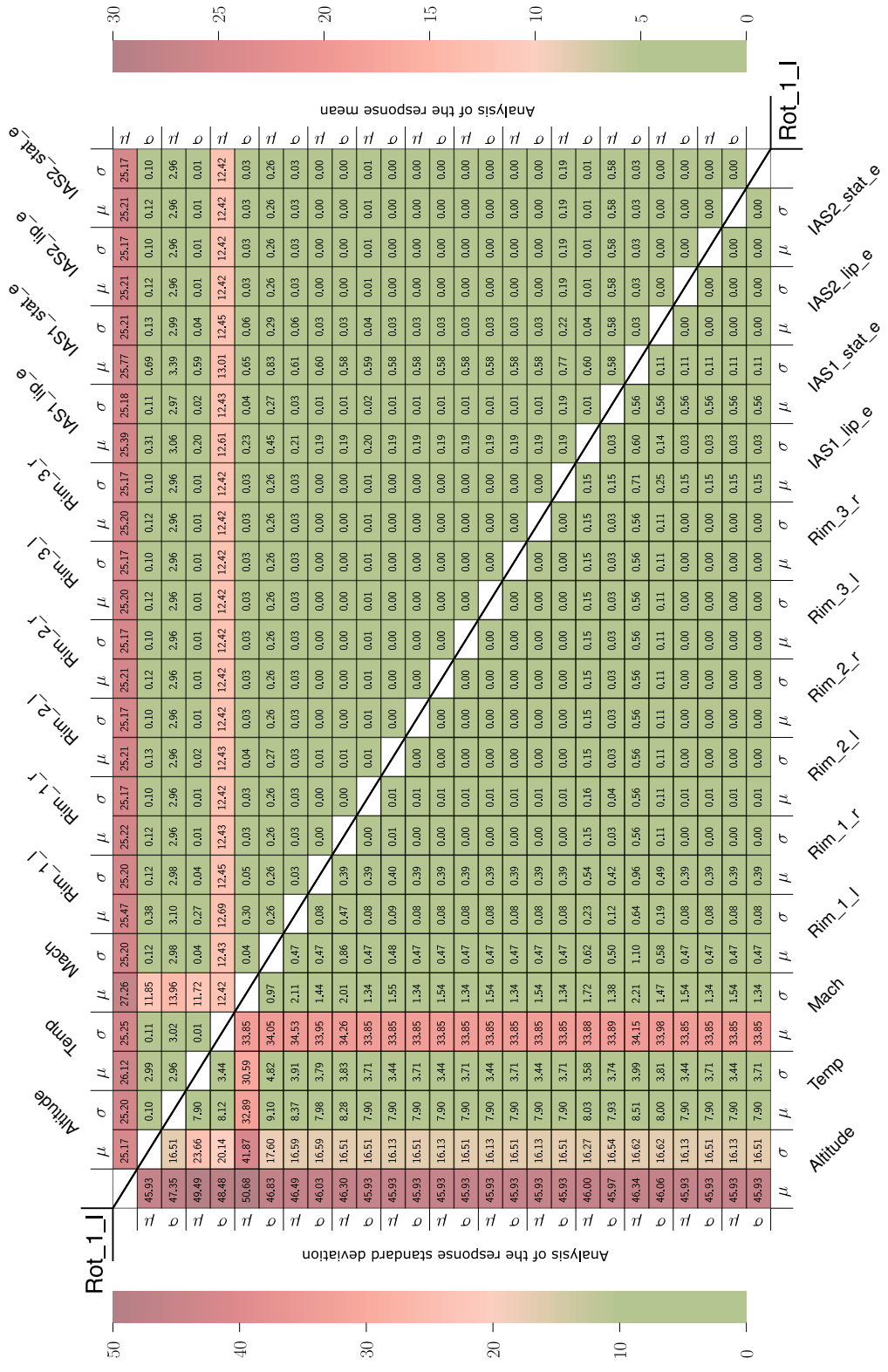

Figure C.6 Variable screening of the interdisciplinary SAS model for $Y_{\text{Rot\_1\_l}}$.

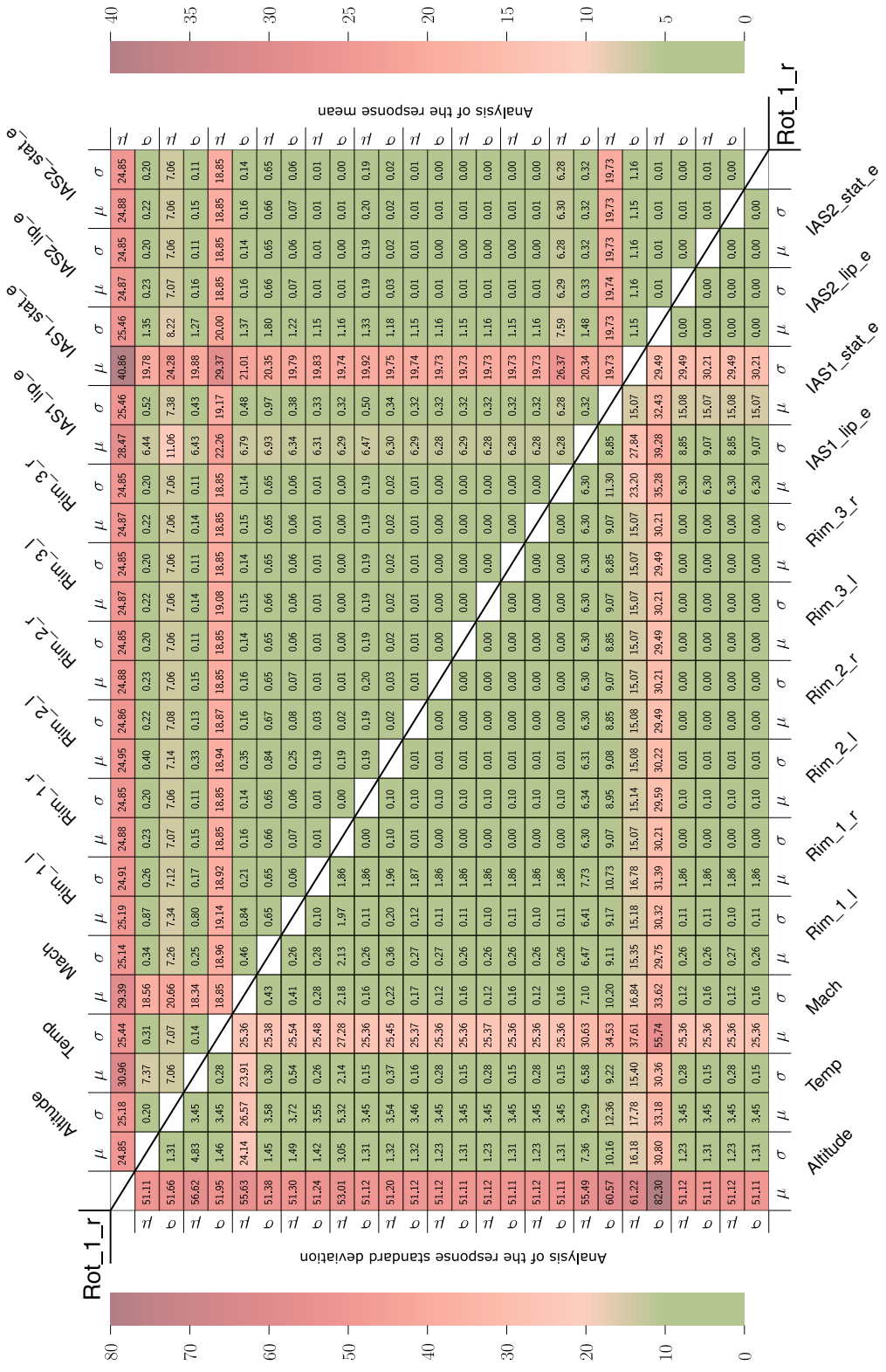

Figure C.7 Variable screening of the interdisciplinary SAS model for $Y_{\text{Rot\_1\_r}}$.

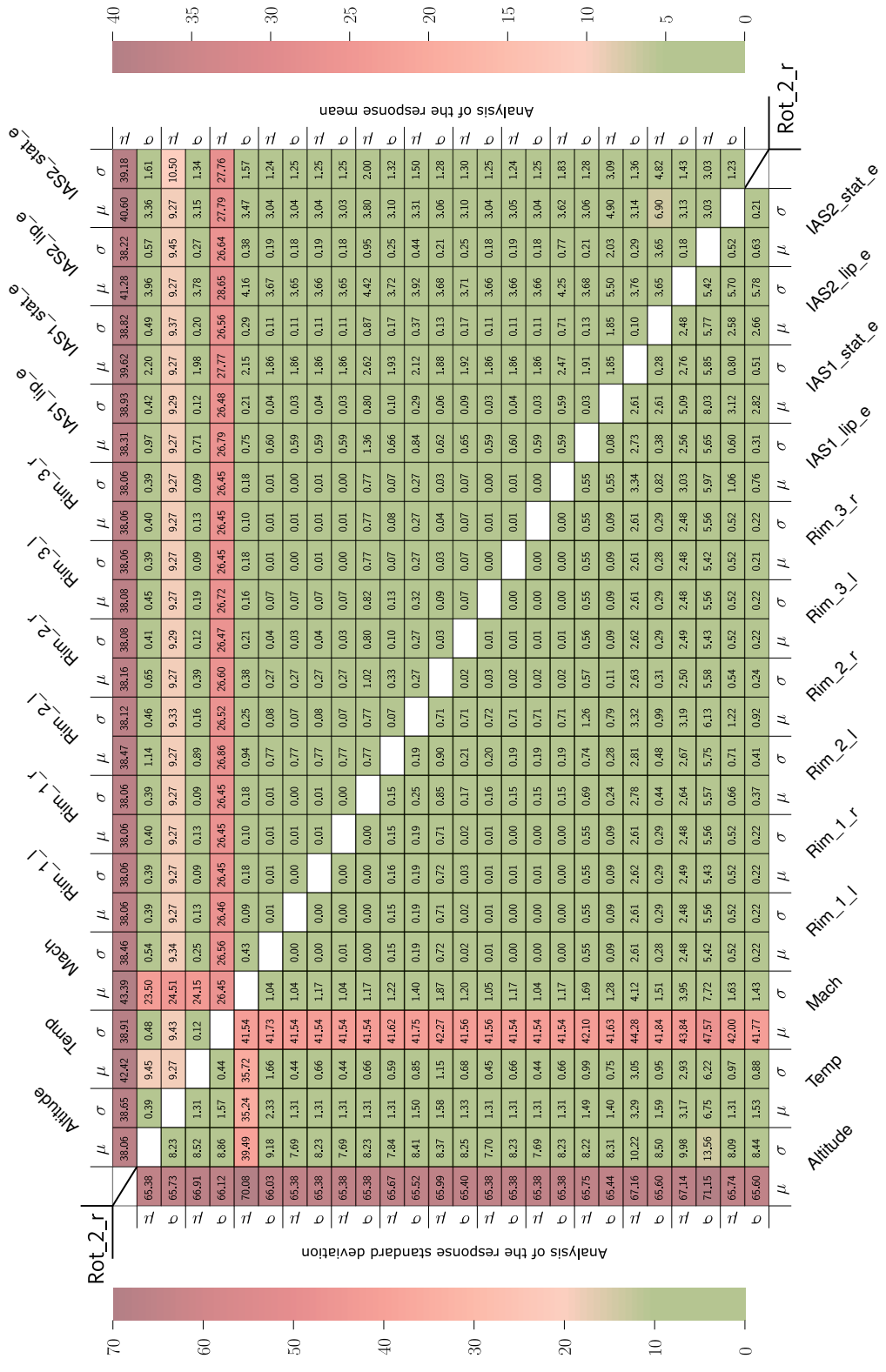

Figure C.8 Variable screening of the interdisciplinary SAS model for $Y_{\text{Rot\_2\_r}}$.

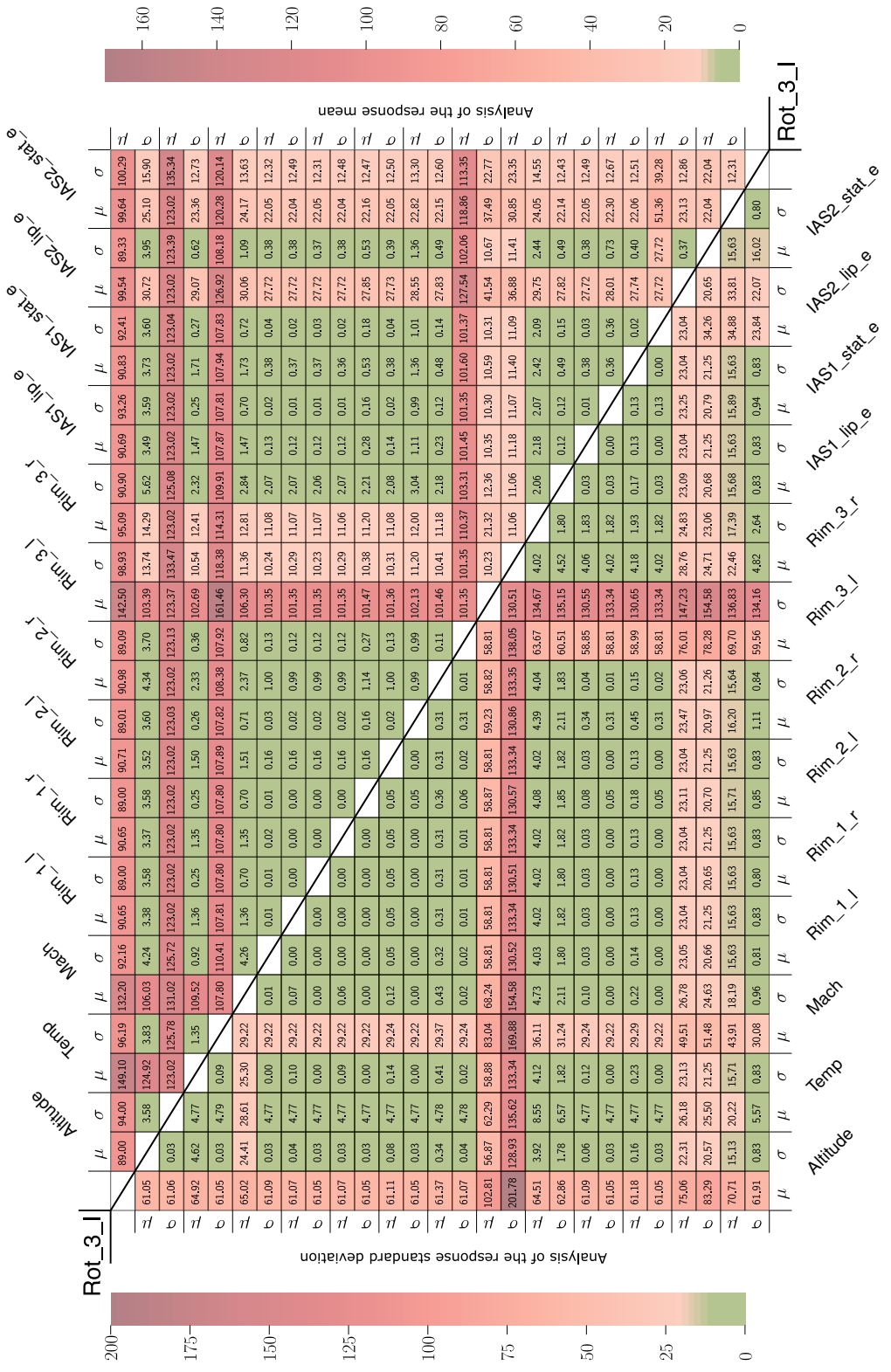

Figure C.9 Variable screening of the interdisciplinary SAS model for $Y_{\text{Rot\_3\_l}}$.

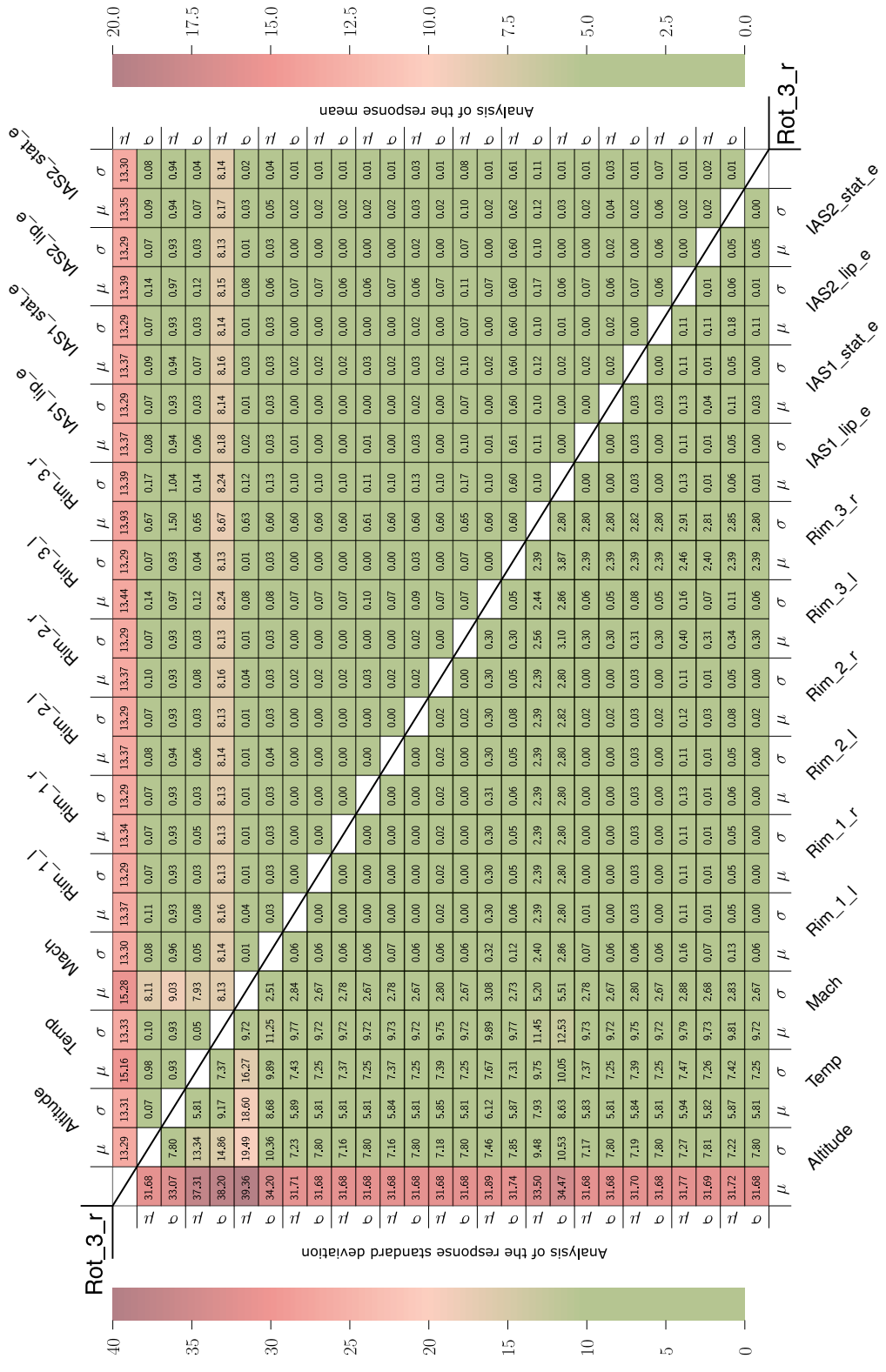

Figure C.10 Variable screening of the interdisciplinary SAS model for $Y_{\text{Rot\_3\_r}}$.

Mathematical Symbols

Random Variable Notation

X	Random input quantity
$\mathbf{X}$	Random input vector
$\mathbf{X}^{\mathsf{d}}$	Design input vector
$\mathbf{X}^{\mathsf{n}}$	Noise input vector
$\mathbf{x}$	Realization of $\mathbf{X}$
$\underline{\mathbf{x}}$	Lower bounds of an interval-valued random variable $\mathbf{X}$
$\overline{\mathbf{x}}$	Upper bounds of an interval-valued random variable $\mathbf{X}$
X_i	i-th element of $\mathbf{X}$
$\underline{x}_i$	i-th element of $\underline{\mathbf{x}}$
$\overline{x}_i$	i-th element of $\overline{\mathbf{x}}$
Y	Random response quantity
$\mathbf{Y}$	Random response vector
$\mathbf{y}$	Realization of $\mathbf{Y}$
y	Realization of Y
Y_i	i-th element of $\mathbf{Y}$
$f_{\mathbf{X}}(\mathbf{x})$	Joint probability density function
$F_{\mathbf{X}}(\mathbf{x})$	Joint cumulative distribution function
$f_X(x)$	Probability density function
$F_X(x)$	Cumulative distribution function of X
$\underline{F}_X(x)$	Lower bound of an input quantity's probability-box
$\overline{F}_X(x)$	Upper bound of an input quantity's probability-box
$Bel(\mathcal{S})$	Measure for the belief in the subset $\mathcal{S} \subset \mathcal{F}_e$
$Pl(\mathcal{S})$	Measure for the plausibility of the subset $\mathcal{S} \subset \mathcal{F}_e$
$F_Y(y)$	Cumulative distribution function of Y
$\underline{F}_Y(y)$	Lower bound of a response quantity's probability-box
$\overline{F}_Y(y)$	Upper bound of a response quantity's probability-box

Stochastic Descriptor Notation

$\boldsymbol{\mu}_x$	Mean value vector for $\mathbf{X}$
$\boldsymbol{\sigma}_x^2$	Variance vector for $\mathbf{X}$
$\boldsymbol{\sigma}_x$	Standard Deviation vector for $\mathbf{X}$

μ_x Mean value of X
σ_x Standard deviation of X
$\check{\mu}_x$ Sample mean value of X
$\check{\sigma}_x$ Sample standard deviation of X
$\tilde{X}$ Median value of X
$\hat{X}$ Mode value of X
γ_x Skewness of X
κ_x Kurtosis of X
σ_x^I Interval-valued standard deviation of X
μ_x^I Interval-valued mean value of X
$\mathbf{\Sigma}_x$ Covariance matrix of $\mathbf{X}$
$\boldsymbol{\mu}_y$ Mean value vector for $\mathbf{Y}$
$\boldsymbol{\sigma}_y^2$ Variance vector for $\mathbf{Y}$
μ_y Mean value of Y
σ_y Standard deviation of Y
$\check{\mu}_y$ Sample mean value of Y
$\check{\sigma}_y$ Sample standard deviation of Y
σ_y^2 Variance of Y
$\mathbf{\Sigma}_y$ Covariance matrix of $\mathbf{Y}$

Hyperparameter Notation

$\theta_x^{I,(i)}$ i-th element of $\mathbf{\Theta}_x^I$
$\theta_x^{(i)}$ i-th element of $\mathbf{\Theta}_x$
$\mathbf{\Theta}_g$ Calibration parameters of the computational model
$\mathbf{\Theta}_x$ Set of hyperparameters of a probabilistic model
$\mathbf{\Theta}_x^I$ Interval-valued set of hyperparameters of a probabilistic model
$\underline{\theta}_x^{(i)}$ Lower bound of the i-th element of $\mathbf{\Theta}_x^I$
$\overline{\theta}_x^{(i)}$ Upper bound of the i-th element of $\mathbf{\Theta}_x^I$

Uncertainty Quantification & Propagation

$\mathcal{U}_\mathsf{s}$ Set of sample points drawn from the unit space
$\boldsymbol{u}_\mathsf{s}^{(i)}$ i-th element of $\mathcal{U}_\mathsf{s}$
$\mathcal{X}_\mathsf{m}$ Set of measurement data related to the model's input quantities
$\mathcal{X}_\mathsf{s}$ Set of sample points drawn from probabilistic distributions of the model's input quantities
$\mathcal{X}_\mathsf{s}^I$ Set of interval bounds drawn from free p-boxes of the model's input quantities
$\boldsymbol{x}_\mathsf{m}^{(i)}$ i-th element of $\mathcal{X}_\mathsf{m}$
$\boldsymbol{x}_\mathsf{s}^{(i)}$ i-th element of $\mathcal{X}_\mathsf{s}$
$\boldsymbol{x}_\mathsf{s}^{I,(i)}$ i-th element of $\mathcal{X}_\mathsf{s}^I$

$\underline{x}_{\mathrm{s}}^{(i)}$ Lower bound of the i-th element of $\mathcal{X}_{\mathrm{s}}^{I}$
$\overline{x}_{\mathrm{s}}^{(i)}$ Upper bound of the i-th element of $\mathcal{X}_{\mathrm{s}}^{I}$
$\mathcal{Y}_{\mathrm{m}}$ Set of measurement data related to the model's response quantities
$\mathcal{Y}_{\mathrm{s}}$ Set of sample points obtained from propagating $\mathcal{X}_{\mathrm{s}}$ throughout a computational model
$\mathcal{Y}_{\mathrm{s}}^{I}$ Set of propagated interval-valued sample points
$y_{\mathrm{m}}^{(i)}$ i-th element of $\mathcal{Y}_{\mathrm{m}}$
$y_{\mathrm{s}}^{(i)}$ i-th element of $\mathcal{Y}_{\mathrm{s}}$
$y_{\mathrm{s}}^{I,(i)}$ i-th element of $\mathcal{Y}_{\mathrm{s}}^{I}$
$\underline{y}_{\mathrm{s}}^{(i)}$ Lower bound of the i-th element of $\mathcal{Y}_{\mathrm{s}}^{I}$
$\overline{y}_{\mathrm{s}}^{(i)}$ Upper bound of the i-th element of $\mathcal{Y}_{\mathrm{s}}^{I}$

Notation related to the Hyperrectangle & Hyperellipsoid approach

$\mathcal{C}_x$ Convex hull describing the uncertainty on $\mathbf{X}$
$\mathcal{E}_x$ Ellipsoid describing the input quantity uncertainty
$\tilde{\mathcal{E}}_x$ Ellipsoid describing the input quantity uncertainty derived from a linearized model
$\mathcal{C}_{\mathcal{Y}_{\mathrm{m}}}$ Convex hull of the measurement set $\mathcal{Y}_{\mathrm{m}}$
$\mathcal{E}_{\mathcal{Y}_{\mathrm{m}}}$ MVEE of the measurement set $\mathcal{Y}_{\mathrm{m}}$
$\mathcal{C}_{\mathcal{Y}_{\mathrm{s}}}$ Convex hull of the propagated sample point set $\mathcal{Y}_{\mathrm{s}}$
$\mathcal{E}_{\mathcal{Y}_{\mathrm{s}}}$ MVEE of the propagated sample point set $\mathcal{Y}_{\mathrm{s}}$
$\tilde{\mathcal{E}}_{\mathcal{Y}_{\mathrm{s}}}$ MVEE of the propagated sample point set drawn from $\tilde{\mathcal{E}}_x$

Dimensionality

n_{f} Number of focal elements in $\mathcal{F}_e$
n_{m} Number of measurement points
n_{p} Number of proposal distributions for the MNISS concept
n_{s} Number of sample points
n_{Θ} Number of hyperparameters
n_{TS} Number of model evaluations for the finite difference method
n_x Number of dimensions in the input space
n_y Number of dimensions in the output space

Performance Parameters

$\eta^{(i)}$ efficiency of the i-th jet engine component
$\Delta W^{(i)}$ flow capacity of the i-th jet engine component
$T^{(i)}$ temperature at the i-th station
$P^{(i)}$ pressure at the i-th station

Abbreviations

ADP	aerodynamic design point
ANOVA	analysis of variance
BPA	basic probability assignment
CBF	cumulative belief function
CDF	cumulative distribution function
CI	confidence interval
CLT	central limit theorem
CoV	coefficient of variation
CPF	cumulative plausibility function
CT	computation time
DEQ	differential equation
DE	differential evolution
DoE	design of experiments
EMCS	extended Monte Carlo sampling
ESA	European Space Agency
FAST	Fourier amplitude sensitivity testing
FCI	flight cost index
FOI	first-order index
HDMR	high-dimensional model representation
HPC	high-pressure compressor
HPT	high-pressure turbine
IAS	inner air seal
i.i.d.	independently and identically distributed
ISA	international standard atmosphere
IS	importance sampling
IVP	interval-valued probability
KS	Kolmogorov-Smirnov
LH	Latin hypercube
LPC	low-pressure compressor
LPT	low-pressure turbine
MCMC	Markov Chain Monte Carlo
MC	Monte Carlo
MMR	minimax regret
MNISS	multi-point non-intrusive imprecise stochastic sampling
MVEE	minimum-volume enclosing ellipsoid
NISS	non-intrusive imprecise stochastic sampling
NM	nautical mile
OAT	one-at-a-time
OLH	optimal Latin hypercube
OPUS	optimization utility system
p-box	probability-box
PBH	power-by-the-hour

PCC	partial correlation coefficient
PDF	probability density function
PI	pinching index
PRCC	partial rank correlation coefficient
QoI	quantity of interest
RDO	robust design optimization
RMSE	root mean square error
SAS	secondary air system
SA	sensitivity analysis
SCM	streamline curvature method
SFC	specific fuel consumption
SI	sensitivity index
SNR	signal-to-noise ratio
SOI	second-order index
SOP	second-order probability
SRC	standard regression coefficient
SRRC	standard rank regression coefficient
SSC	scaled sensitivity coefficient
UQ	uncertainty quantification
WWA	world-wide average

List of Figures

List of Tables

Bibliography

[1] Kjersti Aas, Claudia Czado, Arnoldo Frigessi, and Henrik Bakken. Pair-copula constructions of multiple dependence. *Insurance: Mathematics and economics*, 44(2):182–198, 2009. doi: https://doi.org/10.1016/j.insmatheco.2007.02.001.

[2] MTU Aero Engines AG. Engine Trend Monitoring (ETM). Website. https://www.mtu.de/de/maintenance/customized-solutions-for-aero-engines/serviceplus/engine-trend-monitoring/, Accessed: 2023-04-19.

[3] MTU Aero Engines AG. GTF engine. Website. https://www.mtu.de/engines/commercial-aircraft-engines/narrowbody-and-regional-jets/gtf-engine-family/, Accessed: 2023-03-31.

[4] Christoph Aistleitner, Markus Hofer, and Robert Tichy. A central limit theorem for Latin hypercube sampling with dependence and application to exotic basket option pricing. *International Journal of Theoretical and Applied Finance*, 15(7):1250046, 2012. doi: https://doi.org/10.1142/S021902491250046X.

[5] Janet K. Allen, Carolyn Seepersad, HaeJin Choi, and Farrokh Mistree. Robust Design for Multiscale and Multidisciplinary Applications. *Journal of Mechanical Design*, 128(4):832–843, 2006. doi: https://doi.org/10.1115/1.2202880.

[6] Lena Altherr. *Algorithmic System Design under Consideration of Dynamic Processes*. PhD thesis, Fachbereich Maschinenbau, Technische Universität Darmstadt, Germany, 2016. ISBN: 978-3-8440-4848-3.

[7] Nino Andricevic. *Robustheitsbewertung crashbelasteter Fahrzeugstrukturen*. PhD thesis, Technische Fakultät der Albert-Ludwigs-Universität, Freiburg im Breisgau, Germany, 2016. doi: https://doi.org/10.6094/UNIFR/10848.

[8] Alfredo H-S. Ang and Wilson H. Tang. Analytical Models of Random Phenomena. In *Probability Concepts in Engineering: Emphasis on Applications to Civil and Environmental Engineering*, chapter 3, pages 81–150. John Wiley & Son, 2006. ISBN: 978-0-471-72064-5.

[9] Giulia Antinori. *Uncertainty analysis and robust optimization for low pressure turbine rotors*. PhD thesis, Technische Universität München, München, Germany, 2016. URL: http://nbn-resolving.de/urn/resolver.pl?urn:nbn:de:bvb:91-diss-20160804-1279009-0-6.

[10] Giulia Antinori, Fabian Duddeck, and Andreas Fischersworring-Bunk. Sensitivity Analysis and Uncertainty Quantification for a Coupled Secondary Air System Thermo-Mechanical Model of a Jet Engine Low Pressure Turbine Rotor. In *Second International Conference on Vulnerability and Risk Analysis and Management (ICVRAM) and the Sixth International Symposium on Uncertainty, Modeling, and Analysis (ISUMA)*, pages 1543–1553, 2014. doi: https://doi.org/10.1061/9780784413609.155, ISBN: 978-0-7844-1360-9.

[11] Giulia Antinori, Yannick Muller, Fabian Duddeck, and Andreas Fischersworring-Bunk. Statistical Methods for a Stochastic Analysis of the Secondary Air System of a Jet Engine Low Pressure Turbine. In *ASME Turbo Expo: Power for Land, Sea, and Air*, page V03AT15A009, 2013. doi: https://doi.org/10.1115/GT2013-94881, ISBN: 978-0-7918-5514-0.

[12] ARP 755D - Aircraft Propulsion System Performance Station Designation and Nomenclature. Standard, SAE International, 2014. doi: https://doi.org/10.4271/ARP755D.

[13] Jason Matthew Aughenbaugh and Christiaan J. J. Paredis. Probability Bounds Analysis as a General Approach to Sensitivity Analysis in Decision Making Under Uncertainty. In *SAE World Congress & Exhibition*. SAE International, 2007. doi: https://doi.org/10.4271/2007-01-1480.

[14] A. Azzalini. A Class of Distributions Which Includes the Normal Ones. *Scandinavian Journal of Statistics*, 12(2):171–178, 1985. URL: http://www.jstor.org/stable/4615982.

[15] Adelchi Azzalini. Heavy and adaptive tails. In *The Skew-Normal and Related Families*, Institute of Mathematical Statistics Monographs, chapter 4, pages 95—-123. Cambridge University Press, 2013. doi: https://doi.org/10.1017/CBO9781139248891, ISBN: 9781139248891.

[16] C. Bradford Barber, David P. Dobkin, and Hannu Huhdanpaa. The Quickhull Algorithm for Convex Hulls. *ACM Trans. Math. Softw.*, 22(4):469–483, 1996. doi: https://doi.org/10.1145/235815.235821.

[17] Peter Bastian. Numerische Lösung partieller Differentialgleichungen. Lecture Notes, 2009. Institut für Parallele und Verteilte Systeme, Universität Stuttgart, Germany.

[18] Thomas Bayes. An essay towards solving a problem in the doctrine of chances. By the late Rev. Mr. Bayes, F. R. S. communicated by Mr. Price, in a letter to John Canton, A. M. F. R. S. *Philosophical Transactions of the Royal Society of London*, 53:370–418, 1763. doi: https://doi.org/10.1098/rstl.1763.0053.

[19] Pierre Beaurepaire, Matteo Broggi, and Edoardo Patelli. Computation of the Sobol' Indices using Importance Sampling. In *Second International Conference on Vulnerability and Risk Analysis and Management (ICVRAM) and the Sixth International Symposium on Uncertainty, Modeling, and Analysis (ISUMA)*, pages 2115–2124, 2014. doi: https://doi.org/10.1061/9780784413609.212.

[20] J. L. Beck and L. S. Katafygiotis. Updating Models and their Uncertainties. I: Bayesian Statistical Framework. *Journal of Engineering Mechanics*, 124(4):455–461, 1998. doi: https://doi.org/10.1061/(ASCE)0733-9399(1998)124:4(455).

[21] Michael Beer, Scott Ferson, and Vladik Kreinovich. Imprecise probabilities in engineering analyses. *Mechanical Systems and Signal Processing*, 37(1-2):4–29, 2013. doi: https://doi.org/10.1016/j.ymssp.2013.01.024.

[22] Sifeng Bi, Matteo Broggi, Pengfei Wei, and Michael Beer. The Bhattacharyya distance: Enriching the P-box in stochastic sensitivity analysis. *Mechanical Systems and Signal Processing*, 129:265–281, 2019. doi: https://doi.org/10.1016/j.ymssp.2019.04.035.

[23] Francesco Biscani and Dario Izzo. A parallel global multiobjective framework for optimization: pagmo. *Journal of Open Source Software*, 5(53):2338, 2020. doi: https://doi.org/10.21105/joss.02338.

[24] Thomas Bischoff, Matthias Voigt, Ed Chehab, and Konrad Vogeler. Probabilistic Analysis of Stationary Gas Turbine Secondary Air Systems. In *ASME Turbo Expo 2006: Power for Land, Sea, and Air*, pages 1365–1373, 2006. doi: https://doi.org/10.1115/GT2006-90261, ISBN: 0-7918-4238-X.

[25] Joseph K. Blitzstein and Jessica Hwang. Continuous random variables. In *Introduction to Probability*, chapter 5, pages 195 – 242. Taylor & Francis Group, New York, USA, 2014. doi: https://doi.org/10.1201/b17221, ISBN: 978-1-4665-7559-2.

[26] Joseph K. Blitzstein and Jessica Hwang. Continuous random variables. In *Introduction to Probability*, chapter 6, pages 243 – 276. Taylor & Francis Group, New York, USA, 2014. doi: https://doi.org/10.1201/b17221, ISBN: 978-1-4665-7559-2.

[27] Stephen Boyd and Lieven Vandenberghe. Duality. In *Convex Optimization*, chapter 5. Cambridge University Press, Cambridge, UK, 2004. doi: https://doi.org/10.1017/CBO9780511804441, ISBN: 9780511804441.

[28] Stefan Brack. Probabilistische Analyse des Sekundärluftsystems einer Niederdruckturbine. Diploma thesis, Institut fur Luftfahrtantriebe der Universität Stuttgart, Stuttgart, Germany, July 2013.

[29] Stefan Brack and Yannick Muller. Probabilistic Analysis of the Secondary Air System of a Low-Pressure Turbine. *Journal of Engineering for Gas Turbines and Power*, 137(2):022602, 2014. doi: https://doi.org/10.1115/1.4028372.

[30] Willy J.G. Bräunling. Berechnung realer Triebwerke. In *Flugzeugtriebwerke: Grundlagen, Aero-Thermodynamik, ideale und reale Kreisprozesse, Thermische Turbomaschinen, Komponenten, Emissionen und Systeme*, chapter 14, pages 1349–1484. Springer Vieweg, Berlin, Germany, 2015. doi: https://doi.org/10.1007/978-3-642-34539-5_14, ISBN: 978-3-642-34539-5.

[31] Willy J.G. Bräunling. Thermische Turbomaschinen. In *Flugzeugtriebwerke: Grundlagen, Aero-Thermodynamik, ideale und reale Kreisprozesse, Thermische Turbomaschinen, Komponenten, Emissionen und Systeme*, chapter 8, pages 681–938. Springer Vieweg, Berlin, Germany, 2015. doi: https://doi.org/10.1007/978-3-642-34539-5_8, ISBN: 978-3-642-34539-5.

[32] Willy J.G. Bräunling. Triebwerkssysteme. In *Flugzeugtriebwerke: Grundlagen, Aero-Thermodynamik, ideale und reale Kreisprozesse, Thermische Turbomaschinen, Komponenten, Emissionen und Systeme*, chapter 16, pages 1553–1684. Springer Vieweg, Berlin, Germany, 2015. doi: https://doi.org/10.1007/978-3-642-34539-5_16, ISBN: 978-3-642-34539-5.

[33] Matteo Broggi, Matthias Faes, Edoardo Patelli, Yves Govers, David Moens, and Michael Beer. Comparison of Bayesian and interval uncertainty quantification: Application to the AIRMOD test structure. In *2017 IEEE Symposium Series on Computational Intelligence (SSCI)*, pages 1–8, 2017. doi: https://doi.org/10.1109/SSCI.2017.8280882.

[34] McCracken James R. Brown, Wesley D. and Peter T. Vercellone. Turbine rim configuration, 1991. European Patent Office, EP 0437977 A1, Applicant: United Technologies Corporation, URL: https://data.epo.org/gpi/EP0437977A1-Turbine-rim-configuration.html.

[35] Boxin Tang C. Devon Lin. Latin hypercubes and space-filling designs. In *Handbook of Design and Analysis of Experiments*, chapter 17, pages 593–627. CRC Press, New York, USA, 2015. doi: https://doi.org/10.1201/b18619-23, ISBN: 9781466504332.

[36] Russel E. Caflisch. Monte Carlo and quasi-Monte Carlo methods. *Acta Numerica*, 7:1––49, 1998. doi: https://doi.org/10.1017/S0962492900002804.

[37] Xinjia Chen. A new generalization of Chebyshev inequality for random vectors. *arXiv preprint arXiv:0707.0805*, 2007. doi: https://doi.org/10.48550/arXiv.0707.0805.

[38] H. Cohen, G. F.C. Rodgers, and H. I.H. Saravanamuttoo. Gas turbine cycles for aircraft propulsion. In *Gas turbine theory*, chapter 3, pages 76–108. Longman Scientific & Technical, Harlow, UK, 1987. ISBN: 0-582-30539-X.

[39] Aereos company. Airline Operating Cost Structure. https://aereos.com/changing-aircraft-landscape-boeing-787-der-opportunities/. Accessed: 2023-04-19.

[40] R. I. Cukier, C. M. Fortuin, K. E. Shuler, A. G. Petschek, and J. H. Schaibly. Study of the sensitivity of coupled reaction systems to uncertainties in rate coefficients. I. Theory. *The Journal of Chemical Physics*, 59(8):3873–3878, 1973. doi: https://doi.org/10.1063/1.1680571.

[41] Lorraine Daston. Associationism and the Meaning of Probability. In *Classical Probability in the Enlightenment*, chapter 4, pages 188–225. Princeton University Press, Princeton, New Jersey, USA, 1988. ISBN: 0-691-08497-1.

[42] Armen Der Kiureghian and Ove Ditlevsen. Aleatory or epistemic? Does it matter? *Structural safety*, 31(2):105–112, 2009. doi: https://doi.org/10.1016/j.strusafe.2008.06.020.

[43] S. W. Dharmadhikari and K. Joag-Dev. The Gauss–Tchebyshev Inequality for Unimodal Distributions. *Theory of Probability & Its Applications*, 30(4):867–871, 1986. doi: https://doi.org/10.1137/1130111.

[44] Bastian Dörig, Thorsten Ederer, Peter F. Pelz, Marc E. Pfetsch, and Jan Wolf. Gearbox design via mixed-integer programming. In *Proceedings of the VII European Congress on Computational Methods in Applied Sciences and Engineering*, pages 8294 – 8304, 2016. doi: https://doi.org/10.7712/100016.2414.7601.

[45] Xiaoping Du, Pavan Kumar Venigella, and Deshun Liu. Robust mechanism synthesis with random and interval variables. *Mechanism and Machine Theory*, 44(7):1321–1337, 2009. doi: https://doi.org/10.1016/j.mechmachtheory.2008.10.003.

[46] Fabian Duddeck. Survey on Robust Design and Optimisation for Crashworthiness. In *Euromech Colloquium 482 - Efficient Methods for Robust Design and Optimization*, London, UK, 2007. Queen Mary University of London. URL: http://www.euromech.org/colloquia/events_list?year=2007.

[47] J. J. Duistermaat and J. A. C. Kolk. Taylor Expansion in Several Variables. In *Distributions: Theory and Applications*, pages 59–63. Birkhäuser, Boston, USA, 2010. doi: https://doi.org/10.1007/978-0-8176-4675-2_6, ISBN: 978-0-8176-4675-2.

[48] M.S. Eldred, L.P. Swiler, and G. Tang. Mixed aleatory-epistemic uncertainty quantification with stochastic expansions and optimization-based interval estimation. *Reliability Engineering & System Safety*, 96(9):1092–1113, 2011. doi: https://doi.org/10.1016/j.ress.2010.11.010.

[49] Gal Elidan. Copulas in Machine Learning. In *Copulae in Mathematical and Quantitative Finance*, chapter 3, pages 39–60. Springer, Berlin, Heidelberg, Germany, 2013. doi: https://doi.org/10.1007/978-3-642-35407-6_3, ISBN: 978-3-642-35407-6.

[50] I. Elishakoff and N. Sarlin. Uncertainty quantification based on pillars of experiment, theory, and computation. Part II: Theory and computation. *Mechanical Systems and Signal Processing*, 74:54–72, 2016. doi: https://doi.org/10.1016/j.ymssp.2015.04.036.

[51] Matthias Faes, Matteo Broggi, Edoardo Patelli, Yves Govers, John Mottershead, Michael Beer, and David Moens. Inverse quantification of epistemic uncertainty under scarce data: Bayesian or Interval approach? In *13th International Conference on Applications of Statistics and Probability in Civil Engineering*, 2019. doi: https://doi.org/10.22725/ICASP13.060.

[52] Matthias Faes, Matteo Broggi, Edoardo Patelli, Yves Govers, John Mottershead, Michael Beer, and David Moens. A multivariate interval approach for inverse uncertainty quantification with limited experimental data. *Mechanical Systems and Signal Processing*, 118:534–548, 2019. doi: https://doi.org/10.1016/j.ymssp.2018.08.050.

[53] Matthias Faes, Jasper Cerneels, Dirk Vandepitte, and David Moens. Identification and quantification of multivariate interval uncertainty in finite element models. *Computer Methods in Applied Mechanics and Engineering*, 315:896–920, 2017. doi: https://doi.org/10.1016/j.cma.2016.11.023.

[54] Matthias Faes, Marco Daub, and Michael Beer. Engineering analysis with imprecise probabilities: a state-of-the-art review on P-boxes. In *Proceedings of the 7th Asian-Pacific Symposium on Structural Reliability and its Applications*. University of Tokyo, Japan, 2020. doi: https://doi.org/10.1016/j.strusafe.2021.102092.

[55] Matthias Faes, Marco Daub, Stefano Marelli, Edoardo Patelli, and Michael Beer. Engineering analysis with probability boxes: A review on computational methods. *Structural Safety*, 93:102092, 2021. doi: https://doi.org/10.1016/j.strusafe.2021.102092.

[56] Matthias Faes and David Moens. Multivariate dependent interval finite element analysis via convex hull pair constructions and the Extended Transformation Method. *Computer Methods in Applied Mechanics and Engineering*, 347(15):85–102, 2019. doi: https://doi.org/10.1016/j.cma.2018.12.021.

[57] Matthias Faes and David Moens. Recent Trends in the Modeling and Quantification of Non-probabilistic Uncertainty. *Archives of Computational Methods in Engineering*, 27(3):633–671, 2019. doi: https://doi.org/10.1007/s11831-019-09327-x.

[58] Francesco Fedele, Rafi L. Muhanna, Naijia Xiao, and Robert L. Mullen. Interval-Based Approach for Uncertainty Propagation in Inverse Problems. *Journal of Engineering Mechanics*, 141(1):06014013, 2015. doi: http://dx.doi.org/10.1061/(ASCE)EM.1943-7889.0000815.

[59] Scott Ferson and Lev R Ginzburg. Different methods are needed to propagate ignorance and variability. *Reliability Engineering & System Safety*, 54(2-3):133–144, 1996. doi: https://doi.org/10.1016/S0951-8320(96)00071-3.

[60] Scott Ferson, Vladik Kreinovich, Lev Ginzburg, Davis Myers, and Kari Sentz. Constructing Probability Boxes and Dempster-Shafer Structures. Technical report, Sandia National Laboratories, Albuquerque, New Mexico (USA) and Livermore, California (USA), 2003. doi: https://doi.org/10.2172/809606.

[61] Scott Ferson and W. Troy Tucker. Sensitivity analysis using probability bounding. *Reliability Engineering & System Safety*, 91(10):1435–1442, 2006. doi: https://doi.org/10.1016/j.ress.2005.11.052.

[62] Scott Ferson and W. Troy Tucker. Sensitivity in risk analyses with uncertain numbers. Technical report, Sandia National Laboratories, Albuquerque, New Mexico (USA) and Livermore, California (USA), 2006. doi: https://doi.org/10.2172/886899.

[63] Marshall Freimer, Georgia Kollia, Govind S. Mudholkar, and C. Thomas Lin. A study of the generalized lambda family. *Communications in Statistics - Theory and Methods*, 17(10):3547–3567, 1988. doi: https://doi.org/10.1080/03610928808829820.

[64] Andrew Gelman, John B. Carlin, Hal S. Stern, and Donald B. Rubin. Introduction to multiparameter models. In *Bayesian data analysis*, pages 63 –82. Chapman and Hall/CRC, New York, USA, 2013. doi: https://doi.org/10.1201/b16018, ISBN: 9780429113079.

[65] Donald Gillies. The classical theory. In *Philosophical Theories of Probability*, chapter 2, pages 14–24. Taylor & Francis Group, New York, USA, 2000. ISBN: 0-203-13224-6.

[66] GasTurb GmbH. GasTurb 14 Design and Off-Design Performance of Gas Turbines. Manual, 2023. Copyright © 2023 by GasTurb GmbH, URL: https://gasturb.de/Downloads/Manuals/GasTurb14.pdf.

[67] A. Gray, A. Wimbush, M. de Angelis, P.O. Hristov, D. Calleja, E. Miralles-Dolz, and R. Rocchetta. From inference to design: A comprehensive framework for uncertainty

quantification in engineering with limited information. *Mechanical Systems & Signal Processing*, 165(15):108210, 2022. doi: https://doi.org/10.1016/j.ymssp.2021.108210.

[68] Mircea Grigoriu. Probability Theory. In *Stochastic Calculus: Applications in Science and Engineering*, chapter 2, pages 5–101. Birkhäuser, Boston, USA, 2002. doi: https://doi.org/10.1007/978-0-8176-8228-6_2, ISBN: 978-0-8176-8228-6.

[69] Xianguang Gu, Guangyong Sun, Guangyao Li, Lichen Mao, and Qing Li. A comparative study on multiobjective reliable and robust optimization for crashworthiness design of vehicle structure. *Structural and Multidisciplinary Optimization*, 48(3):669–684, 2013. doi: https://doi.org/10.1007/s00158-013-0921-x.

[70] Jia Guo and Xiaoping Du. Sensitivity analysis with mixture of epistemic and aleatory uncertainties. *AIAA journal*, 45(9):2337–2349, 2007. doi: https://doi.org/10.2514/1.28707.

[71] Thomas Haag and Michael Hanss. Model Assessment Using Inverse Fuzzy Arithmetic. In *Information Processing and Management of Uncertainty in Knowledge-Based Systems. 13th International Conference, IPMU 2010, Dortmund, Germany, June 28–July 2, 2010.*, pages 461–470, 2010. doi: https://doi.org/10.1007/978-3-642-14058-7_48.

[72] Ian Hacking. Duality. In *The Emergence of Probability*, chapter 2, pages 11–17. Cambridge University Press, New York, USA, 1975. ISBN: 9781107266643.

[73] Jim W. Hall. Uncertainty-based sensitivity indices for imprecise probability distributions. *Reliability Engineering & System Safety*, 91(10-11):1443–1451, 2006. doi: https://doi.org/10.1016/j.ress.2005.11.042.

[74] J. C. Helton and F. J. Davis. Illustration of Sampling-Based Methods for Uncertainty and Sensitivity Analysis. *Risk Analysis*, 22(3):591–622, 2002. doi: https://doi.org/10.1111/0272-4332.00041.

[75] J.C. Helton and F.J. Davis. Latin hypercube sampling and the propagation of uncertainty in analyses of complex systems. *Reliability Engineering & System Safety*, 81(1):23–69, 2003. doi: https://doi.org/10.1016/S0951-8320(03)00058-9.

[76] Jon C. Helton, Jay D. Johnson, and William L. Oberkampf. An exploration of alternative approaches to the representation of uncertainty in model predictions. *Reliability Engineering & System Safety*, 85(1-3):39–71, 2004. doi: https://doi.org/10.1016/j.ress.2004.03.025.

[77] Jon C. Helton, Jay D. Johnson, William L. Oberkampf, and Cédric J. Sallaberry. Representation of Analysis Results Involving Aleatory and Epistemic Uncertainty. *International Journal of General Systems*, 39(6):605–646, 2010. doi: https://doi.org/10.1080/03081079.2010.486664.

[78] Jon C. Helton, JD. Johnson, William L. Oberkampf, and Curtis B. Storlie. A sampling-based computational strategy for the representation of epistemic uncertainty in model predictions with evidence theory. *Computer Methods in Applied Mechanics and Engineering*, 196(37-40):3980–3998, 2007. doi: https://doi.org/10.1016/j.cma.2006.10.049.

[79] Rolls-Royce Holdings. Rolls-Royce celebrates 50th anniversary of Power-by-the-Hour. Website. https://www.rolls-royce.com/media/press-releases-archive/yr-2012/121030-the-hour.aspx, Accessed: 2023-04-19.

[80] Myles Hollander, Douglas A. Wolfe, and Eric Chicken. Life Distributions and Survival Analysis. In *Nonparametric Statistical Methods*, chapter 11, pages 535–608. John Wiley & Sons, Ltd, Hoboken, New Jersey, USA, 2015. doi: https://doi.org/10.1002/9781119196037.ch11, ISBN: 9781119196037.

[81] Toshimitsu Homma and Andrea Saltelli. Importance measures in global sensitivity analysis of nonlinear models. *Reliability Engineering & System Safety*, 52(1):1–17, 1996. doi: https://doi.org/10.1016/0951-8320(96)00002-6.

[82] H.P. Hong. An efficient point estimate method for probabilistic analysis. *Reliability Engineering & System Safety*, 59(3):261–267, 1998. doi: https://doi.org/10.1016/S0951-8320(97)00071-9.

[83] Zhen Hu, Xiaoping Du, Nitin S. Kolekar, and Arindam Banerjee. Robust design with imprecise random variables and its application in hydrokinetic turbine optimization. *Engineering Optimization*, 46(3):393–419, 2013. doi: https://doi.org/10.1080/0305215x.2013.772603.

[84] Beiqing Huang and Xiaoping Du. Analytical robustness assessment for robust design. *Structural and Multidisciplinary Optimization*, 34(2):123–137, 2006. doi: https://doi.org/10.1007/s00158-006-0068-0.

[85] Global Market Insights Inc. Power by the Hour (PBH) Market. Website. https://www.gminsights.com/industry-analysis/power-by-the-hour-market, Accessed: 2023-04-19.

[86] E. T. Jaynes. Discrete prior probabilities: the entropy principle. In *Probability Theory: The Logic of Science*, pages 343—-371. Cambridge University Press, 2003. doi: https://doi.org/10.1017/CBO9780511790423, ISBN: 9780511790423.

[87] Stephen Joe and Frances Y. Kuo. Constructing Sobol Sequences with Better Two-Dimensional Projections. *SIAM Journal on Scientific Computing*, 30(5):2635–2654, 2008. doi: https://doi.org/10.1137/070709359.

[88] JR Joseph J. Pignatiello. An Overview of the Strategy and Tactics of Taguchi. *IIE Transactions*, 20(3):247–254, 1988. doi: https://doi.org/10.1080/07408178808966177.

[89] Jari P. Kaipio and Erkki Somersalo. Statistical Inversion Theory. In *Statistical and Computational Inverse Problems*, pages 49–114. Springer, New York, USA, 2005. doi: https://doi.org/10.1007/0-387-27132-5_3, ISBN: 978-0-387-27132-3.

[90] Antonios Kamariotis. Mixed Aleatory-Epistemic Uncertainty Quantification and Sensitivity Analysis. Master's thesis, Professur für Computational Mechanics, Technische Universität München, München, Germany, 2019.

[91] Antonios Kamariotis, Giulia Antinori, Iason Papaioannou, and Fabian Duddeck. Mixed aleatory-epistemic uncertainty quantification and sensitivity analysis. In *17th International Probabilistic Workshop*, Edinburgh, UK, 2019.

[92] L. S. Katafygiotis and J. L. Beck. Updating Models and their Uncertainties. II: Model Identifiability. *Journal of Engineering Mechanics*, 124(4):463–467, 1998. doi: https://doi.org/10.1061/(ASCE)0733-9399(1998)124:4(463).

[93] Leonid G. Khachiyan. Rounding of Polytopes in the Real Number Model of Computation. *Mathematics of Operations Research*, 21(2):307–320, 1996. doi: https://doi.org/10.1287/moor.21.2.307.

[94] A. Kolmogoroff. Confidence Limits for an Unknown Distribution Function. *The Annals of Mathematical Statistics*, 12:461–463, 1941. doi: https://doi.org/10.1214/aoms/1177731684.

[95] Andrej N. Kolmogorov. *Grundbegriffe der Wahrscheinlichkeitsrechnung*. Julius Springer, Berlin, Germany, 1933. doi: https://doi.org/10.1007/978-3-642-49888-6, ISBN: 978-3-642-49596-0.

[96] Friedrich Kost. Ein Verfahren zur Berechnung der Meridionalströmung von Axialturbinen. Technical report, DLR Institut für Antriebstechnik, 2014. URL: https://elib.dlr.de/89589/.

[97] D.P. Kroese, T. Taimre, and Z.I. Botev. Uniform Random Number Generation. In *Handbook of Monte Carlo Methods*, chapter 1, pages 1–23. John Wiley & Sons, Hoboken, New Jersey, USA, 2011. doi: https://doi.org/10.1002/9781118014967.ch1, ISBN: 9781118014967.

[98] Sergei Kucherenko, Daniel Albrecht, and Andrea Saltelli. Exploring multi-dimensional spaces: a Comparison of Latin Hypercube and Quasi Monte Carlo Sampling Techniques. *arXiv preprint arXiv: 1505.02350*, 2015. URL: http://arxiv.org/abs/1505.02350.

[99] K. J. Kutz and T. M. Speer. Simulation of the Secondary Air System of Aero Engines. *Journal of Turbomachinery*, 116(2):306–315, 1994. doi: https://doi.org/10.1115/1.2928365.

[100] Jung-Hwan Lee, Young-Don Ko, Il-Gu Yun, and Kyong-Hee Han. Comparison of Latin Hypercube Sampling and Simple Random Sampling Applied to Neural Network Modeling of HfO_2 Thin Film Fabrication. *Transactions on Electrical and Electronic Materials*, 7(4):210–214, 2006. doi: https://doi.org/10.4313/TEEM.2006.7.4.210.

[101] Genyuan Li, Carey Rosenthal, and Herschel Rabitz. High dimensional model representations. *The Journal of Physical Chemistry A*, 105(33):7765–7777, 2001. doi: https://doi.org/10.1021/jp010450t.

[102] Genyuan Li, Sheng-Wei Wang, and Herschel Rabitz. Practical Approaches To Construct RS-HDMR Component Functions. *The Journal of Physical Chemistry A*, 106(37):8721–8733, 2002. doi: https://doi.org/10.1021/jp014567t.

[103] Haibo Liu, Ming Chen, Chong Du, Jiachang Tang, Chunming Fu, and Guilin She. A copula-based uncertainty propagation method for structures with correlated parametric p-boxes. *International Journal of Approximate Reasoning*, 138:89–104, 2021. doi: https://doi.org/10.1016/j.ijar.2021.08.002.

[104] HB Liu, C Jiang, J Liu, and JZ Mao. Uncertainty propagation analysis using sparse grid technique and saddlepoint approximation based on parameterized p-box representation. *Structural and Multidisciplinary Optimization*, 59(1):61–74, 2019. doi: https://doi.org/10.1007/s00158-018-2049-5.

[105] H.B. Liu, C. Jiang, and Z. Xiao. Efficient uncertainty propagation for parameterized p-box using sparse-decomposition-based polynomial chaos expansion. *Mechanical Systems and Signal Processing*, 138:106589, 2020. doi: https://doi.org/10.1016/j.ymssp.2019.106589.

[106] David Lönn, Greger Bergman, Larsgunnar Nilsson, and Kjell Simonsson. Experimental and finite element robustness studies of a bumper system subjected to an offset impact loading. *International Journal of Crashworthiness*, 16(2):155–168, 2011. doi: https://doi.org/10.1080/13588265.2010.539339.

[107] Norbert Ludwig, Giulia Antinori, Marco Daub, and Fabian Duddeck. Uncertainty Quantification of a Jet Engine Performance Model Under Scarce Data Availability. In *ASME*

Turbo Expo 2021: Turbomachinery Technical Conference and Exposition, 2021. doi: https://doi.org/10.1115/GT2021-58604.

[108] Norbert Ludwig, Fabian Duddeck, and Marco Daub. A Hyper-Ellipsoid Approach for Inverse Lack-of-Knowledge Uncertainty Quantification. *ASCE-ASME J Risk and Uncert in Engrg Sys Part B Mech Engrg*, 7(2), 2021. doi: https://doi.org/10.1115/1.4050162.

[109] George Marsaglia. Choosing a Point from the Surface of a Sphere. *The Annals of Mathematical Statistics*, 43(2):645–646, 1972. doi: https://doi.org/10.1214/aoms/1177692644.

[110] M.A.F. Martins, R. Requião, and Ricardo de Araújo Kalid. Generalized expressions of second and third order for the evaluation of standard measurement uncertainty. *Measurement*, 44(9):1526–1530, 2011. doi: https://doi.org/10.1016/j.measurement.2011.06.008.

[111] Ryan G. McClarren. Local Sensitivity Analysis Based on Derivative Approximations. In *Uncertainty Quantification and Predictive Computational Science: A Foundation for Physical Scientists and Engineers*, chapter 4, pages 95–109. Springer International Publishing, Cham, Germany, 2018. doi: https://doi.org/10.1007/978-3-319-99525-0_4, ISBN: 978-3-319-99525-0.

[112] M. D. McKay, R. J. Beckman, and W. J. Conover. A Comparison of Three Methods for Selecting Values of Input Variables in the Analysis of Output from a Computer Code. *Technometrics*, 21(2):239–245, 1979. doi: https://doi.org/10.2307/1268522.

[113] Lukas Meier. Statistische Tests und Vertrauensintervalle für eine Stichprobe. In *Wahrscheinlichkeitsrechnung und Statistik: Eine Einführung für Verständnis, Intuition und Überblick*, chapter 7, pages 149–188. Springer, Berlin, Heidelberg, Germany, 2020. doi: https://doi.org/10.1007/978-3-662-61488-4_7, ISBN: 978-3-662-61488-4.

[114] Leslie H. Miller. Table of Percentage Points of Kolmogorov Statistics. *Journal of the American Statistical Association*, 51(273):111–121, 1956. doi: https://doi.org/10.2307/2280807.

[115] David Moens and Michael Hanss. Non-probabilistic finite element analysis for parametric uncertainty treatment in applied mechanics: Recent advances. *Finite Elements in Analysis and Design*, 47(1):4–16, 2011. doi: https://doi.org/10.1016/j.finel.2010.07.010.

[116] Bernd Möller and Michael Beer. *Fuzzy Randomness: Uncertainty in Civil Engineering and Computational Mechanics*. Springer, Berlin, Heidelberg, Germany, 2004. doi: https://doi.org/10.1007/978-3-662-07358-2, ISBN: 978-3-662-07358-2.

[117] Bernd Möller and Michael Beer. Engineering computation under uncertainty - Capabilities of non-traditional models. *Computers & Structures*, 86(10):1024–1041, 2008. doi: https://doi.org/10.1016/j.compstruc.2007.05.041.

[118] A. Moore. Gas Turbine Engine Internal Air Systems: A Review of the Requirements and the Problems. In *ASME 1975 Winter Annual Meeting: GT Papers*, 1975. doi: https://doi.org/10.1115/75-WA/GT-1.

[119] William J. Morokoff and Russel E. Caflisch. Quasi-Random Sequences and their Discrepancies. *SIAM Journal on Scientific Computing*, 15(6):1251–1279, 1994. doi: https://doi.org/10.1137/0915077.

[120] Yannick Muller. *Coupled thermomechanical fluid-structure interaction in the secondary air system of aircraft engines*. PhD thesis, Université de Valenciennes et du Hainaut-Cambrésis, Valenciennes, France, 2009. URL: https://uphf.hal.science/tel-03032916.

[121] Vijayan N. Nair, Bovas Abraham, Jock MacKay, John A. Nelder, George Box, Madhav S. Phadke, Raghu N. Kacker, Jerome Sacks, William J. Welch, Thomas J. Lorenzen, Anne C. Shoemaker, Kwok L. Tsui, James M. Lucas, Shin Taguchi, Raymond H. Myers, G. Geoffrey Vining, and C. F. Jeff Wu. Taguchi's Parameter Design: A Panel Discussion. *Technometrics*, 34(2):127–161, 1992. doi: https://doi.org/10.2307/1269231.

[122] Harald Niederreiter. Quasi-Monte Carlo methods and pseudo-random numbers. *Bulletin of the American Mathematical Society*, 84(6):957 – 1041, 1978.

[123] Michael Oberguggenberger and Wolfgang Fellin. Reliability bounds through random sets: non-parametric methods and geotechnical applications. *Computers & Structures*, 86(10):1093–1101, 2008. doi: https://doi.org/10.1016/j.compstruc.2007.05.040.

[124] Michael Oberguggenberger, Julian King, and Bernhard Schmelzer. Classical and imprecise probability methods for sensitivity analysis in engineering: A case study. *International Journal of Approximate Reasoning*, 50(4):680–693, 2009. doi: https://doi.org/10.1016/j.ijar.2008.09.004.

[125] William L. Oberkampf, Jon C. Helton, Cliff A. Joslyn, Steven F. Wojtkiewicz, and Scott Ferson. Challenge problems: uncertainty in system response given uncertain parameters. *Reliability Engineering & System Safety*, 85(1-3):11–19, 2004. doi: https://doi.org/10.1016/j.ress.2004.03.002.

[126] Gyung-Jin Park, Tae-Hee Lee, Kwon Hee Lee, and Kwang-Hyeon Hwang. Robust design: An overview. *AIAA Journal*, 44(1):181–191, 2006. doi: https://doi.org/10.2514/1.13639.

[127] A. Parkinson. Robust Mechanical Design Using Engineering Models. *Journal of Vibration and Acoustics*, 117(B):48–54, 1995. doi: https://doi.org/10.1115/1.2838676.

[128] Nicola Pedroni and Enrico Zio. Hybrid uncertainty and sensitivity analysis of the model of a twin-jet aircraft. *Journal of Aerospace Information Systems*, 12(1):73–96, 2015. doi: https://doi.org/10.2514/1.I010265.

[129] Rik Peels. What Is Ignorance? *Philosophia*, 38(1):57–67, 2009. doi: https://doi.org/10.1007/s11406-009-9202-8.

[130] Peter F. Pelz and Marc E. Pfetsch. Der Unsicherheit von Anfang an auf der Spur. Website, 2015. https://www.pt-magazin.de/de/specials/industrie/der-unsicherheit-von-anfang-an-auf-der-spur_1g8l.html?&highlight=1&keys=&lang=1, Accessed: 2022-01-21.

[131] Peter F. Pelz, Marc E. Pfetsch, Sebastian Kersting, Michael Kohler, Alexander Matei, Tobias Melz, Roland Platz, Maximilian Schaeffner, and Stefan Ulbrich. Types of Uncertainty. In *Mastering Uncertainty in Mechanical Engineering*, chapter 2, pages 25–42. Springer Nature Switzerland AG, Cham, Switzerland, 2021. doi: https://doi.org/10.1007/978-3-030-78354-9_2, ISBN: 978-3-030-78354-9.

[132] M. S. Phadke. Quality Engineering using Design of Experiments. In Khosrow Dehnad, editor, *Quality Control, Robust Design, and the Taguchi Method*, pages 31–50. Springer US, Boston, USA, 1989. doi: https://doi.org/10.1007/978-1-4684-1472-1_3, ISBN: 978-1-4684-1472-1.

[133] Thomas Potthast. Quantification of Epistemic Uncertainties of an Interdisciplinary Performance and Aero Model. Master's thesis, Institute for Risk and Reliability, Leibniz Universität Hannover, Hannover, Germany, 2021.

[134] Alejandro Pozo Dominguez, Nicholas Hills, and Simao Marques. Sensitivity Analysis and Uncertainty Quantification for Rim Seal Ingestion With 1-D Network Models. In *Turbo Expo: Power for Land, Sea, and Air*, 2020. doi: https://doi.org/10.1115/GT2020-15218.

[135] Andriy Prots, Lukas Schlüter, Matthias Voigt, Ronald Mailach, and Marcus Meyer. Impact of Epistemic Uncertainty on Performance Parameters of Compressor Blades. In *ASME Turbo Expo: Power for Land, Sea, and Air*, 2022. doi: https://doi.org/10.1115/GT2022-82579.

[136] Friedrich Pukelsheim. The Three Sigma Rule. *The American Statistician*, 48(2):88–91, 1994. doi: https://doi.org/10.1080/00031305.1994.10476030.

[137] Kandethody M. Ramachandran and Chris P. Tsokos. Statistical Estimation. In *Mathematical Statistics with Applications in R*, chapter 5, pages 219–310. Academic Press, Boston, USA, 2015. doi: https://doi.org/10.1016/B978-0-12-417113-8.00005-9, ISBN: 978-0-12-417113-8.

[138] S.S. Rao. Nonlinear Programming III: Constrained Optimization Techniques. In *Engineering Optimization Theory and Practice*, chapter 7, pages 347–448. John Wiley & Sons, Ltd, New Jersey, USA, 2019. doi: https://doi.org/10.1002/9781119454816.ch7, ISBN: 9781119454816.

[139] Carl Edward Rasmussen and Christopher K. I. Williams. *Gaussian Processes for Machine Learning*. The MIT Press, Cambridge, Massachusetts, USA, 2005. doi: https://doi.org/10.7551/mitpress/3206.001.0001, ISBN: 9780262256834.

[140] Expert Market Research. Global Power by the Hour (PBH) Market Outlook. Website. https://www.expertmarketresearch.com/reports/power-by-the-hour-pbh-market, Accessed: 2023-04-19.

[141] Hans Rick. Betriebsverhalten und Simulation von Turbojet und Turboshaft-Gasturbinen der Flug-, Energie- und Fahrzeugtechnik. In *Gasturbinen und Flugantriebe: Grundlagen, Betriebsverhalten und Simulation*, chapter 7, pages 621–698. Springer Vieweg, Berlin, Germany, 2013. doi: https://doi.org/10.1007/978-3-540-79446-2_7, ISBN: 978-3-540-79446-2.

[142] Hans Rick. Turbomaschinen-Komponenten. In *Gasturbinen und Flugantriebe: Grundlagen, Betriebsverhalten und Simulation*, chapter 4, pages 293–539. Springer Vieweg, Berlin, Germany, 2013. doi: https://doi.org/10.1007/978-3-540-79446-2_4, ISBN: 978-3-540-79446-2.

[143] Hauke Riesch. Levels of Uncertainty. In *Essentials of Risk Theory*, chapter 2, pages 29–56. Springer Netherlands, Dordrecht, Netherlands, 2013. doi: https://doi.org/10.1007/978-94-007-5455-3_2, ISBN: 978-94-007-5455-3.

[144] Markus Rippel, Seung-Kyum Choi, Farrokh Mistree, and Janet Allen. Alternatives to Taylor Series Approximation for the Variance Estimation in Robust Design. In *13th AIAA/ISSMO Multidisciplinary Analysis Optimization Conference*. American Institute of Aeronautics and Astronautics, 2010. doi: https://doi.org/10.2514/6.2010-9083.

[145] Sébastien Roux, Samuel Buis, François Lafolie, and Matieyendou Lamboni. Cluster-based GSA: Global sensitivity analysis of models with temporal or spatial outputs using clustering. *Environmental Modelling & Software*, 140:105046, 2021. doi: https://doi.org/10.1016/j.envsoft.2021.105046.

[146] Neil C. Rowe. Absolute Bounds on the Mean and Standard Deviation of Transformed Data for Constant-Sign-Derivative Transformations. *Journal of Scientific and Statistical Computing*, 9(6):1098—-1113, 1988. doi: https://doi.org/10.1137/0909076.

[147] Rolls Royce. Internal cooling system. In *The Jet Engine*, chapter 9, pages 85–94. 5th edition, 1986. ISBN: 0902121 235.

[148] Wilhelm Rumler, Thomas Günther, U. Weißhaar, and H. Fricke. Flight profile variations due to the spreading practice of cost index based flight planning. In *4th International Conference on Research in Air Transportation*, Budapest, Hungary, 2010. URL: https://api.semanticscholar.org/CorpusID:199366064.

[149] Julian Salomon, Niklas Winnewisser, Pengfei Wei, Matteo Broggi, and Michael Beer. Efficient reliability analysis of complex systems in consideration of imprecision. *Reliability Engineering & System Safety*, 216:107972, 2021. doi: https://doi.org/10.1016/j.ress.2021.107972.

[150] Andrea Saltelli. Sensitivity analysis: Could better methods be used? *Journal of Geophysical Research: Atmospheres*, 104(D3):3789–3793, 1999. doi: https://doi.org/10.1029/1998JD100042.

[151] Andrea Saltelli, Paola Annoni, Ivano Azzini, Francesca Campolongo, Marco Ratto, and Stefano Tarantola. Variance based sensitivity analysis of model output. Design and estimator for the total sensitivity index. *Computer Physics Communications*, 181(2):259–270, 2010. doi: https://doi.org/10.1016/j.cpc.2009.09.018.

[152] Andrea Saltelli and Ricardo Bolado. An alternative way to compute Fourier amplitude sensitivity test (FAST). *Computational Statistics & Data Analysis*, 26(4):445–460, 1998. doi: https://doi.org/10.1016/S0167-9473(97)00043-1.

[153] Andrea Saltelli, Karen Chan, and E. Marian Scott. *Sensitivity Analysis*. John Wiley & Sons, Chichester, UK, 2000. ISBN: 978-0-471-99892-1.

[154] Andrea Saltelli, Marco Ratto, Terry Andres, Francesca Campolongo, Jessica Cariboni, Debora Gatelli, Michaela Saisana, and Stefano Tarantola. *Global Sensitivity Analysis. The Primer*. John Wiley & Sons, Chichester, UK, 2008. doi: https://doi.org/10.1002/9780470725184, ISBN: 978-0-470-05997-5.

[155] Daniel Sandberg, Rami Mansour, and Mårten Olsson. Fatigue probability assessment including aleatory and epistemic uncertainty with application to gas turbine compressor blades. *International Journal of Fatigue*, 95:132–142, 2017. doi: https://doi.org/10.1016/j.ijfatigue.2016.10.001.

[156] Roland Schöbi and Bruno Sudret. Global sensitivity analysis in the context of imprecise probabilities (p-boxes) using sparse polynomial chaos expansions. *Reliability Engineering & System Safety*, 187:129–141, 2019. doi: https://doi.org/10.1016/j.ress.2018.11.021.

[157] René Schenkendorf. A General Framework for Uncertainty Propagation Based on Point Estimate Methods. In *Second European Conference of the Prognostics and Health Management Society*, 2014. doi: https://doi.org/10.13140/2.1.2646.8489.

[158] Roland Schöbi. *Surrogate models for uncertainty quantification in the context of imprecise probability modelling*. PhD thesis, ETH Zürich, Zurich, Switzerland, 2017. doi: https://doi.org/10.3929/ethz-a-010870825.

[159] Alexander Schrijver. *Theory of Linear and Integer Programming*. John Wiley & Sons, New York, USA, 1998. ISBN: 978-0-471-98232-6.

[160] Airbus Customer Services. Getting to grips with the cost index. In *Flight Operations Support & Line Assistance*. Issue II. Blagnac, Fance, 1998.

[161] Glenn Shafer. *A Mathematical Theory of Evidence*. Princeton University Press, Princeton, New Jersey, USA, 1976. ISBN: 9780691100425.

[162] Ilya M. Sobol. Uniformly distributed sequences with an additional uniform property. *USSR Computational Mathematics and Mathematical Physics*, 16(5):236–242, 1976. doi: https://doi.org/10.1016/0041-5553(76)90154-3.

[163] Ilya M. Sobol. Sensitivity Estimates for Nonlinear Mathematical Models. *Mathematical modelling and computational experiment*, 1:407–414, 1993.

[164] Ilya M. Sobol. Global sensitivity indices for nonlinear mathematical models and their Monte Carlo estimates. *Mathematics and Computers in Simulation*, 55(1):271–280, 2001. doi: https://doi.org/10.1016/S0378-4754(00)00270-6.

[165] Jingwen Song, Pengfei Wei, Marcos Valdebenito, Sifeng Bi, Matteo Broggi, Michael Beer, and Zuxiang Lei. Generalization of non-intrusive imprecise stochastic simulation for mixed uncertain variables. *Mechanical Systems and Signal Processing*, 134:106316, 2019. doi: https://doi.org/10.1016/j.ymssp.2019.106316.

[166] Daniel Straub. Lecture Notes in Engineering Risk Analysis. ERA Group, Technical University of Munich, Germany, 2017.

[167] Peng Sun and Robert M. Freund. Computation of Minimum-Volume Covering Ellipsoids. *Operations Research*, 52(5):690–706, 2004. doi: https://doi.org/10.1287/opre.1040.0115.

[168] Yanbo Tang. A Note on Monte Carlo Integration in High Dimensions. *arXiv preprint arXiv: 2206.09036*, 2022. doi: https://doi.org/10.48550/arXiv.2206.09036.

[169] P. Tchébychef. Des valeurs moyennes. *Journal de Mathématiques Pures et Appliquées*, 12:177–184, 1867.

[170] Kwok-Leung Tsui. An Overview of Taguchi Method and Newly Developed Statistical Methods for Robust Design. *IIE Transactions*, 24(5):44–57, 1992. doi: https://doi.org/10.1080/07408179208964244.

[171] Don van Ravenzwaaij, Pete Cassey, and Scott D. Brown. A simple introduction to Markov Chain Monte-Carlo sampling. *Psychonomic Bulletin & Review*, 25(1):143–154, 2016. doi: https://doi.org/10.3758/s13423-016-1015-8.

[172] Warren E. Walker, Poul Harremoës, Jan Rotmans, Jeroen P. Van Der Sluijs, Marjolein B.A. Van Asselt, Peter Janssen, and Martin P. Krayer von Krauss. Defining Uncertainty: A Conceptual Basis for Uncertainty Management in Model-Based Decision Support. *Integrated Assessment*, 4(1):5–17, 2003. doi: https://doi.org/10.1076/iaij.4.1.5.16466.

[173] Pengfei Wei, Zhenzhou Lu, and Jingwen Song. Extended Monte Carlo simulation for parametric global sensitivity analysis and optimization. *AIAA journal*, 52(4):867–878, 2014. doi: https://doi.org/10.2514/1.J052726.

[174] Pengfei Wei, Jingwen Song, Sifeng Bi, Matteo Broggi, Michael Beer, Zhenzhou Lu, and Zhufeng Yue. Non-intrusive stochastic analysis with parameterized imprecise probability models: I. Performance estimation. *Mechanical Systems and Signal Processing*, 124:349–368, 2019. doi: https://doi.org/10.1016/j.ymssp.2019.01.058.

[175] Pengfei Wei, Jingwen Song, Sifeng Bi, Matteo Broggi, Michael Beer, Zhenzhou Lu, and Zhufeng Yue. Non-intrusive stochastic analysis with parameterized imprecise probability models: II. Reliability and rare events analysis. *Mechanical Systems and Signal Processing*, 126:227–247, 2019. doi: https://doi.org/10.1016/j.ymssp.2019.02.015.

[176] Dominik Woelki and Dieter Peitsch. A Framework for Applied Component Zooming in Gas Turbines. In *Deutscher Luft- und Raumfahrtkongress 2019*, 2020. doi: https://doi.org/10.25967/490174.

[177] Wojbor A. Woyczyński. Random Quantities and Random Vectors. In *A First Course in Statistics for Signal Analysis*, chapter 4, pages 91–148. Springer Nature Switzerland AG, Cham, Switzerland, 2019. doi: https://doi.org/10.1007/978-3-030-20908-7_4, ISBN: 978-3-030-20908-7.

[178] Ciyou Zhu, Richard H. Byrd, Peihuang Lu, and Jorge Nocedal. Algorithm 778: L-BFGS-B: Fortran Subroutines for Large-Scale Bound-Constrained Optimization. *ACM Trans. Math. Softw.*, 23(4):550–560, 1997. doi: https://doi.org/10.1145/279232.279236.

[179] Xujia Zhu and Bruno Sudret. Emulation of Stochastic Simulators Using Generalized Lambda Models. *SIAM/ASA Journal on Uncertainty Quantification*, 9(4):1345–1380, 2021. doi: https://doi.org/10.1137/20M1337302.

[180] Enrico Zio. Monte Carlo Simulation: The Method. In *The Monte Carlo Simulation Method for System Reliability and Risk Analysis*, chapter 3, pages 19–58. Springer London, London, UK, 2013. doi: https://doi.org/10.1007/978-1-4471-4588-2_3, ISBN: 978-1-4471-4588-2.